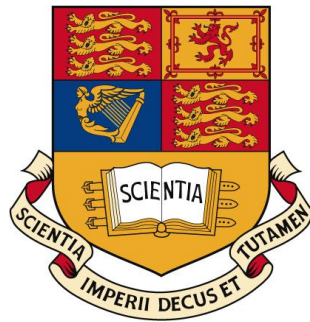


Ambipolar Organic Transistors for Opto-Electronic Applications



John Graham Labram
Department of Physics
Imperial College London

A thesis submitted for the degree of

Doctor of Philosophy

August 31st, 2011

This thesis describes work carried out within the Department of Physics at Imperial College London between October 2008 and August 2011. Except where specific reference is made to the involvement of others, the work presented herein is a product of my own work. The material in this thesis has not been submitted in whole or in part for the award of a degree at this, or any other institution.

John Graham Labram
31st August 2011

Acknowledgements

I would like to first and foremost acknowledge my supervisor Thomas Anthopoulos for his fantastic guidance, advice, knowledge and creative ideas. I have learnt a great deal from him during my PhD and am immensely grateful.

I am incredibly grateful to all the members of Thomas' group, who have trained and assisted me during my work. Specifically I would like to thank Paul Wöbkenberg, Jeremy Smith, James Ball, Aneeqa Bashir, Georges Adamopoulos, Florian Colleaux and Stuart Thomas.

I would like to extend my thanks to all the collaborators who carried out work on my behalf; specifically Ester Buchaca Domingo for carrying out differential scanning calorimetry measurements and James Kirkpatrick for his assistance in my theoretical work.

I would like to acknowledge the following members of the group office; Carolyn Dale, Bhavna Patel, Becky Smith, Claudia Harriott and Juraci Didone for their efficient assistance in admin-related issues. And I would also like to thank Steve Cussell, Alasdair Campbell and the cleanroom committee for their significant efforts to keep the cleanroom an effective place to work. Additionally I would like to thank several other members of the Centre for Plastic Electronics at Imperial who have helped me in some way during my time at Imperial: Donal Bradley, Martin Heeney, Natalie Stingelin-Stutzmann, Jenny Nelson, James Durrant and Iain McCulloch.

Finally, I would like to of course thank my friends and family for their unprecedented levels of support, encouragement and praise during my PhD. I especially thank Liz Ablett for her unwavering support and for tolerating me when times were difficult.

Abstract

This thesis is concerned with the development and study of ambipolar organic field-effect transistors (OFETs), with a specific focus on devices and structures that are relevant to opto-electronic processes. After giving an outline of the relevant theory and experimental methods, the thesis is divided into three experimental chapters.

In the chapter on organic phototransistors (OPTs), the fabrication of low-voltage bilayer OPTs is carried out using self-assembled monolayer gate dielectrics. By combining two low-voltage OPTs, the output voltage of a so-called photo-inverter was observed to be modulated over a range of 1.5 V with an incident optical power density of 0 to 1.2 mWcm⁻². The characteristics of a high-voltage polymer:fullerene blend photo-inverter device are modelled using variable-range hopping and simple circuit models, suggesting that the device operation is dominated by changes in the threshold voltage.

In the second experimental chapter the relationship between the morphology of polymer:fullerene blends and the characteristics of OFETs is studied. It is shown that the thermally-induced clustering of fullerenes is manifest as a reduction in electron mobility, due to a reduction in percolating pathways. It is additionally found that higher molecular-weight fullerenes require greater annealing temperature and/or times for this process to occur.

The final experimental chapter is concerned with polymer:fullerene diffusion processes and the study of such phenomena using bilayer OFETs. A model based upon the diffusion equation and percolation theory is employed to quantify this process. Again, higher molecular-weight fullerenes are observed to require greater annealing temperature for similar phenomena to be observed.

Contents

Contents	5
1 Introduction	9
1.1 Organic Field-Effect Transistors	12
1.2 Thesis Outline	13
2 Theory	15
2.1 Organic Semiconductors	15
2.1.1 Conjugated Small Molecules and Polymers	15
2.1.2 Excitons	18
2.2 Charge-Transport Models	19
2.2.1 Band-Like Transport	19
2.2.2 Multiple Trapping and Release Models	20
2.2.3 Variable-Range Hopping	21
2.2.4 Percolation Theory	23
2.3 Organic Field-Effect Transistors	24
2.3.1 Architecture of Field-Effect Transistors	24
2.3.2 Operating Principles of Field-Effect Transistors	26
2.3.3 Current-Voltage Characteristics	28
2.3.4 OFET Parameter Extraction	30
2.3.5 The dielectric	33
2.4 Ambipolar OFETs	36
2.4.1 Operation of Ambipolar OFETs	37
2.4.2 Routes to Ambipolarity	41
2.5 Organic Phototransistors	43

2.5.1	Operating Principles of OPTs	44
2.5.2	Characterisation of OPTs	46
2.6	Integrated circuits	47
2.6.1	Inverters	47
2.6.2	Opto-electric logic gates	48
2.7	Semiconductor Materials	49
2.7.1	Hole-Transporting Organic Semiconductors	50
2.7.2	Electron-Transporting Organic Semiconductors	50
2.7.3	Ambipolar Organic Semiconductors	54
2.8	Bulk Heterojunction Solar Cells	55
2.8.1	Operating Principle of OPVs	56
2.8.2	Characterisation of OPVs	57
2.8.3	Morphology of Polymer:Fullerene OPVs	59
3	Experimental Methods	62
3.1	Introduction	62
3.2	Transistor Fabrication Techniques	62
3.2.1	Substrate Preparation	63
3.2.2	Application of Self-Assembled Monolayers	63
3.2.3	Solution-Deposition of Organic Materials	64
3.2.4	Vacuum-deposition	65
3.3	Electrical Characterisation	67
3.3.1	Impedance Spectroscopy	67
3.3.2	Current-Voltage Characteristics	67
3.3.3	Light-Sensing Measurements	69
3.4	Other Semiconductor Characterisation Techniques	70
3.4.1	Optical Absorption Spectroscopy	70
3.4.2	Atomic Force Microscopy	71
3.4.3	Polarised Optical Microscopy	71
3.4.4	Differential Scanning Calorimetry	72
4	Organic Phototransistors	73
4.1	Introduction	73

4.2	Bilayer Pentacene:Fullerene Organic Field-Effect Transistors . . .	74
4.2.1	Evaporated small-molecule phototransistors	74
4.2.2	Pentacene:PC ₆₁ BM OFETs	77
4.2.3	Photoresponse of Pentacene:PC ₆₁ BM OFETs	80
4.3	Low-Voltage Pentacene:PC ₆₁ BM Phototransistors	83
4.3.1	Photoresponse of Low-Voltage Pentacene:PC ₆₁ BM OFETs	85
4.4	Organic Opto-Electronic Circuits	87
4.4.1	Low-Voltage Pentacene:PC ₆₁ BM Photo-Inverters	87
4.4.2	MDMO-PPV:PC ₆₁ BM Photo-Inverters	89
4.5	Simulation of Opto-Electronic Circuit Operation	93
4.5.1	Smits Model of Ambipolar Transport in OFETs	94
4.5.2	Fitting the Smits Model to Experimental Data	97
4.5.3	Modelling Complementary-Like Inverters	100
4.6	Conclusions	103
5	Polymer:Fullerene Blend Morphology	106
5.1	Introduction	106
5.2	Detecting Phase Segregation Using OFETs	107
5.2.1	Optical Microscope Images	107
5.2.2	Mobility Evolution in P3HT:PC ₆₁ BM Blend OFETs	109
5.2.3	Dual-Gate Mobility Measurements	114
5.2.4	Time-Dependence of Mobility Evolution	116
5.3	Simulation of OFET Channel Conductivity	118
5.3.1	2-Dimensional Resistor-Network Model	118
5.3.2	Simulating Fullerene-Clustering	120
5.3.3	Calculated Conductivity	122
5.4	Phase Segregation in Blends of P3HT:PC ₆₁ BM and P3HT:PC ₇₁ BM	124
5.4.1	P3HT:PC ₇₁ BM Blend OFETs	125
5.4.2	Time-Dependent P3HT:PC ₇₁ BM Mobility Measurements .	127
5.5	Conclusions	129
6	Polymer:Fullerene Diffusion Processes	131
6.1	Introduction	131

6.2	Evaporated PC ₆₁ BM OFETs	132
6.3	Bilayer P3HT:PC ₆₁ BM OFETs	134
6.3.1	Time-Dependent Mobility Measurements	138
6.4	Modelling the Evolution of Electron Mobility	139
6.4.1	Modelling the Diffusion of Fullerenes	140
6.4.2	Relating Concentration to Mobility	141
6.4.3	Applying the Model to Experimental Data	146
6.5	Bilayer P3HT:PC ₇₁ BM OFETs	148
6.5.1	Time-Dependent Measurements	152
6.5.2	Atomic Force Microscope Images	153
6.6	Conclusions	155
7	Conclusions	157
A	Solution to Diffusion Equation	161
B	List of Publications	167
	References	170

Chapter 1

Introduction

Since the inception of the first transistor,[1–4] the importance of microelectronics has grown exponentially. Today we are at a point where the electronics revolution and the beginning of the information age could be viewed as important, or indeed more-so, than the industrial revolution. With the price of certain transistors approximated as 10^{-7} \$US (when part of an integrated circuit),[5] the average home in a developed country is now likely to have hundreds of integrated circuits in everything from washing machines and toasters to cars and mobile phones.

The rise of this industry has been down to the amazing properties of silicon, a material that is both highly naturally abundant and incredibly well understood.[6–8] The immense commercial and academic interest in silicon has helped maintain the so-called Moore’s Law, whereby the number of transistors that can inexpensively fit onto a single integrated circuit doubles every 24 months, has been maintained for over 40 years.[9]

In the 1970’s,[10] or perhaps (controversially) in the 1960’s,[11–13] it was demonstrated that certain polymers could conduct electricity. This was a feat which earned Alan Heeger, Alan MacDiarmid and Hideki Shirakawa an equal share of the 2000 Nobel Prize in Chemistry. This discovery gave birth to the now enormous research field of organic electronics. Combining the appealing physical properties of organic materials with semiconducting behaviour has led to the realisation of previously unimaginable applications.[14] Since the discovery of conducting polymers, devices such as Schottky diodes,[15–17] photovoltaic cells,[15, 18, 19] light-emitting diodes (LEDs),[20, 21] and field-effect transistors

(FETs)[17, 22, 23] have all been fabricated using organic semiconductors.



Figure 1.1: Example of commercially available products employing organic electronics. (a) Nokia N9 mobile phone. (b) LG 15EL9500 OLED television. (c) Latest Sony Playstation Portable games console.

Organic electronics provides the potential to produce low-cost, large-area electronics compatible with flexible substrates. Organic electronics is anticipated to become a multi-billion dollar industry within the next few years and to completely revolutionise consumer electronics. Displays based upon organic light-emitting diodes (OLEDs) are already in use within several mobile phones, game consoles and televisions (see Figure 1.1 for some examples). In the longer term, several companies expect to produce devices such as solar cells, transistor backplanes and lightbulbs using organic electronics (see Figure 1.2). As an indicator of in-

vestor perception, consider the stock price of Universal Display Corporation, one of the few publicly-listed companies that is exclusively concerned with organic electronics. Its price has risen approximately 400% in the last 5 years despite very challenging economic times.

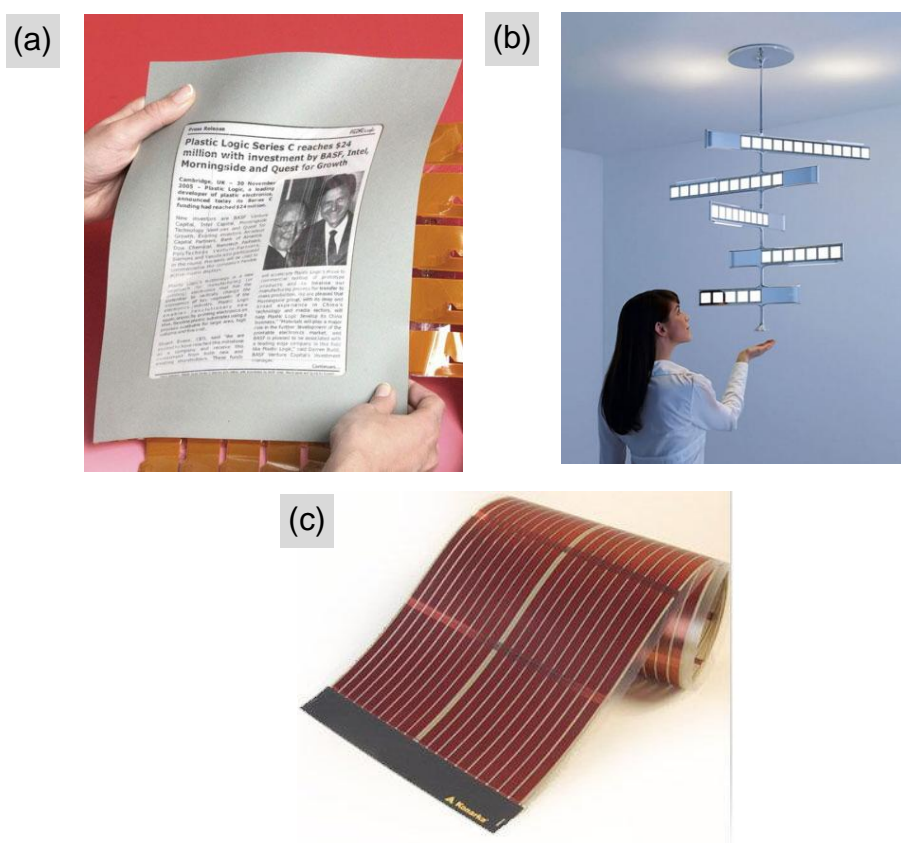


Figure 1.2: Example of prototype products employing organic electronics which are expected to enter the marketplace in the next few years. (a) Flexible newspaper from Plastic Logic. (b) OLED chandelier from Philips. (c) Organic solar cell from Konarka.

Due to their disordered nature, the charge carrier mobility of organic materials is unlikely ever to reach that of crystalline silicon. Hence organic electronics is viewed primarily as an alternative rather than a potential replacement of silicon for microelectronics. Carbon nanotubes and graphene on the other hand have often been mentioned as possible future replacements of silicon due to the

extremely high carrier mobilities observed in such systems.[24–28]

It is none-the-less the advantageous processing techniques and unique properties that give rise to the excitement about organic electronics. The solubility of certain semiconductor materials for example opens the door to highly-scalable and extremely low-cost deposition techniques such as printing.[29–31] Organic materials are in most cases incredibly versatile and are compatible with flexible and stretchable substrates.[32–34] Organic semiconductors are also highly suited for interacting with biological systems,[35, 36] paving the way for many unique medical applications. By employing naturally-occurring organic compounds, devices which are bio-degradable have also been demonstrated.[37, 38]

One of the most attractive features of organic materials is the vast range of optical and electronic properties that can be produced as a result of changes in the chemical structure. By lowering the band gap for example, devices can be made that are sensitive to red and infra-red light,[39, 40] a particularly prominent part of the solar spectrum.[41] Similarly if semiconductors are designed with a wide band gap they could potentially be employed in transparent electronics.

1.1 Organic Field-Effect Transistors

The transistor is an electronic switch, and when combined with others they are capable of processing information.[42] The benefits of organic field-effect transistors (OFETs) with respect to their inorganic counterparts are similar to those of organic electronics in general; i.e. low-cost, high-throughput fabrication techniques compatible with large-area, flexible substrates. Possible applications of OFETs include low-cost radio-frequency identification (RFID) tags[43, 44] and flexible active-matrix electronic displays[33, 45] (see Figure 1.3). Currently however, the charge carrier mobilities of most OFETs reported are not quite high enough to make commercial implementation of these devices viable.

Up until recently OFETs have exclusively been used as unifunctional devices. Now however, devices with additional functionality such as light-emission[46–48] and light-sensitivity[49–51] have been demonstrated. OFETs also provide a very useful environment for testing the electrical and optical properties of different organic semiconductor materials.[52–54]

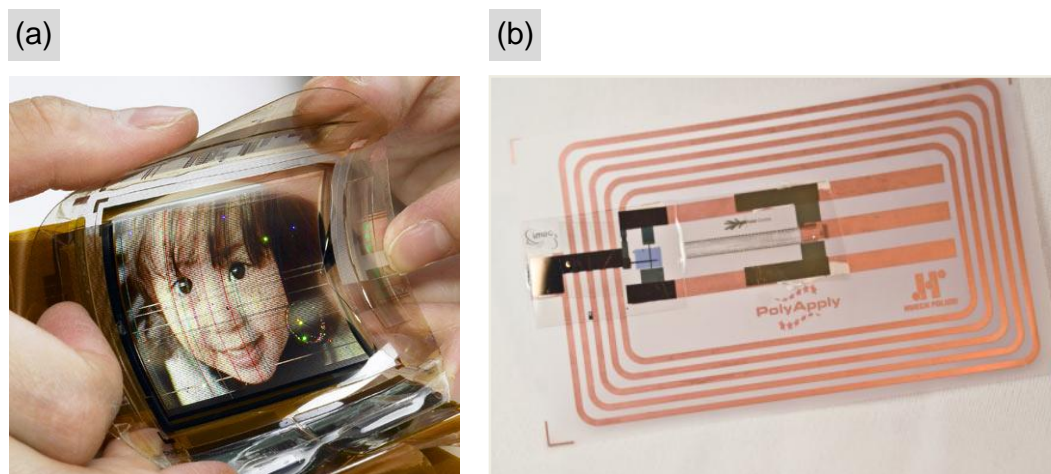


Figure 1.3: Example of prototype products employing OFETs. (a) Flexible video display with OFET backplane from Sony. (b) Flexible radio-frequency identification tag from IMEC.

1.2 Thesis Outline

This thesis concerns itself with the development and study of ambipolar organic field-effect transistors, that is OFETs capable of transporting both holes and electrons. Specifically, the work presented here is restricted to the study of systems relevant for opto-electronic processes.

The second chapter gives an overview of the theory of organic semiconductors, OFETs and organic photovoltaic cells (OPVs). Whilst OPVs are not fabricated or studied directly within this work, the results of OFET measurements presented are however relevant to OPV development. The third chapter describes the experimental techniques and equipment employed throughout this work. The fourth chapter contains measurements made on light-sensitive OFETs; so-called organic phototransistors (OPTs). Both bilayer and blend OPTs are studied, with the goal of lowering operating voltages and producing novel opto-electronic circuits.

In Chapter 5 I have studied how OFETs can be used as tools to characterise other systems relevant for photonic devices, such as organic photovoltaic cells (OPVs). By using the same semiconductor materials as those used within OPVs, I have shown that charge transport measurements made using OFETs can reveal

important characteristics of OPV-relevant semiconductor systems, such as the morphology. In Chapter 6 I have applied OFETs to understand and quantify the diffusion of fullerenes in polymers. This phenomenon is of crucial importance to understanding the stability and efficiency of OPV-relevant systems. The thesis ends with a short conclusion, describing the way in which my work fits into the world of organic electronics more generally and the current outlook for the future.

Chapter 2

Theory

2.1 Organic Semiconductors

In general a molecule can be described as being organic if it consists of at least one carbon atom, although in reality the distinction between organic and inorganic compounds is not strictly defined. Carbon allotropes such as carbon nanotubes[24] and graphene[26] are not widely referred-to as organic semiconductors, whilst buckminsterfullerene[55] for example is. Organic electronics relies on the electrical conductivity of conjugated carbon systems. The basis of how organic systems conduct electricity is best understood in terms of orbital hybridization.

2.1.1 Conjugated Small Molecules and Polymers

Carbon has the ground state electronic structure: $C=1s^22s^22p^2$. If one electron is excited from the 2s state to the 2p state, the configuration becomes: $C^*=1s^22s^12p^3$. The 1s orbital is highly localised and electrons occupying this state do not participate in bonding. By considering a linear combination of the 2s and 2p states, hybridized orbitals can be constructed. Using Dirac notation the sp^2 orbital can be described by equation 2.1.

$$|sp^2\rangle = 1/3 |2s\rangle + 2/3 |2p\rangle \quad (2.1)$$

The 2s and two of the 2p orbitals ‘mix’ or *hybridize* into three highly directional sp^2 orbitals. These orbitals allow a large overlap and readily form σ -bonds. It can be shown[56] that it is energetically favourable for the three sp^2 orbitals to form a planar structure with 120° angles between each node. The remaining 2p orbital is orientated with its lobes above and below the plane of the sp^2 orbitals (see Figure 2.1).

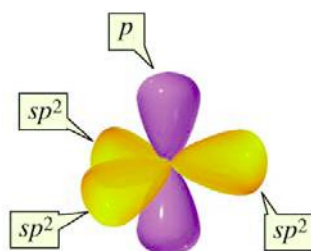
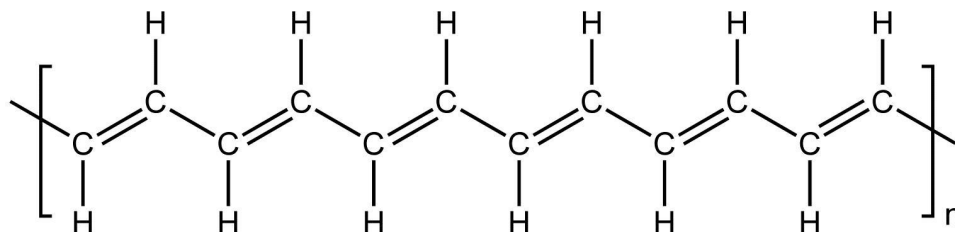
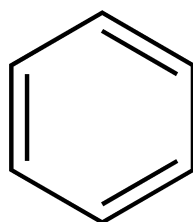


Figure 2.1: Representation of electronic orbitals of carbon atom. The surfaces shown are positions in space where the probability of an electron being measured (i.e. the amplitude of the wavefunction) are equal.[57]

In 1977 Chiang *et. al.* reported[10] the electrical conductivity of the conjugated polymer trans-polyacetylene: CH_x (see Figure 2.2). In this polymer each carbon atom is σ -bonded to a hydrogen atom and two neighbouring carbon atoms, consistent with sp^2 hybridization. The remaining p-orbital forms a π -bond with *one* of the neighbouring carbon atoms, resulting in alternating single and double bonds along the polymer backbone. Molecules consisting of alternating single and double bonds are referred to as conjugated. The π -bonded electrons along the backbone of the polymer can alternatively be described as being delocalised. After Chiang *et. al.* doped the polyacetylene with AsF_5 it was observed to conduct electricity.

A conjugated molecule can be considered to possess a number of delocalised molecular orbitals (MOs). For example consider the annulene benzene (C_6H_6), shown in Figure 2.3. Benzene is conjugated, and the lowest energy MO can be considered to consist of 6 in-phase p-orbitals (see Figure 2.4), delocalised over the molecule. There are however other MOs which are higher in energy than this state, for example 3 adjacent p-orbitals orientated the same way and the other three with swapped phases.

Figure 2.2: Trans-polyacetylene (CH_x).Figure 2.3: Benzene (C_6H_6).

The Pauli Exclusion Principle states that only 2 electrons can occupy each orbital (one for each spin state).[58] Orbitals are filled from the lowest energy to the highest energy according to Hund's Rules.[7] The energy of the molecular orbitals of a benzene molecule are shown in Figure 2.4. The following acronyms are regularly used in the literature of organic chemistry: HOMO (Highest Occupied Molecular Orbital) and LUMO (Lowest Unoccupied Molecular Orbital). It turns out[59] that the LUMO and HOMO levels of benzene are two-fold degenerate in energy, hence each of these energy levels can accommodate 4 electrons.

If the molecular orbital involves more out-of-phase wavefunction overlap than in-phase, the contribution from the π -bonding acts to increase the energy with respect to a state involving no p-orbital overlap. The molecule is less stable in this state and is hence referred to as being in an antibonding state, or π^* state. If electrons are introduced into the LUMO (or similarly holes in the HOMO) they are then free to move in an analogous way to electrons (holes) in the conduction (valence) bands of crystalline inorganic semiconductors.

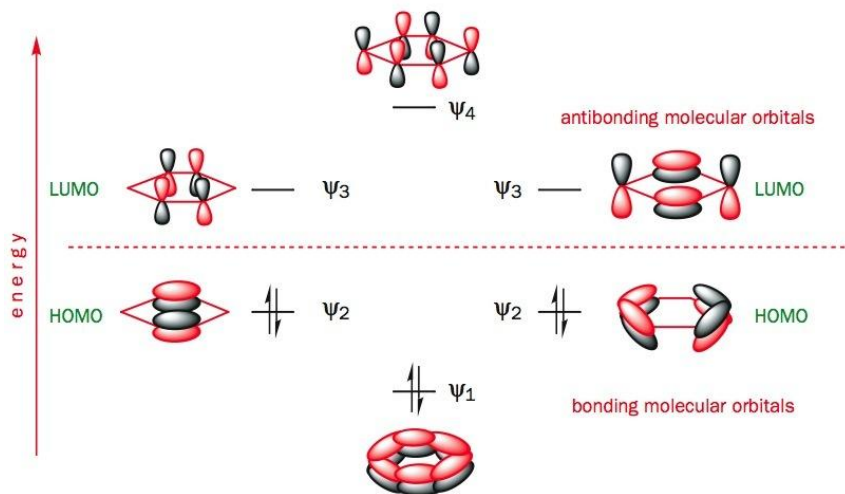


Figure 2.4: Energy levels of the molecular orbitals of benzene.[59] The dotted line shows the energy of an isolated p orbital, all orbitals with lower energy are bonding orbitals, all orbitals with higher energy are antibonding orbitals. The LUMO and HOMOs are two-fold degenerate in energy.

2.1.2 Excitons

In an analogous way to inorganic semiconductors, the difference in energy between the HOMO and LUMO is referred to as the band gap, E_G . Electrons in organic semiconductors can be excited from the HOMO to the LUMO via the absorption of a quantum of energy equal to or greater than the band gap. This excitation creates a hole in the HOMO and an electron in the LUMO, collectively the particle-pair are referred to as an exciton.

Once created the pair will be subjected to the Coulomb attraction due the oppositely charged particle and (if present) an externally applied field. If the effect of the external field is greater than the Coulomb attraction the pair will separate, if not the exciton will recombine. This is further complicated by the fact that the charges will have to overcome a barrier to ‘hop’ between molecules.

Understanding the nature of excitons is of great importance in the study of photovoltaic devices[60–62] and organic phototransistors[63, 64].

2.2 Charge-Transport Models

Understanding the mechanism by which charge is transported in organic semiconductors is crucial to the development of organic electronic devices. Unfortunately the models developed to describe conventional inorganic semiconductors are inadequate for most organic systems. This is due to the high degree of disorder generally present in organic systems. There are various models used to describe charge transport in organic semiconductors and the appropriate one to use depends upon various parameters such as degree of crystallinity and temperature. In this section I give a very brief overview of the common models that have been employed to describe charge-transport in organic semiconductors.

2.2.1 Band-Like Transport

Traditional inorganic semiconductors (such as silicon and germanium) are most often processed into highly ordered periodic crystals. Charge carriers are then described to be within a periodic potential. The Schrödinger equation can be solved with periodic boundary conditions,[7, 8] and the resulting energy-level distribution is two periodic bands in reciprocal space, separated by a region for which there is no solution to the Schrödinger equation. This energy region is forbidden to electrons and is termed the band-gap E_g .

States are then filled using Fermi-Dirac statistics, where the probability of a state of energy E being filled is given by the following distribution:

$$f(E) = \frac{1}{1 + \exp\left(\frac{E - \varepsilon_F}{k_B T}\right)} \quad (2.2)$$

Here ε_F is the Fermi-level for the system, k_B is the Boltzmann constant and T is the temperature. For semiconductors, ε_F is located between the two energy levels, hence at $T = 0$ the lower band (valance band) is filled and the upper band (conduction band) if empty. Inorganic semiconductors devices operate by creating states near the conduction and valance bands (typically by doping) and then thermally exciting carriers from these states to the conduction and valance bands.

Whilst some organic semiconductors have been observed to exhibit band-like transport at low temperatures,[65–67] in the vast majority of cases the band-like model of charge-transport is not appropriate.[68–70]

2.2.2 Multiple Trapping and Release Models

One of the most commonly-employed models for describing disordered semiconductors is multiple-trapping and release (MTR). This concept began in 1958 when Anderson argued that in a disordered system carriers could either be localised or extended.[71] The characteristics of these two states we defined as follows:

Localised:

- Wavefunction is confined to finite region.
- Wavefunction is normalisable.
- Carrier does not contribute to transport.

Extended:

- Wavefunction is delocalised over entire solid.
- Wavefunction is not normalisable.
- Carrier contributes to transport.

Later Mott developed the concept of a mobility edge.[72] He argued that it is meaningless to consider localised and extended states which are degenerate since any linear combination of a localised and an extended state must be extended. Thus the concept of localisation can only be meaningful if there are separate energy regions of localised and extended states, rather like bands and gaps.

It has been argued that carriers can undergo a metal-insulator transition[73] upon reaching a certain energy. Figure 2.5 shows a schematic representation of such a scheme. This approach has been employed to organic field-effect transistors with reasonable success.[68, 69]

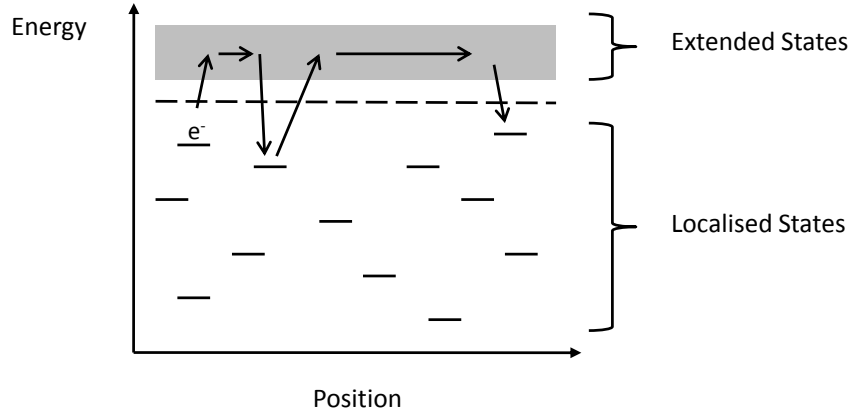


Figure 2.5: Schematic diagram of the way states are distributed in space and energy for the Mott-Anderson theory of charge-transport. The horizontal lines represent localised states and the grey box represents an extended “conduction-band”.

If one assumes that carriers are thermally excited to the conduction band then the mobility of carriers can be described by an Arrhenius relationship:

$$\mu = \mu_0 \exp\left(-\frac{E_A}{k_B T}\right) \quad (2.3)$$

Here E_A is the activation energy for a jump from the localised states to the conduction band. Since in reality there is an ensemble of localised states, E_A is technically the expectation value for any measured state.

It has also been shown[74] that the prefactor μ_0 , in equation 2.3 is dependent upon a factor $k_B T_0$ called the Meyer-Neldel energy. It characterises the width of the localised (trap) states:

$$\mu_0 = \mu_{00} \exp\left(-\frac{E_A}{k_B T_0}\right) \quad (2.4)$$

2.2.3 Variable-Range Hopping

At low temperatures and/or in highly disordered systems, charge transport will take place exclusively via the localised trap states. Under these circumstances carriers will tunnel between states. The hopping probability from state i to state

j can be shown[75, 76] to be given by:

$$P(R_{ij}) = P_0 \exp\left(-2\alpha R_{ij} - \frac{\Delta E_{ij}}{k_B T}\right) \quad (2.5)$$

Here P_0 is a constant, α is the wavefunction overlap parameter, R_{ij} is the spatial distance between the two states and ΔE_{ij} is the energetic offset of the states. The expectation value of the hop distance in a disordered system can be found by minimising the exponent with respect to R . In doing this, a relationship between mobility and time could be derived.[76]

$$\mu = \mu_0 \exp\left(-\left[\frac{T_0}{T}\right]^{1/(d+1)}\right) \quad (2.6)$$

Where d is the dimensionality of the system.

Vissenberg and Matters have successfully applied the above so-called variable range hopping (VRH) model to OFETs.[70] In their approach, they use an exponential density of states to describe the occupation of states near the semiconductor-dielectric interface of an OFET. Using an implementation of percolation theory (see Section 2.2.4), they were able to derive a relationship between the measured field-effect mobility of charge-carriers, temperature and applied gate voltage (see Section 2.3):

$$\mu = \frac{\sigma_0}{e} \left(\frac{\pi (T_0/T)^3}{(2\alpha)^3 B_c \Gamma(1 - T/T_0) \Gamma(1 - T/T_0)} \right)^{T_0/T} \left(\frac{(C_i V_G)^2}{2k_B T_0 \varepsilon_S} \right)^{T_0/T_0 - 1} \quad (2.7)$$

The variables in equation 2.7 are as follows: σ_0 is a conductivity prefactor unique to each semiconductor material, e is the magnitude of the fundamental unit of charge, B_c is the critical criterion for percolation and has been evaluated[77] to be $B_c \simeq 2.8$, C_i is the geometrical capacitance of the gate dielectric (see equation 2.22), V_G is the applied gate voltage and ε_S is the dielectric constant of the semiconductor. The gamma function is defined as follows:

$$\Gamma(z) = \int_0^\infty t^{z-1} e^{-t} dt \quad (2.8)$$

A similar model has also been derived using a Gaussian density of states as opposed to exponential.[78]

2.2.4 Percolation Theory

Due to the disordered nature of organic semiconductor devices, the transport of charges can often be approached via a percolation theory method. Percolation theory concerns its self with the “connectivity” of an inhomogeneous system,[79] and was originally developed in the 1950’s to study the flow of material through a porous random medium.[80] Percolation effects have since been shown to be important with regards to metal-insulator transitions in disordered conductors.[81]

To illustrate the concept of percolation, consider a lattice with N sites, of which there exists a concentration c of these sites that form the percolating system, or are “occupied.” When the concentration is low ($c \ll c_c$, where c_c is the *critical* concentration), most occupied sites are isolated or form only very small clusters. As c is increased the size of the clusters will increase. As c approaches c_c from below the large clusters begin to merge into a so-called “infinite cluster” that spans the extent of the lattice (if N is finite). If $N \rightarrow \infty$ the cluster size diverges when $c > c_c$.

The ratio of the number of sites in the infinite cluster to the number of sites in the lattice can be defined as the site-percolation probability: $p(c)$. In 3 dimensions it has been shown[82] that near the threshold for percolation, the site-percolation probability can be given by:

$$p(c) \propto (c - c_c)^s \quad (2.9)$$

Where s is approximately the same for all 3 dimensional lattices; $0.3 \geq s \geq 0.4$. [82]

The mean number of allowed bonds per lattice site at percolation threshold proves to be an invariant quantity, determined by the dimensionality of the system:

$$n_c \simeq \frac{d}{d-1} \quad (2.10)$$

The conductivity of a system can be determined using a random-resistor net-

work model,[79] in which the conductivity is defined by path of lowest resistance in the lattice.

2.3 Organic Field-Effect Transistors

The majority of the experimental data presented within this thesis is obtained using organic field-effect transistors (OFETs) or related semiconductor structures. Whilst it is likely that much of the knowledge obtained as a result of this work may be more relevant to other devices (such as organic photovoltaic solar cells for example), it has been my intention to keep the experimental focus of this thesis restricted to the study and development of OFETs.

The concept of the field-effect transistor (FET) was first documented in 1925,[1] and was first realised in 1949.[2–4] For their efforts Bardeen, Brattain and Shockley received an equal share of the 1956 Nobel Prize in Physics. FETs, and transistors generally, have since revolutionised the electronics industry and the world in general. Organic field-effect transistors were first demonstrated in 1983,[22] and solution-processed OFETs were first demonstrated in 1997.[83] The field has grown immensely in recent years[84] and is now a vast research area.[14, 84–88]

2.3.1 Architecture of Field-Effect Transistors

A field-effect transistor consists of a thin semiconducting film between two electrodes; the *source* and the *drain*. This film is then separated from a *gate* electrode via an insulating dielectric, often simply referred to as the dielectric. There are several architectures used for organic field-effect transistors (OFETs), but the three most common are: bottom-gate, top-contact (BGTC), bottom-gate, bottom-contact (BGBC) and top-gate, bottom-contact (TGBC). The different OFET device architectures are shown in Figure 2.6 and each can give rise to significant variations in OFET behaviour.

As will be described in Section 2.3.2, charges are conventionally injected from the source electrode, flow along the semiconductor-dielectric interface (they are said to form a *channel*) and are extracted from the drain electrode. Within the BGBC architecture (Figure 2.6 (b)) the charge carriers are directly injected into

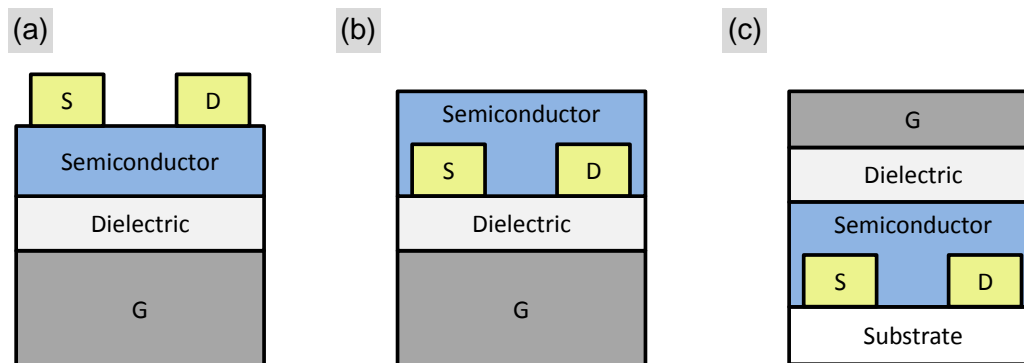


Figure 2.6: Schematic diagrams of three commonly used OFET architectures; (a) bottom-gate, top-contact, (b) bottom-gate, bottom-contact and (c) top-gate, bottom-contact. The diagrams illustrate the position of the source (S), drain (D) and gate (G) electrodes relative to the semiconductor and dielectric.

the transistor channel at the semiconductor-dielectric interface, whereas for the BGTC and TGBC structures (Figures 2.6 (a) and 2.6 (c) respectively) the carriers have to travel significant distances through the semiconductor bulk before they reach the channel.

Although not apparent when considering Figure 2.6, the interfacial area between the source / drain electrodes and the semiconductor varies significantly between device architectures. Since the thickness of the source and drain electrodes are typically only 30 - 100 nm, whilst their area is $\sim 100 \mu\text{m}^2$ to mm^2 , the contact area for BGBC devices (Figure 2.6 (b)) is significantly lower than that of BGTC or TGBC structures (Figures 2.6 (a) and 2.6 (c) respectively). This will lead to an increased contact resistance for the BGBC architecture,[89, 90] potentially reducing charge carrier mobilities.

Whilst the OFETs with the highest reported field-effect mobility are often based on a TGBC or BGTC structure,[91–95] these structures generally are the most difficult to fabricate. For complex electronic circuits[42, 96–98] and OLED display drivers,[33] a BGBC architecture has often been the most straightforward processing route. Similarly, certain dielectrics such as self-assembled monolayers[99, 100] or cross-linkable polymers[92, 101, 102] are not compatible with a top-gate architecture. Finally, various multi-component organic semicon-

ductor systems are known to give-rise to various vertical concentration profiles.[93, 103, 104] In these systems the concentration of the components will be different at the top and bottom interfaces, hence affecting the performance of different device architectures.[93]

2.3.2 Operating Principles of Field-Effect Transistors

Under normal operation, a voltage is applied to the gate (V_G) and drain (V_D) electrodes of FETs, whilst the source is usually held at ground ($V_S = 0$). Whilst the FET is unbiased the semiconducting molecules that make up the transistor channel should have completely filled HOMOs and completely empty LUMOs. Hence, with no applied external fields the semiconductor channel should be insulating. With the application of a voltage to the gate electrode, charges of the opposite sign will be attracted to the semiconductor-dielectric interface from the source and occupy available states in the semiconductor channel.

Semiconductors are in general classified as being either n-type, p-type or ambipolar (see Section 2.7 for some example materials). Electrons can flow in n-type semiconductors, holes can flow in p-type semiconductors and both types of carrier can flow within ambipolar semiconductors. The type of carriers that can flow in a semiconductor depend on the relative position in energy of the HOMO and LUMOs with respect to the work function of the injecting source and drain electrodes (see Figure 2.7 for an example). The metal-semiconductor interface is usually treated as a Mott-Schottky barrier,[105, 106] and a good ohmic contact is expected when the work function of the injecting metal is close to the HOMO or LUMO level of the semiconductor. Otherwise a large potential barrier exists and poor charge-injection results. Other factors such as electron trapping[102] and air exposure[107] also affect the states available within a semiconductor channel. Strictly speaking, a semiconductor should not be defined as p-type, n-type or ambipolar without reference to the injecting electrodes, but often is for convenience.

For a p-type transistor, when a negative voltage is applied to the gate, holes will be attracted from the source electrode and occupy HOMO states on the semiconductor molecules. Similarly, for an n-type transistor, when a positive voltage is applied to the gate, electrons will be attracted from the source electrode

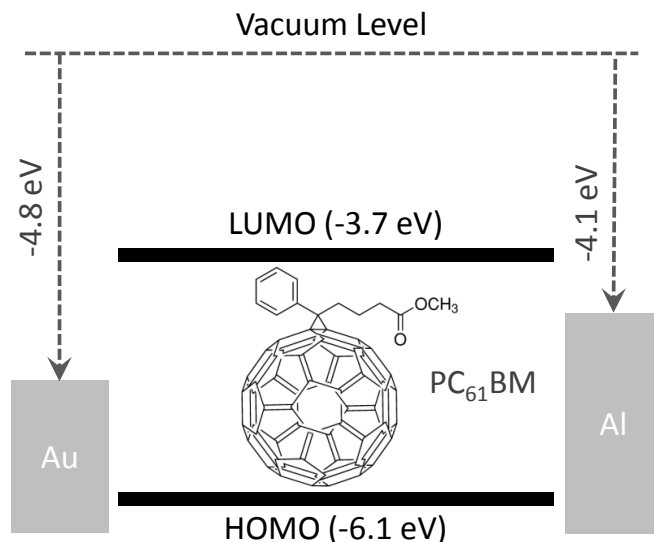


Figure 2.7: Energy levels of [6,6]-phenyl C₆₁-butyric acid methyl ester (PC₆₁BM) relative to the work functions of aluminium and gold.[108–110] With aluminium source and drain electrodes PC₆₁BM is known to be n-type only,[111] whilst with gold source and drain electrodes it has been observed to be ambipolar.[110] The significant offset between the LUMO of PC₆₁BM and the work function of gold should give rise to a significant injection barrier for electrons; $\phi_b(e^-)$. In reality however, this barrier is reduced by the formation of interface dipoles.[112]

and occupy available LUMO states. The number of accumulated charges at the semiconductor-dielectric interface is proportional to both the applied gate voltage and the capacitance of the gate dielectric C_i , (see equation 2.11). The induced free electrons (holes) present in the LUMO (HOMO) are free to move under the influence of an external field and hence a current can flow from the source to drain electrodes. This current is referred to as the source-drain current, or more commonly just the *drain current* I_D .

Not all charge carriers within the channel contribute to the drain current however. Some will fill deep carrier traps, and contribute to a repulsive electric field at the interface. A threshold gate voltage V_T , will have to be overcome before mobile charge carriers are induced in the channel. The injection barrier from the source and drain electrodes into the HOMO or LUMO of the semiconductor will also modify the value of V_T . When OFETs are operated for an extended period

of time V_T is known to increase.[113] When the measurement time of the device is long enough, this effect can manifest itself as hysteresis in the current of forward and reverse scans (see Figure 2.8 for an example). Time-dependent changes in V_T are attributable to various phenomena, such as changes in the occupation density of traps states. Although such phenomena is a rich area of study,[114–116] they are not directly applicable to the work presented within this thesis.

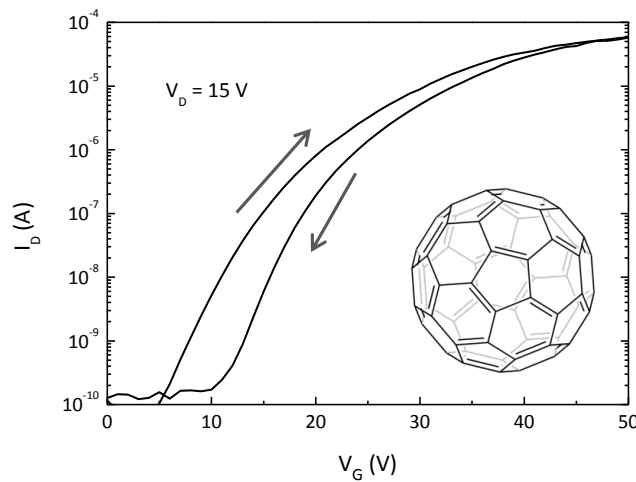


Figure 2.8: Example of hysteresis when measuring the drain current I_D , as a function of applied gate voltage V_G for C_{60} n-type OFET. The arrows indicate the direction of measurements made with increasing time.

2.3.3 Current-Voltage Characteristics

When a voltage greater than the threshold voltage is applied to the gate electrode ($|V_G| > |V_T|$) of an OFET but no voltage is applied across the source and drain electrodes ($V_D = 0$), a uniform density of charge will accumulate (see Figure 2.9(a)). Under these conditions the areal number density of induced mobile charge carriers Q_{mob} , at the semiconductor-dielectric interface is given by equation 2.11. Here C_i is the capacitance per unit area of the gate dielectric.

$$Q_{mob} = C_i(V_G - V_T) \quad (2.11)$$

When a small source-drain voltage of the same sign as the gate voltage is applied ($|V_D| < |V_G - V_T|$) carriers within the channel will be attracted to the drain and a current will flow. Carriers will continue to be injected from the source and a linear variation in charge density across the channel will develop (see Figure 2.9(b)). Under these circumstances the channel resistance at the semiconductor-dielectric interface will remain unchanged as the drain voltage is varied, and hence there will be a linear variation in the drain current I_D , with source-drain voltage. Transistors behaving in this way are said to be operating in the *linear regime*.

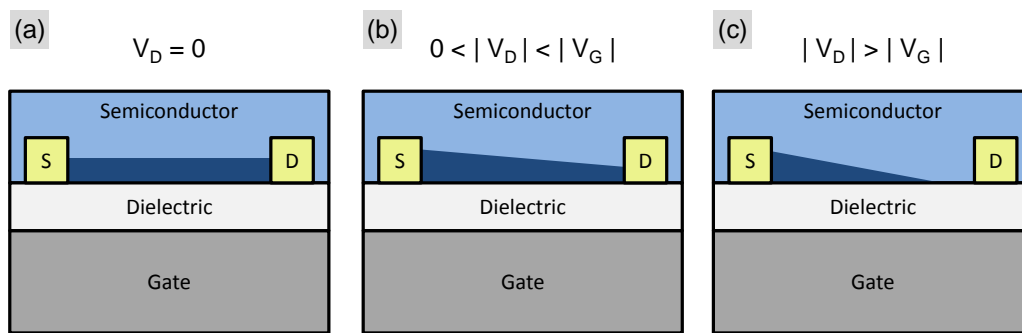


Figure 2.9: Schematic representation of the charge carrier concentration (dark blue) as a function of distance from source electrode (x). (a) When there is no drain current and $|V_G| > |V_T|$, the carrier concentration is uniform. (b) When $|V_D| < |V_G - V_T|$ there is a linear variation in carrier density with x . (c) When $|V_D| \geq |V_G - V_T|$, the channel is pinched-off and a depletion region will form adjacent to the drain electrode.

As V_D is increased, the spatial distribution of charge carriers will become non-linear. This will affect the resistance of the channel and a non-linear variation in I_D with V_D will be observed. Once the point $|V_D| \geq |V_G - V_T|$ is reached the channel will be “pinched off” (see Figure 2.9(c)). Here a depletion region will form next to the drain electrode where no mobile charge carriers are present, the resistance of this region is very high. As the source-drain voltage is increased further the pinch-off point moves towards the source electrode and the depletion region will increase in size. The voltage drop between the source electrode and the pinch-off point will remain constant at $V(x) = V_G - V_T$ as the source-drain voltage is increased, and hence the current will remain constant. The additional voltage

applied is dropped across the high-resistance depletion zone. This is referred to as the *saturation regime*.

When characterising a transistor, typically two sets of measurements are made. The first is a measurement of the drain current (I_D) as a function of applied source-drain voltage (V_D) for a set of different gate voltages (V_G). This is referred to as the output characteristics (see Figure 2.10(a)). The other is a measurement of the drain current (I_D) as a function of gate voltage (V_G) in the linear and saturation regimes, i.e. at a low value of V_D and a high value of V_D . This is referred to as the transfer characteristics (see Figure 2.10(b)).

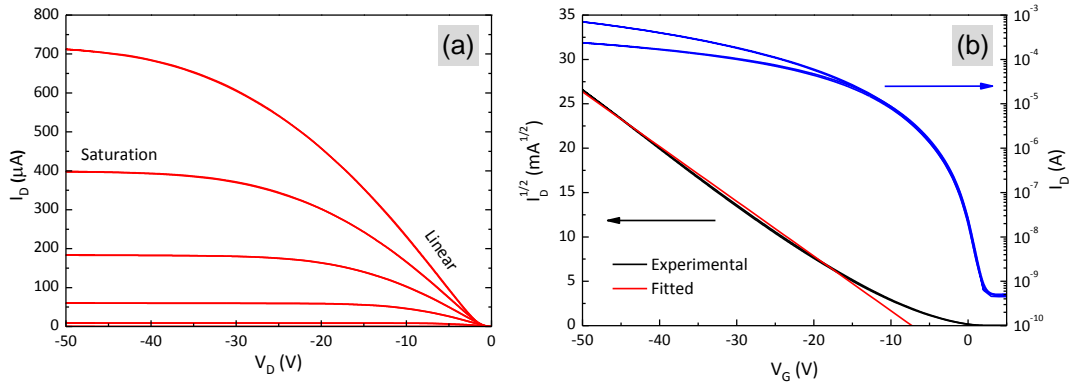


Figure 2.10: (a) Example output characteristics of pentacene p-type OFET. (b) Example transfer characteristics of same pentacene p-type OFET operated in the linear and saturation regimes. On the left the square-root of the drain current is plotted as a function of the gate voltage, to allow the threshold voltage to be estimated via equation 2.19.

2.3.4 OFET Parameter Extraction

To model the conductivity of an OFET channel, and to hence be able to extract useful quantities (such as the charge carrier mobility μ , and threshold voltage V_T), we use the gradual-channel approximation, modified from its original application of inorganic FETs.[117] By considering equation 2.11, the relationship between

the charge density at a distance x from the source electrode can be expressed as:

$$Q(x) = C_i [V_G - V_T - V(x)] \quad (2.12)$$

Here $V(x)$ is the channel bias at position x . To evaluate the drain current in terms of the applied voltages, we can consider the infinitesimal changes in channel resistance dR , with changes in channel position dx :

$$dR = \frac{dx}{WQ(x)\mu} \quad (2.13)$$

Here μ is the charge-carrier mobility and W is the channel width. For this relationship to be valid, we are forced to make the assumption that the length of the channel L , is much greater than the film thickness z , so that the electric field in the x -direction is negligible compared to that perpendicular to the channel. This is valid for most reported OFETs, however those with sub-micron channel lengths,[118–121] do experience so-called *short-channel effects*. We must also assume that the mobility does not depend upon position; $\mu \neq \mu(x)$. This implicitly implies that the mobility does not depend upon the local field, $V(x)$. There have been many studies into the electric-field dependence of the field-effect mobility in OFETs,[68, 70, 83, 122, 123] so at face value this does not seem like a reasonable assumption. However, if we define μ to be the average mobility in the OFET channel, then the it is clear that the below integration is valid.

Using the differential form of Ohm's law, we have:

$$dV(x) = I_D dR \quad (2.14)$$

Substituting from 2.13 and 2.12 and integrating over the OFET channel gives:

$$\int_0^L I_D dx = W\mu \int_0^{V_D} C_i [V_G - V_T - V(x)] dV(x) \quad (2.15)$$

Hence:

$$I_D = \frac{W}{L} \mu C_i \left[(V_G - V_T)V_D - \frac{V_D^2}{2} \right] \quad (2.16)$$

This is the general form of the equation describing the drain current in an OFET as a function of the applied gate and drain voltages. It is from this equation that most relevant parameters are extracted.

The field-effect mobility is generally either quoted in the linear regime or the saturation regime. It turns out that often the quoted saturation regime mobility is marginally higher than the linear regime mobility of the same device (for example see [91]). This is likely to be due to field-dependent mobility effects. In the linear regime we require $|V_D| \ll |V_G - V_T|$. We can then make the approximation:

$$I_D = \frac{W}{L} \mu_{lin} C_i (V_G - V_T) V_D \quad (2.17)$$

By taking the first derivative of the drain current with respect to the gate voltage, the mobility in the linear regime can be expressed as:

$$\mu_{lin} = \frac{L}{WC_i V_D} \frac{\partial I_D}{\partial V_G} \quad (2.18)$$

Hence to extract μ_{lin} from experimental data, the drain current from a relevant transfer curve (see Figure 2.10(b) for example) is numerically differentiated with respect V_G . Ideally the calculated mobility should be independent of gate voltage. However in practise the mobility often shows some field-dependence,[68, 70] especially for highly disordered systems.

In the saturation regime increasing $|V_D|$ beyond $|V_G - V_T|$ has little effect on the measured drain current, and the effective drain current is always $V_D = V_G - V_T$. Substituting this into equation 2.16 gives:

$$I_D = \frac{W}{2L} \mu_{sat} C_i (V_G - V_T)^2 \quad (2.19)$$

The saturation regime can then either be evaluated from the second derivative of I_D with respect to V_G , or the square-root of the first derivative:

$$\mu_{sat} = \frac{L}{WC_i} \frac{\partial^2 I_D}{\partial V_G^2} \quad (2.20)$$

$$\mu_{sat} = \frac{2L}{WC_i} \left(\frac{\partial \sqrt{I_D}}{\partial V_G} \right)^2 \quad (2.21)$$

It is also evident from equation 2.19 that by extrapolating the square-root of I_D in the saturation regime to $I_D^{1/2} = 0$, the threshold voltage can be approximated. An example of this procedure has been carried out in Figure 2.10(b). Other parameters such as the sub-threshold slope and on/off ratio are also often important when assessing the performance of OFETs,[84, 124] but are not of direct relevance to the work presented within this thesis.

2.3.5 The dielectric

The performance of an OFET is highly dependent on the properties of the gate dielectric.[125, 126] The choice of dielectric will affect the morphology of semiconductor films and the roughness of the dielectric-semiconductor interface. Surface roughness will affect the growth of domains within the semiconductor film and hence carrier mobilities.[69] Charge trap states at the semiconductor-dielectric interface are known to significantly affect the threshold voltage (V_T) of OFETs,[127] and the polarity of the dielectric can influence the available energy levels in the semiconductor channel.[102]

As an insulator, the dielectric should have a high resistivity to keep parasitic leakage currents (gate current, I_G) low. It is also desirable for the dielectric to have a high breakdown electric field strength E_B , i.e. the magnitude of the electric field at which the dielectric will become permanently damaged and no longer insulate.

There are three types of gate dielectrics typically employed within OFETs; inorganic, polymeric and self-assembled monolayers (SAMs). Each type have advantages and disadvantages and are best suited to certain situations. It is

not uncommon to use combinations of gate dielectrics. Figure 2.11 shows some example SAMs commonly used for OFET dielectrics.[128]

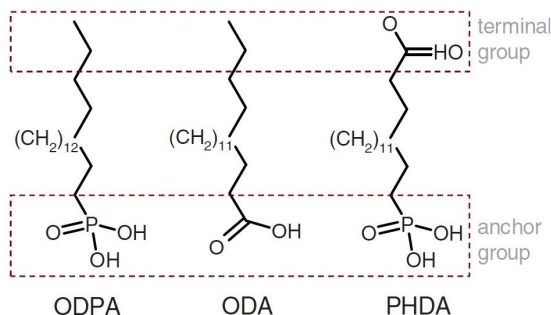


Figure 2.11: Molecular structure of example SAMs commonly used in OFET dielectrics.[128] The example molecules are: octadecylphosphonic acid (ODPA), octadecanoic acid (ODA) and phosphohexadecanoic acid (PHDA).

Bottom gate devices (see Figures 2.6(a) and 2.6(b)) will often employ a metal-oxide layer directly grown on the metal gate surface, e.g. SiO_2 or Al_2O_3 . The surface of metal-oxide dielectrics is strongly dependent on processing history and can lead to changes in operating voltage, threshold voltage and hysteresis. Treating metal-oxide surfaces with self-assembled monolayers such as hexamethyldisilazene (HMDS)[129] or octadecyltrichlorosilane (OTS)[130] has been shown to have significant effects on transistor performance[125]. High- k inorganic dielectrics have been used to fabricate OFETs with operating voltages of $\leq 5\text{V}$. [32]

Polymeric dielectrics are often applied on top of the semiconducting layer in top-gate device structures (see Figure 2.6(c)). Polymer dielectrics have the advantage of being solution processable and hence can be used in low cost fabrication techniques such as printing. The dielectric constant will depend on the material chosen and will hence effect the capacitance C_i . One of the most commonly-employed polymer dielectrics is the fluoropolymer CYTOP™[131]; poly[perfluoro(4-vinyl-1-butene)]. The orthogonality of the solvent used in CYTOP™ makes it compatible with most solution-processed semiconductors and hence top-gate OFET structures. References [125] and [126] list a number of other commonly used polymer dielectrics.

The monomer divinyltetramethyldisiloxane-bis-benzocyclobutene (BCB) has

been shown[101] to crosslink into a polymer and shows promising characteristics as a gate dielectric. Ultra-thin (30-50nm) layers can be applied in solution, resulting in very stable low-voltage (<10V) OFET devices.[101, 102, 132]

Most OFETs reported to date operate at high voltages; typically > |30| V. Certain potential applications of organic electronics, such as portable devices, require operation at much lower voltages. Equation 2.22 shows how the capacitance per unit area of the gate dielectric C_i , depends on the dielectric thickness d , the vacuum permittivity ε_0 and the dielectric constant k .

$$C_i = \frac{\varepsilon_0 k}{d} \quad (2.22)$$

From equation 2.11 it can be seen that for a certain induced charge density, the operating gate voltage is inversely proportional to the capacitance of the gate dielectric. Hence the operating gate voltage is directly proportional to the thickness of the gate dielectric.

The use of self-assembled monolayers (SAMs) as dielectrics was first applied to improve the insulating qualities of native metal oxides and hence reduce leakage current in inorganic devices.[130] When applied directly to the metal gate electrode of an OFET, a tetradecylenyltrichlorosilane SAM with a length of about 2nm was shown[133] to reduce the operating voltage of an OFET to about 2 V. The gate current density of these devices was reported to be 10^{-6}Acm^{-1} compared to 10^{-8}Acm^{-1} in the absence of a semiconducting layer.[134] One possible explanation for the difference is the interpenetration of the SAM by the semiconductor, leading to routes of lower film thickness and hence lower resistance.

To avoid the effects of semiconductor penetration, SAM dielectrics using (18-phenoxyoctadecyl)trichlorosilane (PhO-OTS) have since been applied to silicon gate electrodes.[99] The strong π - π interactions between the phenoxy endgroups of the SAM result in a tighter packing and hence lower leakage current (see Figure 2.12). OFETs with very low leakage currents have also been fabricated using n-octadecylphosphonic acid (ODPA) and n-octadecyltrichlorosilane.[100] Fully solution processable OFETs have since been fabricated using PhO-OTS[135] and ODPA.[136]

In addition to their application with regards to low-voltage OFETs, SAMs are

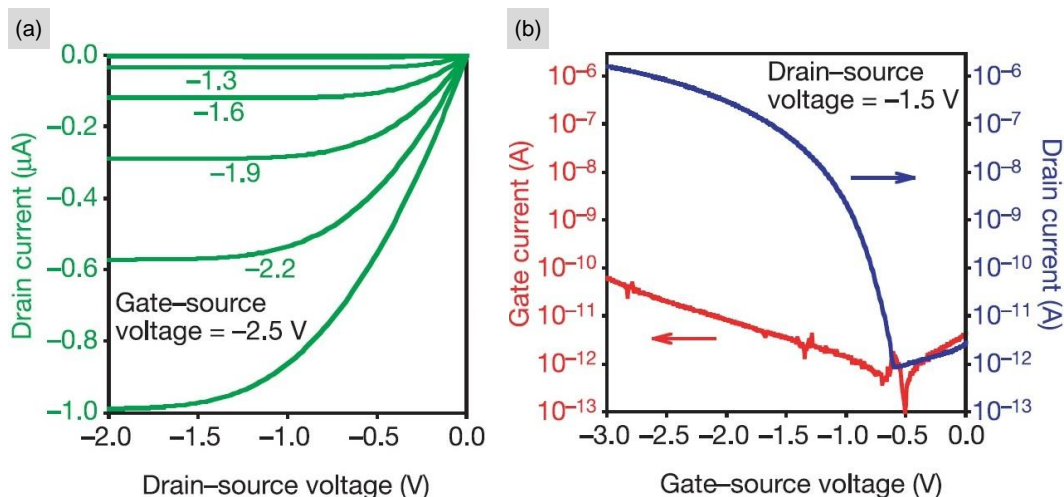


Figure 2.12: (a) Output and (b) transfer characteristics of BGTC pentacene OFET using PhO-OTS SAM as gate dielectric.[99]

also readily employed to passivate dielectric surfaces,[129, 137] improve crystallisation,[91, 138, 139] modify dielectric surface energies[136, 140] or modify threshold voltages.[127]

2.4 Ambipolar OFETs

Although unipolar logic gates[96] and integrated circuits have been demonstrated,[42] using a combination of p-type and n-type organic transistors it is possible to construct complementary inverters[141] and full integrated circuits[43, 98] with lower power dissipation and wider noise margins.[142, 143]

Producing complementary circuits using laterally separated p- and n-type semiconductors on a single substrate requires significantly more complexity than a single material, considerably increasing processing cost. The use of ambipolar transistors which, under appropriate biasing conditions, can show both p- and n-type behaviour, is hence highly desirable. For ambipolar operation to be possible the semiconducting material(s) used must have its (their) LUMO(s) *and* HOMO(s) aligned with the work functions of the injecting electrodes. Since most semiconducting organic molecules have a band gap of ~ 2 eV, for single-metal electrode and single-material channel transistors, the injection of at least one

type of charge carrier can involve a significant barrier.

2.4.1 Operation of Ambipolar OFETs

Due to difference in offset between the injecting electrode work function and the HOMO and LUMO of the relevant semiconductor(s), the energetic barriers for hole injection and electron injection will not necessarily be equal; $\phi_b(h^+) \neq \phi_b(e^-)$. Also, the density of trap states is not likely to be identical for the two carrier pathways, especially if two semiconductors are used.[109] For these reasons the threshold voltage for holes will not in general be equal to the threshold voltage for electrons; $V_{Te} \neq V_{Th}$. As will be shown in Section 4.5.1 however, if this assumption is relaxed the current-voltage relationships of ambipolar OFETs can be derived in a relatively simple manner.[144] None-the-less, in explaining the operation of OFETs in this section, the condition that $V_{Te} \neq V_{Th}$ is enforced.

Within an ambipolar OFET, the current flow can be due to holes, electrons or both carriers simultaneously. The biases applied to the drain and gate electrodes of the OFET will determine the carriers present. When $|V_G - V_T| > |V_D|$, the device will operate in the standard unipolar regime, with the carrier type determined by the sign of the voltage (electrons for positive voltages and holes for negative voltages). This situation is illustrated in Figure 2.13(a) for electrons.

When $V_G - V_{Te}$ is positive and V_D is negative, and when $V_G - V_{Th} > V_D$, the OFET operates as an n-type OFET but with electrons flowing from the drain to the source electrode (i.e. in the reverse direction), see Figure 2.13(c). The gate voltage of an OFET is conventionally quoted with respect to the source voltage V_S , but assuming that the source-gate bias is greater than the drain-gate bias. If $(V_G - V_{Te}) - V_D$ is greater than $(V_G - V_{Te}) - V_S$, then the drain becomes the effective source. To understand why this is the case, we add $-V_D$ to the absolute voltage applied to each terminal. Since it is the relative voltages that are important, we then see that the drain terminal can be considered to be biased at 0, the source biased at $-V_D$ and the gate biased at $(V_G - V_T) - V_D$, under our new scheme. This is illustrated in Figure 2.14. The equivalent situation for when $V_G - V_{Th}$ is negative and V_D is positive (and with $V_G - V_{Te} < V_D$) would be similar to that shown in Figure 2.13(c), but with holes flowing instead of electrons.

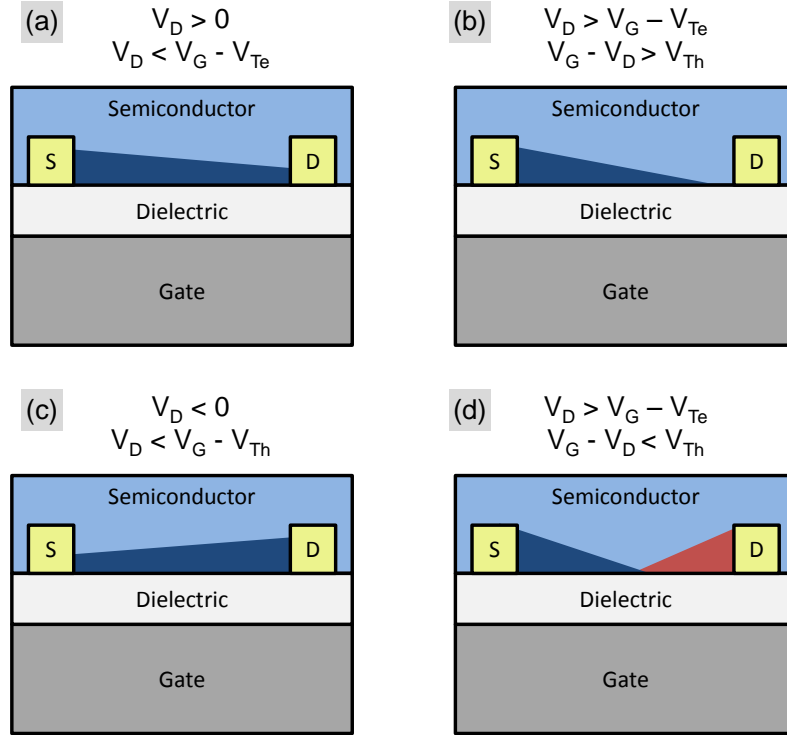


Figure 2.13: Schematic diagram showing the charge density of electrons (blue) and holes (red) as a function of position in the channel of an ambipolar OFET under various biasing conditions when electrons are the main carrier. (a) Standard linear-regime unipolar operation for electrons. (b) Standard saturation-regime unipolar operation for electrons. (c) Linear regime operation where electrons flow backwards from the drain to the source. (d) Ambipolar regime where electrons flow from the source towards the drain and holes flow from the drain towards the source. Under these circumstances the carriers will meet at the recombination zone, producing photons.

For an n-type unipolar OFET, when $0 < V_G - V_{Te} < V_D$ the device will be expected to be pinched-off and operate in the saturation regime. For an ambipolar OFET, holes can also be injected from the drain and travel towards the source when there is an electron depletion region adjacent to the drain electrode. The voltage at which holes will be injected depends on the threshold voltage for holes V_{Th} . If $V_D > (V_G - V_{Te}) > 0$ then electrons will be injected and saturate as expected. If the gate voltage relative to the hole-injecting terminal voltage (drain

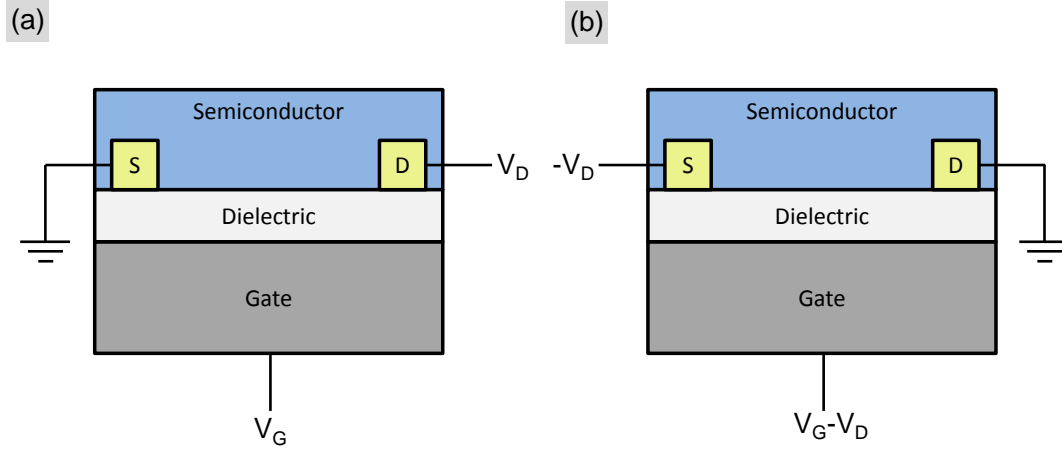


Figure 2.14: Schematic illustrating how the voltages applied to the terminals of an ambipolar OFET can be transformed by $-V_D$ when V_G is of the opposite sign to V_D . (a) Normal picture of OFET when $V_G - V_S > V_G - V_D$. (b) Transformed voltages required when $V_G - V_D > V_G - V_S$.

voltage) can overcome the threshold voltage for holes, then they will be injected *simultaneously* to electrons. This situation is shown in Figure 2.13(d). Otherwise however if $V_G - V_D > V_{Th}$, the device will simply act as a unipolar n-type device operating in the saturation regime (see Figure 2.13(b)). The equivalent situations for holes can easily be deduced by following similar arguments.

When the device is operating in the ambipolar regime, the channel is no longer pinched-off and the drain current will tend to increase with applied drain voltage until the device breaks down. Figure 2.15 shows some example output characteristics of an ambipolar OFET. The characteristics in Figure 2.15 illustrate how difficulty may arise if the saturation regime data is used to extract the threshold voltages (as described in Section 2.3.4), hence extrapolating the drain current in the linear regime to $I_D=0$ (see equation 2.17) is potentially more accurate.

2.4.1.1 Ambipolar Light-Emitting OFETs

When both carriers are present in the channel at the same time, recombination will take place at the pinch-off point; i.e. the position at which the two channels

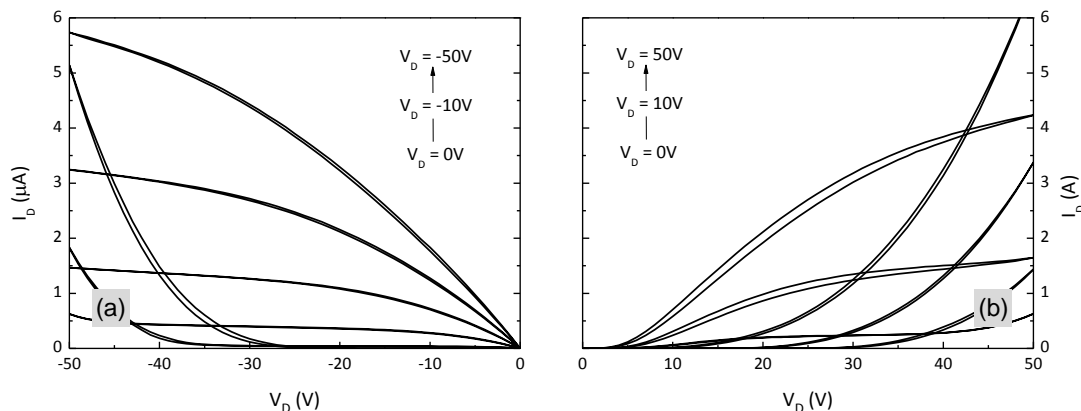


Figure 2.15: Output characteristics of squaraine-based BGBC ambipolar OFET.[145] The device dimensions were $L = 2 \mu\text{m}$, $W = 10 \text{ nm}$.

meet. The efficiency of recombination is not known, but when it comes to modelling such devices, it is generally assumed that bimolecular recombination takes place with an infinite rate constant.[47, 48, 144]

As expected from electron-hole recombination, light emission often takes place in such OFETs, allowing them to be used as light-emitting organic field-effect transistors (LE-OFETs).[47, 48, 146, 147] By modelling the LE-OFET as consisting of adjacent p-channel and n-channels the recombination zone, and hence emission position, can be controlled by the applied voltages.[47]

The assumptions made above about the operation of ambipolar OFETs are not directly applicable to bilayer ambipolar OFETs. The reason for this is that the requirement that one carrier is pinched off before the other can be injected no longer holds. It is perhaps more appropriate to consider bilayer ambipolar OFETs as two separate OFETs in parallel, with their gates connected. For this reason it is anticipated that simple bilayer OFETs should show little recombination and hence low emission efficiencies. More complicated multi-layer structures have conversely been demonstrated with very high emission efficiencies.[148]

2.4.2 Routes to Ambipolarity

There are various ways in which ambipolar OFETs can be realised, using either one or several semiconductor materials. The first ambipolar OFETs were based on bilayer $C_{60}:\alpha$ -6T structures.[149] The idea here is that the C_{60} layer will transport electrons, whilst the α -6T layer will transport holes. Figure 2.16(a) shows a schematic diagram of the bilayer OFET structure used by Dodabalapur and co-workers in this study. The hole channel will form at the interface between the SiO_2 dielectric and the α -6T semiconductor, whilst the electron channel will form at the interface between the two semiconductors. Because the LUMO of α -6T is inaccessible to electrons injected from gold source and drain electrodes, α -6T is insulating to electrons and this layer hence acts as part of the dielectric.

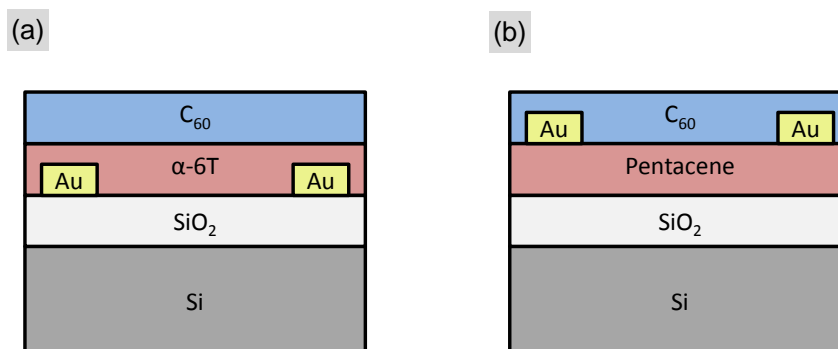


Figure 2.16: Bilayer ambipolar OFET structures employed by (a) Dodabalapur *et. al.*[149] and (b) Kuwahara *et. al.*[150] Structure (a) is an example of a bottom-gate, bottom-contact (BGBC) bilayer OFET, whilst (b) is an example of bottom-gate, middle-contact (BGMC) bilayer OFET.

The structure employed in their work was BGBC (see Figure 2.16(a)), hence for electrons to reach the C_{60} layer and be transported, they must first overcome a significant injection barrier of the α -6T layer. This is expected to reduce the mobility of charge carriers with respect to the equivalent unipolar structures.[149] Ambipolar OFETs have similarly been fabricated using bilayers of pentacene and C_{60} . [150, 151] In this case, a bottom-gate, *middle*-contact (BGMC) structure was found to produce the most promising results (see Figure 2.16(b)).[150] In this case

the source and drain electrodes are in direct contact with both semiconductors, potentially reducing contact resistance effects with respect to a BGBC structure.

Blended semiconductor OFETs are another popular way to achieve ambipolarity. By blending p- and n-type semiconductors, interpenetrating hole and electron networks can be formed, giving rise to ambipolar behaviour.[109, 152, 153] This has previously been carried out by co-evaporating hole-transporting and electron-transporting semiconductors,[153] blending two polymers[154] or blending a polymer and a small-molecule.[109, 152] Whilst the ease of fabrication is greater for blends compared to bilayers, in most cases the field-effect mobilities of holes and electrons in the blended systems are lower than the mobilities in the equivalent single-component systems.[52, 110, 138] An exception to this rule is that of MDMO-PPV,[109] for which the hole mobility increases when it is blended with PC₆₁BM. This is explainable by an extension of the polymer backbone upon blending, caused by the intercalation of the PC₆₁BM molecules.[155, 156] The properties of blends of materials relevant for bulk-heterojunction solar cells (see Section 2.8) have also been studied using OFETs.[52, 157–159]

Single-component ambipolar OFETs can be fabricated by either using asymmetric source and drain electrodes,[47, 147, 160] or by using a low band-gap semiconductor.[48, 95, 110] By choosing source and drain electrodes which respectively match the HOMO and LUMO of the material employed, both holes and electrons can be injected and transported.[160]

Low-band gap organic semiconductors have traditionally been rather scarce, with most reports of so-called ambipolar materials (those capable and injecting holes and electrons when using one electrode material in OFETs) being restricted to small-molecules.[48, 107, 110, 144, 145, 161, 162] Aside from the reduced processability, the mobilities of these materials were also rather low when compared to similar unipolar small molecules. Recently, a number of high-mobility ambipolar polymers have been reported.[54, 95, 163] These materials have simultaneously been synthesised with both low band-gaps and high field-effect mobilities of both holes and electrons. Aside from their use in solar-cells,[164–166] it is these materials which hold the most significant promise with regards low-cost, large-area microelectronics.

2.5 Organic Phototransistors

Organic phototransistors (OPTs) have recently been explored as a potential device for use in low-cost, large area image sensor arrays[167–169] (see Figure 2.17 for example). Traditionally however, the reported spectra-range,[40, 169] quantum efficiency,[169] operating voltage[169] and response-time[168] of organic photodiodes (OPDs) have generally been superior to that of OPTs.[63, 170–172] This can in-part be attributed to the substantial relevant knowledge base already established as a result of the immense volume of research devoted to organic photovoltaic cells (OPVs).[60, 62, 173]

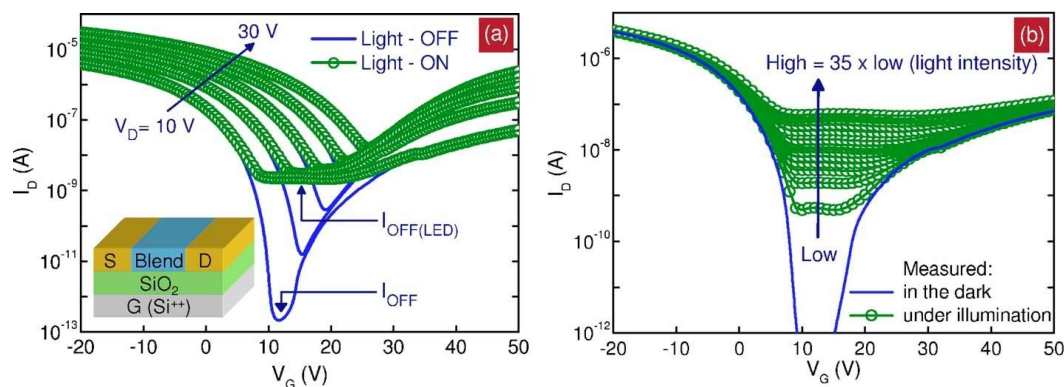


Figure 2.17: Transfer characteristics of an example organic phototransistor based on a blend of [6,6]-phenyl-C₆₁-butyric acid methyl ester (PC₆₁BM) and poly [2-methoxy-5-(3',7'-dimethyloctyloxy-p-phenylene vinylene)] (MDMO-PPV).[51] Measurements were performed in the dark (solid line) and under constant illumination (circles) using an inorganic blue (469 nm) InGaN LED. Inset shows the bottom-gate, bottom-contact transistor architecture employed. (b) Transfer characteristics of the same LS-OFET measured in the dark (solid line) and under illumination at different light intensities (circles) at $V_D = 10$ V. The device dimensions were $L = 2\mu\text{m}$ and $W = 10$ mm in all cases.

The downside to OPDs is that they require a separate switching element for use in photosensor arrays. Conversely, OPTs are a switch by-design, potentially enabling the structural complexity of integrated sensors to be reduced greatly. If OPTs could be demonstrated with similar performance characteristics to those of OPDs then they will likely become a serious contender for the technology of

choice with regards to low-cost, large-area image sensors. Recently, OPTs have been reported with response times of approximately 60 μs [51] and with sensitivity to infra-red light,[145] suggesting improvements are possible.

To a certain extent, the $I - V$ properties of most OFETs show some modification under optical illumination,[49] for this reason (aside from direct OPT application) it is essential that a comprehensive description of the photo-response of OFETs is developed.

2.5.1 Operating Principles of OPTs

When illuminated, the detected drain current of organic phototransistors is observed to increase[49, 51] (see Figure 2.17 for an example). The mechanism behind this observed increase is currently a matter of debate, and appears to vary from device to device. There are three main processes which are believed to result in enhanced drain current under illumination.

1. The first mechanism is exciton creation and dissociation. This is a well studied phenomena within organic semiconductors[174] and is the operating principle of organic solar cells.[61] Several reported OPTs have had the photo-response by default attributed to this affect.[64, 175, 176] Bound electrons and holes are photo-generated in the bulk of the semiconductor in equal numbers and believed to be separated by either an externally applied field (unipolar OFETs)[64] or a charge transfer processes at the n-channel / p-channel interface (2 component OFETs).[63] The photo-generated carriers of the opposite sign to the drain voltage (majority carriers) will then be extracted and detected as an increase in I_D . Carriers of the same sign as the drain voltage (minority carriers) have been suggested to either fill trap states in the channel (see photovoltaic effect), be swept out of the device by the same-sign gate field[53] or be extracted at the source.[50] This mechanism is characterized by fast-response times[169] and modest responsivities.[50, 177] The mechanism has previously been termed the *photoconductive effect*[63, 171] and is considered to be most prominent when the OFET is in the *off-state*.

2. The second mechanism has previously been termed the *photovoltaic effect*[63, 171, 178] and is associated with the release and trapping of carriers at the semiconductor-dielectric interface. This effect is considered to be most prominent when the OFET is in the *on-state* and is commonly observed in pentacene-based OPTs.[179] It is believed that whilst the majority of carrier traps are filled during normal operation in the dark (see section 2.3.5), the minority carrier traps remain unfilled. The photo-generated minority carriers are then trapped under illumination, or the trapped majority carriers are excited out of the trap states. The change in density and / or type of trapped charge carriers is manifest as a shift in the threshold voltage ΔV_T . This process is generally associated with slow response times and high responsivities.[170]
3. A third mechanism which has been proposed is the effect of photo-excited injection from the metal electrodes.[50, 177, 180] When electrodes are selectively illuminated, the drain current I_D , and threshold voltage V_T , are observed to increase.[180] This has been attributed to a modification of the injection barrier at the metal-semiconductor interface.[180] Since this mechanism serves to change the injection barrier and hence V_T , it can be considered to be an example of the photovoltaic effect.

In most systems it is likely that, to a certain extent, all three effects are taking place.

At high incident optical power densities, the increase in photo-induced current I_{PH} , with optical power density (OPD) P_i , due to the photoconductive effect is observed to be sub-linear and eventually level off.[50, 64, 177] This correspondingly results in a reduction in the responsivity (see Section 2.5.2) of the device with increasing illumination density.[50, 177] One explanation for this phenomenon has been attributed to the saturation of photo-generated excitons within the semiconductor channel.[64] This description states that an increase in density of photo-generated carriers will lead to an increase in the frequency of recombination, and hence a lower responsivity.

Under illumination, photo-generated excitons will be created throughout the semiconductor layer, yet the transistor channel only exists within the first few

nanometres of the semiconductor-dielectric interface. A question of interest to those studying organic phototransistors is whether charge carriers created a large distance from the channel contribute to the detected photo-current? A study using terahertz spectroscopy and theoretical models carried out by Lloyd-Hughes *et. al.* suggests that carriers created more than a few nanometres (5 nm) away from the transistor channel do not contribute to the detected photocurrent.[53] This behaviour has been attributed to a higher probability of exciton-dissociation under the strong electric field near the gate electrode. The electric field due to the gate electrode can be shown to decay rapidly with distance.[181]

2.5.2 Characterisation of OPTs

There are various figures of merit quoted when studying organic phototransistors.[50, 177] One of the most regularly used is the responsivity R (see equation 2.23).

$$R = \frac{I_{PH}}{P} = \frac{(I_{D,ill} - I_{D,dark})}{P_i LW} \quad (2.23)$$

Here, $I_{D,ill}$ and $I_{D,dark}$ are the drain currents under illumination and in the dark respectively.

The detected photo-current I_{PH} of organic phototransistors has previously been modelled using methods borrowed from inorganic systems.[117, 178] For photocurrent produced via the photoconductive effect, equation 2.24[117] is used and for photocurrent produced via the photovoltaic effect, equation 2.25[178] is used.

$$I_{PH} = (e\mu nE)Wd = \beta P \quad (2.24)$$

$$I_{PH} = g_M \Delta V_T = \frac{\alpha k_B T}{e} \ln \left(1 + \frac{\eta e \lambda P}{I_{D,dark} h c} \right) \quad (2.25)$$

Here, g_M is the transconductance, ΔV_T is the change in threshold voltage under illumination, α and β are constants of proportionality, k_B is the Boltzmann constant, e is the fundamental unit of charge, n is the carrier density in the channel, E is the magnitude of the electric field in the channel, d is the channel

thickness, h is the Planck constant, c is the speed of light *in vacuo*, λ is the wavelength of incident light and η is the quantum efficiency of the device. Both equations are based on inorganic systems, for which there are slight differences to organic systems. Specifically, equation 2.24 does not take account of the exciton recombination at high intensities, a significant effect in organic systems.[64] These equations have seen relative success in modelling the photocurrent in OPTs.[63, 171, 182] There are various other figures of merit for organic phototransistors that are not of direct relevance to the work in this thesis.[50]

2.6 Integrated circuits

2.6.1 Inverters

The ultimate aim of transistor development is to facilitate their effective implementation in integrated circuits.[42, 96, 98, 141] The basic building block of all logic circuits is the inverter, or NOT gate. This device takes a high voltage as an input V_{in} and produces a low voltage as an output V_{out} , and will similarly produce a high V_{out} for a low V_{in} .

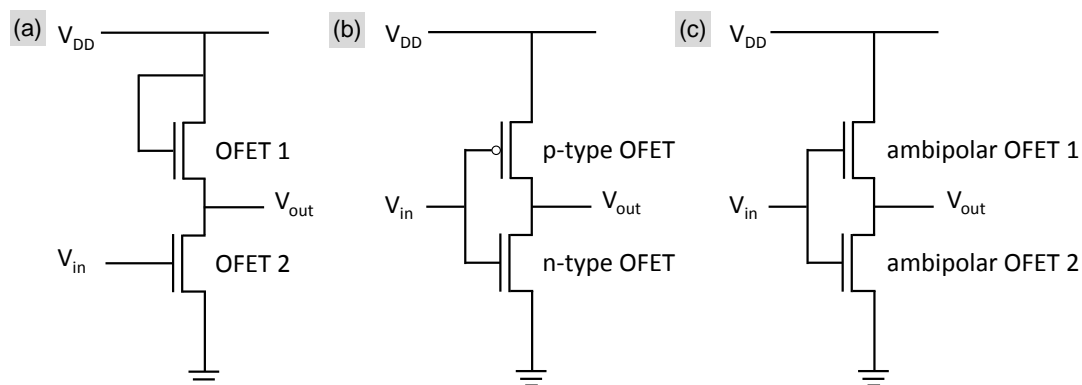


Figure 2.18: Circuit diagrams of organic inverters. (a) Unipolar inverter. (b) Complementary inverter. (c) Complementary-like inverter.

Inverters can be fabricated from unipolar transistors in a variety of ways.[143] An example of a so-called unipolar inverter is given in Figure 2.18(a). Alterna-

tively, inverters can be constructed from a combination of p- and n-type OFETs (see Figure 2.18(b)) called complementary inverters. Inverters based on complementary logic have higher noise margins and greater small-signal gains (see equation 2.26) than unipolar inverters,[141] however unipolar inverters are in general less complex to fabricate. This is due to the need for laterally resolved p- and n-type materials with complementary circuits.

Alternatively, inverters based on ambipolar transistors can be fabricated using a single semiconductor system whilst retaining the advantages of high noise margins and large small-signal gains. Inverters based on ambipolar systems are often called complementary-*like* inverters,[109] see Figure 2.18(c). Using this architecture, the source electrode of OFET1 can be considered to be connected to the supply voltage (V_{DD}) and its drain connected to V_{out} . Similarly, the source electrode of OFET2 can be considered to be connected to ground and the drain connected to V_{out} . When a low positive voltage is applied to V_{in} , the gate-source voltage of OFET1 will be high and negative, hence holes will flow from the supply to the channel, making the effective resistance of OFET1 low. The gate-source voltage of OFET2 will be low and positive hence the effective resistance of OFET2 will be high. Similarly it can be deduced that when V_{in} is high and positive the resistance of OFET1 will be high and the resistance of OFET2 will be low. By considering the device as a potential divider (see Figure 2.19), voltage inverting behaviour should hence be expected.

The small-signal gain of an inverter is simply found from the 1st derivative of V_{out} with respect to V_{in} :

$$g = \frac{\partial V_{out}}{\partial V_{in}} \quad (2.26)$$

There are other parameters of interest for inverters, details are given elsewhere.[183]

2.6.2 Opto-electric logic gates

The fabrication of opto-electrical logic gates based upon LS-OFETs has recently been demonstrated.[51] The idea behind this work was to illustrate that optical signals, as well as electrical signals can be used within organic-based digital signal processing.

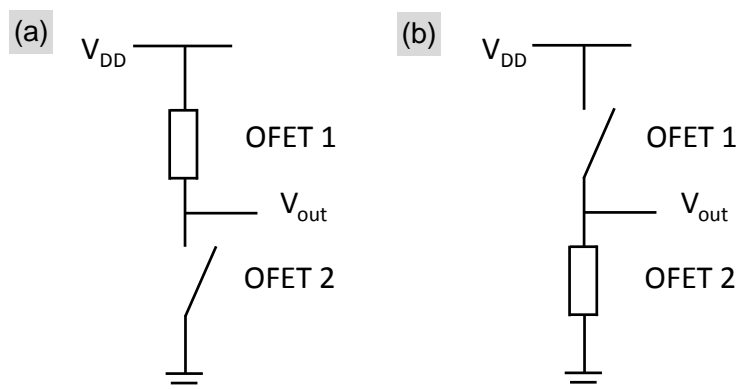


Figure 2.19: Idealised representation of complementary-like inverter as voltage divider. An open switch represents a high resistance and a resistor symbol represents a low resistance. (a) The inverter when $|V_{in}|$ is low. (b) The inverter when $|V_{in}|$ is high.

2.7 Semiconductor Materials

The factor which is perhaps most crucial in the performance of OFETs, and organic electronic devices in general, is the semiconductor material(s) employed. Since the first reported conducting polymer,[184] the field of organic electronic materials has grown vastly.[185–188] Desirable properties from organic semiconductor depend upon the target device and application, but the charge-carrier mobility,[91] structural and electronic stability,[189, 190] processability[191] and cost are all highly sought-after. Often some of these properties are, at least to a certain extent, mutually-exclusive.

Organic semiconductors can be classified in various ways; such as polymers and small molecules, or p-type, n-type or ambipolar. The latter classification can be somewhat ambiguous since, as described in Section 2.3.2, the “type” of material depends upon the injecting electrodes[110] and the dielectric employed in the OFET.[102] For the purposes of this section however I will use this classification scheme, since it is both in-keeping with majority of the literature and is convenient.

2.7.1 Hole-Transporting Organic Semiconductors

High-performance p-type materials have traditionally been more wide-spread than n-type or ambipolar materials. This is in part due to the stability issues,[107, 190] as described in Section 2.7.2. Figure 2.20 shows a selection of commonly used p-type organic semiconductors.

Whilst the highest recorded OFET mobility is for single-crystal ruberene[192–195] (see Figure 2.20(h)), this is not a practical method for producing OFETs. One of the most well-studied and commonly employed p-type-OFET materials is pentacene[196–200] (see Figure 2.20(a)). Despite its impressive performance, the low solubility of pentacene means that it has to be deposited via vacuum sublimation, which in the long-term is not ideal.

The group of John Anthony at the university of Kentucky have synthesised several soluble pentacene and other acene derivatives.[201–204] These materials have improved processability compared to pentacene and field-effect mobilities in excess of $1 \text{ cm}^2\text{V}^{-1}\text{s}^{-1}$. The general structure of such a pentacene derivative is given in Figure 2.20(f).

Polymer semiconductors generally offer greater processability than small-molecules, due to improved surface wetting, solubility and film uniformity. The most well-studied semiconducting polymer is poly(3-hexylthiophene) (P3HT), which is shown in Figure 2.20(e). Aside from its uses within OFETs[129, 205] P3HT is widely used as the benchmark polymer for understanding polymer:fullerene bulk heterojunction solar cells.[103, 206] Other commonly employed polymers include poly(triarylamine) (PTAA),[93, 207] poly(2,5-bis(3-alkylthiophen-2-yl) thieno[3,2-b]thiophene) (pBTTT)[91] and indacenodithiophene benzothiadiazole (IDT-BT).[208] The molecular structure of these polymers are shown in Figures 2.20(d), 2.20(c) and 2.20(g) respectively. The field effect mobility of such polymers tends to increase with crystallinity.[91, 208]

2.7.2 Electron-Transporting Organic Semiconductors

Whilst unipolar logic works well for certain applications,[33] for many electronic devices complementary logic is required.[143] For this reason, it is important to have a selection of both p- and n-type materials with similar performances.

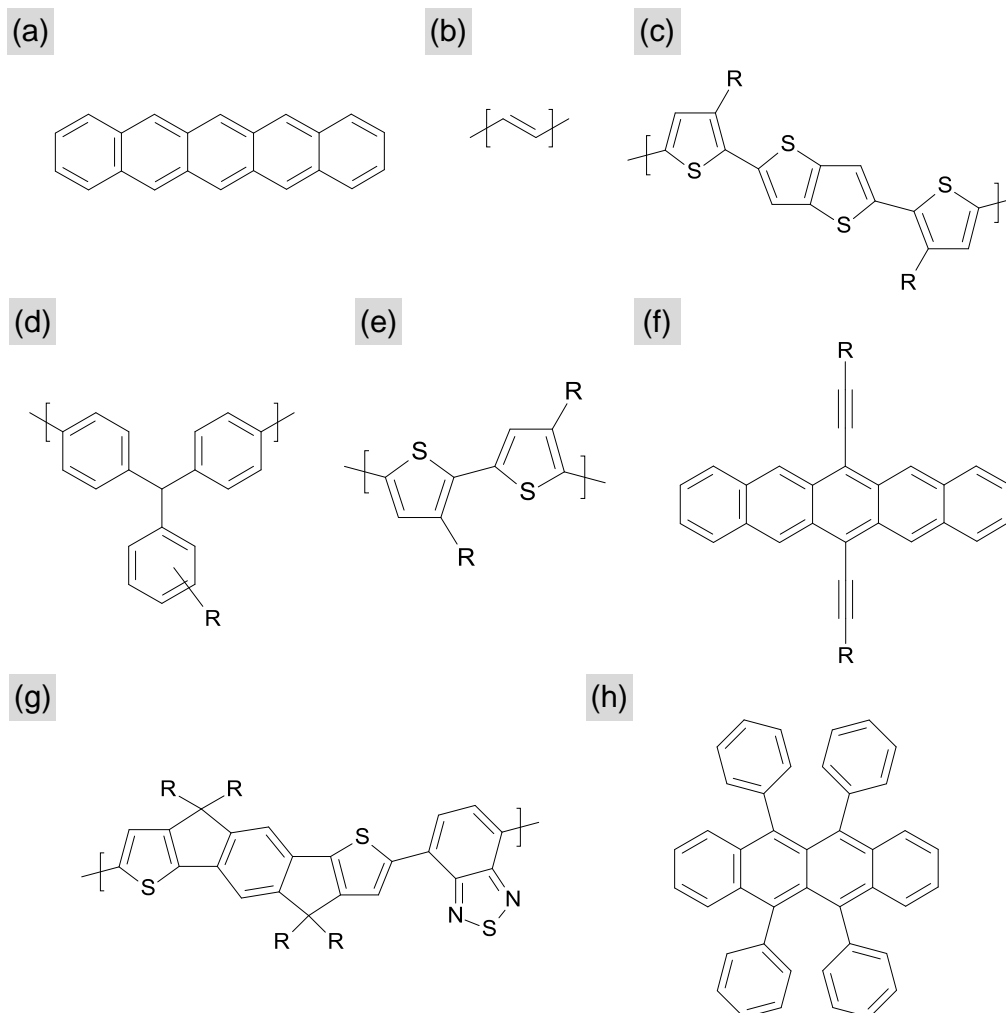


Figure 2.20: Example p-type organic semiconductors commonly used in OFETs: (a) pentacene, (b) polyacetylene, (c) poly(2,5-bis(3-alkylthiophen-2-yl)thieno[3,2-b]thiophene) (pBTTT), (d) poly(triarylamine) (PTAA), (e) poly(3-hexylthiophene) (P3HT), (f) 6,13-substituted pentacene, (g) indacenodithiophene benzothiadiazole (IDT-BT), (h) Rubrene.

It has previously been shown that the molecules with a LUMO below approximately 4 eV are expected to become unstable in the presence of water or oxygen.[107, 190] Water in particular is expected to act as a trap to electrons af-

ter reacting with semiconducting molecules. This, means that many n-type small molecules are poor electron conductors when processed and/or measured in air. This, combined with the fact that the LUMO of most n-type materials is inaccessible to highly-stable (and hence widely-used) gold electrodes, has resulted in n-type materials traditionally not being as advanced as p-type materials.[84] In recent years however, tremendous progress has been made with n-type materials.[188] Some example n-type polymers and small molecules are shown in Figure 2.21.

As is evident from Figure 2.21, many n-type materials are based upon fullerene derivatives. The highest reported field-effect mobility for an n-type polycrystalline semiconductor is approximately $6 \text{ cm}^2\text{V}^{-1}\text{s}^{-1}$, for C_{60} . [92] Since it was first synthesised in the 1980s,[55] C_{60} (Figure 2.21(a)) has had a variety of uses with regards to organic electronics.[209, 210] Field-effect transistors have also been fabricated using the higher molecular weight fullerenes C_{70} and C_{84} . [211, 212] The low solubility of C_{60} however has catalysed the development of more soluble fullerene derivatives, the most widely-used of which is [6,6]-phenyl C_{61} butyric acid methyl ester (PC_{61}BM) (Figure 2.21(c)). [213] At the cost of a reduced field-effect mobility,[111, 214] PC_{61}BM allows n-type OFET devices to be made from solution. Additionally, the use of soluble fullerene derivatives has in-part given birth to the field of bulk heterojunction solar cells.[215, 216]

Higher molecular weight PCBM molecules based on C_{70} [217] and C_{84} [218] (see Figures 2.21(d) and (e) respectively) have also been used for OFETs. Whilst the mobilities of so-called PC_{61}BM and PC_{71}BM are comparable, the measured mobilities for the C_{84} derivative are much lower.[218] This is likely to be due to the large number of isomers present and hence an increase in energetic disorder. Multiple-adduct PC_{61}BM molecules have also been developed and studied. The measured field-effect mobility of electrons in such films decreases with an increasing number of adducts.[219] To date there have been a very large number of fullerene molecules developed, and whilst the electronic properties are known to differ little, the solubility is highly dependent on the properties of the adduct(s) used.[191]

Aside from fullerene derivatives, another class of material that is of great interest at present is perylene derivatives.[94, 220–222] Two examples are given in Figures 2.21(f) and 2.21(g). These materials are reported to be both air-stable

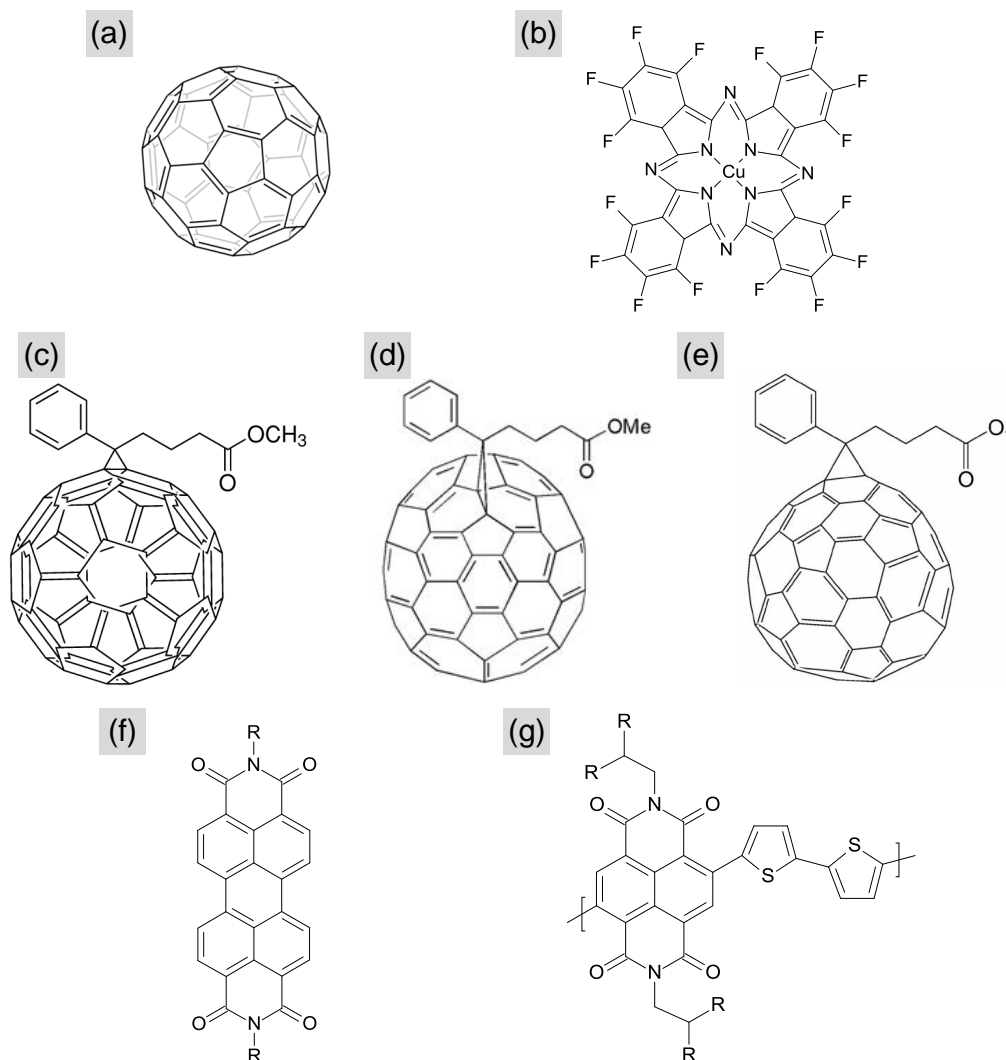


Figure 2.21: Example n-type organic semiconductors commonly used in OFETs: (a) Buckminsterfullerene (C_{60}), (b) fluorinated copper phthalocyanine (FCuPC), (c) [6,6]-Phenyl C_{61} butyric acid methyl ester ($PC_{61}BM$), (d) [6,6]-Phenyl C_{71} butyric acid methyl ester ($PC_{71}BM$), (e) [6,6]-Phenyl C_{85} butyric acid methyl ester ($PC_{85}BM$), (f) perylene-bis(dicarboximide) (PDI), (g) poly{[N,N9-bis(2-octyldodecyl)-naphthalene-1,4,5,8-bis(dicarboximide)-2,6-diyl]-alt-5,59-(2,29-bithiophene)} (P(NDI2OD-T2)).

and have high mobilities.[94] A polymerised version of such a material has also recently been reported.[94, 222] However, at present conjugated-blend systems

rely mainly on fullerenes as the n-type (or acceptor) component.[223]

2.7.3 Ambipolar Organic Semiconductors

For a semiconductor to be classified as “ambipolar”, it is generally expected to conduct both holes and electrons when used in an OFET with the same source and drain electrodes. For this to be possible, the band gap of the material must be sufficiently low as to allow injection from the electrodes into both the LUMO and HOMO of the material. This has until recently been a significant obstacle for synthetic chemists to overcome. In recent years, there have been a number of small molecules and, even more recently, polymers which exhibit both hole and electron transport. A small selection of ambipolar materials are shown in Figure 2.22.

Nickel dithiolene based small molecules (see Figure 2.22(a) for an example) are known to be both ambipolar and air stable.[107, 162] Similarly, squaraine-based small molecules (e.g. Figure 2.22(c)) have been shown to produce ambipolar OFETs with well-balanced hole and electron mobilities.[48, 145] These OFETs have been shown to be capable of both light-emission[48] and light-detection.[145] Unfortunately the difficulty with both of these materials is that the mobility is rather low; typically $\sim 10^{-4} - 10^{-3} \text{ cm}^2\text{V}^{-1}\text{s}^{-1}$.

Ambipolar polymers have until recently been extremely scarce. It has been shown that with the correct choice of dielectric,[102] many traditionally unipolar polymers can exhibit ambipolarity. For example F8BT (see Figure 2.22(b)), has been shown to have well-balanced hole and electron channels, and is also capable of light emission.[147, 224]

In the last couple of years a number of extremely high performance ambipolar polymers have been reported, many based upon the diketopyrrolopyrrole (DPP) unit (see Figure 2.22(d) for an example).[225–229] These materials exhibit well-balanced ambipolarity on many dielectric surfaces, with hole and electron mobilities both in excess of $\sim 0.1 - 1 \text{ cm}^2\text{V}^{-1}\text{s}^{-1}$. [229]

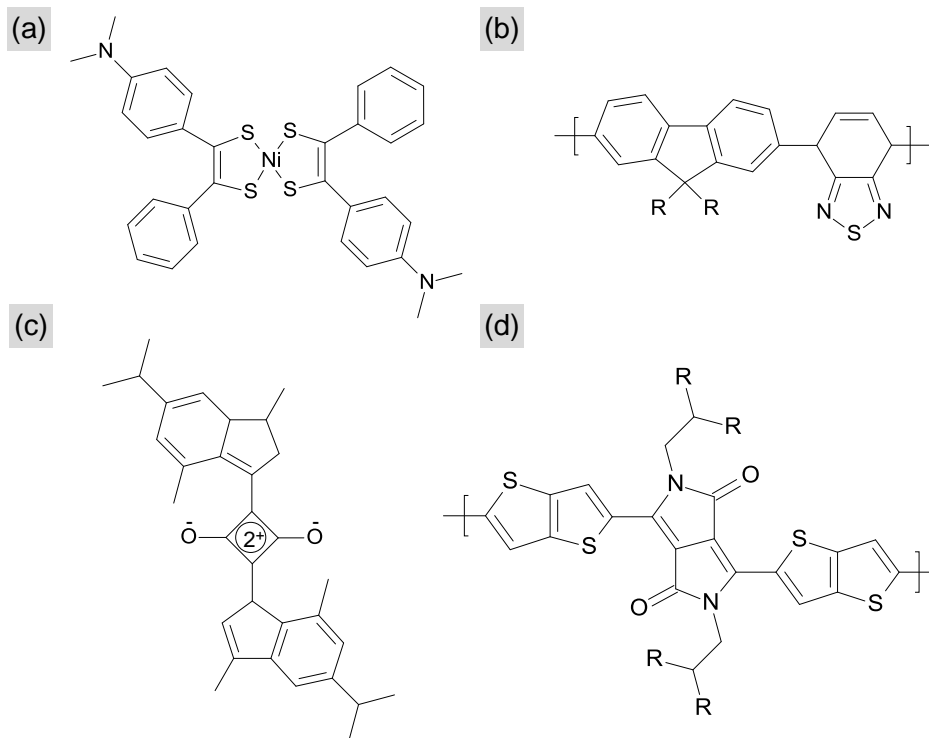


Figure 2.22: Selection of ambipolar semiconductors. (a) bis(4-dimethylaminodithiobenzyl)nickel (NiDT), (b) poly(9,9-di-*n*-octylfluorene-*alt*-benzothiadiazole) (F8BT), (c) Squaraine, (d) poly(thieno[3,2-*b*]thiophene-diketopyrrolopyrrole) (DPP-TT).

2.8 Bulk Heterojunction Solar Cells

Whilst the majority of experimental work presented within this thesis has been carried out using OFET, much of the results are significant with regards to the field of organic photovoltaic cells (OPVs). Since many of my experiments are designed to elucidate characteristics of solar-cell systems, I have here given a very brief overview of bulk heterojunction (BHJ) solar cells. BHJ solar cells are those formed from an interpenetrating mixture of two semiconductors (often a polymer and fullerene). BHJ OPVs at present provide the most impressive power conversion efficiencies,[164–166] when compared to alternative OPV structures.[230]

The field of organic solar cells is an immense research area, comparable to that

of OFETs.[60, 62, 173] The advantages of OPVs over traditional photovoltaics (PVs) are similar to those for OFETs; i.e. the possibility of low-cost, large area devices potentially compatible with flexible substrates. The specific motivation for OPVs, in contrast to OFETs, is of course to supply a low-cost source of renewable energy. Whilst the research efforts for OFETs and OPVs are generally carried out in isolation, there is a significant knowledge overlap (especially in terms of materials used).[52, 157–159]

2.8.1 Operating Principle of OPVs

The method by which BHJ solar cells convert light to electricity is as follows. One component of the blend (typically a polymer *donor*) absorbs an incident photon, leading to the formation of an excited state, or exciton (see Section 2.1.2). The exciton will then diffuse to the interface between the two semiconductor components. The exciton will then be split (dissociate) into an electron and a hole. Normally an electron is transferred from the donor to an acceptor.[210] The charges will then (under the influence of an external field) be transported to the two electrodes via their respective semiconductor networks.

The structure of a BHJ OPV is shown in Figure 2.23(a). Devices are usually fabricated on a glass substrate and illuminated from below. The eventual aim will be also implement high-efficiency OPVs on transparent plastic. To allow as much light to pass into the active layer as possible, the bottom electrode (anode) should have a high transparency. Typically indium tin oxide (ITO) is used, but carbon nanotubes[231] and graphene[232] also offer potentially low-cost alternatives.

The ITO is normally coated with poly(ethylene-dioxythiophene) blended with polystyrenesulfonic acid (PEDOT:PSS), see Figures 2.23(b) and 2.23(c)). This is to improve film-formation properties, reduce the possibility of shorts caused by a rough ITO surface,[173] and improve hole extraction from the LUMO of the donor component via work-function modification.[233]

A donor:acceptor semiconductor blend is then deposited onto the ITO:PEDOT:PSS surface via equivalent solution processing techniques used for OFET fabrication (see Section 3.2.3). Whilst blended P3HT and PC₆₁BM is the most widely-studied semiconductor system used for BHJ solar cells,[103, 206, 234–236] the highest ef-

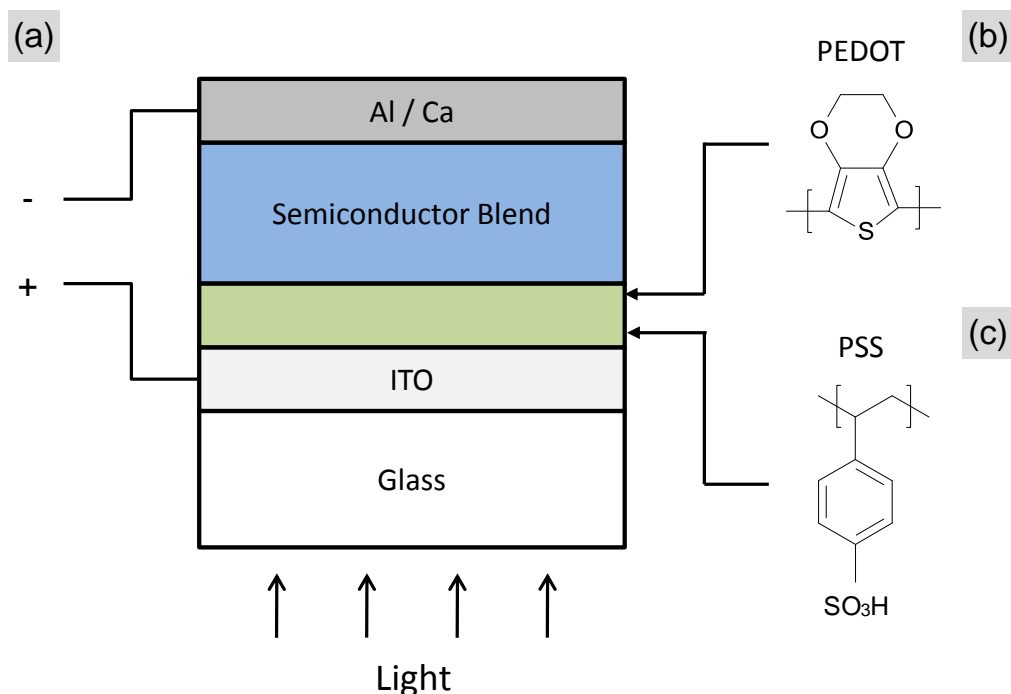


Figure 2.23: (a) Schematic diagram of common architecture for bulk heterojunction solar cells. Molecular structures of (a) poly(ethylene-dioxythiophene) (PEDOT) and (b) polystyrenesulfonic acid (PEDOT:PSS).

efficiency OPVs are now based on lower band gap (and hence often ambipolar) polymers.[164, 165]

A low work-function metal such as aluminium or calcium is then used as the top-electrode (cathode). The work function of this metal is intended to match the HOMO of the acceptor, to allow the efficient extraction of electrons. The offset between the work-function of the two electrodes then provides the internal potential to separate photo-generated charges.

2.8.2 Characterisation of OPVs

Solar cells are characterised by measuring the current as a function of applied voltage, in the dark and under illumination (see Figure 2.24(a) for an example).

If one is to make a measurement comparable to those of others, then a normalised illumination spectrum and intensity is required. The spectrum used is the so-called AM 1.5 spectrum (see Figure 2.24(b)), [41] normalised to an intensity of 1000 Wm^{-2} .

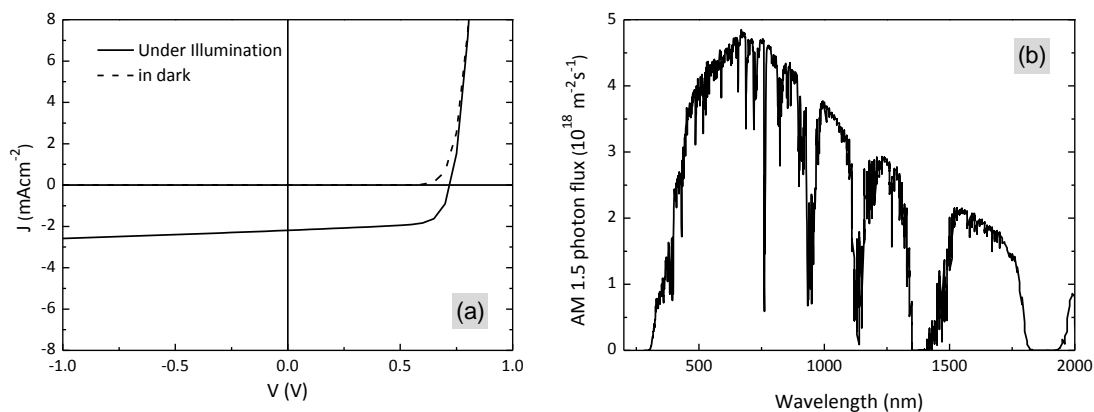


Figure 2.24: (a) Current-Voltage characteristics of an example BHJ solar cell, based upon a blend of PC_{61}BM and a DPP-based polymer (DPP-TT). (b) AM 1.5 Solar spectrum.

The power conversion efficiency of a solar cell is derived from the maximum power point (point at which the product of V and I is greatest) in the current-voltage plot, using the following formula:

$$\eta_e = \frac{V_{oc} I_{sc} FF}{P_{in}} \quad (2.27)$$

Here, V_{oc} is the open circuit voltage (the voltage at which the current is zero under illumination), I_{sc} is the short-circuit current (the current at which the voltage is zero under illumination), P_{in} is the incident light intensity (1000 Wm^{-2} under AM 1.5 conditions) and FF is the fill factor, as given by:

$$FF = \frac{I_{mpp} V_{mpp}}{I_{sc} V_{oc}} \quad (2.28)$$

Here, I_{mpp} and V_{mpp} are the current and voltage at the maximum-point respectively.

The parameters V_{oc} , I_{sc} and FF are all of critical importance to the power

conversion efficiency of OPVs and are discussed in detail elsewhere.[108, 237, 238]

2.8.3 Morphology of Polymer:Fullerene OPVs

It turns out that due to the low dielectric constant of organic materials, there is a strong Coulombic attraction between the electron and hole of a bound exciton. The diffusion length of excitons in typical organic materials is $\sim 10\text{nm}$, [239] hence excitons must be created very close to the interface between the two phases for efficient exciton-dissociation to occur. This is why the morphology of BHJ structures is very important to the performance of OPVs. The study of BHJ morphology is a very active research area, [239–242] hence I here only very briefly summarise the field.

Aside from the efficiency of exciton dissociation, the morphology of the two phases will have a strong influence over various other solar-cell processes, such as:

- The material order (and inherent carrier mobility of the two phases) will influence exciton and separated-charge transport.
- The continuity and percolation-properties will influence charge transport and collection.
- Vertical segregation will effect electrode sensitivity.

Additionally, the optical absorption spectra of certain polymer:fullerene systems has shown to be affected by the morphology of the blend. [103, 234] In general, the desired OPV microstructure should have a high interfacial area between the two components, whilst maintaining percolating pathways for both phases to their respective electrodes. A schematic representation of a so called “ideal” BHJ structure is given in Figure 2.25. [173, 243] The two phases of the donor and acceptor are separated with a length-scale similar to the exciton diffusion length in those materials. The pathways to the electrodes are continuous, and pure donor and acceptor phases at the hole- and electron-collecting electrodes also ensure that recombination losses are minimised.

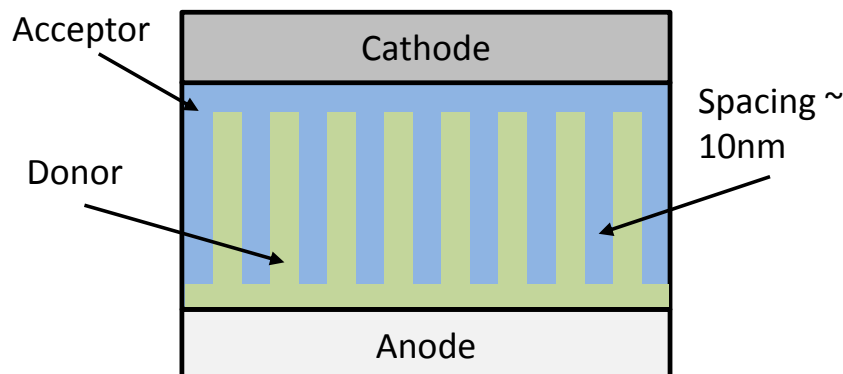


Figure 2.25: Schematic representation of so-called “ideal” morphology for donor-acceptor OPV.[173, 243]

Creating such a structure is not straight-forward. Although some groups are pursuing nano-scale imprinting as a possible means to achieve similar structures,[244–246] in most cases the targeted BHJ morphology should possess some of the properties of the ideal structure, with the simplicity associated with standard solution-processing techniques.

The morphology of polymer:fullerene blends is highly sensitive to most processing parameters. By changing parameters such as the solvents used,[247] polymer molecular weight,[248] polymer regioregularity[249] or fullerene solubility,[191] OPV device performances have been shown to vary significantly.

One of the most common post-processing techniques used to control the microstructure of polymer:fullerene blends is post-processing annealing.[206, 235, 236] In P3HT:PC₆₁BM OPVs for example, the PCE has been shown to increase significantly after annealing at 140 °C (see Figures 2.26(a) and 2.26(b)). This has been attributed to a crystallisation of the polymer component and the clustering of PC₆₁BM.[39, 103, 206, 234–236, 250] This is believed to be due to a significant improvement in charge-extraction pathways, at the expense of a slight reduction in the interfacial area between the two components. The mobilities of holes and electrons have been shown to increase significantly in such OPV structures upon annealing.[236] This process is illustrated schematically in Figure 2.26(c).

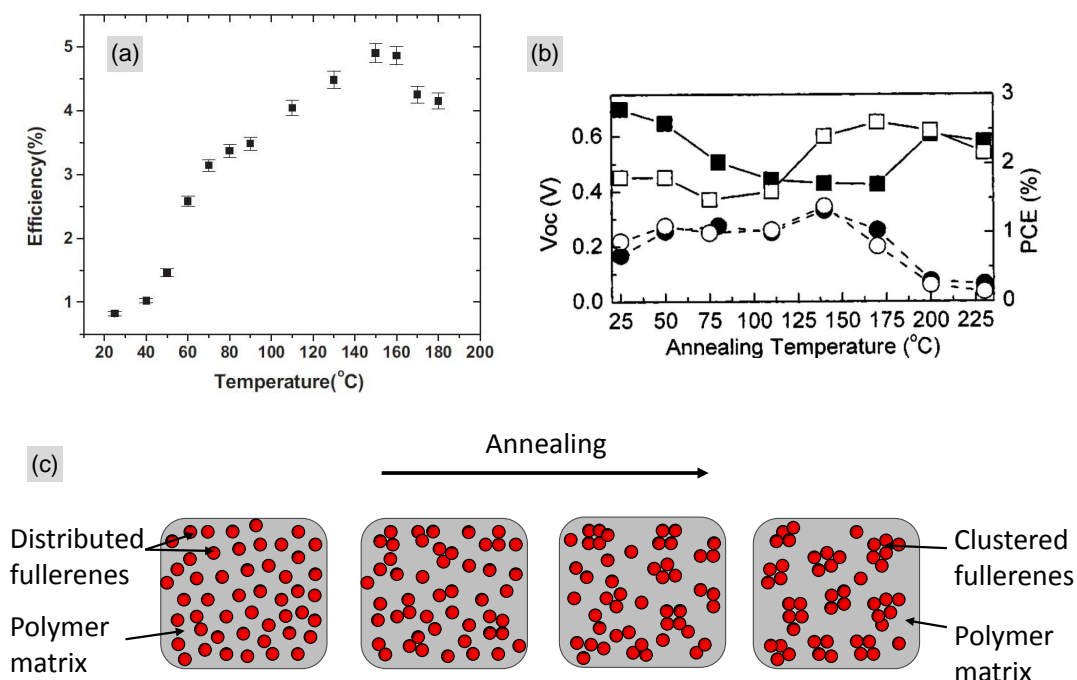


Figure 2.26: (a) Average Power conversion efficiency of >100 P3HT:PC₆₁BM OPVs plotted as a function of annealing temperature.[206] The device structure employed was ITO/PEDOT:PSS/P3HT:PC₆₁BM/Al. The blend ratio was 1.0:0.8 (wt%) P3HT:PC₆₁BM, and the annealing time was 15 minutes for each step. (b) Power conversion efficiency (circles) of P3HT:PC₆₁BM OPVs plotted as a function of annealing temperature.[235]. Again an ITO/PEDOT:PSS/P3HT:PC₆₁BM/Al structure was employed, but this time with a blend ratio of 1:1 (wt%) P3HT:PC₆₁BM. The filled circles represent data for a device made using chlorobenzene as the solvent and the open circles are data from di-chlorobenzene based devices. (c) Schematic representation of 2-dimensional cross-section of a polymer:fullerene blend undergoing phase-segregation.

Whilst post-processing annealing enhances performance in P3HT:PC₆₁BM OPVs, the PCE in other systems is not affected by such annealing.[164, 165]

Chapter 3

Experimental Methods

3.1 Introduction

The way in which novel organic field-effect transistor (OFET) architectures are realised and optimised is fundamental to the work presented within this thesis. Understanding the properties of such structures and their respective components is vital to the study of such devices, hence a robust set of tools and techniques are required. Within this chapter I describe some of the experimental fabrication and characterisation techniques employed within my work. With a solid familiarity and understanding of such techniques in place, unique and insightful studies can then be carried out in subsequent chapters.

3.2 Transistor Fabrication Techniques

In this section I describe some of the techniques used to fabricate organic field-effect transistors (OFETs) and other relevant organic thin-film structures. Due to the known oxidation properties of many n-type organic semiconductors,[162, 190] the vast majority of OFET fabrication, processing and characterisation is carried out under atmospheric-pressure N_2 . To achieve this a Jacomex glovebox with integrated probe station, spin-coater, hotplate and thermal evaporator has been employed. For measurements where the electronic properties of the film are unimportant, such as structural or optical measurements, the films were exposed

to air.

3.2.1 Substrate Preparation

For OFETs and other thin film structures a variety of different substrates are employed. These include highly-doped conducting silicon (to act as a bottom gate electrode) with a 200 nm - 400 nm thermally-grown silicon dioxide layer on top (to act as a global gate dielectric). Additionally, some pre-patterned bottom-gate, bottom-contact (BGBC) OFET substrates were acquired from our industrial partners; Philips Research Laboratories. These substrates similarly employed a highly-doped silicon substrate as the gate electrode and a thermally grown 200 nm SiO₂ layer as the gate dielectric. Gold source and drain electrodes were defined using standard lithographic techniques, with a thin titanium oxide adhesion layer between the gold and the SiO₂ surface. A hexamethyldisilazane (HMDS) passivation layer was applied to these substrates as described in Section 3.2.2.

Glass substrates are usually alkaline-earth boro-aluminosilicate sheet glass (Corning EAGLE2000), and quartz (specB) is used for optical absorption measurements.

In general the cleaning procedures for all substrates are the same. The substrates are submerged in solvents, usually acetone followed by isopropyl alcohol (IPA), and sonicated for approximately 5 minutes in each case. The substrates are then rinsed in IPA and dried with N₂. Metal-oxide dielectric surfaces are often exposed to an oxygen plasma to further remove impurities and to increase the substrate surface energy, by introduction of polar surface groups. The plasma was created in a low pressure oxygen atmosphere using radio frequency electromagnetic energy, with an Emitech K1050X plasma-asher.

3.2.2 Application of Self-Assembled Monolayers

As discussed in Section 2.3.5, self-assembled monolayers (SAMs) have a variety of uses within organic electronics. They can be used to adjust the work function of injecting electrodes,[251] to modify dielectric surface energy,[136, 140] for surface passivation[129, 137] or modification of threshold voltage.[127] SAMs have

also recently been employed as organic semiconductors in OFETs.[42, 252] The application of a SAMs is usually carried via drop-casting, dip-coating or adsorption from vapour. Octyltrichlorosilane (OTS) for example is applied by repeated drop-casting and rinsing from an IPA solution. Hexamethyldisilazane (HMDS) on the other hand is deposited onto substrates by exposure to an HMDS-rich atmosphere. A solution of HMDS in IPA is raised to an elevated temperature under a beaker containing the relevant substrates. After exposure for approximately 3 hours the substrates are removed and rinsed with IPA.

Prior to the deposition of SAMs, substrates are often exposed to an oxygen plasma, as described in Section 3.2.1. This is carried out in order for the surface to be as free from adsorbed impurities as possible and have sufficient reactive groups exposed, hence allowing the monolayer coverage to be maximised.

3.2.3 Solution-Deposition of Organic Materials

Thin-films formed from soluble organic materials are most-often deposited via spin coating. The substrate is placed on a chuck and held in place by small pillars (see Figure 3.1). The solution is deposited and the chuck is spun. For most organic semiconductor solutions, a volume of approximately 100 μL is adequate to get a complete coverage of the substrate surface. The spinning speed and length of time used will vary depending on solvent viscosity, substrate surface energy, solvent boiling point etc., but speeds and times of 500-2000 rpm and 45-90 seconds respectively, are typically used.

Insulating polymer-based dielectrics such as CYTOPTM[125] and divinyltetramethyl disiloxane bis-benzocyclobutene (BCB)[101, 102] tend to have higher viscosity than semiconducting polymers and small molecules, and hence typically require greater spinning speeds. BCB is cross-linkable and hence requires curing. For thin films (~ 50 nm) thermal curing alone is adequate,[101] however for thicker films a combination of thermal curing and exposure to ultraviolet (UV) light is necessary.[111]

The surface energy properties of some small molecules make spin-casting incompatible with certain substrates (especially highly hydrophobic SAM surfaces such as OTS). Under these circumstances these molecules may have to be de-



Figure 3.1: Photograph of spin-coater used during this work. The chuck has 8 small pillars to hold the substrates in position.

posited via drop-casting.

Drop-casting tends to result in thicker films than those formed from spin-coating, and hence the on/off ratios of OFETs formed from such films are correspondingly lower.

3.2.4 Vacuum-deposition

Vacuum-deposition is primarily used for the deposition of metals and insoluble organic materials. Samples are loaded into a holder and placed within a vacuum-chamber (see Figure 3.2 for a schematic diagram). For the deposition of metal electrodes, a mask is placed in front of the sample substrates with a set of OFET-electrode patterns etched into it. For the deposition of organic semiconductors, the samples are left unmasked.

The chamber is then evacuated and the pressure reduced to a value around 10^{-6} mbar. This pressure is maintained whilst the metal or organic source crucibles are heated. Once the sublimation temperature of the material is reached, a feedback routine is implemented and the deposition rate controlled. Deposition

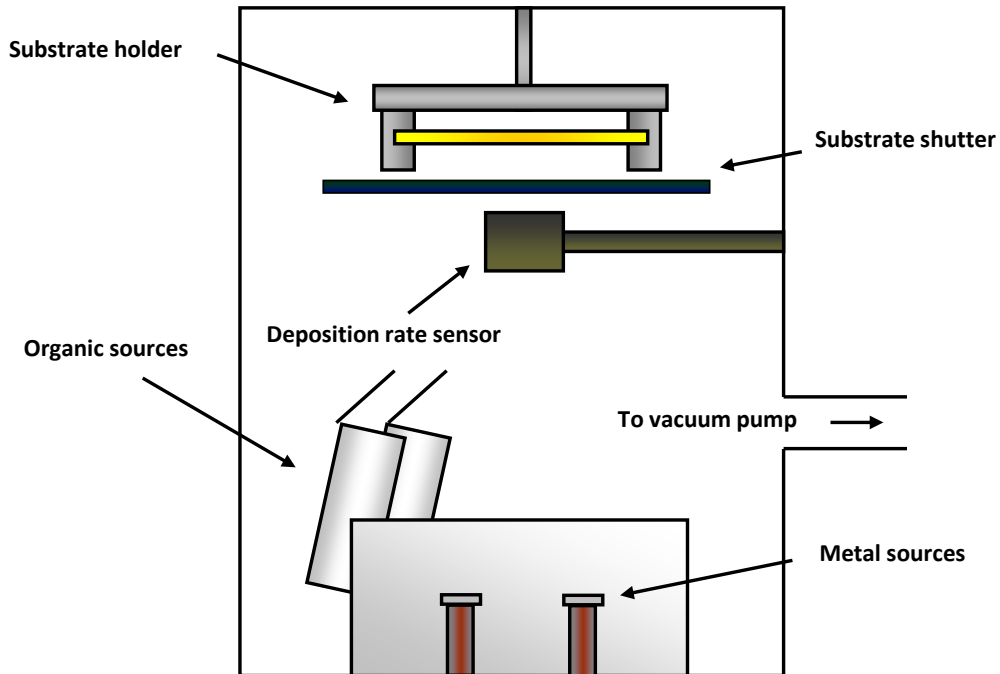


Figure 3.2: Schematic diagram of vacuum chamber used for the deposition of metals and organic semiconductors.

rates of 1 \AA s^{-1} for metals and 0.5 \AA s^{-1} for organic materials are typically used. Since the quality of films formed from evaporated organic materials is in general more crucial than those of metals, extra care is taken to ensure that the purity of organic materials is high upon deposition. The material purity can be improved by *pre-heating* organic materials at a temperature just below their sublimation temperature. Generally some impurities will evaporate during this phase. The resolution of features obtainable using metals and shadow masks is typically $\sim 10 \text{ \mu m}$.

3.3 Electrical Characterisation

3.3.1 Impedance Spectroscopy

In order to calculate the mobility and various other parameters associated with an OFET (see Section 2.3.4), it is necessary to know the capacitance per unit area (geometrical capacitance) C_i . This is normally calculated from impedance measurements, made across the gate dielectric. Here a Solartron 1260 impedance analyser is used. The relevant OFET is measured as a capacitor by attaching one probe to the gate electrode and one probe to a source or drain electrode, the electrode overlap (and hence capacitor area) can be found via optical microscopy.

A small amplitude (typically 50 mV) oscillating signal is applied across the dielectric and the current flow is measured. From these measurements the imaginary and real parts of the capacitor impedance ($\tilde{Z} = R + iX$) can be determined. It can be shown[117] that the capacitance of the dielectric depends on the applied frequency via equation 3.1.

$$C = \frac{1}{2\pi fX} \quad (3.1)$$

Under certain circumstances, it may be necessary to apply a DC voltage across the capacitor whilst making the impedance measurements using the low-amplitude AC signal. This is useful in bi-layer devices, where the capacitance will be different for each channel (see Figure 2.16). With an appropriate voltage applied across the dielectric, carriers will flow into the lower semiconductor film and form a conducting layer. The conducting layer can then be considered to be the top plate of the capacitor being measured.

3.3.2 Current-Voltage Characteristics

The performance of transistors is primarily assessed through their current-voltage characteristics. From these measurements many of the parameters of interest (see Section 2.3.4) can be determined. When a sample has been fabricated it will generally consist of several OFETs on a single substrate. To test an individual OFET, contact is made with the transistor electrodes via a set of micro-position needles.

The electrodes are then connected to a semiconductor parameter analyser (here either an Agilent 4156C, a Keithley 4200 or a Keithley 4200-SCS) and voltages are applied across the OFET terminals (see Figure 3.3(a)). The current flow at the three OFET terminals is then measured for each voltage. Similarly, when measuring voltage inverters (see Figure 3.3(b)) a voltage is applied to the supply and input voltages, whilst the output voltage is measured. The two constituent OFETs are connected together via micro-position needles and interconnect cables.

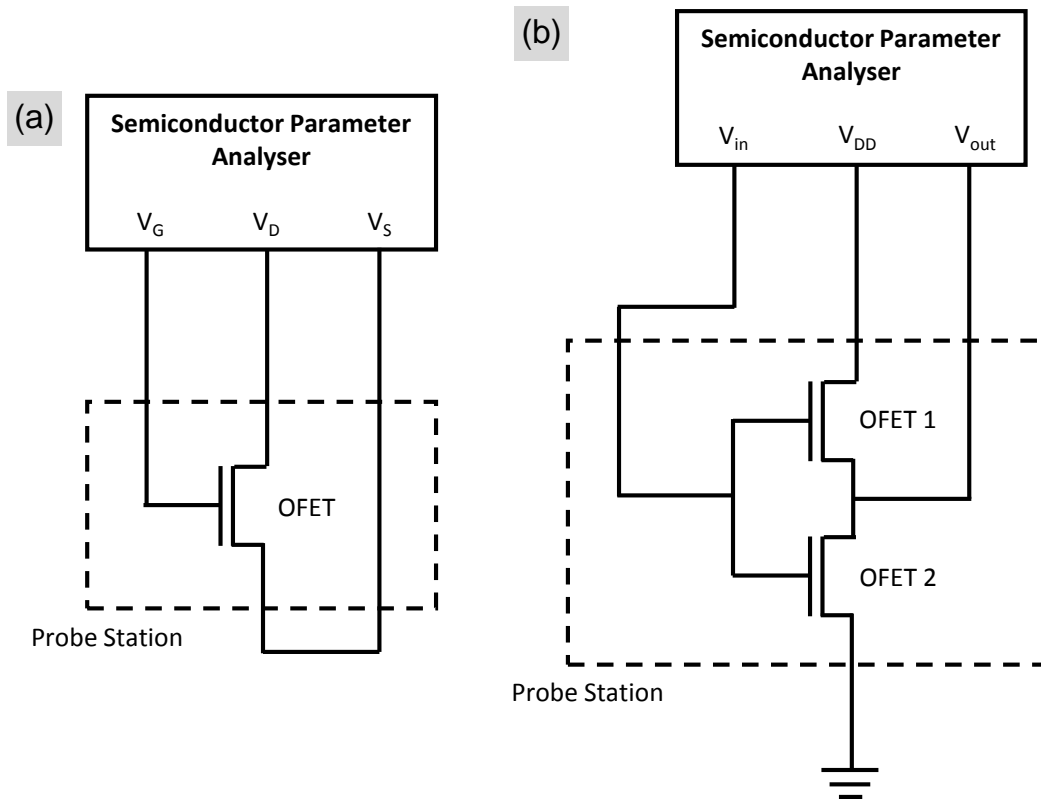


Figure 3.3: Schematic representation of the experimental setup for carrying out electrical characterisation of (a) OFETs and (b) complementary-like inverters.

Temperature-dependent measurements are carried out within a cryostat-integrated probe station, under high-vacuum (typically 10^{-5} mbar). This system incorporates both a heating stage and a liquid nitrogen-compatible cooling system.

All OFET fabrication and characterisation presented within this thesis is carried out under an inert nitrogen atmosphere or high-vacuum. This is to avoid the effects of O₂- and H₂O-related electron transport degradation.[162, 190] For certain measurements (such as in-situ annealing, see Section 5.2.4 for example) exposure of the OFETs to air is unavoidable. Under these circumstances the OFETs are generally encapsulated before transfer from the glovebox, and the encapsulation is removed prior to measurement when under vacuum. The insulating polymer CYTOP™ is used for this purpose.

3.3.3 Light-Sensing Measurements

Light-sensing characterisation was generally conducted in a similar way to as described in Section 3.3.2. Transfer characteristics are measured in the dark and under illumination from a high power LED at various applied currents. By replacing the OFET with an optical power meter (here, a 1935-C Newport Powermeter) the incident optical power density could then be determined for each applied current

When the time-dependence of an organic phototransistor is measured an oscilloscope and a current amplifier are generally used instead of a semiconductor parameter analyser (see figure 3.4).

The current amplifier used here is a Stanford Research Systems SR570, the oscilloscope is a Tektronix TPS 2024, the power supplies are Keithley 2400s and the signal generator is a TTi TG4001 40 DDS function generator. The OFET is held at constant biasing conditions and illuminated with light from an LED connected to the signal generator. The source current is then amplified using the current amplifier and measured as a voltage using the oscilloscope.

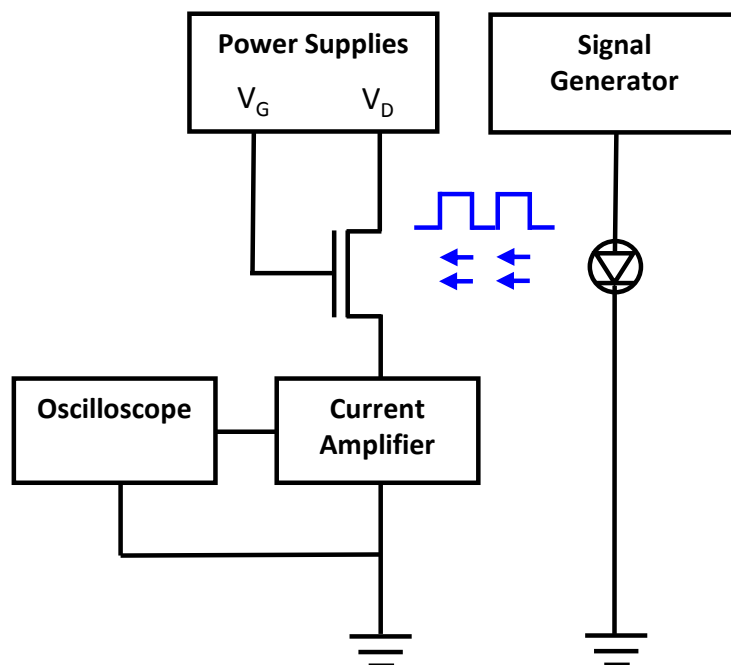


Figure 3.4: Setup for measuring dynamic electrical response of an organic phototransistor to incident light .

3.4 Other Semiconductor Characterisation Techniques

3.4.1 Optical Absorption Spectroscopy

When working with light-sensitive devices it is useful to know the optical absorption properties of the material(s) in use. To obtain this information, the material is usually deposited onto a quartz substrate and measured using a Ultraviolet-visible (UV-Vis) spectrometer. For the measurements in this thesis a Shimadzu UV-2550 UV-Vis spectrophotometer is used.

The optical absorption of samples are measured as a function of incident wavelength, using a diffraction grating system. The measurements are always carried out with respect to the absorption of a *reference sample*, which is subtracted from the sample of interest. A reference sample is simply the transparent substrate

(usually quartz) without the organic material present.

3.4.2 Atomic Force Microscopy

Atomic force microscopy (AFM) is used to examine the surface topography of samples on the sub-micron length scale. A cantilever is raster-scanned across the surface of the sample. The force between the tip of the cantilever and the sample gives rise to a deflection of the cantilever. This deflection is measured using a laser beam, which is reflected off the back of the cantilever. The height of the cantilever is then adjusted using a feedback mechanism to maintain a constant distance between the sample surface and the cantilever tip. The vertical height of the sample can then be calculated and plotted as a function of lateral position.

Tapping mode (or AC mode) AFM is most often carried out when imaging organic (or other soft) materials. In this case the cantilever oscillates near to its resonant frequency. Tapping mode AFM reduces the damage done to the sample surface and avoids problems with short-range forces causing the tip to stick to the sample surface. Throughout this work AFM is carried out in tapping mode using an Agilent 5500 atomic force microscope in ambient-pressure air. The approximate resonance frequency of the cantilever is 250 kHz and the force constant is approximately 60 Nm^{-1} .

3.4.3 Polarised Optical Microscopy

This technique allows crystalline regions of a film to be identified. Unpolarised white light is passed through a polariser to produce linearly polarised light. This is then passed through the sample. Any crystalline regions will cause birefringence and the angle of polarisation will change. The light is then passed through a second analyser at a 90° angle to the first, before entering the camera. Hence only light that has had its polarisation angle changed by birefringence will be visible. These measurements were carried out using a Nikon LV100 microscope.

3.4.4 Differential Scanning Calorimetry

Differential scanning calorimetry (DSC) is a technique employed to study and identify changes in phase within materials. The difference in heat energy required to increase the temperature of a sample is compared to that of a reference sample. The heat flow and heat release from samples allowed endotherms and exotherms to be identified. The thermograms were recorded in nitrogen at $10\text{ }^{\circ}\text{Cmin}^{-1}$ using a Mettler Toledo DSC822 instrument.

Chapter 4

Organic Phototransistors

4.1 Introduction

The field of organic phototransistors (OPTs), whilst clearly in its infancy, is growing quickly. OPTs have recently been demonstrated with response times of approximately 60 μs ,[51] and a sensitivity to infra-red light,[145] illustrating the potential of OPTs as an alternative to organic photodiodes. Organic phototransistors are known to have a responsivity which is modulated by the gate bias[50, 177], a property for which there is no analogue within photodiodes. OPTs also combine light detection and switching into a single device, potentially making the fabrication of light-sensing elements significantly less complex and hence cheaper than with photodiodes. Sensor arrays based on photodiodes need a significant amount of signal processing away from the sensor to reconstruct the image, OPTs on the other hand could possibly handle some of this processing “on-board”,[51] an essential property for self-contained, portable devices.

In this chapter, I have attempted to understand and tackle some of the problems of OPT performance and have also explored some interesting potential OPT-based device applications. Using self-assembled monolayer (SAM) gate dielectrics it can be shown that the operating voltage of OPTs can be easily reduced with little change in device performance. By fabricating OFETs using blended polymer and fullerene semiconductors, it can be shown that the bulk heterojunction (BHJ) system that has been so successful for OPV applications[164, 165] can also

produce working OPTs with high photoresponses and response times. Finally, by combining two OPTs, photo-responsive complementary-like inverter circuits are demonstrated. By employing OFET charge-transport models[144] and inverter circuit models[253] the operating mechanisms of these structures have also been studied.

4.2 Bilayer Pentacene:Fullerene Organic Field-Effect Transistors

Most reported OPTs have either been based on unipolar,[49, 50, 171, 179] or single-component ambipolar[145] semiconductor systems. It has recently been argued[63, 157] that one should expect improved exciton-dissociation efficiencies when using a donor-acceptor structure, following similar arguments to those used in OPVs. For this reason it is anticipated that as a prerequisite to observing a strong so-called photoconductive effect (see Section 2.5), a two-component donor-acceptor system is required. In this section I have demonstrated a novel bilayer donor-acceptor organic phototransistor, modelled upon similar bilayer OPV devices.[254] Whilst several bilayer ambipolar organic field-effect transistors (OFETs) have previously been reported,[149, 150] their photoresponse has to date never been discussed.

4.2.1 Evaporated small-molecule phototransistors

Whilst techniques such as orthogonal solvents,[189, 255, 256] stamp-transfer[257–259] and cross-linkable semiconductors[260] have been successfully implemented, the vast majority of multilayer organic semiconductor structures have been fabricated using thermal evaporation.[148–150, 254] The approach taken here is a combination of both vacuum-deposition and spin-casting. As a first step, it is hence important to understand the photoresponse of single-layer, vacuum-deposited small-molecule OFETs.

Here, single layer pentacene and C₆₀ OFETs have been characterised under optical illumination. The molecular structures of C₆₀ and pentacene are shown in Figures 4.1(a) and 4.1(b) respectively. A bottom-gate, top-contact (BGTC)

OFET architecture has been employed using gold source and drain electrodes. A BGTC structure is used here because it is the most relevant for comparison with the bottom-gate, middle-contact (BGMC) bilayer OFETs studied in Section 4.2.2 (see Figure 4.2(c)). Similarly, whilst not-optimised for charge transport in fullerenes,[92, 111] gold source and drain electrodes allow injection of holes/electrons into pentacene/ C_{60} ,[92, 199] making it the ideal electrode for pentacene:fullerene bilayer OFETs.[150]

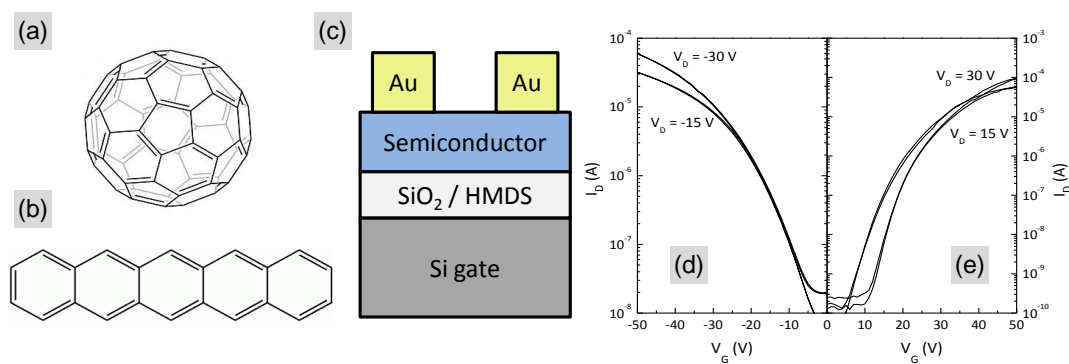


Figure 4.1: Molecular structures of (a) C_{60} and (b) pentacene. (c) Schematic diagram of bottom-gate, top-contact (BGTC) OFETs employed for this study. Transfer characteristics of (d) pentacene- and (e) C_{60} -based BGTC OFETs with gold source and drain electrodes. The channel lengths of the pentacene and C_{60} OFETs were $L = 30 \mu\text{m}$ and $L = 50 \mu\text{m}$ respectively, whilst width of both devices was $W = 500 \mu\text{m}$.

Highly doped silicon was used as both the sample substrate and global gate electrode. A 200nm thick SiO_2 layer was then thermally grown to act as the gate dielectric. HMDS was applied to the SiO_2 to passivate the surface[190] and improve crystal structure.[129] Pentacene (100nm) and C_{60} (50nm) were then deposited onto the substrates via vacuum-sublimation under high vacuum ($\sim 10^{-9}$ bar), at an average rate of 1 \AA s^{-1} . 50nm gold source and drain electrodes were deposited via vacuum-sublimation through shadow masks, once again under high vacuum. A schematic of the completed OFET structure is given in Figure 4.1(c). Example transfer characteristics of these devices are shown in Figures 4.1(d) and 4.1(e). Using equation 2.21, the saturation regime mobilities of holes in the pentacene OFET and electrons in the C_{60} OFET were extracted from

Figures 4.1(d) and 4.1(e) to be $0.35 \text{ cm}^2\text{V}^{-1}\text{s}^{-1}$ and $2.1 \text{ cm}^2\text{V}^{-1}\text{s}^{-1}$ respectively.

The pentacene and C_{60} OFETs were then illuminated with red ($\lambda = 625 \text{ nm}$) and blue ($\lambda = 470 \text{ nm}$) light respectively. These wavelengths were chosen because they are close to the respective optical absorption peaks of the two materials (see Figure 4.2(a)). The light sources were commercial (inorganic) LEDs. The full-width at half-maxima (FWHM) of the source was approximately 10 nm , and the optical power density was 0.8 mWcm^{-2} in each case. Figures 4.2(b) and 4.2(c) show the linear-regime transfer characteristics of the pentacene and C_{60} OFETs under optical illumination from red and blue light respectively. Upon illumination the threshold voltages were observed to shift by $\Delta V_{Th} = 0.6 \text{ V}$ and $\Delta V_{Te} = -1.7 \text{ V}$ for the pentacene and C_{60} OFETs respectively, whilst there is little change in the off-current. This data is representative of that expected for OPTs operating primarily in the photovoltaic mode (see Section 2.5.1), and are hence of limited interest for optical sensor applications.

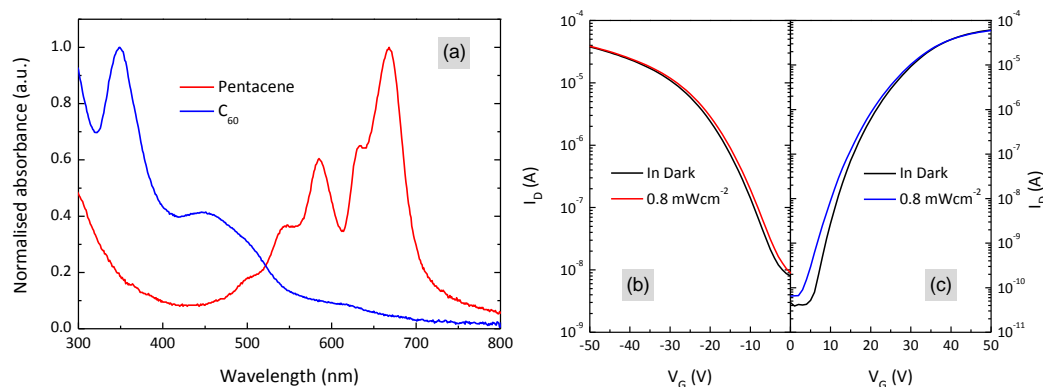


Figure 4.2: (a) Normalised optical absorption spectra of C_{60} and pentacene. Transfer characteristics of (b) pentacene- and (c) C_{60} -based BGTC OFETs with gold source and drain electrodes in the dark and under illumination from red ($\lambda = 625 \text{ nm}$) and blue ($\lambda = 470 \text{ nm}$) light respectively. The channel lengths of the pentacene and C_{60} OFETs were $L = 30 \text{ }\mu\text{m}$ and $L = 50 \text{ }\mu\text{m}$ respectively, whilst width of both devices was $W = 500 \text{ }\mu\text{m}$. The incident optical power density was 0.8 mWcm^{-2} in each case, and applied drain voltage was $V_D = \mp 15 \text{ V}$ for the pentacene and C_{60} OFETs respectively.

4.2.2 Pentacene: C_{60} BM OFETs

Bilayer pentacene: C_{60} ambipolar OFETs have previously been fabricated using a middle-contact (BGMC) structure.[150, 261] Attempts to reproduce this device here unfortunately failed. In our device an SiO_2 /HMDS dielectric was once again used, with 50nm gold source and drain electrodes. The pentacene and C_{60} layers were 100nm and 50nm respectively. A schematic diagram of the BGMC OFET structure employed here is shown in Figure 4.3(c). The resulting device was unipolar (p-type) only. Attempts to fabricate an inverted structure (C_{60} :pentacene) resulted in n-type only behaviour (data not shown). This suggests that it is the surface properties of the bottom layer that is hampering transport in the upper layer. The surface properties of dielectrics are known[127] to have a significant effect on the charge transport in OFET.

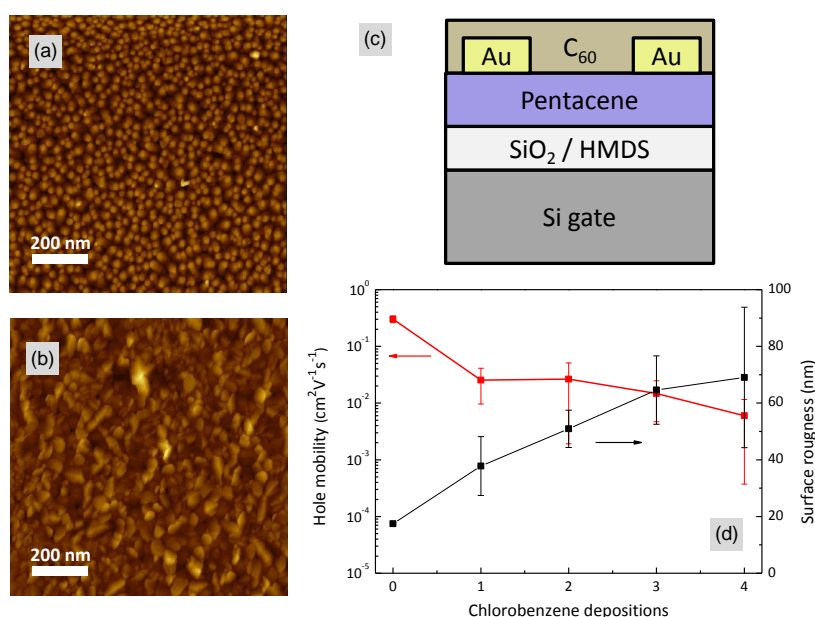


Figure 4.3: Atomic force microscope (AFM) topography images of 100nm thick pentacene films (a) before and (b) after a single application of chlorobenzene. (c) Schematic diagram of bottom-gate, middle-contact (BGMC) pentacene: C_{60} bilayer OFET. (d) Evolution of the average hole mobility of BGMC bilayer OFETs and average pentacene surface roughness after an increasing number of chlorobenzene applications to the surface of the pentacene.

To gain a better insight into this problem I attempted to modify the surface roughness of the bottom pentacene layer by applying the solvent chlorobenzene. This was applied via spin-coating and the volume applied to the substrate was 100 μL . Figure 4.3 shows atomic force microscope (AFM) images of the topography of 100nm-thick pentacene layers deposited onto HMDS-treated SiO_2 (a) before and (b) after an application of chlorobenzene. The root-mean-squared (rms) surface roughness of the pentacene surface before and after chlorobenzene application was 7nm and 23nm respectively. Bilayer pentacene: C_{60} OFETs were fabricated after the application of CB to the pentacene layer (which was in-turn before electrode deposition). Once again no n-channel was measured. Figure 4.3(d) shows the average saturation-regime hole mobility of 5 bilayer pentacene: C_{60} OFETs and the corresponding average rms roughness of 5 positions in pentacene films after an increasing number of chlorobenzene depositions. This reduction in mobility suggests that the chlorobenzene is dissolving the pentacene film and hence disrupting the intermolecular packing.[196] It is also evident that the roughness of the pentacene layer increases with the number of chlorobenzene applications.

In an attempt to approach the problem from a different direction, I then fabricated bilayer BGMC OFETs employing the semiconductors pentacene and [6,6]-phenyl- C_{61} -butyric acid methyl ester (PC_{61}BM). The structure of these devices are identical to that of Figure 4.3(c) but with the C_{60} replaced by PC_{61}BM . A 100nm thick layer of pentacene was deposited onto HMDS-treated SiO_2 before 50nm gold source and drain electrodes were deposited onto the pentacene. The PC_{61}BM was spin-cast from chlorobenzene solution onto the pentacene/Au surface. The molecular structures of PC_{61}BM and pentacene are given in Figures 4.4(b) and 4.4(c). A schematic representation of this OFET structure is given in Figure 4.4(a). Example output and transfer characteristics of such a bilayer device are given in Figure 4.4. We now see that this device displays characteristics representative of ambipolar behaviour.[144] The device exhibits low hysteresis and well-balanced hole and electron channels. The hole mobility was evaluated in the saturation regime to be $3.6 \times 10^{-2} \text{cm}^2 \text{V}^{-1} \text{s}^{-1}$, whilst the electron mobility was evaluated to be $1.9 \times 10^{-2} \text{cm}^2 \text{V}^{-1} \text{s}^{-1}$.

The reason why the pentacene: PC_{61}BM OFETs showed ambipolar behaviour whereas the pentacene: C_{60} OFETs did not is not immediately obvious. Effects

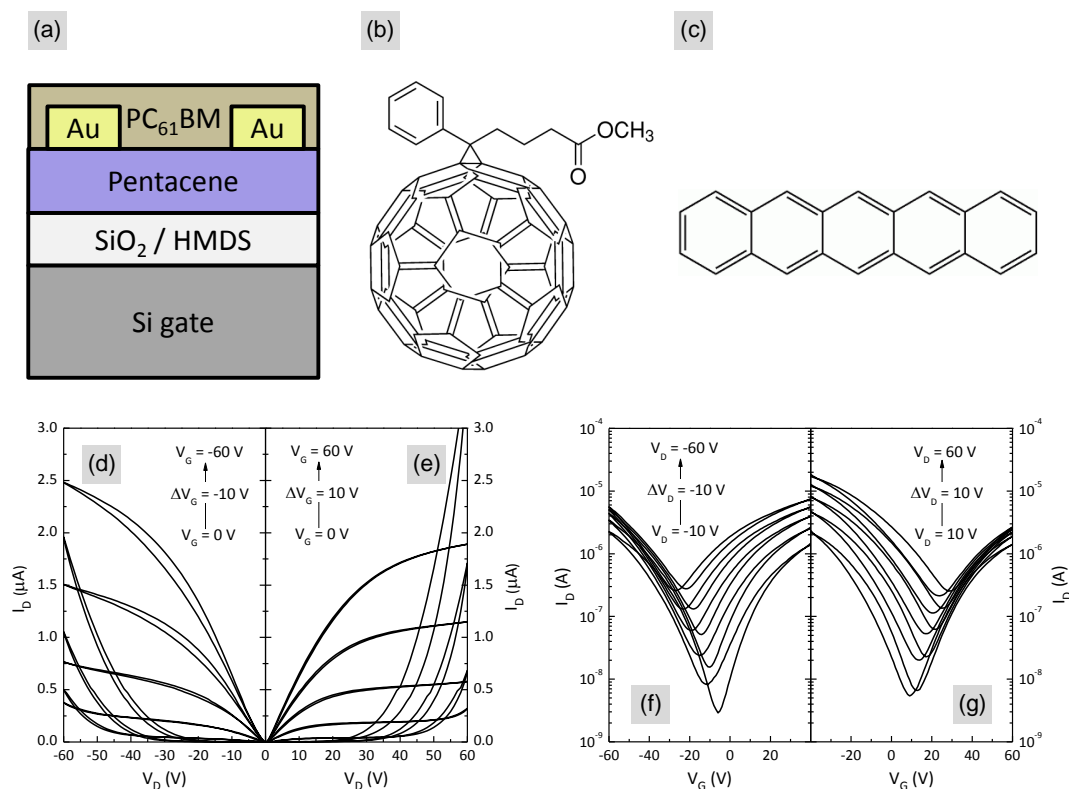


Figure 4.4: (a) Schematic diagram of bottom-gate, middle-contact (BGMC) pentacene:PC₆₁BM bilayer OFET. Molecular structures of (b) PC₆₁BM and (c) pentacene. Output characteristics of bottom-gate, middle-contact pentacene:PC₆₁BM bilayer OFET with (d) negative gate voltages and (e) positive gate voltages. The OFET had channel dimensions of $W = 1000 \mu\text{m}$ and $L = 50 \mu\text{m}$. Transfer characteristics of same bilayer OFET with (f) negative drain voltages and (g) positive drain voltages.

due to differences in the energetic and charge-transport properties of C₆₀ and PC₆₁BM can be ruled out, because attempts at fabricating pentacene:PC₆₁BM OFETs with vacuum-deposited PC₆₁BM once-again yielded p-type only devices (data not shown, see Section 6.2 for details of vacuum-deposited PC₆₁BM OFETs). It is possible that spin-casting PC₆₁BM onto the pentacene layer results in a system with some properties of a bulk-heterojunction (BHJ), due to the partial dissolution of the pentacene and potential for PC₆₁BM diffusion. If a significant

PC₆₁BM percolation-pathway is present at the semiconductor-dielectric interface then this could lead to the formation of an n-channel.[109] In the paper by Kuwahara *et. al.*, the electron mobility of their pentacene:C₆₀ OFETs was found to increase upon annealing.[150] Given the recent observation of interdiffusion in other bilayer systems upon annealing,[259, 262] it is possible that they were perhaps also measuring something possessing some BHJ properties rather than a strict bilayer device. Annealing single-layer pentacene and C₆₀ OFETs at temperatures up to 160°C was found to have little impact on device performance (data not shown), suggesting that the increases observed[150] were not due to improvements in microstructure alone. It should be noted however that whilst a hole mobility of $3.6 \times 10^{-2} \text{cm}^2 \text{V}^{-1} \text{s}^{-1}$ is clearly lower than expected for a pristine pentacene film,[199] the measured electron mobility of $1.9 \times 10^{-2} \text{cm}^2 \text{V}^{-1} \text{s}^{-1}$ is close to what is expected for an optimised single-layer PC₆₁BM OFET with gold-source and drain electrodes,[111] and significantly higher than most reported for polymer:PC₆₁BM BHJ blends.[52, 63] The high electron mobility is hence indicative of an undisturbed pristine PC₆₁BM layer.

4.2.3 Photoresponse of Pentacene:PC₆₁BM OFETs

Regardless of the exact reason behind the observed ambipolarity, the working device now allows its suitability as a photodetector to be investigated. The bilayer was illuminated with monochromatic (FWHM = 10nm) blue ($\lambda = 470 \text{ nm}$) light. The optical absorption spectra of the bilayer structure and the constituent layers are shown in Figure 4.5(a).

The transfer characteristics of an example pentacene:PC₆₁BM OFET under illumination from 470 nm light are shown in Figure 4.5(b). The applied drain voltage was $V_D = 40 \text{ V}$ and the device dimensions were: $W = 1000 \mu\text{m}$ and $L = 50 \mu\text{m}$. The incident optical power density was varied between 0 mWcm^{-2} and 1.6 mWcm^{-2} . Here we see effects that are representative of both the photoconductive and the photovoltaic OPT effects. The threshold voltages of the hole and electron channels were found to shift by $\Delta V_{Th} = -1.9 \text{ V}$ and $\Delta V_{Te} = -3.6 \text{ V}$ respectively, whilst the off-current increased by a factor of 1.5. Using the data from Figure 4.5(b) and equation 2.23, the peak responsivity of the OPT was found to be

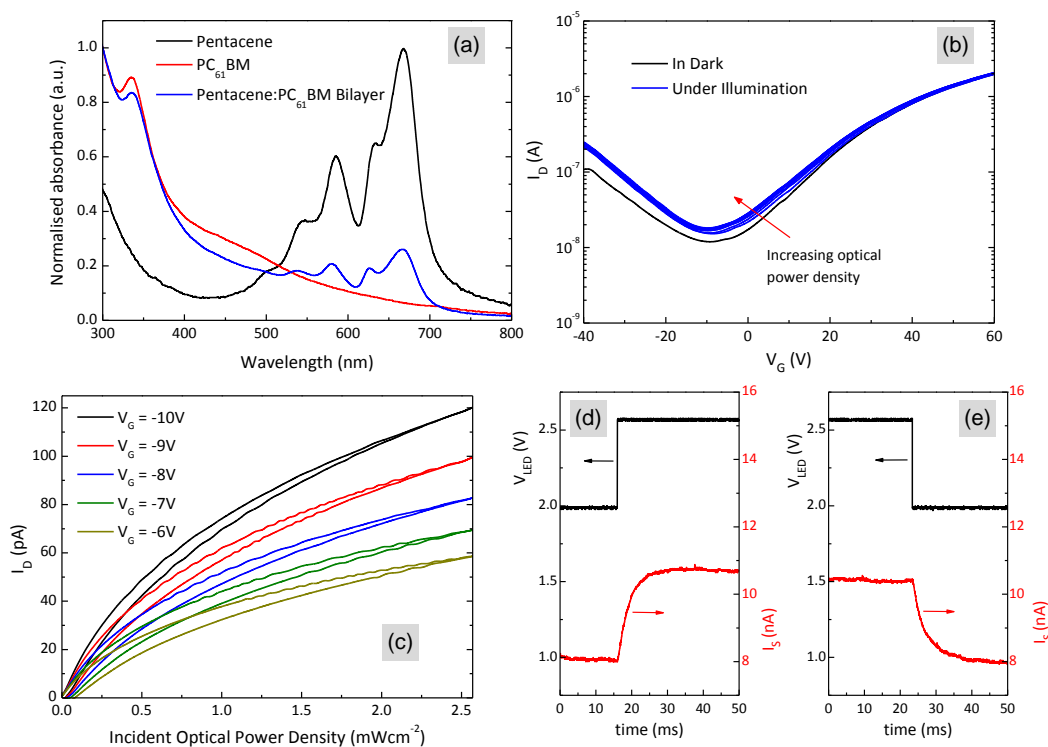


Figure 4.5: (a) Optical absorption spectra of pentacene, PC₆₁BM and pentacene:PC₆₁BM bilayer. (b) Saturation-regime ($V_D = 40$ V) transfer characteristics of pentacene:PC₆₁BM bottom-gate, middle-contact (BGMC) bilayer OFET measured in the dark and under illumination from blue ($\lambda = 470$ nm) light. The OFET had channel dimensions of $W = 1000$ μm and $L = 50$ μm . The incident optical power density was varied between 0 mWcm^{-2} and 1.6 mWcm^{-2} . (c) Drain current of same bilayer OFET as function of incident optical power density, whilst held at a constant drain ($V_D = 20$ V) and gate voltages. (d) and (e) Time-dependent response of bilayer OFET source current (I_S) to changes in the voltage applied to the LED (V_{LED}), whilst being held at constant drain and gate voltages; $V_D = 20$ V, $V_G = 11$ V.

approximately 150 mAW^{-1} .

The relationship between drain current and optical power density is an important one. With regards to optical sensors, a linear dependence of the measurable quantity (often a device current) on incident optical power density is highly sought-after.[117] Figure 4.5(c) shows the drain current of a pentacene:PC₆₁BM bilayer OFET as a function of incident optical power density, whilst the OFET

is held at a constant drain ($V_D = 20$ V) and gate voltage. The two lines show the forward (lower) and reverse (upper) LED optical power-density scans for each gate voltage. The relationship is clearly sub-linear. This is likely to be due the saturation of photo-generated charge carriers, as described in Section 2.5.[64] There is a small amount of hysteresis between the forward and reverse scans. This can be explained by long-term changes in trap-occupation density at the semiconductor-dielectric interface,[113] resulting in small changes in threshold voltage.

The long-term (photovoltaic) effect manifest as hysteresis in Figure 4.5(c) is generally too slow for realistic use in commercial photodetectors.[113, 170, 172] The faster response times observed in OPTs are generally attributed to an increase in the off-current due to the generation and dissociation of excitons (the photoconductive effect).[51] The response time of the pentacene:PC₆₁BM OPTs was characterised by pulsing the light source and monitoring the time-dependence of the source current. The gate and drain voltages of the OFET were held constant at $V_D = 20$ V and $V_G = 11$ V. The source current was measured with a Tektronix TPS 2024 oscilloscope after being amplified using a Stanford Research Systems SR570 amplifier, with a sensitivity of 5 nAV⁻¹. The 470 nm LED was then pulsed at a frequency of 10 Hz. The voltage applied across the LED and the measured source current are plotted as the OPT turns (d) on and (e) off in Figure 4.5.

The structure of an FET could lead to some capacitive effects, which may be the limiting factor in optical-response time, in much the same way as the electrical response.[88] If we hence assume the response is RC-limited, then we can model the rise and decay of the source current as being exponentially-dependent on time. Using this assumption the following equations can be derived to describe the change in source current resulting from turning the LED on or off:

$$I_S(t) = I_{on} - (I_{on} - I_{off})e^{-t/\tau_{on}} \quad (4.1)$$

$$I_S(t) = I_{off} + (I_{on} - I_{off})e^{-t/\tau_{off}} \quad (4.2)$$

Here $I_S(t)$ is the measured source current at a time t after the LED has been

switched on/off, I_{off} is the source current when the LED is constantly off, I_{on} is the source current when the LED is constantly on, and τ_{on} and τ_{off} are the time constants associated with the switch-on and switch-off processes. By fitting the data in Figures 4.5(d) and 4.5(e) to equations 4.1 and 4.2 (data not shown), the time constants associated with this device were found to be: $\tau_{on} = 3.5$ ms and $\tau_{off} = 3.9$ ms. Although clearly slower than the fastest OPTs reported,[51] these response times are quite impressive and are certainly comparable with values reported for OPDs.[168]

4.3 Low-Voltage Pentacene:PC₆₁BM Phototransistors

Perhaps one of the most noticeable differences between OPTs and OPDs is the typical operating voltage. Most OPDs are reported to operate with applied voltages in the range of 1 - 5 V,[169] whereas all OPTs reported to date operate at voltages in excess of 20 V.[49, 50, 63, 157, 171, 177, 179] Aside from being undesirable with regards to power consumption, operating voltages in the range reported for OPTs would render them useless for any portable or battery-powered applications. So in terms of turning OPTs into commercially-viable components for sensors, a reduction in operating voltage is crucial.

As described in Section 2.3.5, the operating voltages of OFETs have been successfully reduced using self-assembled monolayer (SAM) gate dielectrics.[99, 100] In this section I have attempted to reduce the operating voltage of the bilayer pentacene:PC₆₁BM organic phototransistors using a similar approach. By using an ultra-thin metal-oxide layer combined with SAMs, our group have recently developed dielectrics with geometrical capacitances in the range of 600 - 800 nFcm⁻²[136] and leakage current densities on the order of 10⁻⁹ Acm⁻². [128] As has previously been shown[136] the surface-energy properties of most SAMs make solution-deposition methods such as spin-coating difficult for many semiconductor systems. Hence the combination of vacuum-deposition and spin-coating techniques employed in Section 4.2 are ideal for this dielectric.

Aluminium gate electrodes were thermally deposited onto glass substrates

under high vacuum. The surfaces of the gate electrodes were oxidized in oxygen plasma leading to the formation of native alumina a few nanometres thick.[99] A 1.7 mgml^{-1} solution of octadecylphosphonic acid (ODPA) in isopropanol was drop-cast onto the electrodes followed by rinsing with pure isopropanol. The substrates were then thermally annealed for 20 h at 140°C at ambient-pressure in N_2 . Following this a pentacene layer (100 nm) was deposited by thermal sublimation under high vacuum (10^{-9} bar) at a rate of 1\AA s^{-1} . Gold source and drain electrodes (45 nm) were then thermally deposited onto the pentacene layer. Finally, a solution of PC_{61}BM in chlorobenzene was spin-cast onto the devices. Figure 4.6(a) shows the structure of these low-voltage BGMC devices.

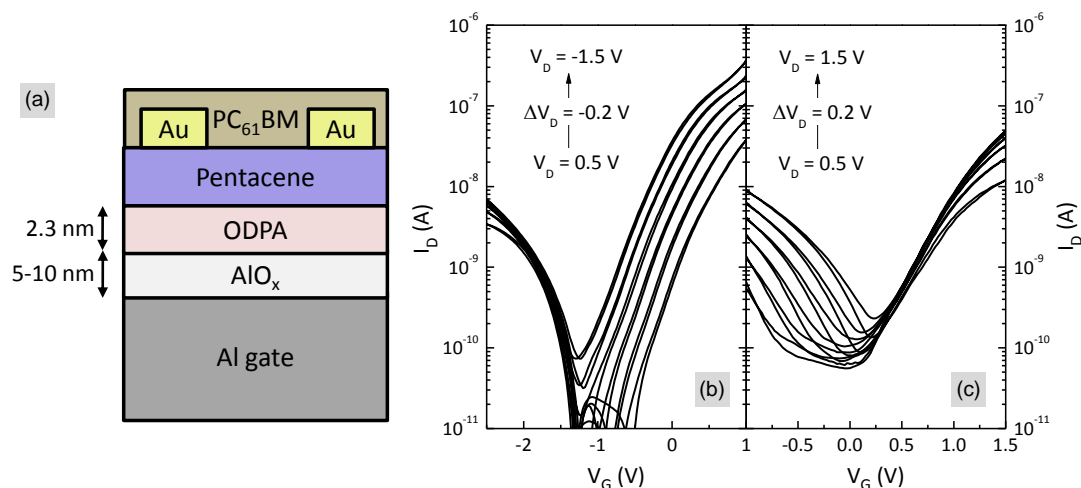


Figure 4.6: (a) Schematic diagram of low-voltage bottom-gate, middle-contact (BGMC) pentacene: PC_{61}BM bilayer OFET. Transfer characteristics of low-voltage pentacene: PC_{61}BM bilayer OFET with (b) negative and (c) positive drain voltages. The OFET had channel dimensions of $W = 1000 \mu\text{m}$ and $L = 50 \mu\text{m}$.

The transfer characteristics of an example low-voltage pentacene: PC_{61}BM bilayer OFET are shown in Figures 4.6(b) and 4.6(c). The devices clearly exhibit ambipolar behaviour, illustrating that the bilayer pentacene: PC_{61}BM structure is compatible with SAM gate dielectrics. The dielectric is different for the two different channels. For the hole channel the dielectric is just the AlO_x /SAM layers, whereas for the electron channel the dielectric will also include the pentacene layer. This is because pentacene is insulating to electrons but not to holes. Since

the pentacene layer is 100 nm thick, equation 2.22 indicates that this will have a significant impact on the geometrical capacitance of the gate dielectric. The geometrical capacitance of the two dielectrics in the OFET in Figure 4.6 were measured using a Solartron 1260 impedance analyser at a frequency of 400 Hz. By changing the bias applied between the source and gate electrodes, the pentacene layer was changed from being insulating (positive voltages) to conducting (negative voltages). This allowed the geometrical capacitance of the AlO_x/SAM and $\text{AlO}_x/\text{SAM}/\text{pentacene}$ dielectrics to be evaluated as 880 nFcm^{-2} and 70 nFcm^{-2} respectively.

Using equation 2.21, the saturation-regime field-effect mobility was calculated from figures 4.6(b) and 4.6(c) to be $\mu_h = 7 \times 10^{-4} \text{ cm}^2\text{V}^{-1}\text{s}^{-1}$ and $\mu_e = 0.1 \text{ cm}^2\text{V}^{-1}\text{s}^{-1}$ for holes and electrons respectively. The low hole mobility can again be attributed to a slight dissolution of the pentacene layer, whilst the very high electron mobility is somewhat surprising. It is possibly due to the formation of a favourable microstructure and interface with the pentacene layer, or it may be because the PC_{61}BM has diffused through the pentacene, meaning the value of $C_i = 70 \text{ nFcm}^{-2}$ would be an under estimate for the mobility calculation.

4.3.1 Photoresponse of Low-Voltage Pentacene: PC_{61}BM OFETs

As with the high-voltage OFETs from Section 4.2.3, the aptitude of low-voltage pentacene: PC_{61}BM bilayer OFETs for light-sensing applications was investigated. The bilayer OFETs were illuminated with the same monochromatic blue ($\lambda = 470 \text{ nm}$) light from the previous section. Figure 4.7(a) shows the transfer characteristics of an example low-voltage pentacene: PC_{61}BM bilayer OFET in dark and under illumination from blue light with optical power densities between 0 mWcm^{-2} and 3.2 mWcm^{-2} . The applied drain current was $V_D = 1 \text{ V}$, and the OFET had channel dimensions of $W = 1000 \text{ }\mu\text{m}$ and $L = 50 \text{ }\mu\text{m}$. It is clear that this device again exhibits both photoconductive and photovoltaic effects. The off-current increased by a factor of 43 at its minimum point, whilst the threshold voltages of the p- and n-channels shifted by $\Delta V_{Th} = -0.02 \text{ V}$ and $\Delta V_{Te} = -0.23 \text{ V}$ respectively.

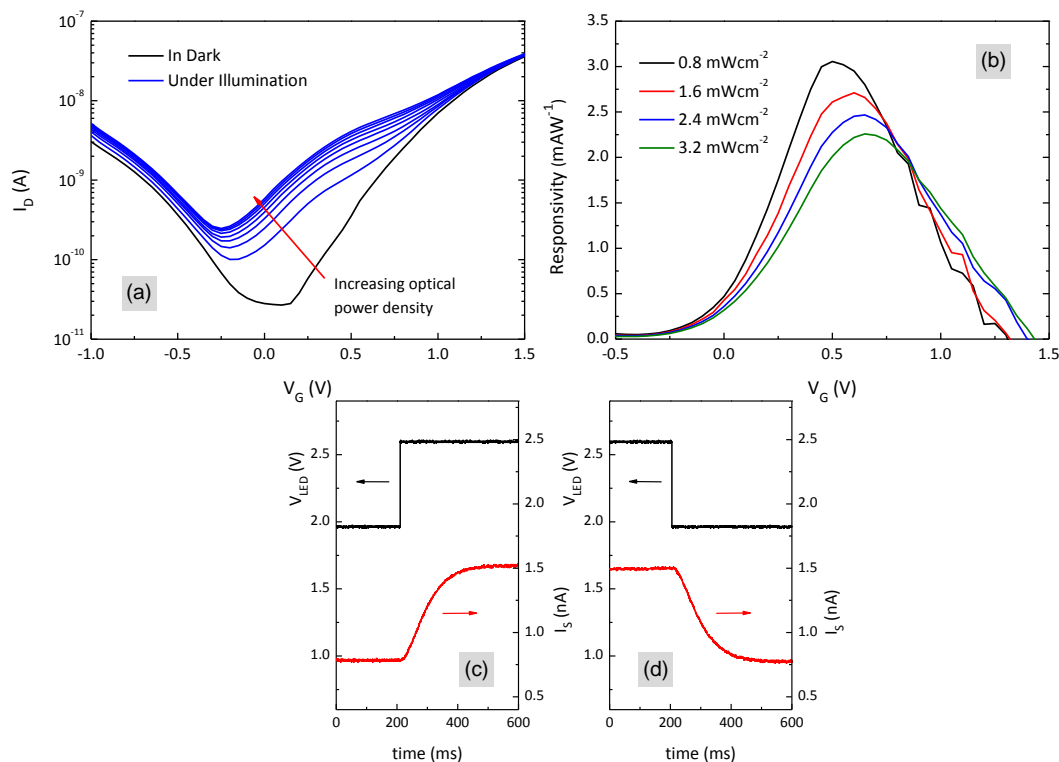


Figure 4.7: (a) Transfer characteristics of low-voltage bottom-gate, middle-contact (BGMC) pentacene:PC₆₁BM bilayer OFET in dark and under illumination with blue light ($\lambda = 470$ nm). The applied drain current was $V_D = 1$ V, and the OFET had channel dimensions of $W = 1000$ μm and $L = 50$ μm . The incident optical power density was varied between 0 mWcm^{-2} and 3.2 mWcm^{-2} . (b) Responsivity of same bilayer OPT calculated using equation 2.23. The applied voltage was in this case $V_D = 0.5$ V. (c) and (d) Time-dependent response of low-voltage bilayer OPT source current (I_S) to changes in the voltage applied to the LED (V_{LED}), whilst being held at constant drain and gate voltages; $V_D = 1$ V, $V_G = 0.5$ V.

Using equation 2.23, the responsivity of the low-voltage OPT was calculated and plotted as a function of gate voltage for several different incident optical power densities in figure 4.7(b). The applied drain voltage was in this case $V_D = 0.5$ V. The fact that the responsivity of the device can be modulated by the applied gate voltage is another appealing feature of OPTs.[50, 177] The peak responsivity of the device is observed to fall as the incident optical power density is increased.

This can be explained by the saturation of photo-generated excitons,[64] the same effect responsible for the sub-linear increase in drain current with optical power density in Figure 4.5(c). Figures 4.7(c) and 4.7(d) show the response time of the same low-voltage bilayer OPT. By fitting this data to equations 4.1 and 4.2, the time constants associated with the switch-on and switch-off processes were found to be: $\tau_{on} = 93$ ms and $\tau_{off} = 98$ ms respectively. The response is hence significantly slower than the high-voltage equivalent device from Section 4.2.3, however this can be explained by the higher geometrical capacitance of the low-voltage dielectric. It hence appears that there will be some trade-off between operating voltage and response time, much like with electrical response.[88]

4.4 Organic Opto-Electronic Circuits

The ease with which OPTs could potentially be integrated with driving electronics is the main motivation for their study. The simplest example of an integrated circuit is the inverter. As discussed in Section 2.6.1, an inverter consists of two OFETs and is designed to take a high input signal and output a low signal, or vice-versa. An advantage of ambipolar OFET systems in comparison to unipolar OFETs is that they can easily be incorporated into the complementary architecture (see Figure 2.18), improving noise margins and power-dissipation greatly, with little increase in structural complexity.

Here I have investigated the effect of light on complementary-like[109] inverters based upon ambipolar OPTs. The purpose of this section is to better understand how OPT-based circuits may perform as potential light-sensing elements[51] and to attempt to gain some insight into their operating mechanism.

4.4.1 Low-Voltage Pentacene:PC₆₁BM Photo-Inverters

By combining two low-voltage bilayer Pentacene:PC₆₁BM OFETs a complementary-like inverter was fabricated. Figure 4.8 shows the (a) schematic and (b) measured characteristics of the low-voltage complementary-like inverter employed here. The inverter exhibits a low operating voltage, low hysteresis and high small-signal gain (see Figure 4.8(c)).

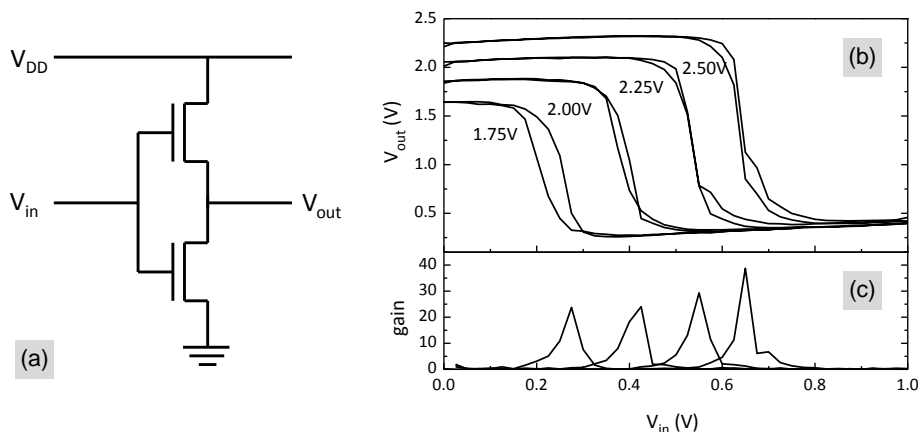


Figure 4.8: (a) Schematic diagram of complementary-like inverter comprising two low-voltage bilayer pentacene:PC₆₁BM OPTs. (b) Output voltage V_{out} , of complementary-like inverter as function of input voltage V_{in} , for several different supply voltages V_{DD} . The channel widths of the bottom and top OPTs in sub-figure (a) were $W = 1$ mm and $W = 0.5$ mm respectively, whilst the channel length of both OPTs was $L = 50$ μm . (c) Small-signal gain of same low-voltage inverter calculated from sub-figure (b), using equation 2.26.

To achieve a high noise margin, and hence a high yield of working circuits when combining several inverters, it is desirable to have the switching voltage of the inverter at half the supply voltage; $V_{DD}/2$.^[142] The switching voltage is the approximate voltage at which the inverter makes the transition from giving a high output to giving a low output. Unfortunately the switching voltage of the low-voltage inverters shown in Figure 4.8 is significantly below $V_{DD}/2$. This is likely to be because the mobility, and therefore drain currents, of the hole- and electron-channels of these OFETs are unbalanced.

The low-voltage inverter from Figure 4.8 was then illuminated with 470 nm light and the device characteristics were again measured. Both constituent OPTs received equal incident optical power densities between 0 and 1.2 mWcm^{-2} . Figure 4.9(a) shows that whilst the output voltages for the on- and off-states remain unchanged, the switching voltage changes significantly. The reason behind this shift is likely to be mainly due to changes in the threshold voltages of the two OPTs (the photovoltaic effect), and is discussed further in Section 4.5.

Upon inspection of Figure 4.9(a) one would expect that by biasing the photo-

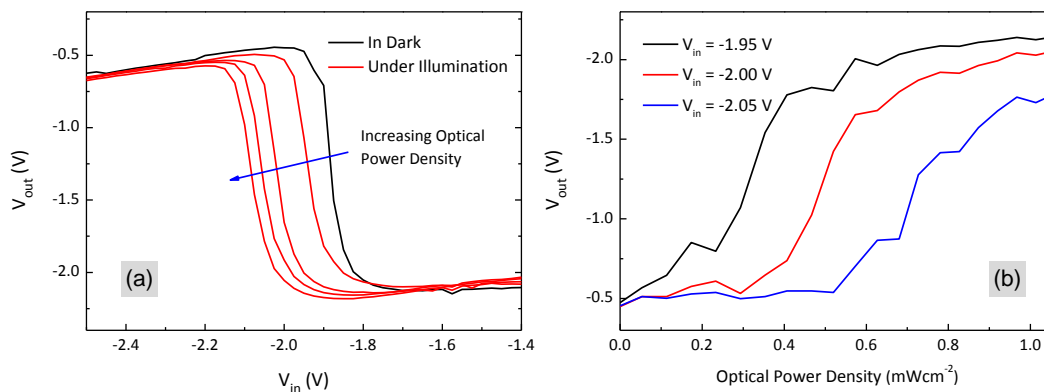


Figure 4.9: (a) Characteristics of low-voltage inverter from Figure 4.8 measured in the dark and under illumination from 470 nm light. The supply voltage was $V_{DD} = -2.5$ V and the incident optical power density was varied between 0 and 1.2 mWcm^{-2} . (b) Output voltage of same low-voltage photo-inverter held at constant $V_{in} = -2.5$ V and $V_{DD} = -2.5$ V, plotted as a function of incident optical power density.

inverter input voltage at a constant value close to its switching voltage, a very significant modulation of the output voltage could be achieved over a reasonably small range of incident optical power densities. To illustrate this effect, the output voltage of the low-voltage photo-inverter has been plotted as a function of incident optical power density for several input voltages in Figure 4.9(b). It is evident from Figure 4.9(b) that the output voltage can be modulated over a range of 1.5 V by the incident light. This amplification effect is an apt illustration of the potential advantages of using OPT-based optical sensors.

4.4.2 MDMO-PPV:PC₆₁BM Photo-Inverters

The data shown in Figure 4.9 suggests that a further investigation into the performance of photo-inverters is worthwhile. Whilst the bilayer OPTs from Section 4.3 showed impressive performance, it is perhaps more beneficial to develop an understanding of how the more thoroughly-studied[51, 63] BHJ OPTs perform when employed in photo-inverters. BHJ OPTs have the advantage of improved processability compared to bilayers, but due to the surface-energy properties of some dielectrics,[136] are incompatible with certain device architectures. Here I

have used the blend of the polymer poly[2-methoxy-5-(3',7'-dimethyloctyloxy-*p*-phenylene vinylene)] (MDMO-PPV) and PC₆₁BM, as with previously-reported opto-electronic circuits.[51] The molecular structure of MDMO-PPV is shown in the inset to Figure 4.10(b).

In this case bottom-gate, bottom-contact (BGBC) OPTs were fabricated on highly doped silicon wafers which acted as the global gate electrode. A 200 nm thermally-grown silicon dioxide layer was used as the gate dielectric. Gold source and drain electrodes were defined using standard photolithographic techniques. The silicon dioxide surfaces were again passivated with HMDS. A 1:6 (wt %) blend of MDMO-PPV:PC₆₁BM was then spin cast from a chlorobenzene solution onto the transistor substrate. A schematic diagram of this structure is shown in Figure 4.10(a).

The optical absorption spectrum of the MDMO-PPV:PC₆₁BM blend is shown in Figure 4.10(b). It is evident that this blend is significantly blue-shifted with respect to that of the pentacene:PC₆₁BM bilayers shown in Figure 4.5(a). This is due to both the increase in volume fraction of PC₆₁BM here and the larger bandgap of MDMO-PPV with respect to pentacene. We should hence expect a much more significant photoconductive effect in these OPTs from blue light than from red light. Figure 4.10 shows the transfer characteristics of an MDMO-PPV:PC₆₁BM blend OPT in the dark and under illumination from (c) 625 nm and (d) 470 nm light. The incident optical power density was varied between 0 and 3.3 mWcm⁻² for the red light and 0 and 1.6 mWcm⁻² for the blue light. Whilst there is a small shift in threshold voltages under both blue and red light, the off-current increases by a factor of 71 for the blue light whilst only 3 for the red light. Using equation 2.23, the peak responsivities for red and blue light were calculated to be 3.1 mA W⁻¹ and 82 mA W⁻¹ respectively. This difference seems reasonable given the optical absorption spectrum of Figure 4.10(a).

The dynamic response of this OPT to blue light is shown in Figures 4.10(e) and 4.10(f). Using equations 4.1 and 4.2 the time constants associated with this device were extracted to be: $\tau_{on} = 1.8$ ms and $\tau_{off} = 1.9$ ms. These values are comparable to the extracted values for the bilayer pentacene:PC₆₁BM bilayer OFETs with a similar dielectric (see Section 4.2.3). This observation adds weight to the hypothesis that the response-times of these OPTs are limited by

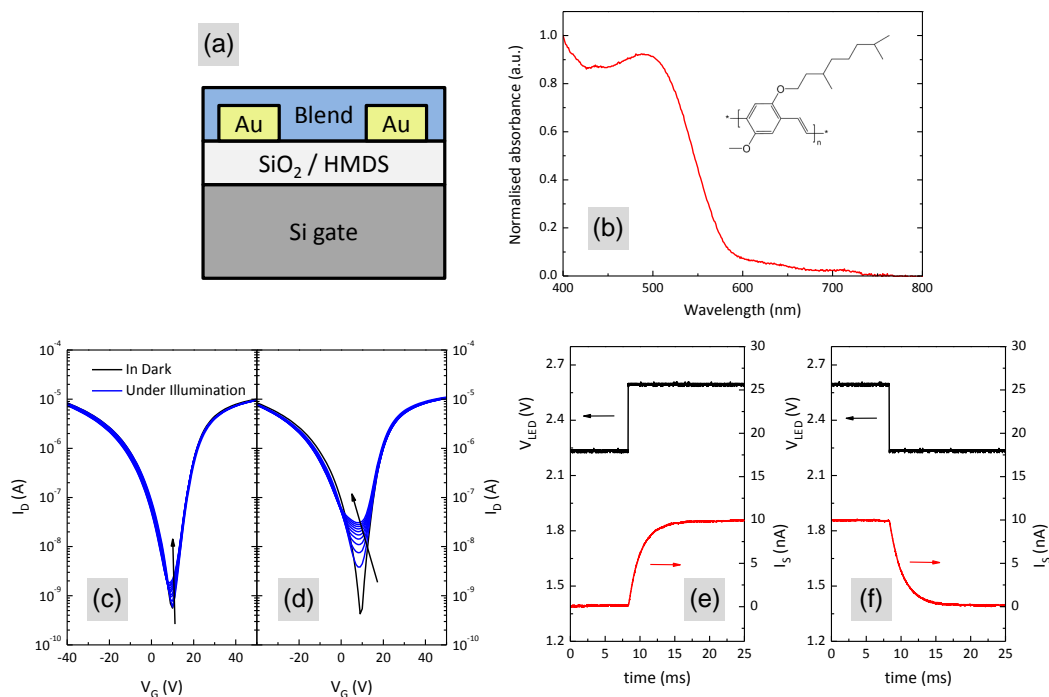


Figure 4.10: (a) Schematic diagram of bottom-gate, bottom-contact (BGBC) MDMO-PPV:PC₆₁BM organic phototransistor. (b) Optical absorption spectrum of 1:6 (wt %) MDMO-PPV:PC₆₁BM blend. Inset: molecular structure of MDMO-PPV. Transfer characteristics of MDMO-PPV:PC₆₁BM blend BGBC OPT in dark and under illumination from (c) red ($\lambda = 625$ nm) and (d) blue ($\lambda = 470$ nm) light. The OPT dimensions were $L = 10$ μm and $W = 10$ μm , and the applied drain voltage was $V_D = 15$ V in each case. The incident optical power density was varied between 0 and 3.3 mWcm^{-2} for the red light (sub-figure (c)) and 0 and 1.6 mWcm^{-2} for the blue light (sub-figure (d)). The arrows indicate an increase in optical power density. The (e) rise and (f) fall of the OPT source current as a function of time for a pulsed light source.

capacitative effects.

Two MDMO-PPV:PC₆₁BM blend OPTs were combined to form a complementary-like photo-inverter (see Figure 4.8(a) for schematic of this circuit). The dimensions of the two constituent OFETs were $L = 10$ μm and $W = 20$ μm in each case. Figures 4.11(a) and 4.11(b) show the characteristics of this inverter measured in the dark. The observed rise in the magnitude of the output voltage with increasing (absolute) input voltage is a characteristic of complementary-

like inverters.[109] This phenomenon is due to the fact that ambipolar OFETs will allow injection and transport of both charge carriers under certain biasing conditions,[144] and hence that the devices will rarely be in the strict off-state they would be in equivalent unipolar-OFET-based complementary inverters.[98]

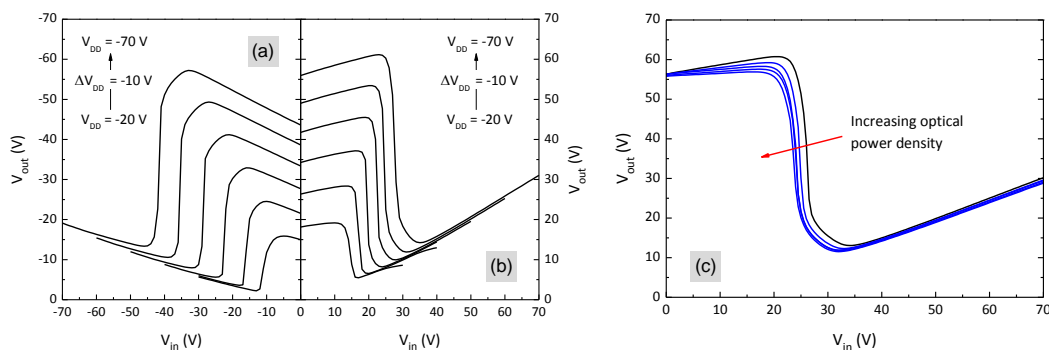


Figure 4.11: Characteristics of MDMO-PPV:PC₆₁BM blend inverter with (a) negative and (b) positive supply voltages (V_{DD}) measured in the dark. The device dimensions of the two constituent OFETs were $L = 10 \mu\text{m}$ and $W = 20 \text{mm}$ in each case. (c) Characteristics of same MDMO-PPV:PC₆₁BM blend inverter in dark and under illumination from 470 nm light, with a supply voltage of $V_{DD} = 70 \text{V}$. The incident optical power density was equal for both OFETs and was varied between 0 and 2.0mWcm^{-2} .

Upon illumination, the switching voltage of these inverters is also observed to change; see Figure 4.11(c). This effect is again attributed to changes in the threshold voltage of the two constituent OFETs. To gain a better understanding of the operation of these photo-inverters and to probe their suitability as potential optical sensors, the output voltage was then measured as a function of incident optical power density for constant supply and input voltages. This data is shown in Figure 4.12.

The characteristics shown in Figure 4.12 again illustrate how the output voltage of photo-inverters can be modulated over a significant range ($\sim 8 \text{V}$) by a relatively low intensity optical source. It is clear however that the relationship between V_{out} and incident optical power density is a complicated one. If one were to consider using photo-inverters or similar OPT-based circuits as optical sensors, then a better understanding of this relationship is needed. Developing an analytical model to describe the data in Figure 4.12 would clearly be a formidable task.

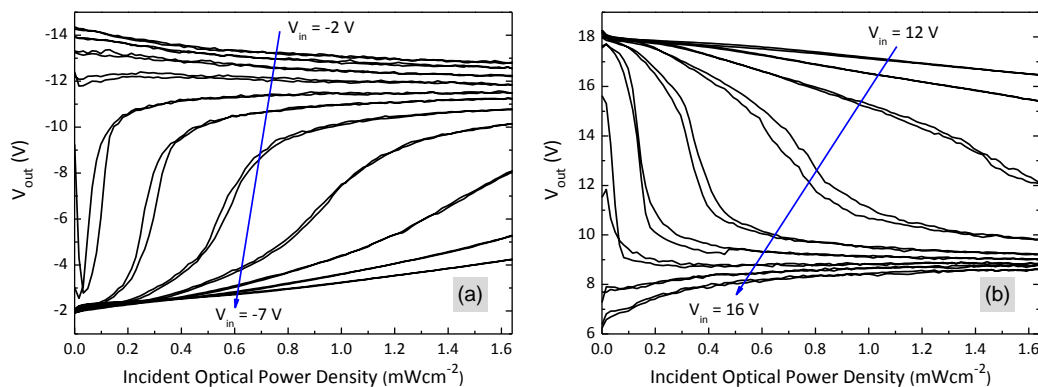


Figure 4.12: Output voltage of MDMO-PPV:PC₆₁BM blend photo-inverter measured as a function of incident optical power density with constant applied supply and input voltages. The supply voltages were (a) $V_{DD} = -20$ V and (b) $V_{DD} = 20$ V. The applied input voltages were varied between (a) $V_{in} = -2$ V and $V_{in} = -7$ V and (b) $V_{in} = 12$ V and $V_{in} = 16$ V, with a voltage step of $\Delta V_{in} = \mp 0.5$ V respectively. The incident light was monochromatic blue ($\lambda = 470$ nm).

Therefore in the next section I have used a numerical model to simply describe how the characteristics of complementary-like inverters would change if parameters such as OFET drain current or threshold voltage were to change. These parameters are in-turn known to be modified by optical illumination.

4.5 Simulation of Opto-Electronic Circuit Operation

Due to the sparse literature relating to organic phototransistors, a thorough understanding of their operating mechanisms does not exist.[113] To date there have been no comprehensive attempts to relate OPT characteristics (such as drain current or threshold voltage) to the intensity of incident light analytically. This is likely to be in-part due to the complex behaviour of these devices,[64, 113] and partly due to the minimal attention OPTs have received in the literature. Rather than modelling the response of photo-inverters to light, it is therefore felt that a more realistic undertaking is to relate the measured complementary-like inverter characteristics to changes in OFET parameters. It will then be possible to say

qualitatively what effect light will have on these parameters, and hence what can be expected to happen to the inverter characteristics under illumination.

4.5.1 Smits Model of Ambipolar Transport in OFETs

As a starting point it is necessary to describe the drain current of an ambipolar OFET in terms of the applied gate and drain voltages. The approach taken here is similar to that employed by Smits *et. al.*[144] In their work they build upon the theory developed by Vissenberg and Matters, where charge transport in unipolar OFETs is described by a variable range hopping mechanism.[70] The model developed by Smits *et. al.*, hereafter referred to as the *Smits model*, makes the simplification that the threshold voltages for both electrons and holes are equal: $V_{Te} = V_{Th} \equiv V_T$. Due to the differences in injection barriers and trap states of the two channels this is unlikely to be true. However for the purposes of this work it will be shown that this is both an adequate and necessary assumption. The Smits model has previously been shown to successfully reproduce experimental ambipolar OFET data from measured unipolar parameters.[48, 144]

If $V_{Te} = V_{Th}$, ambipolar OFETs are believed to operate in several distinct regimes, as defined by the voltages applied to the gate and drain terminals of the OFET.[144] This behaviour was described more fully in Section 2.4.1. For $V_G - V_T > V_D$ and $V_D > 0$ the device will operate in the unipolar linear regime for electrons. Similarly, for $V_G - V_T < V_D$ and $V_D < 0$ the OFET will be operating in the unipolar linear regime for holes. When $V_G - V_T < V_D$ and $V_D > 0$ electrons will flow from the source and holes will flow from the drain, with carriers undergoing bimolecular recombination at the position where the two channels meet. If $V_G - V_T > V_D$ and $V_D < 0$ holes will flow from the source and electrons will flow from the drain.

In the interest of conciseness, when $V_D > 0$ electrons will be referred to as the *majority* carrier and holes will be referred to as the *minority* carrier. And when $V_D < 0$ holes will then be referred to as the majority carrier and electrons will be referred to as the minority carrier.

4.5.1.1 Unipolar Operation

In each regime the device behaviour is different and hence the drain current is described by a different equation. In the unipolar regimes, only one type of charge carrier is present in the channel and the devices hence behave as the equivalent unipolar OFETs would. In the n-type regime, the OFET drain current can be shown to be given by equation 4.3. This equation was derived by integrating the conductivity of the semiconductor system over the transistor channel volume. Details of this derivation are given in the publication by Smits *et. al.*[144]

$$I_D = \gamma \frac{W}{L} \frac{T}{2T_0} \frac{T}{2T_0 - T} \left[\left(V_G - V_T \right)^{2T_0/T} - \left(V_G - V_T - V_D \right)^{2T_0/T} \right] \quad (4.3)$$

Here I_D is the magnitude of the drain current, T is the operating temperature, $k_b T_0$ is the width of the density of states of the charge transport state for this carrier,[70] γ is a constant prefactor for a certain temperature, given by equation 4.4, and all other symbols take their usual meaning.

$$\gamma = \frac{\sigma_0}{e} \left(\frac{(T_0/T)^4 \sin(\pi T/T_0)}{(2\alpha)^3 B_c} \right) \left(\frac{1}{2k_b T_0 \varepsilon_S \varepsilon_0} \right)^{(T/T_0)-1} C_i^{(2T_0/T)-1} \quad (4.4)$$

Here σ_0 is a prefactor for conductivity, e is the magnitude of the charge of an electron, α is the wavefunction overlap parameter for the semiconductor, B_c is the critical parameter for percolation,[79] and is known to be ~ 2.8 for an amorphous three-dimensional system,[77] ε_S is the relative permittivity of the semiconductor and ε_0 is the vacuum permittivity.

By following similar arguments, the drain current in the p-type unipolar regime can be expressed by equation 4.5.

$$I_D = \gamma \frac{W}{L} \frac{T}{2T_0} \frac{T}{2T_0 - T} \left[\left(V_T - V_G \right)^{2T_0/T} - \left(V_T - V_G + V_D \right)^{2T_0/T} \right] \quad (4.5)$$

Since the transport for holes takes place in the semiconductor HOMO and for electrons it takes place in the semiconductor LUMO, one can assume that

the parameters T_0 , σ_0 and α will be different for the different channels, even if a single-component[48, 95, 107] ambipolar semiconductor is used.

4.5.1.2 Ambipolar Operation

When both holes and electrons are present in the OFET simultaneously the channel can be modelled as adjacent p- and n-type OFETs operating in saturation, and a series-resistor model can be applied. Using this approach, it can be shown that the resulting expression for the drain current is independent of the position of the recombination position x_0 , and hence the size of the two channels. If $V_G - V_T < V_D$ and $V_D > 0$ the device will be operating in the ambipolar regime with electrons as the majority carrier. Under these circumstances, the drain current can be shown[144] to be given by equation 4.6. Note: The error in the equation in reference [144] has been corrected in equation 4.6.

$$I_D = \frac{W}{L} \left[\gamma_e \frac{T}{2T_{0e}} \frac{T}{2T_{0e} - T} (V_G - V_T)^{2T_{0e}/T} + \gamma_h \frac{T}{2T_{0h}} \frac{T}{2T_{0h} - T} (V_D - V_G + V_T)^{2T_{0h}/T} \right] \quad (4.6)$$

It can similarly be shown that when holes are the majority carrier the drain current can be described by equation 4.7:

$$I_D = \frac{W}{L} \left[\gamma_h \frac{T}{2T_{0h}} \frac{T}{2T_{0h} - T} (V_T - V_G)^{2T_{0h}/T} + \gamma_e \frac{T}{2T_{0e}} \frac{T}{2T_{0e} - T} (V_T - V_G + V_D)^{2T_{0e}/T} \right] \quad (4.7)$$

Under the assumption that the Smits model provides an adequate description of ambipolar OFETs, the four equations above can completely describe charge transport in the constituent OFETs of our complementary-like inverters.

4.5.2 Fitting the Smits Model to Experimental Data

To employ equations 4.3, 4.5, 4.6 and 4.7 for the calculation of inverter characteristics, it is necessary to know the following parameters: V_T , T_0 and γ for each channel. Experimental determination of the threshold voltage of unipolar OFETs is routine and widely reported.[84, 124] In Section 2.3.4 it was shown that the threshold voltage for a unipolar OFET could be found by extrapolating a plot of $I_D^{1/2}$ measured in the saturation regime to $I_D = 0$. Since ambipolar OFETs (as described by the Smits model) never saturate, to evaluate the values of V_T the linear regime data must be used. From equation 2.16, the drain current in an n-type unipolar OFET can be given by:

$$I_D = \frac{W}{L} \mu C_i \left[(V_G - V_T) V_D - \frac{1}{2} V_D^2 \right] \quad (4.8)$$

For the extreme values of the linear regime we can say: $V_D \ll V_G$ and hence:

$$I_D = \frac{W}{L} \mu C_i (V_G - V_T) V_D \quad (4.9)$$

So if $I_D = 0$ then $V_G = V_T$. Therefore by extrapolating a plot of I_D against V_G to $I_D = 0$ in the regions where $V_D \ll V_G$, the threshold voltages can be obtained. Figures 4.13(a) and (b) show such a threshold voltage extraction for an ambipolar MDMO-PPV:PC₆₁BM OFET.

The applied drain voltages were purposefully chosen to be very low so the approximation that $V_D \ll V_G$ remained valid. The dimensions of this OFET were $L = 10 \mu\text{m}$ and $W = 10 \text{mm}$. The threshold voltages for the p- and n-channels were approximated to be $V_{Th} = -17 \text{V}$ and $V_{Te} = 35 \text{V}$. Therefore for the purposes of the modelling employed here, an average of $V_T = 9 \text{V}$ will be used.

The remaining two parameters; γ and T_0 can be determined for this system by fitting equations 4.3 and 4.5 to the respective n- and p-type transfer characteristics of a relevant ambipolar OFET operating in the linear regimes. Figures 4.13(c) and 4.13(d) show equations 4.5 and 4.3 fitted to experimentally obtained data for an MDMO-PPV:PC₆₁BM OFET operating in the p- and n-type linear regimes respectively. Although the value of the threshold voltage used as a parameter in

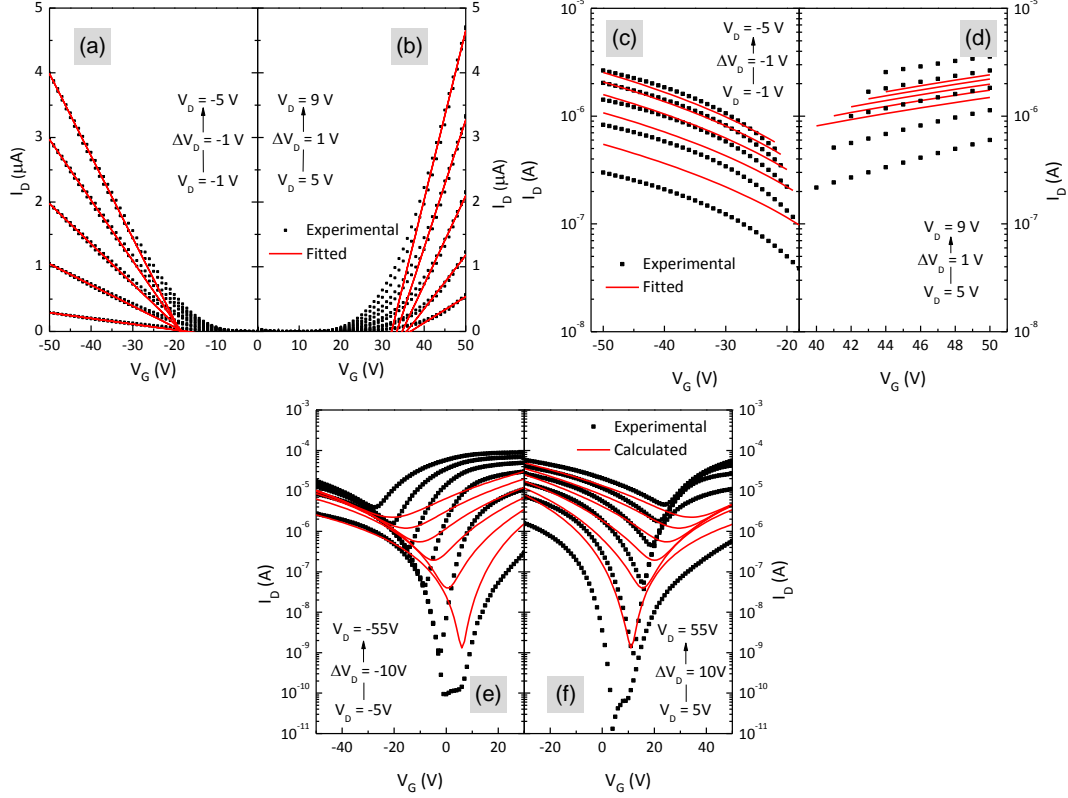


Figure 4.13: Transfer characteristics of MDMO-PPV:PC₆₁BM blend OFET operating in the linear ($V_D \ll V_G$) regime, plotted on a linear scale with (a) negative and (b) positive applied drain voltages. The red lines are straight-line fits used to extract approximate values of the threshold voltage for the hole and electron channels. (c) Equation 4.5 fitted to the p-type linear-regime transfer characteristics of MDMO-PPV:PC₆₁BM blend OFET. (d) Equation 4.3 fitted to the n-type linear-regime transfer characteristics of MDMO-PPV:PC₆₁BM blend OFET. (e) and (f) The calculated and experimental transfer characteristics of same MDMO-PPV:PC₆₁BM blend OFET operating in the p- and n-type ambipolar regimes respectively. The theoretical characteristics were calculated using equations 4.7 and 4.6, and the parameters from Table 4.1. The device dimensions were $L = 10 \mu\text{m}$ and $W = 10 \text{ mm}$ in all cases.

the fit was $V_T = 9 \text{ V}$ in both figure 4.13(c) and figure 4.13(d), the region of data considered is just that where $V_G - V_{Th} \leq V_D$ for holes and $V_G - V_{Th} \geq V_D$ for electrons. Table 4.1 shows the values of the parameters extracted from these fits.

Given the data in Figures 4.13(c) and 4.13(d), it is apparent that the model

	Holes	Electrons
$\gamma (\times 10^{-13})$	1.7	3.7
$T_0(K)$	443	465

Table 4.1: Parameters used in the Smits model of ambipolar charge transport as extracted from the data in figures 4.13(c) and 4.13, using equations 4.5 and 4.3.

does not capture the dependence of the drain current on the drain voltage correctly. This suggests there is a problem with the model employed. Whilst previous[48, 144] applications of this model have produced good agreement between theory and experiment, here this is not the case. There are several possible explanations for the discrepancy observed, all of which can be related to assumptions made within the model. One assumption that is particularly likely to give rise to difficulties is the neglect of contact resistance.[144] For nickel dithiolene[144] and squaraine semiconductors,[48] the injection barrier from gold into the LUMO is small in comparison to the barrier from gold into the LUMO of PC₆₁BM.[110, 214] For the MDMO-PPV:PC₆₁BCM OFETs studied here, the effect of the contact resistance could indeed be significant.

Whilst the Smits model is clearly not appropriate for our particular semiconductor system, we will none-the-less use the parameters from Table 4.1 and proceed to calculate photo-inverter characteristics as if these parameters were representative of a real system. It turns out that the form of the characteristics obtained will be rather general and insensitive to the semiconductor system parameters.

In Figures 4.13(e) and 4.13(f) the transfer characteristics under ambipolar operation have been calculated and plotted alongside the equivalent experimental data. Since the OFET operates in 4 distinct regimes depending upon the applied voltages, the drain currents were calculated using a different equation for the different sections of the figures. For Figure 4.13(e) equation 4.5 is used where $V_G - V_T < V_D$ and equation 4.7 is used where $V_G - V_T \geq V_D$. Similarly, for Figure 4.13(f) equation 4.3 is used where $V_G - V_T > V_D$ and equation 4.6 is used where $V_G - V_T \leq V_D$.

The calculated characteristics, despite not agreeing with the corresponding experimental data, exhibit the form expected for an ambipolar OFET. The fact

that the calculated off-currents are not as low as the experimental values is likely to be due to the simplification that the threshold voltage is the same for both holes and electrons. Encouragingly, there is a good agreement in calculated drain current in the region where the OFET makes the transition from unipolar operation to ambipolar operation (i.e. when $V_G - V_T \simeq V_D$).

4.5.3 Modelling Complementary-Like Inverters

With a set of equations describing the current-voltage relationship of ambipolar OFETs and an approximate set of relevant parameters for the p- and n-channels of MDMO-PPV:PC₆₁BM blend OPTs, the inverter characteristics of a relevant complementary-like inverter can now be calculated. Complementary-like inverter characteristics have previously been calculated for MDMO-PPV:PC₆₁BM blend OPTs,[109] but no specific details of the model were given. Instead I have here adapted a model developed for ambipolar amorphous silicon-based inverters.[253] Using this approach, the inverter is modelled as two resistors in series (see Figure 4.14(a)).

The output voltage of the inverter can then be described as a voltage divider using the following equation:

$$V_{out} = \frac{R_2}{R_1 + R_2} V_{DD} \quad (4.10)$$

Where R_1 and R_2 are the channel resistances of OFETs 1 and 2 respectively. If we consider the output terminal of the inverter to comprise the two drain terminals of the constituent OFETs, we can then view each individual OFET to be biased as in Figures 4.14(b) and (c). The channel resistance of the two OFETs can then be described as:

$$R_1 = \frac{V_{out} - V_{DD}}{I_1} \quad (4.11)$$

$$R_2 = \frac{V_{out}}{I_2} \quad (4.12)$$

Where I_1 and I_2 are the currents flowing between the source and drain terminals of OFET 1 and OFET 2 respectively. To determine the values of I_1 and

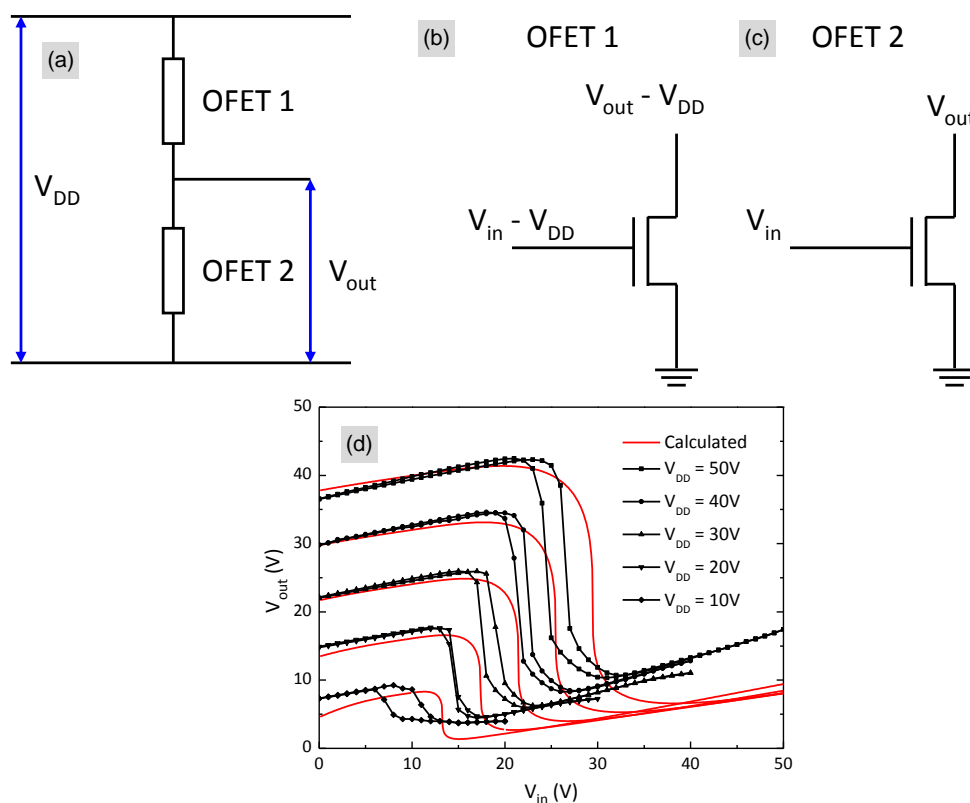


Figure 4.14: (a) Circuit diagram of voltage divider formed from two ambipolar OFET channels. (b) and (c) Effective biases applied to the two constituent ambipolar OFETs of a complementary-like inverter, if we consider the drain terminals of both OFETs to be connected to form the output terminal of the inverter. (d) Experimental characteristics of complementary-like inverter formed of two MDMO-PPV:PC₆₁BM blend (1:6 wt %) ambipolar OFETs with identical channel dimensions ($L = 10 \mu\text{m}$, $W = 10 \text{nm}$), measured in the dark. The red lines show the characteristics calculated for an inverter of identical dimensions, using equation 4.13 and the parameters from Table 4.1.

I_2 , equations 4.5, 4.3, 4.7 and 4.6 can be used, with the drain and gate voltages replaced by the appropriate voltages as given in figure 4.14. If we define the drain current flowing in an ambipolar OFET to be $I_D(V_D, V_G)$, then equations 4.10, 4.11 and 4.11 can be combined to give an expression for the output voltage

of the inverter:

$$V_{out} = \frac{I_D(V_{out} - V_{DD}, V_{in} - V_{DD}) V_{out}}{(2V_{out} - V_{DD}) I_D(V_{out}, V_{in})} \quad (4.13)$$

Since the right hand side of equation 4.13 contains V_{out} terms, it is non-linear and hence cannot be solved analytically. It can however be solved numerically by inputting a starting “guess” value of $V_{out} = V_{DD}/2$ and then iteratively evaluating 4.13, passing the calculated V_{out} back in as an input. This is repeated until the solution converges. The equation used to evaluate $I_D(V_D, V_G)$ depends upon the values of V_D and V_G and hence the algorithm contains a decision statement.

Figure 4.14(d) shows the characteristics of a complementary-like inverter formed from two MDMO-PPV:PC₆₁BM (1:4 wt%) blend ambipolar OFETs measured in the dark. The dimensions of both OFETs were equal and were $L = 10 \mu\text{m}$ and $W = 10 \text{mm}$. Equation 4.13 has been evaluated and plotted in the same figures, given the applied values of V_{DD} and V_{in} , and the parameter values given in Table 4.1. Although the calculated characteristics again do not match the experimental characteristics, the form of the solution is very-much as expected for complementary-like inverters.[109, 145] So despite there clearly being some significant over-simplifications made in the Smits model, it can none-the-less reproduce the behaviour of complementary-like circuits with reasonable accuracy.

4.5.3.1 Modelling Photo-Inverters

With a reasonably accurate model in place to describe the operation of complementary-like inverters, we can now simulate the effect of optical illumination and modify some of the relevant parameters in the model. As described in Section 2.5.1, under optical illumination, two main effects are believed to manifest themselves; a direct increase in source-drain current and a change in threshold voltage caused by a modification of the trap density in the film.

As is shown in Figure 4.7(b) for example, the responsivity of OPTs depends upon the biases applied. This makes the modelling the so-called photoconductive effect rather complicated. If one were to increase the current flowing in each OPT by an equal proportion of their respective dark currents, there would be no change

in the inverter characteristics. If however the current flowing in only one OPT were to increase, there would be a noticeable change in inverter characteristics. Figure 4.15(a) shows the characteristics of a complementary-like inverter calculated using equation 4.13 and the parameters from Table 4.1. The current flowing through OFET1 was increased by a certain percentage with respect to the value calculated using equations 4.5, 4.3, 4.7 and 4.6. Although it is unlikely that upon illumination one OPT will exhibit an increase in drain current and the other will not, it is certainly possible that percentage increase for the different OPTs in the inverter will be different depending on their biasing conditions. Hence, the data in Figure 4.15(a) can be used to illustrate what would be expected to happen to the characteristics of a photo-inverter if both OPTs were operating via the photoconductive mechanism alone.

Figure 4.15(b) shows the characteristics of an inverter calculated for several different values of V_T . This is intended to illustrate the effect of the photovoltaic mechanism on the inverter characteristics. It is immediately evident that this data is very similar to that obtained experimentally for MDMO-PPV:PC₆₁BM blend and pentacene:PC₆₁BM bilayer photo-inverters (see Figures 4.11(c) and 4.9(a) respectively). This suggests that the photo-inverter operation appears to mainly driven by the photovoltaic effect. Figure 4.15(c) shows the output voltage of a complementary-like inverter calculated as a function of the OPT threshold voltages. On comparison with Figure 4.12 for example, it is again clear that the main operating mechanism of photo-inverters is likely to be due to the photovoltaic, not the photoconductive effect.

4.6 Conclusions

In summary, organic phototransistors (OPTs) show significant promise as an alternative to organic photodiodes (OPDs) for potential low-cost, large-area optical sensors. Whilst the mechanism by which OPTs operate is at times unclear, their impressive characteristics suggest they are a technology worth pursuing.

In this chapter I have developed OPTs based on a pentacene:fullerene bilayer structure, and shown that such architectures are compatible with self-assembled monolayer (SAM) gate dielectrics and can hence operate at low voltages. As has

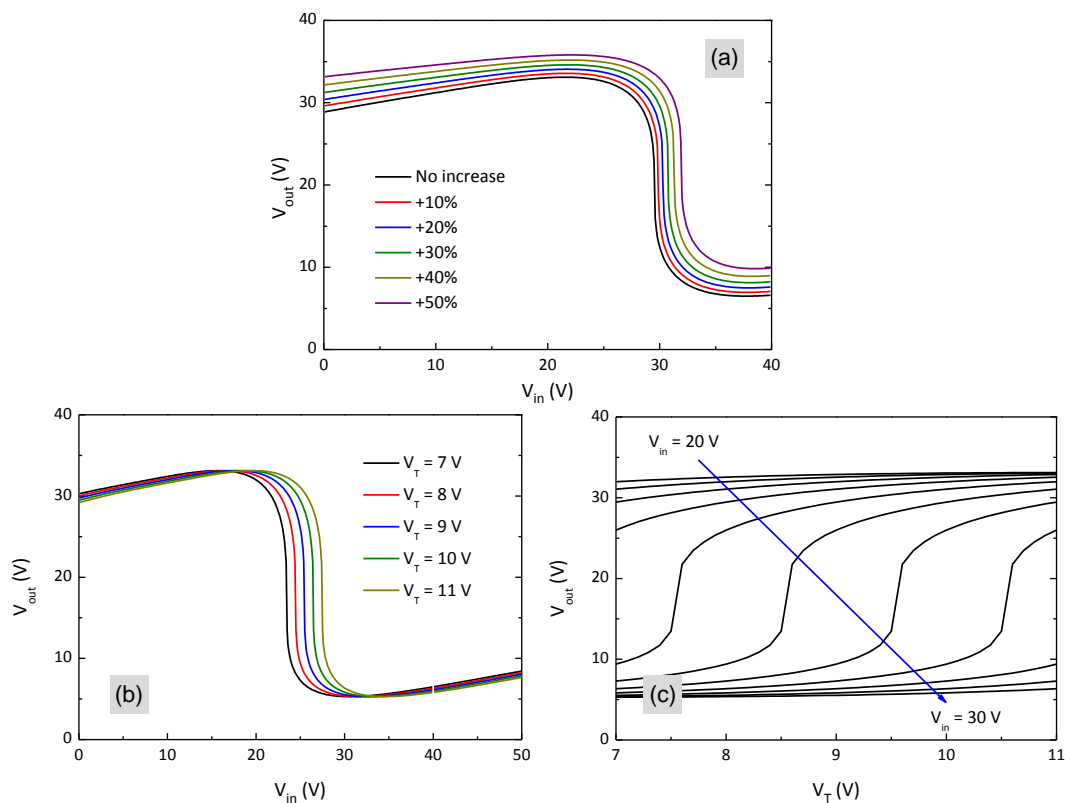


Figure 4.15: (a) Complementary-like inverter characteristics calculated using equation 4.13 and the parameters from Table 4.1, with the drain current in OFET1 increased by a certain percentage. (b) Inverter characteristics calculated using same parameters, but with the the value of V_T changed by small amount for both OPTs. (c) Output voltage of inverter calculated as a function of V_T for various constant input voltages. The dimensions of both OFETs were $L = 10 \mu\text{m}$ and $W = 10 \text{mm}$, and the supply voltage was $V_{DD} = 40 \text{V}$ in each case.

been shown previously[50, 177], the responsivity of such OPTs is dependent upon the applied voltages. By measuring the dynamic response of the OPTs to pulsed incident light, it seems likely that the response time of OPTs are (at least in-part) limited by capacitive filtering effects, caused by the gate dielectric.

By combining two similar OPTs, photo-sensitive complementary-like inverters were also demonstrated. By biasing these devices at constant voltages, the output voltage could be modulated over a significant range by a small variation in incident optical power density. Using an established model for ambipolar

transport in organic field-effect transistors,[144] the characteristics of example complementary-like inverters were calculated. By modifying certain parameters (such as the threshold voltage) within these calculations the mechanism by which photo-inverters operate could be probed. The results presented within this chapter suggest that the primary operating mechanism for these inverters is the photovoltaic effect.

Chapter 5

Polymer:Fullerene Blend Morphology

5.1 Introduction

In the previous chapter I presented some work on the development of ambipolar organic field-effect transistors (OFETs) for potential device applications. Whilst the majority of OFET-based research is targeted towards improvements in device performance,[92–94, 99] OFETs have also proven to be excellent test-beds for studying the characteristics of semiconducting material systems and evaluating semiconductor performance.

OFETs can be used to probe many relevant phenomena observed in organic semiconductors, such as charge-transport mechanisms,[68, 70, 198, 263, 264] charge-trapping behaviour,[113, 265] photo-physical processes,[53, 157] and morphological properties.[52, 104, 158] In this chapter I have studied how changes in the morphological properties of polymer:fullerene blends are manifest as changes in field-effect mobility, and how OFETs can hence be used as probes of microstructure. Despite their use in ambipolar OFETs[109] and organic phototransistors,[51] the overwhelming majority of reports on polymer:fullerene blends are with regards to the development of organic photovoltaic cells (OPVs).[60, 62, 173] The internal microstructure and morphological behaviour of the polymer:fullerene blend system is of vital importance to the carrier-transport and exciton-dissociation effi-

ciency of OPVs, and is currently the subject of intense studies.[239–242] Despite the enormous interest in polymer:fullerene blends, the number of comprehensive studies carried out on this system using OFETs has so-far been surprisingly small.[52, 158, 159, 266]

5.2 Detecting Phase Segregation Using OFETs

5.2.1 Optical Microscope Images

Post-production annealing is known to lead to improved power conversion efficiencies in polymer:fullerene bulkheterojunction (BHJ) solar cells.[39, 103, 206, 234–236, 267, 268] This is attributed to a red-shift in the absorption spectrum of certain polymer:fullerene blends[234] and improved charge-carrier transport properties.[206, 236, 269, 270] These improvements are believed to arise from a thermally-induced phase-separation of the polymer and fullerene components.[103, 206, 234, 247, 250, 269–271] Upon annealing the polymer is believed to recrystallise, while the fullerene molecules are reported to form clusters.[234, 247, 250, 270] This phase-segregation is believed to improve the charge transport of holes in the polymer and electrons in fullerenes,[236] aiding charge dissociation.

In the system of blended poly(3-hexylthiophene) (P3HT) and [6,6]-phenyl C₆₁-butyric acid methyl ester (PC₆₁BM) for example, this phase segregation has been observed by Campoy-Quiles *et. al.* using optical microscopy.[103] In their report, crystallites with dimensions on the order of microns were clearly visible and were attributed to be PC₆₁BM-rich entities. Other techniques such as transmission electron microscopy (TEM) have resolved fullerene crystallites on much smaller scales,[271] indicating that the phase segregation process can induce a wide range of micro-morphologies. Independent of their size however, at higher temperatures the melting of these PC₆₁BM crystallites has been observed using optical microscopy, which was attributed to a eutectic phase behaviour.[268]

Here I have used polarized optical microscopy to reproduce this behaviour. A Blend of P3HT:PC₆₁BM (1:1 wt% ratio) was spin-cast onto HMDS-treated silicon dioxide and annealed at temperatures between 60 °C and 300 °C in 20 °C steps. Each annealing step lasted for 30 minutes, after which the thin film

was quenched to room temperature (by being removed directly from the hotplate into N_2). The annealing was cumulative, so the sample imaged after annealing at 80 °C for example would also have been annealed at 60 °C, and so on. This substrate was chosen because it allows a direct comparison with the equivalent OFET measurements carried out in Section 5.2.2.

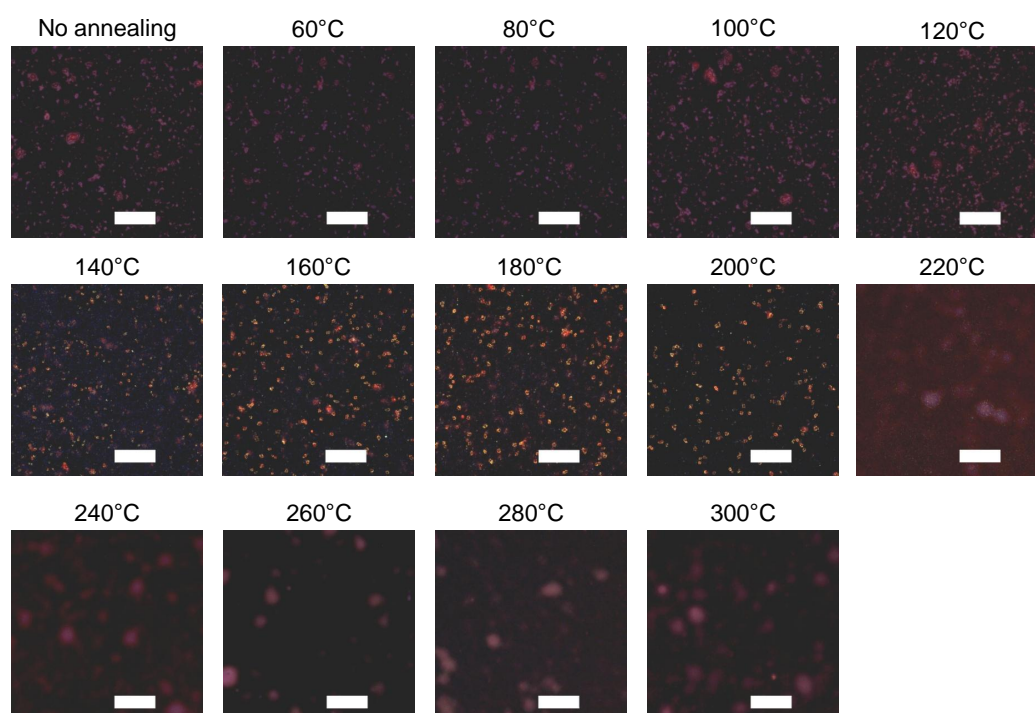


Figure 5.1: Polarised optical microscope images of P3HT:PC₆₁BM (1:1 wt% ratio) films taken after annealing at various temperatures between 60 °C and 300 °C, for 30 minutes in each case. The films were deposited onto HMDS-treated silicon dioxide. The scale bar is 50 μ m and the exposure time was 200 ms in each case.

Polarised optical micrographs of the resulting microstructure of such heat-treated films were then taken and are shown in Figure 5.1. A 20-times magnification was used, the polarisers were crossed for all images and the exposure time was 200 ms. The scale bar is 50 μ m in each case. From these images, it can clearly be seen that films quenched from annealing temperatures of 140 °C and below resulted in predominantly amorphous structures. In agreement with earlier reports,[206, 234, 250] heat treatments at $140\text{ }^\circ\text{C} \leq T \leq 220\text{ }^\circ\text{C}$,

in contrast, resulted in thin-film architectures comprising crystallites that were readily visible by optical microscopy. These are believed to be PC₆₁BM-rich regions. The temperature of this behaviour is in agreement with previous reports on P3HT:PC₆₁BM phase segregation.[206, 234, 250] In structures that were heat treated at higher temperatures however these crystallites were no longer visible, in agreement with a eutectic phase behaviour, in which above 205 °C (the melting temperature of P3HT:PC₆₁BM binaries[250]) the polymeric component melts while the PC₆₁BM-rich crystallites gradually dissolve.[268] Rapid cooling from these partial melts will result in amorphous structures, as also observed elsewhere.[250]

5.2.2 Mobility Evolution in P3HT:PC₆₁BM Blend OFETs

The three-terminal structure of OFETs allows the selective injection and transport of carriers into the different components of the polymer:fullerene blend.[109] This unique property allows the long-range microstructure of each component to be probed independently, in the absence of carrier recombination. Previous OFET-studies of this system have investigated the effect of different solvents,[52] polymer molecular weights,[52] blend compositions,[158, 266] and transistor gate dielectrics.[159] Little however has been said about the morphological changes that take place as a result of post-processing annealing steps.[206, 235]

Bottom-gate, bottom-contact (BGBC) OFETs were fabricated from neat P3HT, neat PC₆₁BM and a 1:1 (wt%) blend of these two components. A 1:1 blend ratio was chosen because ratios close to this value are known to yield OPV devices with the highest efficiencies.[268] These devices were fabricated on highly doped (n⁺⁺) silicon wafers which acted as a global gate electrode, with a 200 nm thermally grown silicon dioxide layer as the gate dielectric. The silicon dioxide surfaces were then passivated with hexamethyldisilazane (HMDS). Gold source and drain electrodes were defined using standard photolithographic techniques. Solutions of P3HT, PC₆₁BM, and blends of these molecules were then deposited onto the substrates. P3HT and P3HT:PC₆₁BM blends were deposited via spin coating and the neat PC₆₁BM was deposited via drop-casting at room temperature (due to problems wetting the surface). The concentration of the solutions used was 10

mgml^{-1} and the solvent was chlorobenzene in all cases.

Transfer characteristics of an as-cast P3HT:PC₆₁BM OFET are shown in Figures 5.2(b) and 5.2(c). The device clearly exhibits ambipolar operation with well-balanced hole and electron channels. The work function of gold (4.8 eV) is well aligned with the Highest Occupied Molecular Orbital (HOMO) of P3HT (see Figure 5.2(a)). There is an offset between the work function of gold and the Lowest Unoccupied Molecular Orbital (LUMO) of PC₆₁BM. However, as described in Section 2.3.2, electron injection and transport is known to take place from gold into PC₆₁BM because of a reduction in the potential barrier, due to the formation of interface dipoles.[110] Therefore holes and electrons can easily be injected and transported in the P3HT and PC₆₁BM networks respectively, but not visa-versa. As a consequence, P3HT:PC₆₁BM OFETs are ambipolar and through appropriate biasing conditions[144] selective injection and transport of holes and/or electrons can take place into the appropriate materials.[109] Hence, by measuring the mobility at different biasing conditions the long-range crystallinity and percolation pathways of each material network can then be probed independently. The mobility of charge carriers depends exponentially on the hopping distance between adjacent molecules in the film.[70] Therefore changes in the packing/structure of the film should be reflected in the measured field-effect mobility. It has been shown[181] that charge transport in OFETs occurs within the first few nanometres from the semiconductor-dielectric interface, suggesting that any changes in observed mobility will be representative of changes at this interface.

It should be noted that previous studies have shown that when using gold source and drain electrodes, hole injection and transport can take place in PC₆₁BM.[110] However, in this case the mobility is significantly lower than that of holes in P3HT[138] and hence one can assume that hole field-effect mobility measurements made in a 1:1 (wt%) P3HT:PC₆₁BM blend should be representative of the P3HT network only, with a negligible modification due to the PC₆₁BM network.

In order to correlate with the changes in the film microstructure inferred from the data in Figure 5.1, these OFETs were annealed at temperatures between 60 °C and 300 °C in 20 °C steps, with each annealing step lasting 30 minutes. As with the measurements made in Figure 5.1, the annealing was cumulative. The saturation-regime field-effect mobility of holes and electrons in four OFETs

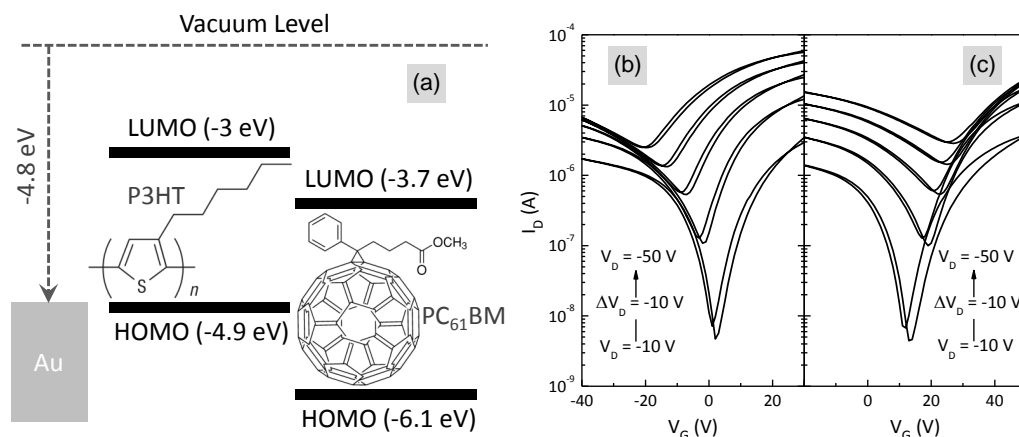


Figure 5.2: (a) Molecular structures and energy levels of P3HT and PC₆₁BM, relative to the vacuum level and the work function of gold (injecting electrodes in OFETs used in this study). (b) P-type and (c) n-type transfer characteristics of 1:1 (wt%) P3HT:PC₆₁BM blend ambipolar bottom-gate, bottom-contact (BGBC) organic transistor ($L = 10 \mu\text{m}$, $W = 20 \text{mm}$).

were measured at room temperature after each annealing step. The average field-effect mobilities of holes in neat P3HT and electrons in neat PC₆₁BM are plotted against annealing temperature in Figure 5.3(a). Figures 5.3(b) and 5.3(c) display differential scanning calorimetry (DSC) heating thermograms of neat P3HT and neat PC₆₁BM respectively.

DSC measurements were carried out on P3HT, PC₆₁BM and P3HT:PC₆₁BM blends. Powders were produced by preparing homogeneous solutions of ~ 1 wt% total material content in chlorobenzene, followed by casting onto glass slides. The solvent was evaporated at ambient pressure in air. 1 to 5 mg material from such films was used for the DSC experiments, which was conducted under nitrogen at scan rate of $10 \text{ }^\circ\text{Cmin}^{-1}$ with a Metler Toledo DSC822 instrument. The DSC was carried out by collaborators for The Department of Materials at Imperial College London; Ester Buchaca Domingo and Natalie Stingelin-Stutzmann.

In neat P3HT an approximately constant hole mobility is observed until $240 \text{ }^\circ\text{C}$, where it decreases by a factor of 3. This can be attributed to the melting of this polymer, as deduced from the endotherm observed around $240 \text{ }^\circ\text{C}$ in the DSC thermogram (see Figure 5.3(b)). Subsequent rapid-cooling will hinder

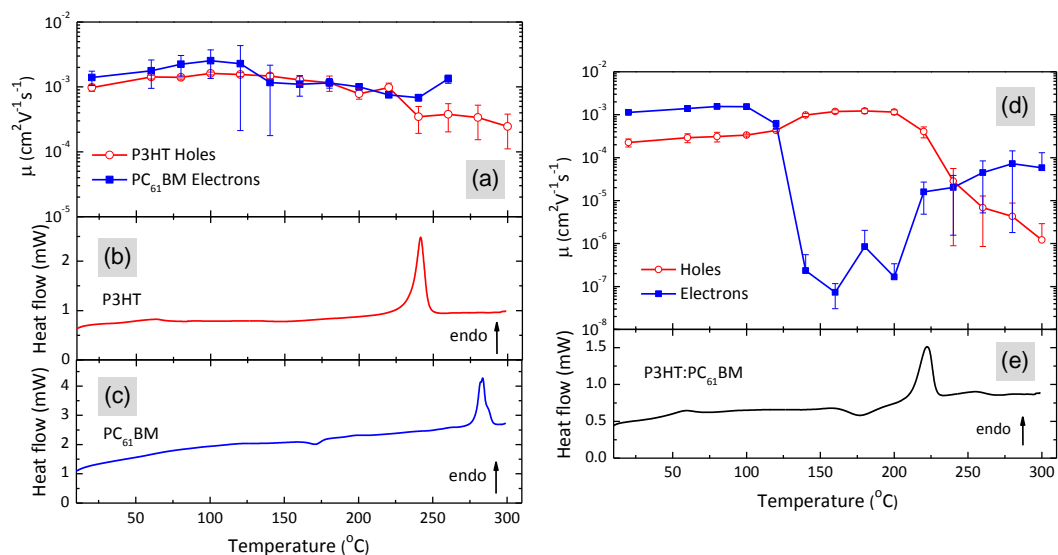


Figure 5.3: (a) Average saturation-regime field-effect mobility of holes and electrons in four P3HT and four PC₆₁BM bottom-gate, bottom-contact (BGBC) OFETs measured as a function of annealing temperature. The annealing was cumulative and each annealing step lasted 30 minutes. The error bars represent the standard deviation in the mobility measurements. Differential scanning calorimetry (DSC) heating thermograms of (b) neat P3HT and (c) neat PC₆₁BM. (d) Average saturation-regime field-effect mobility of holes and electrons in four 1:1 (wt %) P3HT:PC₆₁BM blend BGBC OFETs measured as a function of annealing temperature. (e) DSC heating thermogram of P3HT:PC₆₁BM blend films.

crystallisation of this material due to its macromolecular nature, resulting in a less crystalline architecture of lower charge carrier mobility. The electron mobility in neat PC₆₁BM is relatively constant, independent of the heat treatment the thin-film structures were subjected to, apart from a small decrease observed after annealing to 140 °C. This feature is most likely due to the recrystallisation of the PC₆₁BM film, as deduced from thermal analysis, where an exotherm is observed in this temperature regime (onset \sim 120 °C). When heating PC₆₁BM OFETs above the PC₆₁BM melting temperature of 280 °C (see Figure 5.3(c)) followed by quenching to room temperature, their on/off ratios drop to approximately 3 (data not shown), hence mobilities for these devices are not plotted.

The average field-effect mobilities of holes and electrons in the 1:1 (wt %)

P3HT:PC₆₁BM blend BGBC OFETs are shown in Figure 5.3(d). Figure 5.3(e) shows the DSC heating thermogram of P3HT:PC₆₁BM. Figure 5.3(d) shows that the hole and electron mobilities of the P3HT:PC₆₁BM blend OFETs remain approximately constant until 140 °C, at which point the hole mobility rises and the electron mobility falls drastically. This behaviour is attributed to P3HT-crystallisation and PC₆₁BM clustering, as can be deduced from the relatively pronounced exotherm between 150 °C and 190 °C observed in DSC analysis of such blends (Figure 5.3(e)), as well as polarized optical microscopy (Figure 5.1). Note, the onset of recrystallisation will be rate dependent, with recrystallisation occurring over prolonged times already at significantly lower temperatures than what is observed in DSC.

The resulting increase in crystallinity in the P3HT is expected to improve inter-chain transport and hence hole mobility.[236] The drop in electron mobility is attributed to the clustering of PC₆₁BM and associated reduction of PC₆₁BM concentration in the regions between clusters.[272] Whilst clearly detrimental to the performance of ambipolar OFETs, this drop in lateral electron mobility is representative of a morphological change which is in general associated with improved charge transport,[236] and enhanced efficiencies[206, 235] in OPV structures. Hence by probing the lateral carrier transport (as opposed to perpendicular transport in OPVs) over long distances an alternative technique for detecting and studying phase-segregation in polymer:fullerene blends has been illustrated. The apparent conflict with previously reported improvements in electron mobility in P3HT:PC₆₁BM blend devices upon annealing[236] can be explained by the significant differences in device structure/architecture, and the distances over which charges are transported in these two systems. The short carrier-transport distances (thickness \sim 100-200 nm) and large active layer area (device dimensions typically \sim mm²) of OPVs suggest that PC₆₁BM clusters will provide enhanced electron-pathways between the anode and cathode.[236] The detrimental effect of PC₆₁BM clustering on electron conductivity in OFET channels is considered in more detail in Section 5.3.

For devices annealed at 220°C the hole mobility drops and the electron mobility partially recovers. This is in agreement with a melting of the polymeric component at temperatures above 205°C (the eutectic temperature) and a result-

ing re-distribution of fullerene molecules.

5.2.3 Dual-Gate Mobility Measurements

It has previously been shown that microstructural changes in polymer:fullerene blends do not occur homogeneously throughout the film, but that a certain degree of vertical-dependence exists.[103] In their study Campoy-Quiles *et. al.* showed how changes in the relative depth-concentration profile of the two materials upon annealing depend upon the substrate properties. Similarly, a previous study of P3HT:PC₆₁BM using OFETs has illustrated how the relative strength of hole/electron transport depends critically on the interface used.[159] Both reports suggest that morphological changes that are detected within the first few nanometres of the film (where charge transport takes place in OFETs)[181] may not be representative of the bulk properties.

In an attempt to gain a better understanding of the vertical morphology evolution in P3HT:PC₆₁BM blends, bottom-contact, dual-gate OFETs were fabricated. In these OFET structures, the mobility of charge carriers can be measured at the top and bottom of films simultaneously. Although dual gate OFETs have previously been used to study the vertical phase-segregation of small molecules and polymers in high-performance, solution-processed OFETs,[93, 104] the technique has never been employed for the study of OPV-relevant materials.

Dual-gate, bottom-contact OFETs were fabricated on highly doped silicon and silicon dioxide. The silicon dioxide layer was in this case passivated with a thin (~ 50 nm) layer of divinyltetramethyldisiloxane-bis(benzocyclobutene) (BCB).[101] BCB was chosen as a passivation layer for these devices instead of HMDS to demonstrate how phase-segregation can be detected at other semiconductor-dielectric interfaces, provided the surface is passivated. A bare SiO₂ surface cannot be used in this study, since it is known to impede transport in certain n-type semiconductors.[102, 190] Gold source and drain electrodes were then deposited by thermal evaporation under high vacuum. P3HT:PC₆₁BM blends were spin-cast onto the BCB surfaces from a 10 mgml⁻¹ solution in chlorobenzene. As before, a 1:1 (wt%) blend ratio was used. A fluorocarbon polymer (CYTOP™) was then spin-cast as the top gate dielectric before aluminum gate electrodes

were deposited by thermal evaporation. The device structure is shown in Figure 5.4(a).

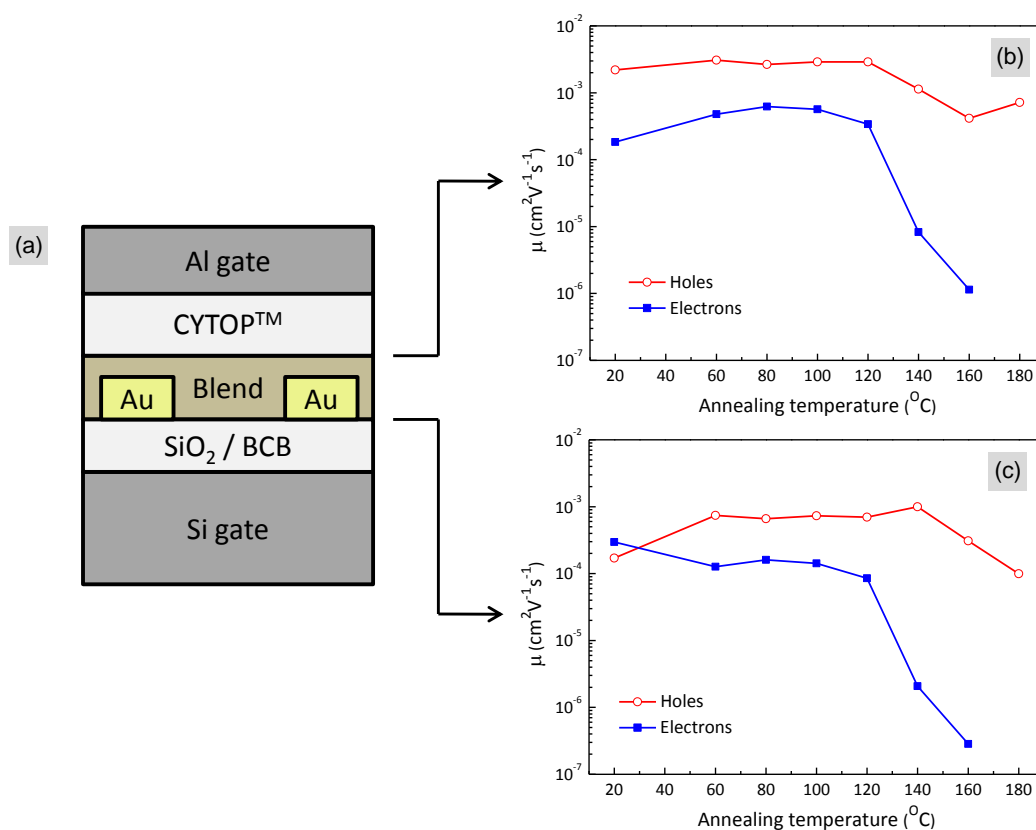


Figure 5.4: (a) Schematic diagram of dual-gate, bottom-contact P3HT:PC₆₁BM 1:1 (wt%) blend OFET employed in this study. (b) and (c) Saturation-regime field-effect mobility of holes and electrons measured at the top and bottom interfaces respectively of dual-gate P3HT:PC₆₁BM OFET after being annealed at various temperatures. Each annealing step lasted for 30 minutes. The device dimensions were $L = 30 \mu\text{m}$ and $W = 500 \mu\text{m}$.

These OFETs were annealed at temperatures between 60°C and 180°C in 20°C steps, with each annealing step lasting for 30 minutes. The saturation field effect mobility of holes and electrons at both the bottom and top interfaces of a dual gate OFET (dimensions: $L = 30 \mu\text{m}$ and $W = 500 \mu\text{m}$) were measured at room temperature, after each annealing step. The field-effect mobilities of holes and electrons in the blend are plotted against annealing temperature for the

top interface in Figure 5.4(b) and the bottom interface in Figure 5.4(c). After annealing to 160°C and above, the CYTOP™ dielectric began to break down, increasing gate leakage current. When the leakage current becomes comparable (approximately within one order of magnitude) to the drain current, the device can no longer behave as a transistor and mobility calculation becomes impossible. This limited the temperature range of the analysis.

A drop in electron mobility is clearly observed after annealing to 140°C at both interfaces. This is again attributed to the formation of PC₆₁BM clusters as outlined previously. This observation suggests that regardless of the position in the film, or the interface properties at the film boundaries, a certain degree of phase-segregation does take place upon annealing. The small increase (reduction) in electron mobility at the top (bottom) interface upon annealing to 60°C is possibly due to a change in the vertical concentration profile of PC₆₁BM in the film.[103] Similarly, the drop in hole mobility above 140°C, could be due to migration of P3HT from both interfaces into the bulk of the film. This is in contrast to what is observed at an HMDS interface. Despite the properties of both semiconductor-dielectric interfaces being different to each other and to the interface employed in the previous section, the important feature of Figure 5.4 is that phase-segregation can still be detected at any position in the film.

5.2.4 Time-Dependence of Mobility Evolution

The performance of P3HT:PC₆₁BM blend OPVs has previously been measured as a function of annealing time.[206] It was found that the device efficiency increased for about 30 minutes whilst being annealed at 150°C, after which the efficiency levelled off. Recently, the time-dependence of the recrystallisation process of P3HT and PC₆₁BM has been studied independently using variable-angle spectroscopic ellipsometry (VASE) and OPV device characterisation.[103] It was suggested that, whilst being annealed at 140°C, P3HT will recrystallise over a period of approximately 5 minutes only, whilst for PC₆₁BM this process will occur over a longer time-scale.

Here field-effect mobility measurements are used to reveal more about the time-dependence of polymer:fullerene blend recrystallisation. BGBC OFETs

were again fabricated in ambient pressure N_2 from P3HT:PC₆₁BM blends of a 1:1 (wt%) composition. The devices were encapsulated and transferred, via air, to a high vacuum cryostat. The encapsulation was removed before measurement/annealing. The samples were then heated to 130°C and 160°C, and the saturation-regime field-effect mobilities were measured at these temperatures as a function of time. The results are shown in Figure 5.5.

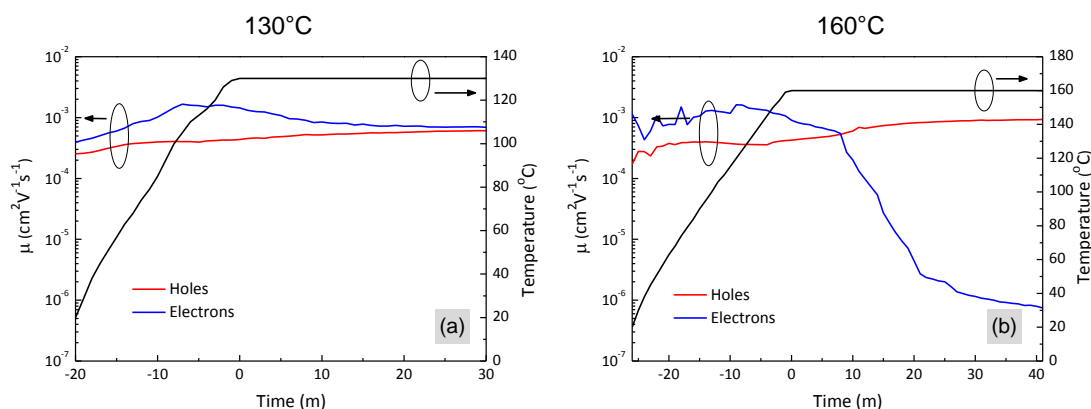


Figure 5.5: Field-effect mobility of holes and electrons in a 1:1 (wt%) P3HT:PC₆₁BM blend ambipolar bottom-gate, bottom-contact OFET as function of time, whilst being annealed at: (a) 130°C and (b) 160°C. $L = 5 \mu\text{m}$, $W = 10\text{mm}$ for both OFETs.

Whilst annealing at 130°C (Figure 5.5(a)) it is clear that a small increase and subsequent fall in electron mobility takes place. The increase is attributed to the evaporation of oxygen and water, both of which are known to impede electron transport.[190] The fall may attributed to the onset of formation of fullerene crystalline entities. The slight increase in hole transport is likely to be due to the temperature-dependence of carrier transport[70] (rather than a recrystallisation effect), as it was found to be reversible upon cooling back to room temperature (data not shown). During annealing at 160°C (Figure 5.5(b)) the hole and electron mobilities remain constant for approximately 10 minutes, after which the electron mobility begins to drop rapidly, indicating the loss of percolation due to the aggregation of fullerene-rich crystallites. The hole mobility, in contrast, is observed to increase. The latter observation can be attributed to both the recrystallisation of the P3HT, in agreement with thermal analysis

described above, as well as temperature-dependent transport effects. The drop in electron mobility appears to stop after approximately 30 minutes, suggesting the PC₆₁BM clusters have reached a stable size. It is therefore clear that OFETs can be utilized to probe the microstructure development of polymer:fullerene blends with temperature and time. As a consequence, this technique can be used to gain insight how to optimize OPV post-production treatments for multi-component semiconductor systems, as demonstrated here on the P3HT:PC₆₁BM binary.

5.3 Simulation of OFET Channel Conductivity

According to the hypothesis laid-out in Section 5.2.2, the electron mobility (and hence conductivity) of a quasi-2D channel should drop significantly upon phase-segregation. This is believed to be due to a reduction in concentration of electron-transporting fullerenes in regions between PC₆₁BM crystallites. To test this explanation computationally, a simple percolation-theory-based simulation has been carried out.

5.3.1 2-Dimensional Resistor-Network Model

Whilst previous studies have modelled electron transport in polymer:fullerene blends by evaluating transfer matrices,[243] here transport is described by the variable-range-hopping mechanism derived by Vissenberg and Matters.[70] In their model, transport is described by the thermally-activated tunnelling of carriers between localized states (see Section 2.2.3). The energy associated with each tunnelling event, or ‘hop’, in a conduction pathway is dependent on the distance between the two sites and their difference in energy. Within this model the conductance of a hop between site i and site j can be approximated by:

$$G_{ij} = G_0 e^{-s_{ij}} \quad (5.1)$$

Here G_0 is a constant and the term s_{ij} is given by the following equation:

$$s_{ij} = 2\alpha R_{ij} + \frac{|\varepsilon_i - \varepsilon_F| + |\varepsilon_j - \varepsilon_F| + |\varepsilon_i - \varepsilon_j|}{2k_B T} \quad (5.2)$$

Here, α is the wavefunction overlap parameter of the two states, R_{ij} is the distance between the states, ε_i , ε_j and ε_F are the energies of state i , state j and the Fermi-level respectively, k_B is the Boltzmann constant, and T is the temperature. The first term on the right-hand side of equation 5.2 describes the tunnelling process. This is characterised by the distance between states and their respective wavefunctions (here assumed to be identical). The second term on the right-hand side of equation 5.2 takes account of the activation energy for a hop upwards in energy from site i to site j and their respective occupational probabilities.

The conductivity of a bulk system can then be evaluated computationally using a resistor-network model and an implementation of percolation theory.[79] This is carried out as follows. The conductance of every hop in a system is calculated and a reference conductance G , is defined. All hops with $G_{ij} > G$ are considered part of the conducting system. As G is reduced from a high to a low value, there will be a critical conductance G_C , at which the first infinite cluster is formed, this value of G_C is taken as the conductivity of the system.

Here I have simply considered how the conductivity of a 2-dimensional, 2-component channel depends on the distance between sites and ignored the effect of the energy offset. Since charges are only transported in the first few nanometres in OFETs,[181] the above approximation is considered valid for the purposes of this study. Were a 3-dimensional film to be considered, there would be a spatial-dependence on the gate field.[122] Hence the state-occupation would not be homogeneous and this assumption would be invalid. If the energy offset between all states was set to a constant value of E_{off} , then equation 5.2 can be written as:

$$s_{ij} = 2\alpha R_{ij} + \frac{E_{off}}{2k_B T} \quad (5.3)$$

This can then be substituted into equation 5.1 to give:

$$G_{ij} = \tilde{G}_0 e^{-2\alpha R_{ij}} \quad (5.4)$$

Where:

$$\tilde{G}_0 = G_0 e^{-E_{off}/2k_B T} \quad (5.5)$$

I.e. \tilde{G}_0 is the conductivity of a hop between two states in the same position.

5.3.2 Simulating Fullerene-Clustering

To elucidate the potential impact of fullerene-clustering on electron transport in polymer:fullerene OFETs, the above resistor-network model was applied to fullerenes embedded in a polymer matrix. In contrast to previous studies,[243] here the polymer component is here considered insulating to electrons and hence electron transport in the polymer is forbidden.

To carry out this simulation a discreet 2-dimensional grid of potential fullerene positions was established. Positions in the grid were then defined as occupied or unoccupied. Unoccupied positions are considered to be the polymer matrix and hence do not allow electron transport. A Monte-Carlo algorithm is then applied to allocate the fullerene positions and simulate the clustering. The algorithm loops over every unoccupied position in the grid and has a very small (e.g. $\sim 10^{-5}$) chance of occupying each position with a fullerene molecule. The algorithm loops over the entire grid several thousand times, until a desired fullerene concentration C , is reached.

In order to simulate fullerene clustering, the random-allocation algorithm was modified to include a weighting parameter, w . This parameter ranged from 0 to 1, and modified the probability of a position being allocated with a fullerene molecule, depending upon the occupation of adjacent positions. If $w = 1$, the probability of a position not adjacent to any already-occupied positions being occupied is zero. Similarly, if $w = 0$ the probability of occupying all positions is equal. To induce a significant degree of phase segregation values of $w > 0.9$ are typically required. Figure 5.6 shows some example 200×200 , 2-dimensional grids occupied using the above-described algorithm and various values of the clustering parameter w .

The example data shown in Figure 5.6 illustrates that the algorithm does work as expected, and a control of the degree of phase-segregation is hence possible. It should be noted that the shape of the clusters are not circular or rectangular such as those observed in Figure 5.1 or reference [103] for example. This is due to the fact that algorithm only considers two possible cases for each unoccupied

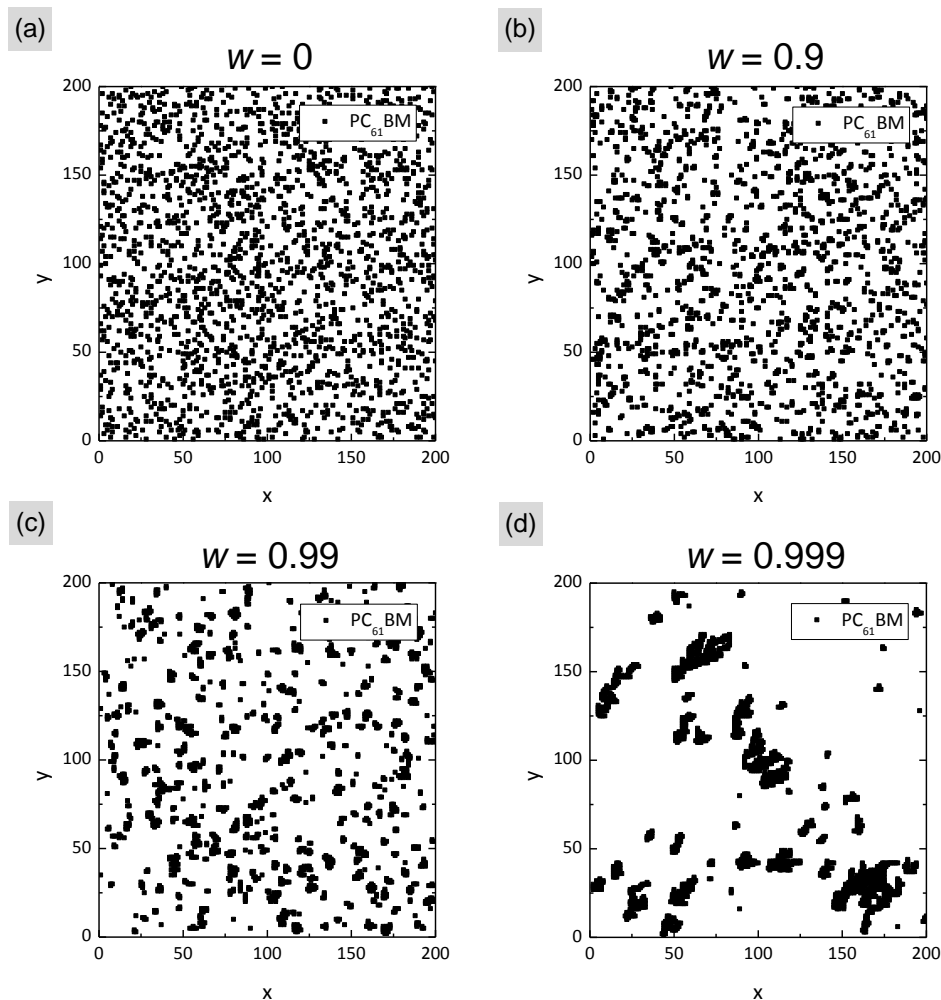


Figure 5.6: Simulated clustering of fullerene molecules in polymer matrix for a 200×200 , 2-dimensional grid. The phase segregation was simulated by varying the parameter w , in the Monte-Carlo algorithm described in Section 5.3.2

site; either one or more adjacent position is occupied or no adjacent positions are occupied. A more involved method could involve determining the size of each adjacent cluster and modifying the occupation probability depending on that. Unfortunately such an algorithm would be computationally very intensive. An alternative approach such as a weighted random-walk could perhaps produce better results, but is beyond the scope of this study. Since it is the change in fullerene concentration between clusters that is critical for this study, it is felt

that the clustering illustrated in Figure 5.6 is adequate.

5.3.3 Calculated Conductivity

With a method now in place for simulating phase-segregated, 2-dimensional polymer:fullerene systems, their electron-conductivity can be studied. This is carried out using the random resistor-network implementation of percolation theory outlined in Section 5.3.1. In the interest of saving computational resources, a small grid size of 200×200 was used for this study. If one makes the assumption that one grid space is approximately $1 \text{ nm} \times 1 \text{ nm}$ (the approximate area of a PC_{61}BM molecule) then this would give rise to a grid size of $200\text{nm} \times 200\text{nm}$. This grid can be replicated many times to simulate an area the size of an OFET channel ($\sim 10 \mu\text{m}^2$). This simplification assumes that the size of clusters do not get larger than the grid size. Figure 5.1 illustrates how this is clearly not the case. However implementing the simulation in this way is necessary due to computational cost, and still allows a study of conductivity with phase-segregation to be carried out.

For the purposes of this simulation, an infinite cluster will be defined as a cluster which joins the left and right sides of the simulation grid. Hence the weakest hop in this pathway will define the critical conductance G_C for the source to drain electrodes in the OFET channel. Determining the distance between every fullerene molecule and every other fullerene molecule would again be computationally impossible. Therefore a smaller number of the nearest-neighbours were considered for each molecule. Since we are modelling the system as a resistor network, the charge will always travel via the lowest resistance route and hence large hops can be ignored where shorter ones are available.

With the critical hop-distance (R_C) of the system determined, equation 5.4 can be evaluated to provide the conductivity of the film. The parameter \tilde{G}_0 is potentially very difficult to measure, so the conductivity of each film is here expressed as G/\tilde{G}_0 . The purpose of our study is to observe a general trend and confirm our suspicion that fullerene-clustering leads to a drop in electron conductivity in a 2-dimensional system, not extract a physical parameter. Hence evaluating G/\tilde{G}_0 is perfectly valid for our study. The wavefunction-overlap parameter α , has not previously been evaluated for PC_{61}BM , but has been deter-

mined for pentacene to be: $\alpha^{-1} = 0.22$ nm. For this study I will set the prefactor $(2\alpha)^{-1} = 1$ nm. Although in reality α will be larger than this, for the purposes of this simulation the numbers work rather well.

Figure 5.7(a) shows the conductivity of 150 different 200×200 2-dimensional grids calculated with various degrees of phase segregation, plotted as a function of average cluster size. The average cluster size is simply defined to be the sum of the sizes of the cluster (formed of adjacent fullerenes) each fullerene resides in, divided by the total number of fullerenes. As expected, the conductivity of the system decreases sharply as the average fullerene cluster size increases, i.e., as the system becomes more phase-segregated. Since this simulation relies heavily on randomly distributed molecules, the variation in conductivities is significant, but a clear trend still exists. This result is unsurprising since the conductivity of a system, as evaluated using percolation theory, is determined by the ‘worst’ hop in the conduction pathway.

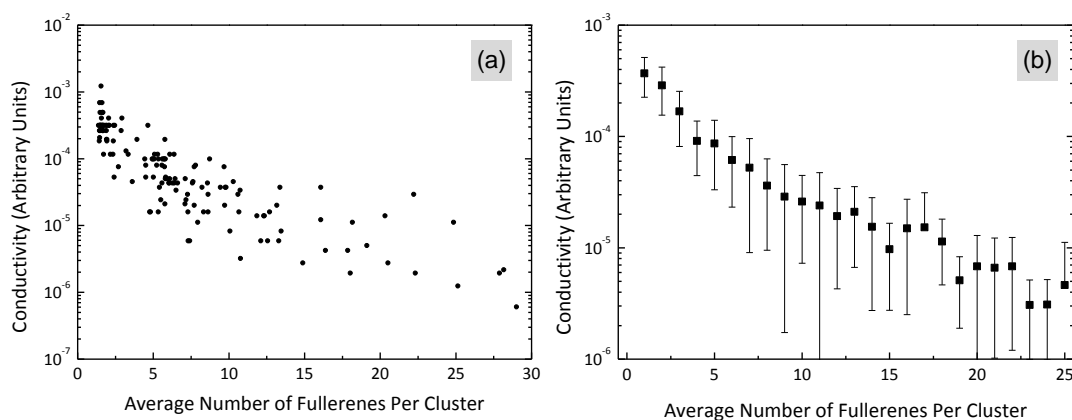


Figure 5.7: (a) Conductivity of 150 different 200×200 2-dimensional grids calculated with various degrees of phase segregation, plotted as a function of average cluster size. (b) Calculated conductivity of 1500 200×200 2-dimensional grids, quantised to integer bins.

To illustrate the relationship more clearly, the simulation was carried out for 1500 grids and the results were quantised. The average cluster sizes were put into bins depending on the nearest integer value. The average and standard deviation of conductivity are plotted for each bin in Figure 5.7(b). From this data the

relationship between conductivity and average cluster size can perhaps be viewed more clearly.

5.4 Phase Segregation in Blends of P3HT:PC₆₁BM and P3HT:PC₇₁BM

The data presented in Sections 5.2 and 5.3.2 provides solid evidence to suggest that phase segregation in polymer:fullerene blends can be detected as a fall in electron field-effect mobility. Using time-dependent measurements such as those illustrated in Figure 5.5, important information with regards to OPV fabrication and optimisation procedures can hence be elucidated. In this Section I have utilised OFET mobility measurements to investigate how the phase-segregation process in polymer:fullerene blends is affected by the molecular weight of the fullerene molecule.

Recently, many high-performance OPVs are reported to be increasingly employing PC₇₁BM (C₇₁-butyric acid methyl ester) as opposed to PC₆₁BM as the acceptor molecule in OPV blends.[164–166] Due to its lower symmetry, the absorption spectrum of PC₇₁BM is red-shifted significantly with respect to the more commonly used PC₆₁BM,[273] giving it an improved overlap with the AM 1.5 solar spectrum. With certain high-performance polymer:fullerene systems requiring a relatively high concentration of fullerene acceptor,[165, 166] this extra absorption is expected to result in significant improvements in solar-cell PCE's under AM 1.5 conditions.

It has previously been shown that despite these differences in optical properties, the charge transport characteristics of PC₇₁BM are very similar to those of PC₆₁BM.[111] The effect of fullerene solubility on film microstructure and OPV performance has previously been studied,[191] but there have to-date been few comparisons of how the morphological and microstructural properties of polymer:fullerene blends change with fullerene molecular weight alone.[268] It is hence felt that employing OFET mobility measurements to study such differences is both a timely and worthwhile endeavour. Although P3HT-based OPVs exhibit impressive performance,[206] the highest PCE devices are now based on lower

band-gap polymers.[164–166] P3HT is still none-the-less widely used as the standard system for studies aimed at understanding the microstructure and morphology of polymer:fullerene blends,[103, 206, 235, 236, 268, 272, 274] and is hence employed here.

5.4.1 P3HT:PC₇₁BM Blend OFETs

To make comparison with the data presented in Section 5.2 as relevant as possible, a similar BGBC OFET architecture was again employed. As before, gold source and drain electrodes were used and an HMDS monolayer was applied to an SiO₂ dielectric. Again a 1:1 (wt %) blend ratio of P3HT:PC₇₁BM was used here. As with P3HT:PC₆₁BM blend OFETs, it is anticipated that hole field-effect mobility measurements should reveal information about the P3HT network whilst electron mobility measurements should reveal information about the PC₇₁BM network. Whilst hole transport in PC₇₁BM has previously been observed using gold source and drain electrodes,[217] the mobility is low enough that it is not likely to interfere with the measured mobility of holes in the polymer network. The p- and n-type transfer characteristics of a 1:1 (wt %) blend P3HT:PC₇₁BM OFET are shown in Figures 5.8(a) and 5.8(b) respectively. The device dimensions were $L = 10 \mu\text{m}$ and $W = 10 \text{mm}$.

To study phase segregation in these blends, four BGBC OFETs were annealed at temperatures between 60°C and 300°C in 20°C steps. As with the previous measurements, each annealing step lasted for 30 minutes. The annealing was again cumulative. The average hole and electron saturation field-effect mobilities were then extracted from the p- and n-type transfer characteristics respectively and plotted in Figure 5.8(c). The error bars show the standard deviation of the 4 measured mobilities. The first point to note is that both the as-cast hole and electron mobilities in the P3HT:PC₇₁BM blend are very similar to those in the P3HT:PC₆₁BM blend. This is as expected given previous studies into the differences in charge-transport behaviour of PC₆₁BM- and PC₆₁BM-based OFETs.[111]

Figure 5.8(c) shows that the electron and hole mobilities stay approximately constant until the 160°C annealing step, where the hole mobility increases by

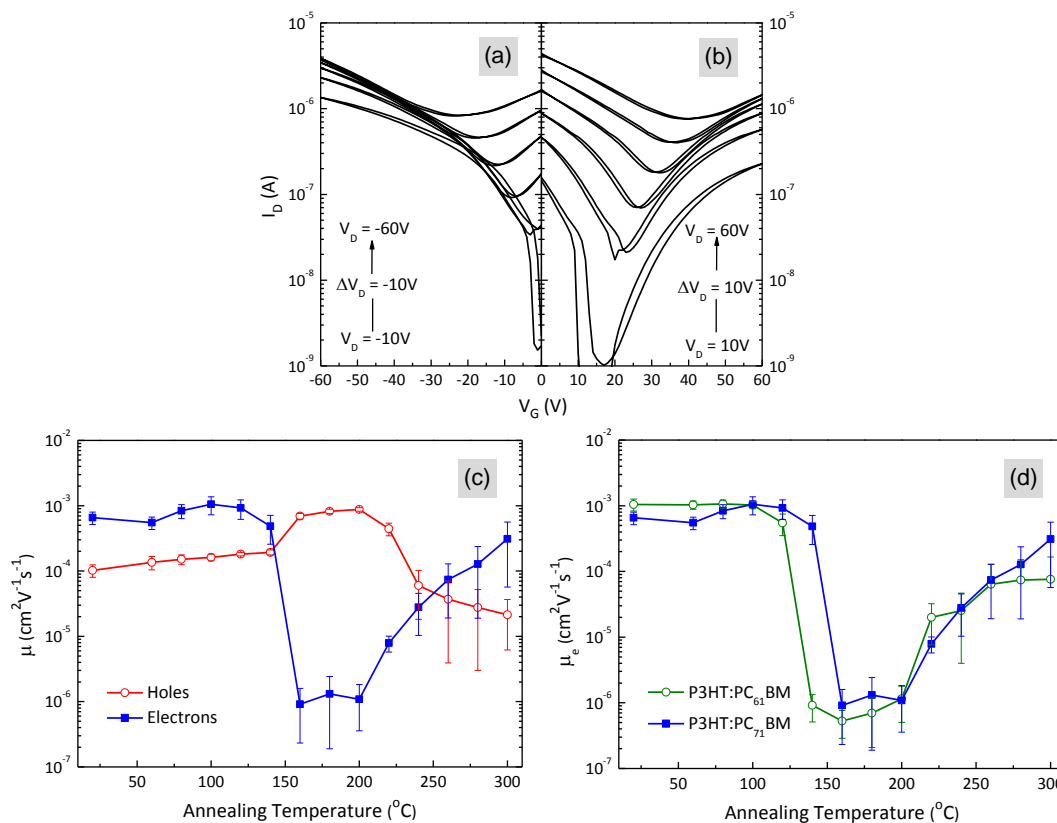


Figure 5.8: Transfer characteristics of an example BGBC 1:1 (wt %) blend P3HT:PC₇₁BM OFET measured with (a) negative and (b) positive drain voltages. The device dimensions were $L = 10 \mu\text{m}$ and $W = 10 \text{mm}$. (c) Average saturation-regime field-effect mobility of holes and electrons in four 1:1 (wt %) P3HT:PC₇₁BM blend BGBC OFETs measured at room temperature under ambient-pressure N₂ after being annealed at various temperatures for 30 minutes. The error bars represent the standard deviation in the measured field-effect mobility. (d) Average electron saturation-regime field-effect mobility from (c) plotted alongside similar electron field-effect mobility measurements made on four 1:1 (wt %) P3HT:PC₆₁BM blend BGBC OFETs, taken from Figure 5.3(d).

a factor of 3.5 and the electron mobility falls by a factor of 500. As in Section 5.2, The former effect is attributed to improved inter-chain transport, due to polymer-crystallisation, whilst the later effect is attributed to a reduction in percolation pathways between fullerene-rich clusters. Upon annealing at 220 $^\circ\text{C}$ the hole mobility starts to fall and the electron mobility begins to recover. This

phenomenon is again attributed to a melting of the blend and a re-distribution of fullerene molecules, re-opening electron percolation pathways.

Figure 5.8(d) shows the average electron saturation-regime field-effect mobility from Figure 5.8(c) plotted alongside similar electron field-effect mobility measurements made on four 1:1 (wt %) P3HT:PC₆₁BM blend BGBC OFETs, taken from Figure 5.3(d). It is immediately clear that there is a striking similarity between the two plots, suggesting that the phase-segregation processes in the two systems are very similar. The interesting difference between the two graphs is the temperature at which phase-segregation is detected; for P3HT:PC₇₁BM it is 160°C, whereas for P3HT:PC₆₁BM it is 140°C. It is proposed that the higher prerequisite annealing temperature for phase-segregation in the P3HT:PC₇₁BM system is due to an increase in required thermal energy in the former system. Due to their increased volume, the frictional drag of PC₇₁BM molecules is anticipated to be higher than that of PC₆₁BM molecules when dispersed in P3HT. This would hence be expected to lead to a higher activation-temperature for PC₇₁BM diffusion in P3HT. The diffusion of both PC₆₁BM and PC₇₁BM in P3HT is studied in more detail in Chapter 6.

5.4.2 Time-Dependent P3HT:PC₇₁BM Mobility Measurements

To investigate how phase-segregation in these blends evolves in real-time, the field-effect mobilities of holes and electrons in a P3HT:PC₇₁BM blend (1:1 wt%) BGBC OFET were measured every two minutes whilst being annealed at a constant temperature of 160°C. The OFETs were fabricated in an identical manner to those studied in Section 5.4.1. They were then encapsulated and transferred to a cryostat-integrated vacuum probe station where the encapsulation was removed prior to measurement. To electrically insulate the OFETs from the heating element, a mica-plate was placed between the OFET substrate and the heated chuck.

The saturation-regime electron and holes mobilities are plotted as a function of annealing time in Figure 5.9(a). Here an increase in electron mobility is observed whilst the hole mobility changes very little. The increase in electron mobility is

likely to be due to the evaporation of water and oxygen that was absorbed by the fullerene molecules upon transfer to the probe station (water and oxygen absorption are known to impede electron transport in certain n-type molecules[190]). Other possible explanations include a change in the vertical concentration-profile of the PC₇₁BM upon annealing.[103] Regardless of the reason behind this feature, the important observation here is that the electron mobility does not fall, indicating that a significant degree of phase-segregation does not take place. The fact that a mica slide is present between the OFET substrate and the heating chuck in the cryostat suggests comparing the temperatures of Figure 5.9(a) and Figure 5.8 is not directly possible. This can explain why the significant fall in electron mobility upon annealing is not observed in Figure 5.9(a), whilst it is in Figure 5.8(a) after annealing to 160°C. Direct comparison with blends of P3HT:PC₆₁BM as carried out in Figure 5.5 is however possible. As hypothesized earlier, the absence of a severe fall in electron mobility in Figure 5.9(a) is attributed to the larger fullerene volume and hence lower activation temperature for diffusion. The fact that electron mobility initially rises more significantly upon annealing in Figure 5.9(a) than in Figure 5.5 could perhaps be due to differences in encapsulation material (CYTOP™) batches.

In an attempt to induce phase-segregation in blends of P3HT:PC₇₁BM, the cryostat temperature was raised to 190°C and the experiment was repeated. The field-effect mobilities of both holes and electrons were again measured every two minutes and plotted as a function of time in 5.9(b). Similarly, the mobilities for a P3HT:PC₆₁BM blend OFET are plotted as a function of time in Figure 5.9(c). By comparing 5.9(b) and 5.9(a) it is clear that, under identical conditions, the phase-segregation process in P3HT:PC₇₁BM takes approximately 10 - 15 minutes longer to complete than for P3HT:PC₆₁BM, whilst annealing at 190°C. Whilst absolute annealing temperature, blend ratio, polymer regioregularity etc. are likely to affect the difference in required annealing time, the results from Figure 5.9 illustrate how the post-processing annealing treatments applied to OPVs should in general be lengthened when replacing PC₆₁BM with PC₇₁BM, keeping all other variables unchanged.

The data presented within this section illustrates how OFET measurements can provide useful information with regards to OPV-relevant systems. Whilst I

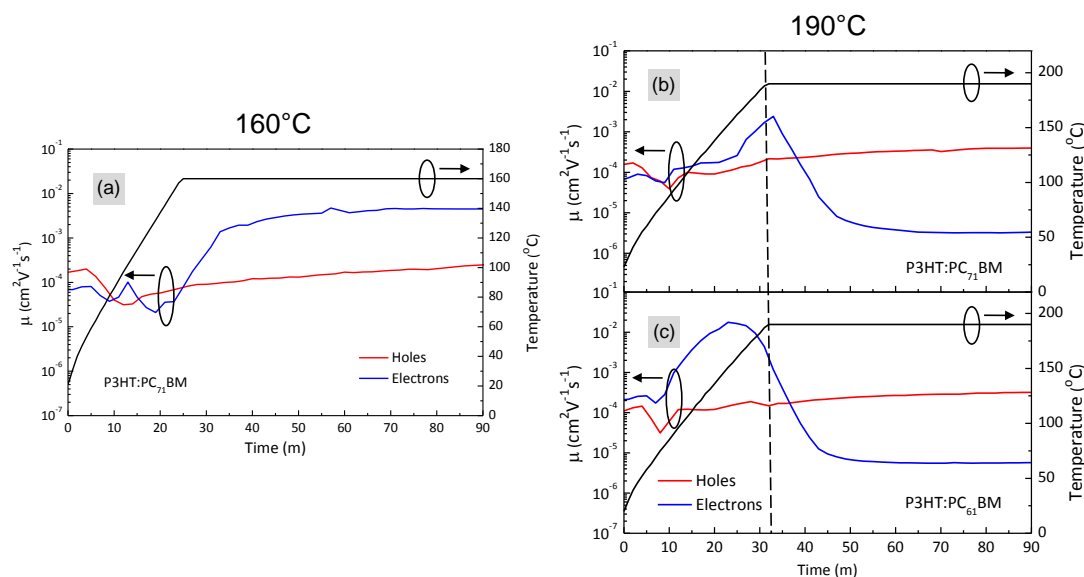


Figure 5.9: (a) Saturation-regime field-effect mobility of holes and electrons in a 1:1 (wt %) P3HT:PC₇₁BM blend ambipolar bottom-gate, bottom-contact (BGBC) OFET measured as a function of time, whilst being annealed at 160°C . Saturation-regime mobility of holes and electrons in (b) 1:1 P3HT:PC₇₁BM and (c) 1:1 P3HT:PC₆₁BM blend BGBC OFET measured as a function of time, whilst being annealed at 190°C . Channel dimensions were: $L = 10 \mu\text{m}$, $W = 10 \text{mm}$ and measurements carried out under high-vacuum in each case.

have here studied only one polymer system, it is anticipated that the observation that P3HT:PC₇₁BM phase-segregation requires greater annealing temperatures and / or times than P3HT:PC₆₁BM, will be applicable to other polymer systems also.

5.5 Conclusions

In this chapter I have studied the relationship between the morphology of polymer:fullerene blends and the charge-carrier mobility measured using field-effect transistors. By gaining an understanding of this relationship, organic field-effect transistors (OFETs) were then shown to be capable of probing the microstructure of such blends.

By using polarised optical microscopy and the benchmark polymer:fullerene

system of poly(3-hexylthiophene) (P3HT) and [6,6]-phenyl C₆₁-butyric acid methyl ester (PC₆₁BM), it was observed that upon annealing the system undergoes significant phase-segregation, in agreement with previous reports. It was shown that this phase-segregation is manifest as a drastic reduction in electron mobility in OFETs. By utilising in-situ measurements, the time-scale of phase-segregation could be probed with great temporal resolution, illustrating a potentially very-useful application of such measurements.

The observed reduction in electron-mobility in OFETs upon annealing is attributed to the large-scale aggregation of fullerenes in the blends, and subsequent reduction in fullerene percolation-pathways. To test this concept computationally, a percolation theory-based model was developed and implemented. A random-resistor network model was employed for a 2-dimensional grid of fullerenes and the conductivity evaluated. By adjusting the degree of fullerene-clustering in these grids, the effect of phase-segregation could be simulated. It was observed that, in agreement with experiment, the conductivity of the system fell strongly with an increase in phase-segregation.

Finally, these OFET-mobility measurements were then employed to attempt to understand the affect of changing the molecular weight of the PCBM molecule. By studying phase-segregation in blends of C₇₁-butyric acid methyl ester (PC₇₁BM) and P3HT it was concluded that, in this system at least, increasing the molecular weight of PCBM increases the required annealing temperature and / or time for phase-segregation to take place. This was attributed to an increase in the frictional drag of PC₇₁BM in P3HT with respect to PC₆₁BM, caused by the former's larger volume.

Chapter 6

Polymer:Fullerene Diffusion Processes

6.1 Introduction

Whilst the polymer:fullerene bulk heterojunction (BHJ) appears to be a clear front-runner with regards to organic photovoltaic (OPV) cell performance,[164–166] its internal microstructure makes it inherently complicated to study.[239–242] Recently, equivalent bilayer structures have allowed for interesting insights into polymer:fullerene systems.[189, 255–259, 262] Using deposition techniques such as stamp-transfer[257–259] and orthogonal solvents,[189, 255, 256] several groups have now reported bilayer structures based upon the benchmark system of poly(3-hexylthiophene) (P3HT) and [6,6]-phenyl C₆₁-butyric acid methyl ester (PC₆₁BM).

Using techniques such as dynamic secondary ion mass spectrometry (DSIMS),[259, 262] neutron reflectometry[256] and transmission electron microscopy,[189] it has been observed that PC₆₁BM will diffuse into P3HT upon annealing. This is a phenomenon distinct from the widely-reported polymer-crystallisation and fullerene-clustering process generally associated with improvements in OPV power-conversion efficiency.[206, 235, 236] Until recently this process was largely unknown and hence absent from any OPV processing and optimisation procedures.

In the previous chapter I illustrated how organic field-effect transistors (OFETs)

could be used as probes of the microstructure of polymer:fullerene blend systems. In this chapter I have employed bilayer OFETs to study the diffusion of fullerenes in polymers. By monitoring the evolution of hole and electron field-effect mobilities in polymer:fullerene systems, changes in the percolation properties of these two networks at the semiconductor-dielectric interface can hence be inferred. With a knowledge of how changes in morphology are reflected in field-effect mobility, as obtained in Chapter 5, information about the diffusion of fullerenes in polymers can be revealed.

6.2 Evaporated PC₆₁BM OFETs

Whilst most previous attempts to fabricate polymer:fullerene bilayers have been carried out using either stamp-transfer techniques[257–259] or orthogonal solvents,[189, 255, 256] here vacuum-deposited PC₆₁BM is employed. This approach is used because the orthogonal solvent method is known to cause layer ‘swelling’,[256] whilst stamp-transfer is only compatible with thick (~ 100 nm) films,[259] reducing the control we have over the diffusion parameters.

Since PC₆₁BM has never been reported to have been deposited via thermal sublimation, it is important to ensure that the PC₆₁BM has indeed been deposited as expected, without degradation due to heating for example. 30 nm of PC₆₁BM was deposited onto quartz substrates via thermal sublimation, at an average rate of 0.3 \AA^{-1} , and was also deposited via spin-coating. The PC₆₁BM started to sublime at a temperature of 220°C , approximately 200°C lower than for C₆₀. The normalised optical absorption spectra of vacuum-deposited PC₆₁BM, spin-cast PC₆₁BM and vacuum-deposited C₆₀ are shown in Figure 6.1(b). These films were measured with a Shimadzu UV-2550 ultraviolet-visible spectrophotometer.

Bottom-gate, top-contact (BGTC) pristine PC₆₁BM OFETs were also fabricated on highly doped silicon and silicon dioxide. The silicon dioxide layer was passivated with a thin (~ 50 nm) layer of divinyltetramethyldisiloxane-bis(benzocyclobutene) (BCB). 50 nm aluminium source and drain electrodes were then deposited via thermal evaporation under high vacuum through shadow masks, at an average rate of 1 \AA^{-1} . The transfer characteristics of ten vacuum-deposited and ten spin-cast BGTC PC₆₁BM OFETs were measured under N₂

without annealing. Example transfer characteristics of (c) vacuum-deposited and (d) spin-cast PC₆₁BM OFETs are shown in Figure 6.1. A schematic representation of this OFET structure is given in Figure 6.1(a).

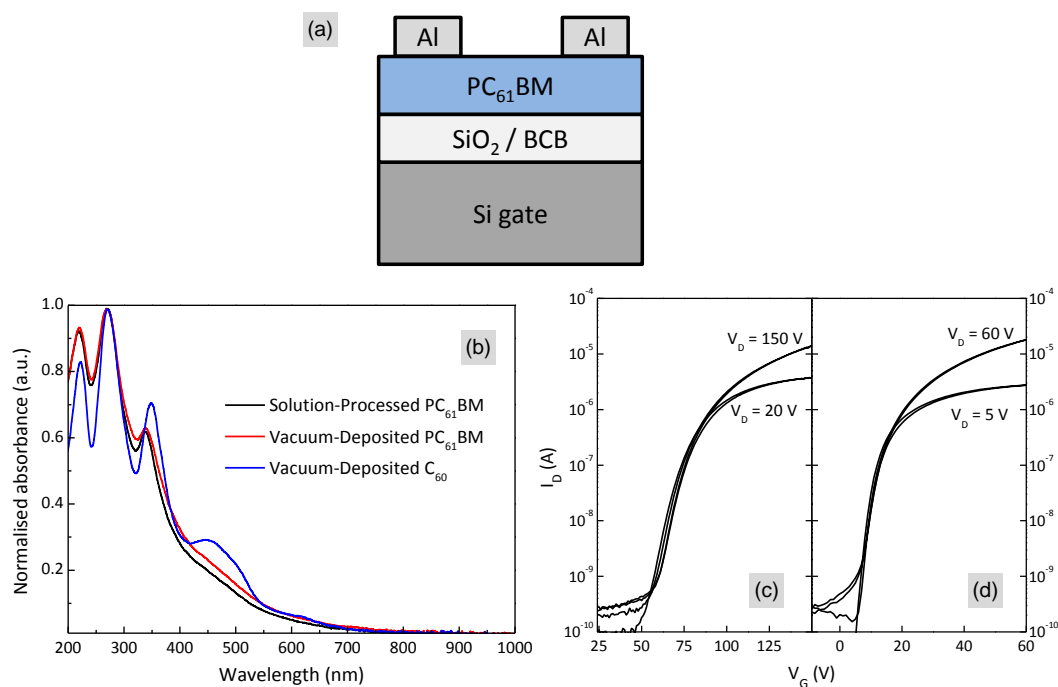


Figure 6.1: (a) Schematic diagram of bottom-gate, top-contact (BGTC) PC₆₁BM OFET. (b) Normalised optical absorption spectra of spin-cast PC₆₁BM, vacuum-deposited PC₆₁BM and vacuum-deposited C₆₀. Transfer characteristics of (c) spin-cast PC₆₁BM and (d) vacuum-deposited PC₆₁BM BGTC OFETs on BCB-coated SiO₂ with aluminium source and drain electrodes. The devices were characterized under ambient-pressure in N₂ without being annealed. In both cases the transistors had channel lengths and widths of 40 μm and 1000 μm respectively.

Figure 6.2 shows tapping mode atomic force microscope (AFM) topography images of spin-cast and vacuum-sublimed PC₆₁BM, deposited onto HMDS-treated SiO₂. The route-mean squared roughnesses of the spin-cast and vacuum-sublimed PC₆₁BM were measured to be 1.9 Å and 2.7 Å respectively.

The data in Figure 6.1 provides strong evidence that the material being deposited via thermal sublimation is indeed PC₆₁BM, as opposed to (say) C₆₀ formed from PC₆₁BM that underwent degradation during the evaporation process. The average electron field-effect mobility was measured to be $3 \pm 2 \times 10^{-2}$

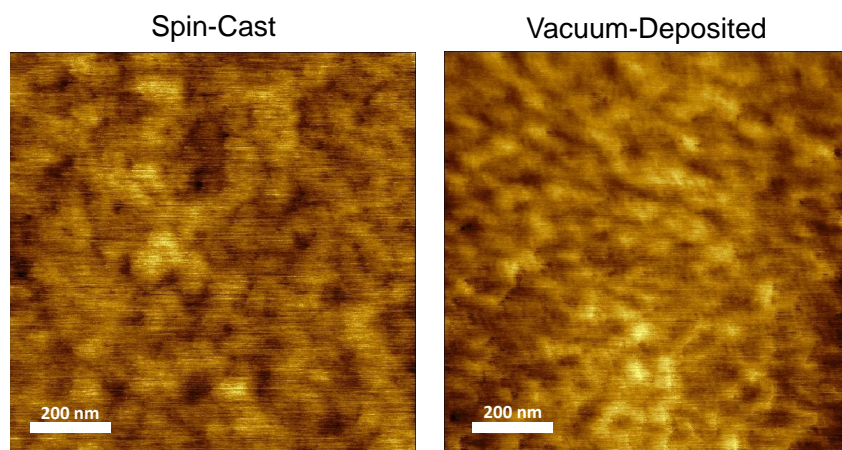


Figure 6.2: Atomic force microscope (AFM) topography images of spin-cast and vacuum-sublimed PC₆₁BM, deposited onto HMDS-treated SiO₂. Both layer thicknesses were approximately 30nm and the measurements were carried out in tapping-mode. The measured peak-to-peak height was 2 nm for spin-cast PC₆₁BM and 2.7 nm for vacuum-deposited PC₆₁BM.

cm²V⁻¹s⁻¹ for the vacuum-deposited PC₆₁BM OFETs and $8.1 \pm 0.7 \times 10^{-2}$ cm²V⁻¹s⁻¹ for the spin-cast PC₆₁BM OFETs. These values are comparable with previous reports of PC₆₁BM OFETs on BCB substrates[111] and are significantly lower than similar devices with C₆₀ as the active layer.[92] The difference in the average and standard deviation of the mobilities is attributed to differences in the film microstructure, caused by the different deposition methods. Similarly, the higher threshold voltage observed for vacuum-deposited PC₆₁BM (see Figure 6.1(c)) with respect to spin-cast PC₆₁BM (see Figure 6.1(d)) is attributed to differences in the microstructure at the semiconductor-electrode interfaces.

6.3 Bilayer P3HT:PC₆₁BM OFETs

Bilayer bottom-gate, bottom-contact (BGBC) OFETs were fabricated on highly doped (n⁺⁺) silicon wafers, which acted as the gate electrode, with a 200 nm thermally grown silicon dioxide layer as the gate dielectric. The silicon dioxide surfaces were then passivated with hexamethyldisilazane (HMDS). Gold source and drain electrodes were defined using standard photolithographic techniques.

Solutions of P3HT were then deposited onto the substrates via spin-coating. The solvent used was chlorobenzene. PC₆₁BM was deposited onto the P3HT via thermal sublimation as described above. The bilayer structure employed is shown in Figure 6.3(a).

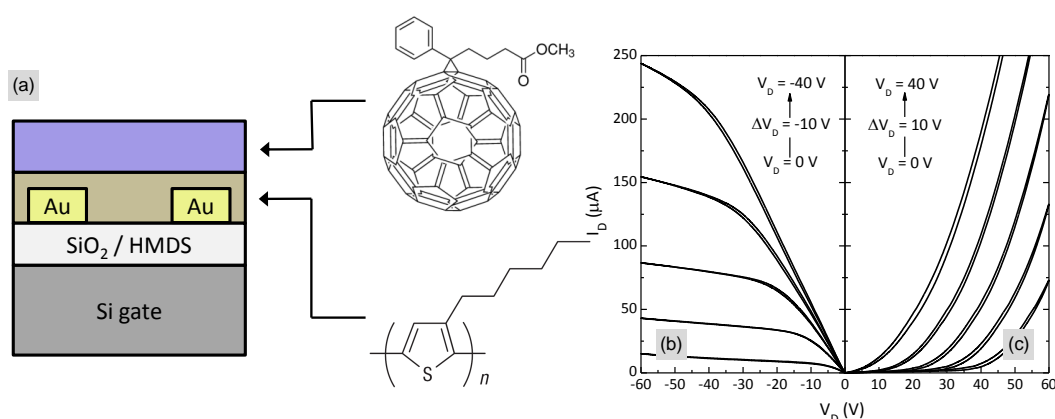


Figure 6.3: (a) Schematic diagram of bottom-gate, bottom-contact (BGBC) bi-layer OFET structure used in this study and molecular structures of PC₆₁BM (top) and P3HT (bottom). Output characteristics of example bi-layer P3HT:PC₆₁BM BGBC OFETs measured under ambient-pressure N₂ before annealing with (a) negative applied gate voltages and (b) positive applied gate voltages. This device had a channel length and width of 7.5 μm and 10 mm respectively, and P3HT and PC₆₁BM thicknesses of 8 nm and 31 nm respectively.

Example output characteristics of a P3HT:PC₆₁BM bilayer OFET are shown in Figure 6.3. The thicknesses of the P3HT and PC₆₁BM layers in this case were 8 nm and 31 nm respectively. The observed characteristics are indicative of unipolar (p-type) behaviour.[144] Since initially only P3HT is in contact with the source and drain electrodes and with the semiconductor-dielectric interface, and because carrier transport only takes place within the first few nanometers of the semiconductor-dielectric interface,[181] this behaviour is as expected. Bilayer ambipolar OFETs have previously been demonstrated for electronic,[150] and light sensing applications (see Section 4.3), but in both these cases the architectures have been so-called “middle-contact”, where the source and drain electrodes have been in direct contact with both semiconductor systems. In such bilayer devices the bottom semiconductor layer acts as the dielectric for the top semiconductor,

as described in Section 2.4.2.

Multi-layer ambipolar systems have however previously been demonstrated using BGBC[149] and BGTC[148] architectures, where the electrodes have been in direct contact with one semiconductor only. This is in contrast to our system, where no n-channel is measurable initially. This difference in behaviour is likely to be due to differences in the energy levels of the semiconductors and electrodes. Fully annealed (inter-diffused) bilayer P3HT:PC₆₁BM OFETs have recently been shown[189] to exhibit ambipolar behaviour, as expected from a standard BHJ structure.[109] Given the data shown in Figures 6.3(b) and 6.3(c) we can hence be confident that in our devices the measured mobility is representative of the state of the semiconductor system at the semiconductor-dielectric interface.

Several bilayer OFETs were annealed at temperatures between 60°C and 300°C in 20°C steps, with each annealing step lasting 30 minutes. In this case the P3HT and PC₆₁BM layer thicknesses were 8 nm and 40 nm respectively. As with measurements carried out in Chapter 5, the annealing was cumulative, so for example the devices annealed at 80°C for 30 minutes had also been annealed at 60°C for 30 minutes, and so on. The hole and electron mobilities of 5 OFET were then measured in the saturation regime at room temperature after each annealing step. All annealing steps and measurements were carried out under N₂ without exposure to air. The average field-effect mobilities of these 5 devices are plotted as a function of annealing temperature in Figure 6.4(a). Initially, no electron mobility is measurable in any device and the average is therefore plotted as 10⁻⁹ cm²V⁻¹s⁻¹ (which is close our measurement limits).

Up to an annealing temperature of 100°C the hole mobility remains constant and the electron mobility is undetectable. This is likely to be because the extent of PC₆₁BM diffusion has not been sufficient for a strong percolation network to form at the semiconductor-dielectric interface. Although some diffusion is expected to take place at temperatures as low as 50°C, the PC₆₁BM miscibility in P3HT is known[259] to be temperature-dependent. Since the PC₆₁BM layer is 5 times as thick as the P3HT layer, it is therefore anticipated that there will be a strong dependence of electron mobility on annealing temperature.

After annealing to 120°C the electron mobility becomes measurable. This is believed to be due to PC₆₁BM having diffused from the top layer of the device

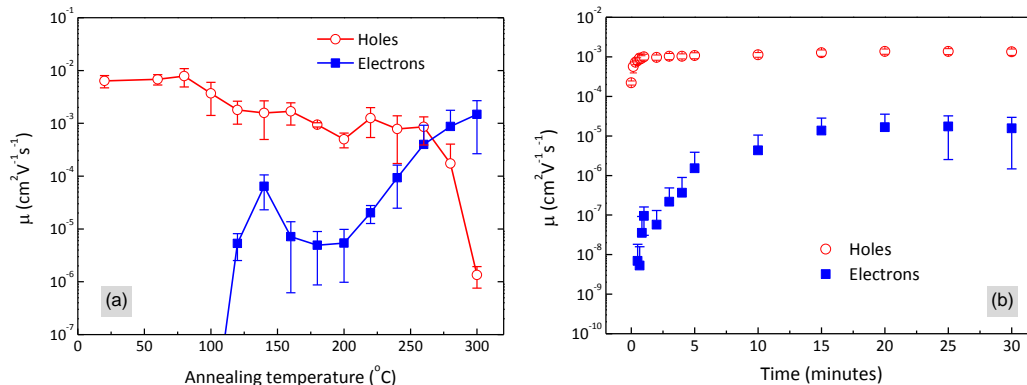


Figure 6.4: (a) Average saturation-regime field-effect mobility of holes and electrons in 5 bi-layer P3HT:PC₆₁BM OFETs measured at room temperature under ambient-pressure N₂ after being annealed at various temperatures for 30 minutes. The error bars represent the standard deviation in the measured field-effect mobility. When the electron mobility was not detectable it was plotted as 10^{-9} $\text{cm}^2\text{V}^{-1}\text{s}^{-1}$. The thicknesses of the P3HT and PC₆₁BM layers were 8nm and 40nm respectively. (b) Average saturation-regime field-effect mobility of holes and electrons in 5 bi-layer P3HT:PC₆₁BM transistors measured under ambient-pressure N₂ after being annealed at 130°C, plotted as a function of time. The thicknesses of the P3HT and PC₆₁BM layers were in this case 25 nm and 31 nm respectively.

through the P3HT to the semiconductor-dielectric interface. Between 80°C and 140°C the hole mobility falls by a factor of 5. This is attributed to the presence of diffused PC₆₁BM disrupting the P3HT packing at the bottom interface. Although the presence of diffused PC₆₁BM is known not to disrupt the crystalline P3HT domains in thick (~ 100 nm) films,[259] here we have an 8 nm thin film and the two systems are therefore not likely to be directly comparable. The fact that at 100°C the hole mobility falls, whilst the electron mobility remains un-measurable is likely to be due to the insufficient concentration of PC₆₁BM at the bottom interface for percolation to occur.

At an annealing temperature of 160°C, the electron mobility falls to a value $\sim 10^{-6}$ $\text{cm}^2\text{V}^{-1}\text{s}^{-1}$. This is attributed to the thermally-induced P3HT-crystallisation and PC₆₁BM-clustering process, described in Chapter 5. This process is believed to lead to a reduction in the concentration of PC₆₁BM in regions between

clusters,[272] and therefore a reduction in electron percolation-pathways, causing a measurable reduction in electron field-effect mobility. At temperatures of 220°C and above the electron mobility is observed to rise, and the hole mobility begins to fall. This is due to the melting of the P3HT:PC₆₁BM blend and subsequent cooling into an amorphous state.

6.3.1 Time-Dependent Mobility Measurements

Figure 6.4(b) shows the average hole and electron mobilities of 5 bilayer P3HT:PC₆₁BM OFETs (P3HT and PC₆₁BM thicknesses: 25nm and 31nm respectively) measured at room temperature after various periods of annealing at 130°C. Note that in contrast to Figure 5.5 for example, the measurements were not made in-situ, but at room temperature under N₂. The reason behind this decision is three-fold. Firstly, for the bilayer measurements we are concerned with an increase in electron mobility, not a fall, hence temperature-dependent increases[70] could give rise to ambiguity in the mobility analysis. Secondly, the in-situ measurements require a certain ‘ramp-up’ time before reaching full temperature, making it impossible to quantify the diffusion process. Finally, as Figure 5.9 suggests, there is a possibility that upon transfer to the cryostat-integrating probe-station, water and oxygen could be absorbed by the PC₆₁BM molecules leading to a reduction in field-effect mobility.[190] As the OFETs are then heated, the H₂O is expected to evaporate, again interfering with an increase in mobility due to microstructure changes.

The hole mobility is observed to rise by a factor of 4 in the first 60 seconds of annealing then saturate at a constant value. This is possibly due to enhanced charge-transport pathways caused by P3HT-crystallisation. The fact that the hole mobility does not fall as PC₆₁BM diffuses through it is consistent with previous reports of the P3HT crystalline domains not being disrupted by the presence of PC₆₁BM.[259] The apparent discrepancy with the data in Figure 6.4(a), where the hole mobility falls as PC₆₁BM diffuses through the P3HT, is attributed to differences in P3HT thickness and hence different crystalline domain sizes.

The electron mobility is not measurable for the first 20 seconds of annealing, after which it rises quickly, before slowly saturating to a constant value. This is

believed to be due to fullerenes diffusing from the PC₆₁BM layer into the P3HT and finally reaching a homogeneous distribution. The time-scale of this process is markedly different than that observed in the study by Treat *et. al.*, where the diffusion process was observed to be complete after just 30s of annealing.[259] It is likely that factors such as the difference in annealing temperature (150°C compared to 130°C here) or possible differences in P3HT molecular weight and regioregularity,[249] may be the cause of this discrepancy. It is also possible that, once percolation has been reached, OFET mobility measurements will reveal changes in concentration that may not be detectable via alternative techniques. The mobility of charge carriers in a field-effect transistor device are known to be exponentially dependent on the hopping distance between states (see equation 2.5 for example). Hence even very small changes in the PC₆₁BM concentration at the semiconductor-dielectric interface are expected to lead to significant changes in the measured field-effect mobility. It should be noted however that such OFET measurements are limited by the onset of percolation, before which the sensitivity of the technique is inadequate for the statements about the fullerene concentration to be made. Despite the observed discrepancy with previous results, the data presented in Figure 6.4(b) suggests that, given this structure and the material parameters employed here, the diffusion of PC₆₁BM in P3HT takes place with a time scale of minutes.

6.4 Modelling the Evolution of Electron Mobility

The time-dependence of electron mobility as exhibited in Figure 6.4(b) should allow a rough estimate of the diffusion coefficient for this process to be made. In this section a simple model based upon Fick's 2nd Law (i.e. the diffusion equation) and percolation theory is derived, relating the electron field-effect mobility to the annealing time and the diffusion coefficient of PC₆₁BM in P3HT. Given the simplicity of the bilayer system, we can consider diffusion in 1 dimension only. It should be noted that the purpose of this section is to extract an approximate value for the diffusivity of PC₆₁BM in P3HT, not provide a rigorous theoretical

description of the diffusion process.

To date little has been said about the physical mechanism by which the diffusion of PC₆₁BM into P3HT takes place in such structures.[259] By gaining a solid understanding of this process, one could be given much greater control over desired OPV structures for potential device applications. With an accurate model describing the process, a calculation of relevant concentration profiles could be carried out and hence the composition profile of such OPVs could in the future be “tailor-made”.

6.4.1 Modelling the Diffusion of Fullerenes

The diffusion equation in one dimension is given by equation 6.1:

$$\frac{\partial C(x, t)}{\partial t} = D \frac{\partial^2 C(x, t)}{\partial x^2} \quad (6.1)$$

Here $C = C(x, t)$ is the concentration of fullerenes a distance x , from the semiconductor-dielectric interface at a time t , after the diffusion process has begun. D is the diffusion coefficient of PC₆₁BM in P3HT at the appropriate temperature.

By considering the structure of the OFET in Figure 6.3, the initial distribution of PC₆₁BM can be expressed as:

$$C(x, 0) = \begin{cases} 0 & \text{for } 0 \leq x \leq x_p \\ C_0 & \text{for } x_p \leq x \leq x_c \end{cases} \quad (6.2)$$

Here we can say C_0 is the 2-dimensional PC₆₁BM concentration in the pristine PC₆₁BM layer, x_p is the distance of the P3HT:PC₆₁BM interface from the dielectric-semiconductor interface (i.e. the P3HT thickness) and x_c is the distance of the top of the PC₆₁BM layer from the dielectric-semiconductor interface (i.e. the P3HT thickness + the PC₆₁BM thickness). It is assumed that all interfaces are perfectly flat.

We assume that both the semiconductor-dielectric and the top PC₆₁BM interfaces allow no material flow across them. This assumption then leads to the

following two boundary conditions:

$$\frac{\partial C(0, t)}{\partial x} = 0 \quad (6.3)$$

$$\frac{\partial C(x_c, t)}{\partial x} = 0 \quad (6.4)$$

Given the initial distribution 6.2, and the boundary conditions 6.3 and 6.4, equation 6.1 can be solved using standard techniques (see Appendix A) to give the two-dimensional PC₆₁BM concentration as a function of time, distance from the semiconductor-dielectric interface, and the diffusion coefficient of PC₆₁BM in P3HT:

$$C(x, t) = C_0 \left(1 - \frac{x_p}{x_c} \right) - C_0 \sum_{n=1}^{\infty} \frac{2}{n\pi} \sin \left(\frac{n\pi x_p}{x_c} \right) \exp \left(-\frac{n^2 \pi^2 D t}{x_c^2} \right) \cos \left(\frac{n\pi x}{x_c} \right) \quad (6.5)$$

This equation has been evaluated and plotted as a function of x for various times in Figure 6.5. As $x \rightarrow \infty$ the concentration becomes homogeneous throughout the device, with a value of C/C_0 equal to $(x_c - x_p)/x_c$, i.e. the thickness of the PC₆₁BM layer divided by the thickness of both layers combined.

Since charge accumulation and transport only take place within the first few nanometers from the semiconductor-dielectric interface, the concentration calculated at $x = 0$ can be assumed to be representative of that measured using our bilayer BGBC OFETs. Setting $x = 0$, we find:

$$C(0, t) = C_0 \left(1 - \frac{x_p}{x_c} \right) - C_0 \sum_{n=1}^{\infty} \frac{2}{n\pi} \sin \left(\frac{n\pi x_p}{x_c} \right) \exp \left(-\frac{n^2 \pi^2 D t}{x_c^2} \right) \quad (6.6)$$

6.4.2 Relating Concentration to Mobility

With a description now in place for the time-dependent fullerene concentration at the semiconductor-dielectric interface, we now seek a relationship between the fullerene concentration and measured electron field-effect mobility. A com-

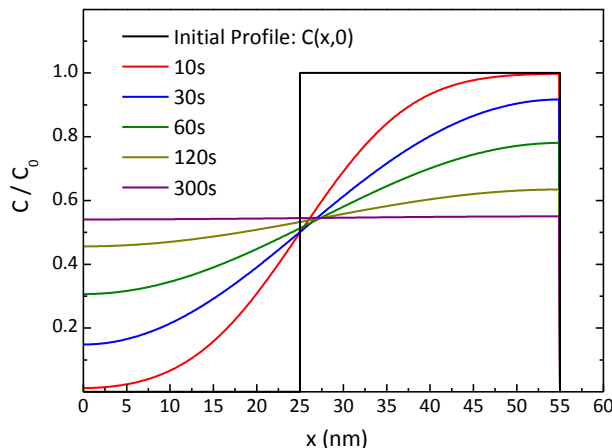


Figure 6.5: Initial 2-dimensional concentration profile (C/C_0) of PC_{61}BM in bi-layer P3HT: PC_{61}BM OFET with P3HT and PC_{61}BM thicknesses of 25nm and 30nm respectively, and PC_{61}BM concentration profile calculated using equation 6.5, evaluated at various times. The parameters used in this calculation were: $x_p = 25$ nm, $x_c = 55$ nm and $D = 5$ nm^2s^{-1} .

mon approach[275] to charge-transport in fullerene-based systems is percolation theory.[79] Here a model is derived in which the effect of fullerene concentration on percolation pathways is considered. The majority of the work within Sections 6.4.2 and 6.4.3 was carried out by a collaborator from the Department of Mathematics at The University of Oxford; James Kirkpatrick.

We assume that a 2-dimensional plane is randomly filled with fullerenes, with each site having an occupation probability $c = C/C_0$. In this situation each fullerene is connected to every other fullerene by a resistor. The conductance of the resistor between site i and site j is given by:

$$\sigma_{ij} = \sigma_0 e^{R_{ij}\alpha^{-1}} \quad (6.7)$$

Here σ_0 is a constant, α is the wavefunction overlap parameter and R_{ij} is the distance between sites i and j . The random-resistor problem is normally treated in terms of bond percolation with each resistor of unit conductance. As was described in Section 2.2.4, the percolation of bonds can be quantified by the parameter p , which is the ratio of the number of bonds in a percolating

(“infinite”) cluster to the total number of bonds. There exists a critical value of this bond percolation occupation p_c , referred to as the percolation threshold. Computational studies have shown[79] that the conductivity of a system follows a power law dependence:

$$\sigma \sim (p - p_c)^s \tag{6.8}$$

The critical exponent has been calculated to be $s \simeq 1.43$ for a 2-dimensional system.[276] For the purposes of our study we wish to work with a *site occupation probability* c , not the bond occupation probability p . To make this conversion consider a lattice of size $N \times N$. For a concentration c the expectation value for the number of sites will hence be cN^2 . If we define each site to be connected to z neighbours, the total number of nearest neighbours (bonds) will be $c^2N^2z/2$ (the division by 2 ensures no double-counting). The total number of bonds is $N^2z/2$, hence the bond occupation probability is:

$$p = c^2 \tag{6.9}$$

If only nearest neighbours were connected, we would expect that when $c^2 < p_c$ the conductivity would be zero. For a two-dimensional lattice, the bond percolation threshold has been proven to be $1/2$.[277] We would therefore expect that at concentrations below $\sqrt{0.5} \simeq 0.7$ the conduction would drop to 0. By inspecting Figure 6.4(b) and considering the thickness of the two components however, it is evident that concentrations below 0.7 do still give rise to conduction (assuming a homogeneous distribution at $t = 30$ m). Hence we must also consider the conduction between next nearest neighbours.

If we also considered next-nearest neighbours then we can then replace 2×2 lattice points with one “super” lattice point. The new super lattice points are considered occupied if any one of the four original points were occupied. This is illustrated in Figure 6.6. Increasing the size of the lattice constant will vastly increase the connectivity of a system. By increasing the lattice constant we can increase the percentage of bonds that are occupied and therefore reach percolation. Of course by increasing the lattice constant, the conductivity of each bond will decrease. A reasonable model for conduction could be obtained by averaging

the conductivities of lattices of increasing large lattice constant. As the lattice grows the bond occupation probability p will increase, but the conductivity of each bond will decrease. We will therefore compute the increase in lattice constant $a(p, c)$ necessary to result in a bond occupation probability p given that the site occupation is c .

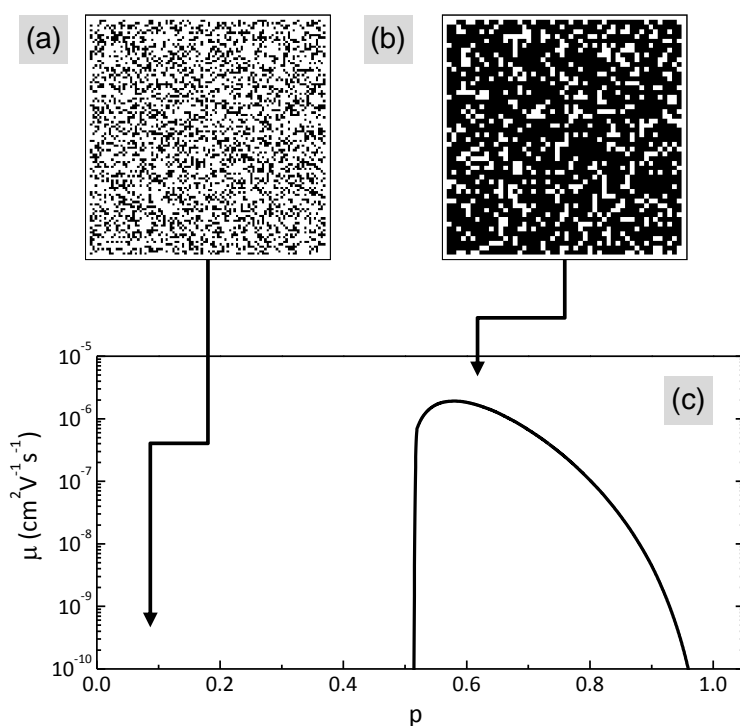


Figure 6.6: (a) 100×100 random lattice with $c = 0.3$ and $a = 1$. This corresponds to a bond occupation probability of $p = 0.09$ and hence a mobility of zero. (b) The same lattice rescaled with $a = 2$. The lattice is now much better connected, and the mobility is non-zero. Note the conductance is severely limited by the increase in lattice constant. (c) Graphic illustrating how the electron field-effect mobility is computed for $\alpha = 0.1 \text{ nm}^{-1}$, $\mu_{0e} = 1 \text{ cm}^2 \text{V}^{-1} \text{s}^{-1}$ and $c = 0.3$ using equation 6.14. The x axis shows the desired bond occupation probability p . As p is increased, the lattice constant necessary to obtain that particular p is also increased.

If the the lattice constant is increased by a , then the probability of lattice sites being occupied rises to $1 - (1 - c)^{a^2}$. Given equation 6.9, the corresponding

bond occupation probability will hence be:

$$p = \left(1 - (1 - c)^{a^2}\right)^2 \quad (6.10)$$

Inverting equation 6.10 gives:

$$a(p, c) = \sqrt{\frac{\ln(1 - \sqrt{p})}{\ln(1 - c)}} \text{ if } p, c < 1 \quad (6.11)$$

Notice that there is one trivial case for this equation: if the site occupation probability is 1, the bond occupation probability must be 1 at a lattice constant of 1. By substituting $R_{ij} = a(p, c)$ into equation 6.7, an equation can be derived for the conductivity of a system as a function of concentration and bond occupation probability:

$$\sigma(c, p) = \sigma_0 (p - p_c)^{1.43} \exp\left[-\frac{a(p, c) - 1}{\alpha}\right] \text{ if } p, c < 1 \quad (6.12)$$

Taking the maximum with respect to p gives:

$$\sigma(c) = \sigma_0 \max\left[(p - p_c)^{1.43} \exp\left(-\frac{a(p, c) - 1}{\alpha}\right)\right] \text{ if } p > p_c, p > c^2 \quad (6.13)$$

Notice the two conditions that the bond occupation must satisfy: it must be greater than the percolation threshold and it must be greater than c^2 , to ensure that the lattice constant is always greater than one. A maximum of conductance will be obtained when $c = 1$, in this case the conductance becomes $(1/2)^{1.43}$. With this in mind and remembering that conductance and mobility are directly proportional, we model mobility as:

$$\mu_e(c) = \mu_{0e} 2^{1.43} \max\left[(p - p_c)^{1.43} \exp\left(-\frac{a(p, c) - 1}{\alpha}\right)\right] \text{ if } p > p_c, p > c^2 \quad (6.14)$$

Here μ_{0e} is the mobility of electrons in a pristine film (i.e. with $c = 1$). This equation is plotted as a function of p in Figure 6.6(c) for the following parameters: $\alpha = 0.1 \text{ nm}^{-1}$, $\mu_{0e} = 1 \text{ cm}^2\text{V}^{-1}\text{s}^{-1}$ and $c = 0.3$. Equation 6.14 infact takes the maximum from this plot for a certain value of c .

This model assumes that the conductance between two molecules depends only on the distance between them and not, for example, on energetic disorder. This assumption can be made using similar arguments to those made in Section 5.3; i.e. because the purpose of this study is to understand how the electron mobility varies with 2-dimensional fullerene concentration, not on other effects such as that of the gate field.[70] Furthermore we assume that the bond percolation threshold is the same as for a square lattice, whereas the fullerene molecule's position is free to occupy any point in space. Note however that the universal exponents will not be changed by changes in the lattice shape.[276] A more significant assumption is that the position of fullerene molecules is random. This implies that there are no correlations in the position of the molecules, i.e. that there is no aggregation. Intuitively, we expect that aggregation would greatly increase the percolation threshold and - for a given concentration - diminish the effective mobility. This was illustrated in Section 5.3.

6.4.3 Applying the Model to Experimental Data

As is evident from Figure 6.4(b), at long times (e.g. > 15 minutes) the PC_{61}BM in the P3HT: PC_{61}BM bilayers diffuses to an even distribution equal to the average concentration as $t \rightarrow \infty$. Combined with similar data for a bilayer device with a P3HT thickness of 8 nm (data not shown), this allows us to extract the ratio of the mobility at two concentrations, which is independent of μ_{0e} . The value of α that we obtain is 0.11. If we assume that the lattice constant is 1 nm (due to the approximate size of PC_{61}BM molecules), this corresponds to a distance of 1.1 Å. If furthermore we assume that the conductance is proportional to the square of a tunnelling matrix element, this would suggest the decay length for the matrix element is approximately 0.5 Å. It is now possible to fit μ_{0e} as $5.2 \times 10^{-3} \text{ cm}^2\text{V}^{-1}\text{s}^{-1}$, which agrees well with previous experimental measurements of pristine PC_{61}BM OFETs using a similar BCBG architecture (see Figure 5.3(a))

or reference [110] for example).

Knowing the relationship between concentration and mobility, we can convert the experimentally measured time-dependent electron mobility into a relationship between time and concentration at the bottom of the film, allowing direct comparison with equation 6.6. The only free parameter is now the diffusivity D , which we fit to the data for the 25 nm polymer film and find to be $5 \text{ nm}^2\text{s}^{-1}$, this is shown in Figure 6.7.

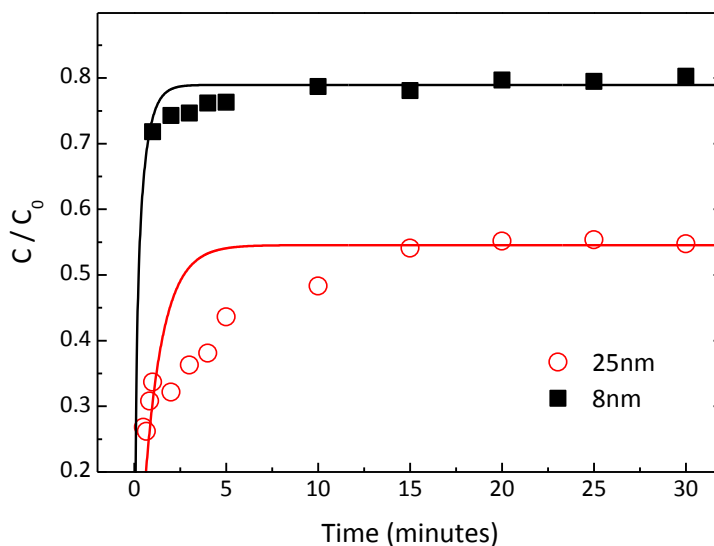


Figure 6.7: Points: average PC_{61}BM concentration at semiconductor-dielectric interface calculated using equation 6.14. The values μ_e used in equation 6.14 are the electron saturation-regime field-effect mobility of electrons measured using two sets of bi-layer P3HT: PC_{61}BM transistors measured under ambient-pressure N_2 after being annealed at 130°C , with different P3HT layer thicknesses. The PC_{61}BM thickness was 31 nm in both sets of devices. The curves represent a best-fit to the experimental data using equation 6.6. The extracted diffusion coefficient in this case was found to be: $D = 5 \text{ nm}^2\text{s}^{-1}$.

This value of diffusivity seems reasonable given the length and time scales involved, but is significantly lower than the value of $D = 3 \times 10^{-10} \text{ cm}^2\text{s}^{-1}$ reported in the study by Treat *et. al.*[259] As mentioned in Section 6.3.1, it is believed that this difference can be explained by either differences in the material systems and/or annealing temperature, or possibly the extremely strong dependence of

FET mobility measurements on fullerene concentration once percolation has been reached. Whilst there are no observable changes in concentration profile after annealing at 150°C for more than 30 seconds via DSIMS, it is expected the extreme relationship between mobility and concentration in equation 6.14 will result in further time-dependent information being revealed at times beyond that resolvable with DSIMS. Discrepancies between our evaluated value of D and that previously reported for the P3HT-crystallisation / PC₆₁BM-clustering process[272] can be ignored because it is a process distinct from that being studied here.

The diffusion coefficient computed for the thicker polymer film describes the thinner one reasonably well (see Figure 6.7), however the experimental concentration is observed to rise more quickly initially than the model suggests, and then saturate more slowly. The description of the relationship between mobility and concentration is based on the assumption that fullerenes are placed at random. This is equivalent to assuming that fullerenes do not interact with each other and aggregate. However this is unlikely to be true; PC₆₁BM aggregation has previously been observed in P3HT:PC₆₁BM blends with annealing temperatures as low as 130°C.[234] This is likely to result in the concentration being underestimated for low values of t . Additionally, the fact that the miscibility of PC₆₁BM is known to be temperature-dependent[259] suggests that less PC₆₁BM molecules could be diffusing in the P3HT than assumed by the model here. None-the-less, it is felt that this model serves as a good first attempt to quantify the diffusion process in this system and that the extracted value of diffusivity could serve to help future understanding and optimisation of polymer:fullerene systems for OPV applications.

6.5 Bilayer P3HT:PC₇₁BM OFETs

In Section 5.4 the effect of changing the fullerene component in P3HT:PC₆₁BM blends to PC₇₁BM was studied. It was observed that, keeping all other variables constant, a higher prerequisite annealing temperature and/or time was required to induce a similar degree of phase-segregation in the two systems. It was suggested that the increased volume of PC₇₁BM is expected to give rise to a larger frictional drag when in P3HT, and hence result in a larger activation temperature for

diffusion. As was mentioned in Section 5.4, understanding the differences in morphological properties caused by changing the molecular weight of the fullerene is important because most high-performance OPV are now employing PC₇₁BM as opposed to PC₆₁BM as the acceptor molecule.[164–166]

With an understanding of how the diffusion of PC₆₁BM in P3HT takes place in bilayer OFET now obtained, the differences between PC₇₁BM and PC₆₁BM can be investigated more directly. Although the vertical diffusion of PC₇₁BM in P3HT within a bilayer structure is clearly not the same process as the clustering of PC₇₁BM in P3HT:PC₇₁BM blends, both are likely to be dependent upon the molecular mobility of the fullerene in the polymer and are hence expected to be strongly related.

Unipolar OFETs were fabricated from spin-cast and vacuum-deposited PC₇₁BM, using a BCBG architecture with gold source and drain electrodes (see Figure 6.8(a)). The n-type transfer characteristics of example spin-cast and vacuum-deposited devices are shown in Figures 6.8(b) and 6.8(c) respectively. The characteristic ambipolarity[217] of these devices is observed for both deposition techniques. The electron field-effect mobility of 5 spin-cast and 5 vacuum-deposited OFETs were measured in the saturation-regime. The average and standard deviation mobilities were determined to be $4 \pm 2 \times 10^{-3} \text{ cm}^2\text{V}^{-1}\text{s}^{-1}$ and $2.0 \pm 0.2 \times 10^{-3} \text{ cm}^2\text{V}^{-1}\text{s}^{-1}$ for spin-cast and vacuum-deposited PC₇₁BM respectively. These values are comparable to each other and to previous reported values using a similar architecture.[217]

Bilayer P3HT:PC₇₁BM OFETs were fabricated in a BCBG architecture. P3HT was spin-cast onto the OFET substrates before PC₇₁BM was deposited on top of the P3HT via vacuum sublimation. The bilayer device architecture is identical to that shown in Figure 6.3(a) but with PC₆₁BM replaced with PC₇₁BM. Transfer and output characteristics of such unannealed bilayer P3HT:PC₇₁BM OFET were found to give rise to p-type only behaviour (data not shown). Upon annealing it is hoped that, like PC₆₁BM, the PC₇₁BM will diffuse from the top layer, through the P3HT and reach the semiconductor-dielectric interface. The formation of a percolating fullerene pathway at the interface should then be detectable as a measurable electron field-effect mobility.

Five bilayer P3HT:PC₇₁BM bilayer OFETs were annealed at temperatures

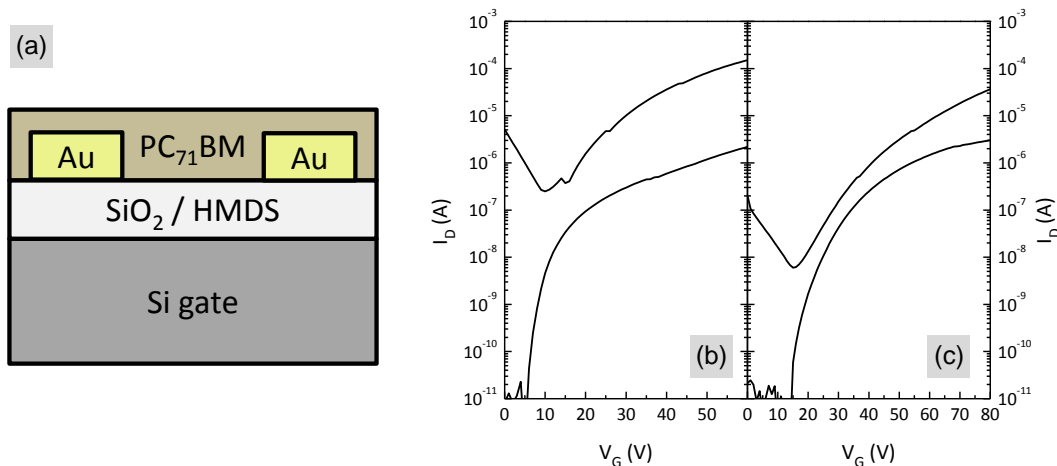


Figure 6.8: (a) Schematic diagram of bottom-gate, bottom-contact (BGBC) PC₇₁BM OFET structure. Transfer characteristics of (b) spin-cast PC₇₁BM and (c) vacuum-deposited PC₇₁BM BGBC OFETs fabricated on HMDS-treated SiO₂ with gold source and drain electrodes. These devices were measured under ambient-pressure N₂ without being annealed. In both cases the OFETs had channel lengths and widths of 10 μ m and 20 nm respectively.

between 60°C and 300°C and measured at room temperature after each annealing step. As before, each annealing step lasted for 30 minutes and the annealing was cumulative. The thickness of the P3HT and PC₇₁BM layers were both 25 nm. The average saturation-regime field-effect mobility is plotted as a function of annealing temperature in Figure 6.9(a). Figure 6.9(b) shows electron field-effect mobility data for similar BCBG P3HT:PC₆₁BM bilayer OFETs (from Figure 6.4(a)) combined with the electron mobility from the P3HT:PC₇₁BM bilayer OFETs. It should be noted however that the thickness of the P3HT and PC₆₁BM layers were in this case 8nm and 40nm respectively.

The electron mobility for the P3HT:PC₇₁BM bilayers remains undetectable until after annealing at 160°C, after which it rises to 10^{-5} cm²V⁻¹s⁻¹. This is attributed to the diffusion of PC₇₁BM through the P3HT and the formation of percolation-pathways at the semiconductor-dielectric interface. Upon annealing at 180°C the electron mobility begins to fall significantly. This is attributed to the large-scale aggregation of PC₇₁BM, as described in Section 5.4. As the melting temperature[268] of the system is approached, the electron mobility rises. This

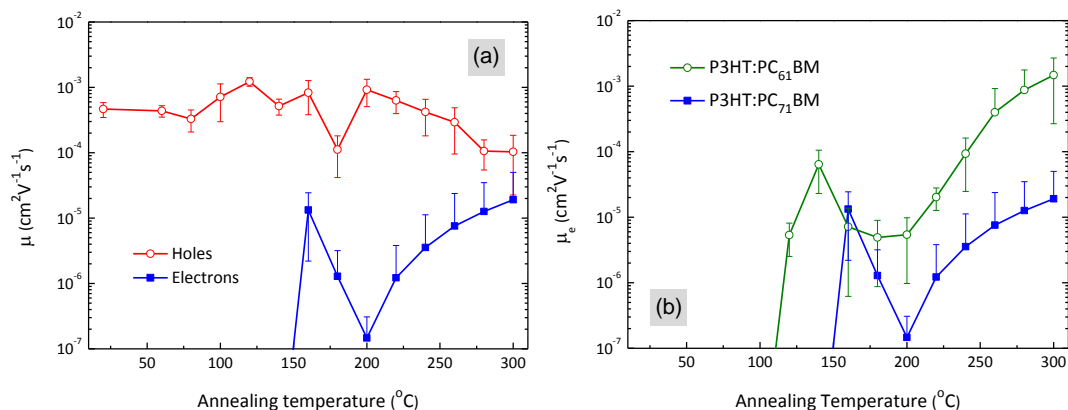


Figure 6.9: (a) Average saturation-regime field-effect mobility of holes and electrons in 5 bi-layer P3HT:PC₇₁BM OFETs measured at room temperature under ambient-pressure N₂ after being annealed at various temperatures for 30 minutes. The error bars represent the standard deviation in the measured field-effect mobility. When the electron mobility was not detectable it was plotted as 10^{-9} $\text{cm}^2\text{V}^{-1}\text{s}^{-1}$. The thicknesses of the P3HT and PC₇₁BM layers were both 25nm. (b) Electron field-effect mobility from (a) plotted with similar electron field-effect mobilities from similar P3HT:PC₆₁BM OFETs measured under identical conditions, taken from Figure 6.4(a). Note that the layer thicknesses were different for the two different sets of measurements: The thicknesses of the P3HT and PCBM layers were 25nm and 25nm respectively in the P3HT:PC₇₁BM OFETs and 8nm and 40nm respectively in the P3HT:PC₆₁BM OFETs.

is again attributed to the redistribution of fullerenes in the film and quenching into an amorphous state upon cooling to room temperature.

The hole mobility stays approximately constant until an annealing temperature of 180°C is reached. At 180°C the hole mobility falls by approximately an order of magnitude, only to recover upon annealing at 200°C . This is rather difficult to explain given the data in Figure 6.4 for example. A possible explanation is that the P3HT is significantly disrupted by the presence of diffused PC₇₁BM, however why this would occur at 180°C and not 160°C is unclear. After annealing to 220°C and above the hole mobility falls, in-keeping with our description of the results of melting the blend (see section 5.4 for example).

On comparison with the electron mobility data from the P3HT:PC₆₁BM bi-layer system, it is noticeable that the electron mobility evolution for the P3HT:PC₇₁BM bilayer is strikingly similar. The difference in the magnitude of the electron mo-

bility is likely to be due to the different PCBM concentrations, which is in turn due to the different thicknesses of the constituent layers. The onset temperatures of the respective fullerene- diffusion and clustering processes are observed to be higher for the P3HT:PC₇₁BM system. This is consistent with the data from Section 5.4, suggesting that the required temperature and/or time for PCBM-aggregation are higher in P3HT:PC₇₁BM blends than P3HT:PC₆₁BM blends. Hence given the data presented here, one can conclude that the activation temperature for diffusion in P3HT is higher for PC₇₁BM than it is for PC₆₁BM.

6.5.1 Time-Dependent Measurements

The time-dependence of this process was then investigated by measuring the field-effect mobility of bilayer OFETs as a function of annealing time. Figure 6.10(a) shows the average saturation-regime hole and electron mobility of 5 bilayer P3HT:PC₇₁BM OFETs (thickness of each layer: 25nm), plotted as a function of annealing time. The annealing temperature was 160°C and the devices were measured at room temperature.

As in Section 6.4.3, equation 6.14 was used to convert the average electron field-effect mobility to 2-dimensional concentration at the semiconductor-dielectric interface. These concentrations were then fitted to equation 6.6, for $x_p = 25$ nm, $x_c = 50$ nm. This data is shown in Figure 6.10(b). The parameters extracted from the fit were $\mu_{0e} = 7.5 \times 10^{-2} \text{ cm}^2\text{V}^{-1}\text{s}^{-1}$ and $D = 1.1 \text{ nm}^2\text{s}^{-1}$.

It is immediately obvious that the fit to the data in Figure 6.10 is much closer than that of Figure 6.7. Exact reasons for this are unclear, however the previous observation[259] of a temperature-dependent miscibility may be partially responsible. This may similarly be able to help explain why the extracted value of μ_{0e} is much higher for PC₇₁BM than PC₆₁BM.

Despite the annealing temperature being 30°C higher, the diffusion coefficient observed here is slightly lower than than measured for PC₆₁BM in similar bilayer structures ($D = 5 \text{ nm}^2\text{s}^{-1}$) in Section 6.4.3. The higher prerequisite annealing temperature is attributed to a higher activation temperature for PC₇₁BM diffusion in P3HT with respect to PC₆₁BM, as described above. This higher prerequisite temperature could have a significant impact on future device processing

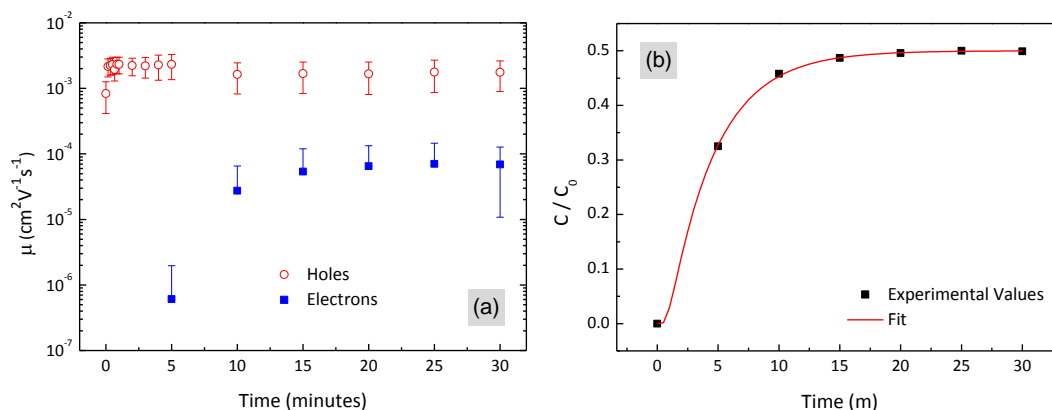


Figure 6.10: (a) Average saturation-regime field-effect mobility of holes and electrons in 5 bi-layer P3HT:PC₇₁BM OFETs measured under ambient-pressure N₂ after being annealed at 160°C, plotted as a function of time. The thicknesses of the P3HT and PC₇₁BM layers were both 25nm. (b) PC₇₁BM concentration calculated using equation 6.14 and average saturation-regime field-effect mobility of electrons measured from set of bilayer P3HT:PC₇₁BM OFETs as function of time, shown in (a). The curve represents a best-fit to the experimental data using equation 6.6. The extracted diffusion coefficient in this case was found to be: $D = 1 \text{ nm}^2 \text{ s}^{-1}$.

and optimisation procedures for OPVs. It is also worthy of note that a higher activation-temperature for diffusion would be expected to lead to a better *structural* stability, were phase-segregated polymer:fullerene structures to be kept at elevated temperatures for a significant period of time.

6.5.2 Atomic Force Microscope Images

In an attempt to gain a better understanding of the nature of the PC₇₁BM-diffusion process, atomic-force microscopy (AFM) has here been utilized to characterize the relevant surfaces before and after annealing. Figure 6.11 shows $10 \mu\text{m} \times 10 \mu\text{m}$ tapping-mode AFM topography images of P3HT, PC₇₁BM and P3HT:PC₇₁BM bilayers before and after annealing. The films were deposited onto HMDS-treated SiO₂ in order for a comparison with the corresponding OFETs to be as relevant as possible. The P3HT and PC₇₁BM layer thicknesses were both 25 nm. The annealing was carried out at 160°C for 30 minutes in each case.

It appears that on this length scale there is very little difference between

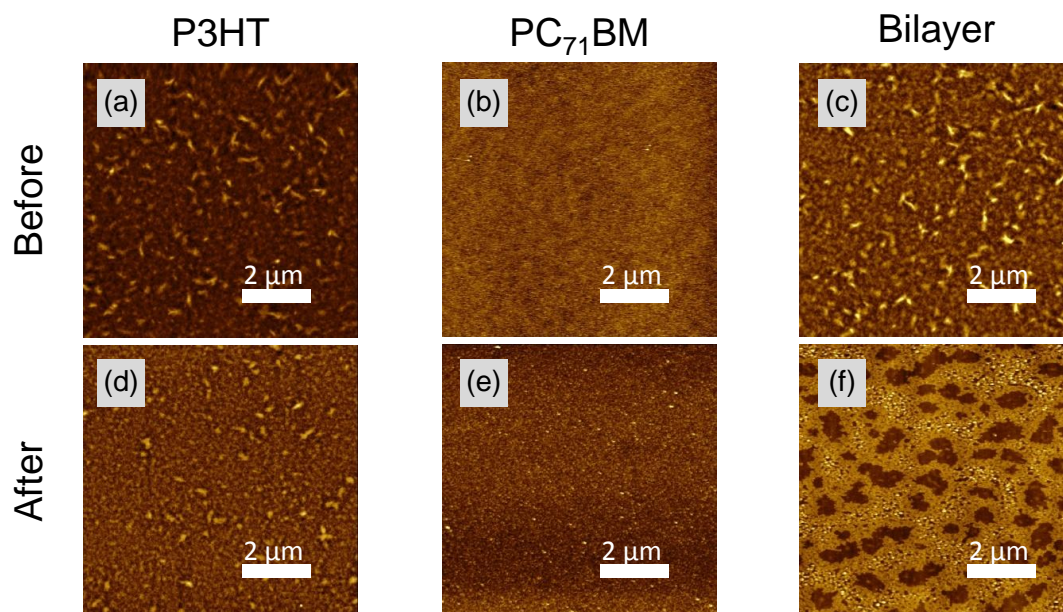


Figure 6.11: Atomic force microscope topography images of P3HT, PC₇₁BM and P3HT:PC₇₁BM bilayers before and after annealing at 160°C for 30 minutes. The thickness of the P3HT and PC₇₁BM layers were both 25nm and the films were deposited onto HMDS-treated SiO₂. The measured peak-to-peak height for the 6 measurements were as follows: (a) 41 nm, (b) 5.1 nm, (c) 42nm, (d) 40nm, (e) 8.5 nm and (f) 100nm.

the topography of unannealed and annealed P3HT (Figures 6.11(a) and 6.11(d) respectively). The large elements are perhaps small-scale crystalline regions that formed upon deposition. P3HT is well-known[268, 274] to undergo recrystallization at temperatures around 140°C, but this appears to have made no significant observable impact on the AFM images at the resolution employed here. The as-deposited PC₇₁BM film was measured to have a route-mean-squared surface roughness of 0.2 nm (Figure 6.11(b)). This is similar to that measured for vacuum-deposited PC₆₁BM; 0.3 nm (see Figure 6.2). Upon annealing there is again little change in surface topography for the PC₇₁BM film (Figure 6.11(e)). It can perhaps be argued that some small crystalline grains do start to appear, but it is difficult to say so with any certainty. Pristine PC₆₁BM films are known to crystallise at temperatures similar to those of P3HT.[274]

The unannealed P3HT:PC₇₁BM bilayer is observed to have a very similar surface topography to that of pristine P3HT (see Figures 6.11(c) and 6.11(a)). Given the low surface roughness of the pristine PC₇₁BM film, it seems likely that the PC₇₁BM has here “templated” the underlying P3HT surface. This is similar to the previous observation of C₆₀ templating the underlying pentacene layer in pentacene:C₆₀ OPV structures.[278] After annealing, the bilayer surface changes significantly (Figure 6.11(f)). It appears that there are several depressed regions in an otherwise homogeneous top-layer. This suggests that, contrary to as previously believed, the diffusion of PCBM into P3HT does not take place homogeneously across the device area, but in several isolated regions. This could partially explain why a simple 1-dimensional Fickian diffusion model was not found to accurately describe the diffusion of PC₆₁BM in P3HT (see Section 6.4.3), although it should be noted that the fit shown in Figure 6.10 is none-the-less rather good. Previous AFM measurements of P3HT:PC₆₁BM bilayers have revealed a change in surface morphology, but in this case it was attributed to a change in crystallinity, not PC₆₁BM diffusion.[255]

6.6 Conclusions

In this chapter I have studied the diffusion of fullerenes in polymers using bilayer organic field-effect transistors (OFETs). By using a bottom-gate, bottom-contact (BGBC) architecture and a P3HT:PC₆₁BM structure, these devices are observed to be initially p-type only. This is because the injecting source and drain electrodes are initially in direct contact with the (bottom) P3HT layer only. Gold source and drain electrodes allow the injection and transport of holes in the P3HT and electrons in the PC₆₁BM respectively. Hence any diffusion of PC₆₁BM from the top layer, through the P3HT, should be detectable as a measurable electron mobility, via the formation of a percolating PC₆₁BM pathway at the semiconductor-dielectric interface.

By annealing these bilayer devices, the diffusion properties of PC₆₁BM in P3HT were studied. After annealing at a temperature of 100°C, an electron mobility could be measured, suggesting that a significant quantity of PC₆₁BM had diffused through the P3HT to the semiconductor-dielectric interface. By

measuring the evolution of the electron mobility as a function of annealing time, an insight into the time-dependence of this process is gained. Using a combination of Fick's 2nd Law (the diffusion equation) and percolation theory, the time-dependence of the process could be modelled and a diffusion coefficient could be extracted.

Finally, by fabricating bilayer P3HT:PC₇₁BM OFETs, differences in the diffusion properties of PC₆₁BM and PC₇₁BM were probed. It was found that a higher annealing temperature was required to observe this phenomenon in P3HT:PC₇₁BM systems when compared to P3HT:PC₆₁BM systems. This was attributed to a higher activation temperature for diffusion for the larger fullerene because of its expected greater frictional drag when in P3HT. This description is consistent with the work presented in Chapter 5, wherein it was observed that a higher temperature was required to induce polymer:fullerene phase segregation for P3HT:PC₇₁BM blends when compared to P3HT:PC₆₁BM.

Chapter 7

Conclusions

The work within this thesis describes some advances in the performance and understanding of photo-active organic semiconductor systems and devices. Specifically I have looked at organic phototransistors and the morphology and diffusion properties of polymer:fullerene blends. Here I briefly review the conclusions drawn in each chapter and indicate possible future directions for research in this field.

The first experimental results chapter (Chapter 4) focusses on the development and understanding of organic phototransistors (OPTs). After studying how single-layer pentacene- and C₆₀-based OFETs respond to light, attempts were made to fabricate bilayer pentacene:C₆₀ bilayer ambipolar OFETs. Unfortunately such devices were found to be unipolar, with only the bottom layer being able to transport charges. This was attributed to a high surface-roughness of the bottom semiconductor layer, hindering transport in the upper layer. Bilayer OFETs formed of pentacene and [6,6]-phenyl-C₆₁-butyric acid methyl ester (PC₆₁BM) OFETs, where the PC₆₁BM was deposited via spin-coating, were however found to show ambipolar behaviour. The reason why pentacene:C₆₀ OFETs were unipolar whilst pentacene:PC₆₁BM OFETs were ambipolar is not entirely clear. It could be due to an interdiffusion of PC₆₁BM into the lower pentacene layer or a smoothing of the underlying layer via partial dissolution.

These ambipolar OFETs were found to respond to light and could hence be used as OPTs. The maximum responsivity was found to be around 150 mA W⁻¹ and the time constants associated with the response to light were found to be between 3 and 4 ms. These structures were found to be compatible with self-

assembled monolayer (SAM) gate dielectrics, allowing the OPTs to be operated at voltages below 2.5 V. By combining two of these phototransistors, low-voltage photo-inverters were demonstrated. By biasing these devices at constant input and supply voltages it was shown that the output voltage could be modulated over a significant range by a relatively small incident optical power density.

Photo-inverters were also studied based upon blends of PC₆₁BM and the polymer poly[2-methoxy-5-(3',7'-dimethyloctyloxy-p-phenylene vinylene)] (MDMO-PPV). These devices showed similar characteristics to the photo-inverters based upon the pentacene:PC₆₁BM system, but operated at higher voltages. Using a model based upon variable-range hopping and by treating the inverters as potential dividers, the expected characteristics of these devices were simulated under various changes in parameters. These results suggest that the characteristics observed by changing the intensity of optical illumination incident on such photo-inverters is as expected were the threshold of these devices to change.

The fifth chapter is concerned with studying the relationship between the morphology of polymer:fullerene blends and the measured mobility of charge carriers in corresponding OFETs. By annealing blends of poly(3-hexylthiophene) (P3HT) and PC₆₁BM a phase-segregation process was observed using polarised optical microscopy. This process, whereby the P3HT becomes more crystalline and the PC₆₁BM forms large-scale clusters, is believed to give rise to a significant improvement in the power-conversion efficiency of P3HT:PC₆₁BM organic photovoltaic solar cells (OPVs). By measuring the evolution of the mobility in equivalent OFETs under similar annealing conditions, changes in measured field-effect mobility can be correlated with changes in the morphology of the two components.

A significant fall in electron field-effect mobility is observed upon annealing at temperatures similar to those at which phase-segregation is visibly observed in the same system (~ 140 °C). This is attributed to a reduction in percolation pathways in the quasi 2-dimensional OFET channel. A simple percolation-theory-based simulation was carried out to confirm that this behaviour was as expected. Dual-gate P3HT:PC₆₁BM OFETs were also employed to study the mobility evolution at two parts of the film simultaneously; once again a significant reduction in electron mobility was observed at both interfaces upon annealing at approxi-

mately 140 °C. By carrying out these measurements in-situ, information was also be revealed about the time-scale of this process.

With an understanding of how P3HT:PC₆₁BM phase-segregation is expected to affect the mobility of holes and electrons in OFETs, the molecular weight of the fullerene component was changed. By replacing PC₆₁BM with PC₇₁BM it was observed that a higher prerequisite annealing temperature and/or time was required to induce a similar degree of phase segregation to that observed in the equivalent P3HT:PC₆₁BM blend. This was attributed to the expected higher drag-coefficient of PC₇₁BM in P3HT, and hence higher activation temperature for diffusion.

In Chapter 6 the use of OFETs to probe the properties of polymer:fullerene systems was extended to bilayer systems. By using a P3HT:PC₆₁BM bilayer with gold source and drain electrodes and a bottom-gate, bottom-contact architecture, OFETs were fabricated that were initially unipolar (p-type) only. By then annealing these OFETs and monitoring the mobility of electrons, information could be inferred about the concentration of PC₆₁BM molecules at the semiconductor-dielectric interface. Hence by annealing such bilayer OFETs, information about the temperature- and time-dependence of PC₆₁BM diffusion in P3HT could be inferred. It was identified that when annealing P3HT:PC₆₁BM bilayer OFETs with thicknesses of 25nm and 31nm respectively at 130 °C, the PC₆₁BM will diffuse to an equilibrium state after approximately 15 minutes.

By using a simple model based upon the 1-dimensional diffusion equation, combined with an implementation of percolation theory, the time-dependence of this process could be roughly quantified. By making a number of assumptions, the diffusion coefficient of PC₆₁BM in P3HT was approximated to be 5 nm²s⁻¹ at 130°C. Upon replacing PC₆₁BM with PC₇₁BM a higher temperature was required to observe a similar rise in electron field-effect mobility. These results are consistent with the hypothesis put forward in Chapter 5 that the activation temperature for diffusion is higher for PC₇₁BM in P3HT when compared to PC₆₁BM.

The results presented in this thesis are hoped to (a) improve the understanding and performance of organic phototransistor-based devices and (b) illustrate how OFETs can be used to study the morphological properties of polymer:fullerene blends. Whilst the operation of organic phototransistors is at times convoluted,

it is hoped that with further development their performance can be improved to the point where they can be considered to rival organic photodiodes as the technology of choice for large-area, flexible image sensors. For this to happen it is of the utmost importance that the operating mechanisms of OPTs are fully understood and optimizable. At present it appears that most reported OPT have vastly different sets of performance parameters. Whilst we are able to hypothesise possible explanations for this on a case-by-case basis, a rigid description is not yet in place, and it is this that is likely to be one of the most difficult hurdles to overcome with regards to OPTs.

Reports of OFETs being used to probe the morphology of polymer:fullerene blends have to date been surprisingly scarce. The techniques presented within this thesis are hence hoped to be noteworthy because of both their novelty and the potentially unique information they reveal. Despite the fact that these measurements are probing the morphology indirectly (certain assumptions about how morphology is expected to modify charge transport are made), they have some very attractive characteristics. Being able to monitor the two semiconductor systems independently of each other for example is quite difficult to do via any other technique. Similarly being able to probe the bottom interface of a film in isolation has previously been quite challenging. It is felt that such a technique could prove useful in the processing and optimisation procedure for OPVs.

Whilst the thermally-activated diffusion of fullerenes in polymers has only begun to be studied in any great detail fairly recently, it is a subject that is highly relevant to the stability and reliability of polymer:fullerene systems. By developing a very basic quantitative model of this process (and its effect on the field-effect mobility of electrons in OFETs) the first step has been taken to get to grips with this process. By gaining a fuller understanding this process, certain statements about the structural stability of phase-segregated systems could be made for example. Additionally, by fabricating polymer:fullerene bilayers then annealing them one could perhaps imagine being able to make OPVs with “tailor-made” concentration profiles.

Appendix A

Solution to Diffusion Equation

The diffusion equation in one-dimension is given by equation 6.1:

$$\frac{\partial C(x, t)}{\partial t} = D \frac{\partial^2 C(x, t)}{\partial x^2} \quad (\text{A.1})$$

Here $C = C(x, t)$ is the concentration of fullerenes a distance x , from the semiconductor-dielectric interface at a time t , after the diffusion process has begun. D is the diffusion coefficient of PC₆₁BM in P3HT at the appropriate temperature.

The solution to equation A.1 can then be carried out using well-established techniques.[279] We start by using the separation of variables approach:

$$C(x, t) \equiv X(x)T(t) \quad (\text{A.2})$$

Substituting this into equation A.1 we find:

$$\frac{1}{DT(t)} \frac{\partial T(t)}{\partial t} = \frac{1}{X(x)} \frac{\partial^2 X(x)}{\partial x^2} \quad (\text{A.3})$$

If this is true for all x and t we can set each side of equation A.1 equal to a

constant and hence get 2 ordinary differential equations (ODEs):

$$\frac{\partial T(t)}{\partial t} = -\lambda^2 DT(t) \tag{A.4}$$

$$\frac{\partial^2 X(x)}{\partial x^2} = -\lambda^2 X(x) \tag{A.5}$$

We start with equation A.5. To solve this ODE we must consider three possible ranges for λ ; $\lambda < 0$, $\lambda = 0$ and $\lambda > 0$, and use the range which gives the expected behaviour. First, if $\lambda < 0$ then the solution is of the form:

$$X(x) = \phi e^{-\lambda x} + \psi e^{\lambda x} \tag{A.6}$$

Consider the following boundary condition (equation 6.3):

$$\frac{\partial C(0, t)}{\partial x} = 0 \tag{A.7}$$

This leads to:

$$\phi = -\psi \tag{A.8}$$

Hence equation A.6 can be written as:

$$X(x) = \psi(e^{\lambda x} - e^{-\lambda x}) \tag{A.9}$$

The second boundary condition (equation 6.4) is:

$$\frac{\partial C(x_c, t)}{\partial x} = 0 \tag{A.10}$$

We can therefore say:

$$\lambda\psi(e^{\lambda x_c} + e^{-\lambda x_c}) = 0 \quad (\text{A.11})$$

Hence: $\phi = \psi = 0$. Suggesting $\lambda \neq 0$.

Next consider $\lambda = 0$. This would give the solution:

$$X(x) = \phi x + \psi \quad (\text{A.12})$$

If this were the case, then:

$$\frac{\partial X(x)}{\partial x} = \phi \quad (\text{A.13})$$

From equation A.7 we see that this would give rise to constant concentration with position, which is unphysical for our system. Therefore $\lambda \neq 0$. Finally, we consider $\lambda > 0$. Under these circumstances the solutions to equations A.4 and A.5 are given by equations A.14 and A.15:

$$X(x) = \phi \sin(\lambda x) + \psi \cos(\lambda x) \quad (\text{A.14})$$

$$T(t) = \beta e^{-\lambda^2 D t} \quad (\text{A.15})$$

Substituting back into equation A.2 we hence can say:

$$C(x, t) = \beta e^{-\lambda^2 D t} (\phi \sin(\lambda x) + \psi \cos(\lambda x)) \quad (\text{A.16})$$

This is the general solution to equation A.1. We can now apply the boundary conditions from equations A.7 and A.10 to remove the unknown prefactors β , ϕ , ψ and λ . First consider equation A.7; differentiating (A.16) we get:

$$\frac{\partial C(x,t)}{\partial x} = \lambda\beta e^{-\lambda^2 Dt} (\phi \cos(\lambda x) - \psi \sin(\lambda x)) \quad (\text{A.17})$$

Hence applying A.7 we get:

$$\lambda\beta e^{-\lambda^2 Dt} \phi = 0 \quad (\text{A.18})$$

The only non-trivial solution here is $\phi = 0$. Hence equation A.16 becomes:

$$C(x,t) = \alpha e^{-\lambda^2 Dt} \cos(\lambda x) \quad (\text{A.19})$$

where $\alpha = \beta\psi$. Now consider the second boundary condition, equation A.10. Differentiating A.19 gives:

$$\frac{\partial C(x,t)}{\partial x} = -\lambda\alpha e^{-\lambda^2 Dt} \sin(\lambda x) \quad (\text{A.20})$$

Therefore when considering equation A.10:

$$-\lambda\alpha e^{-\lambda^2 Dt} \sin(\lambda x_c) = 0 \quad (\text{A.21})$$

The only non-trivial solution is:

$$\sin(\lambda x_c) = 0 \quad (\text{A.22})$$

Hence $\lambda x_c = \pi n$, where $n = 0, 1, 2, 3, \dots$. Substituting this into equation (A.19)

gives:

$$C(x, t) = \alpha \exp\left(-\frac{n^2\pi^2 Dt}{x_c^2}\right) \cos\left(\frac{n\pi x}{x_c}\right) \quad (\text{A.23})$$

We can write this as a linear super-position of many solutions:

$$C(x, t) = \sum_{n=0}^{\infty} \alpha_n \exp\left(-\frac{n^2\pi^2 Dt}{x_c^2}\right) \cos\left(\frac{n\pi x}{x_c}\right) \quad (\text{A.24})$$

We define the initial concentration profile as $C(x, 0) \equiv f(x)$. I.e.

$$C(x, 0) = f(x) = \sum_{n=0}^{\infty} \alpha_n \cos\left(\frac{n\pi x}{x_c}\right) \quad (\text{A.25})$$

This is a cosine Fourier series for $f(x)$ over $0 \leq x \leq x_c$. It can therefore be said that:

$$\alpha_n = \begin{cases} \frac{1}{x_c} \int_0^{x_c} f(x) dx & \text{if } n = 0 \\ \frac{2}{x_c} \int_0^{x_c} f(x) \cos\left(\frac{n\pi x}{x_c}\right) dx & \text{otherwise} \end{cases}$$

The initial concentration-profile of fullerenes is illustrated by the black line in Figure 6.5, and given by equation 6.2.

$$f(x) = \begin{cases} 0 & \text{for } 0 \leq x \leq x_p \\ C_0 & \text{for } x_p \leq x \leq x_c \end{cases} \quad (\text{A.26})$$

We can hence evaluate the integrals for α_n as follows:

$$\begin{aligned} \alpha_0 &= \frac{1}{x_c} \int_{x_p}^{x_c} C_0 dx \\ &= \frac{C_0(x_c - x_p)}{x_c} \end{aligned} \quad (\text{A.27})$$

$$\begin{aligned}\alpha_n &= \frac{2}{x_c} \int_{x_p}^{x_c} C_0 \cos\left(\frac{n\pi x}{x_c}\right) dx \\ &= -\frac{2C_0}{n\pi} \sin\left(\frac{n\pi x_p}{x_c}\right)\end{aligned}\tag{A.28}$$

So by combining equations A.27 and A.28 with our solution to the diffusion equation (equation A.24) we have a complete description of the concentration as a function of time and distance from interface:

$$C(x, t) = C_0 \left(1 - \frac{x_p}{x_c}\right) - C_0 \sum_{n=1}^{\infty} \frac{2}{n\pi} \sin\left(\frac{n\pi x_p}{x_c}\right) \exp\left(-\frac{n^2\pi^2 Dt}{x_c^2}\right) \cos\left(\frac{n\pi x}{x_c}\right)\tag{A.29}$$

Appendix B

List of Publications

[1] Wöbkenberg, P.H., Labram, J.G., Swiecicki, J.M., Parkhomenko, K., Sredojevic, D. Gisselbrecht, J.P., de Leeuw, D.M., Bradley, D.D.C., Djukic, J.P., Anthopoulos, T.D. Ambipolar organic transistors and near-infrared phototransistors based on a solution-processable squarilium dye. *J. Mater. Chem.* **20**, 3673-3680 (2010).

[2] Afonina, I., Skabara, P.J., Vilela, F., Kanibolotsky, A.L., Forgie, J.C., Bansal, A.K., Turnbull, G.A., Samuel, I.D.W., Labram, J.G., Anthopoulos, T.D., Coles, S.J., Hursthouse, M.B. Synthesis and characterisation of new diindenodithienothiophene (DITT) based materials. *J. Mater. Chem.* **20**, 1112-1116 (2010).

[3] Labram, J.G., Wöbkenberg, P.H., Bradley, D.D.C., Anthopoulos, T.D. Low-voltage ambipolar phototransistors based on a pentacene/PC₆₁BM heterostructure and a self-assembled nano-dielectric. *Org. Electron.* **11**, 1250-1254 (2010).

[4] Al-Hashimi, M., Labram, J.G., Watkins, S., Motevalli, M., Anthopoulos, T.D., Heeney, M. Synthesis and Characterization of Fused Pyrrolo[3,2-d:4,5-d']bisthiazole-Containing Polymers. *Org. Lett.* **12**, 5478-5481 (2010).

[5] McEntee, G.J., Vilela, F., Skabara, P.J., Anthopoulos, T.D., Labram, J.G.,

Tierney, S., Harrington, R.W., Clegg, W. Self-assembly and charge transport properties of a benzobisthiazole end-capped with dihexyl thienothiophene units. *J. Mater. Chem.* **21**, 2091-2097 (2011).

[6] Keyworth, C.W., Chan, K.L., Labram, J.G., Anthopoulos, T.D., Watkins, S.E., McKiernan, M., White, A.J.P., Holmes, A.B., Williams, C.K. The tuning of the energy levels of dibenzosilole copolymers and applications in organic electronics. *J. Mater. Chem.* **21**, 11800-11814 (2011).

[7] Labram, J.G., Domingo, E.B., Stingelin, N., Bradley, D.D.C., Anthopoulos, T.D. In-Situ Monitoring of the Solid-State Microstructure Evolution of Polymer: Fullerene Blend Films Using Field-Effect Transistors. *Adv. Funct. Mater.* **21**, 356-363 (2011).

[8] Agostinelli, T., Lilliu, S., Labram, J.G., Campoy-Quiles, M., Hampton, M., Pires, E., Rawle, J., Bikondoa, O., Bradley, D.D.C., Anthopoulos, T.D., Nelson, J., Macdonald, J.E. Real-Time Investigation of Crystallization and Phase-Segregation Dynamics in P3HT:PCBM Solar Cells During Thermal Annealing. *Adv. Funct. Mater.* **21**, 1701-1708 (2011).

[9] Labram, J.G., Kirkpatrick, J., Bradley, D.D.C., Anthopoulos, T.D. Measurement of the diffusivity of fullerenes in polymers using bilayer organic field effect transistors. *Phys. Rev. B* **84**, 075344 (2011).

[10] Dalgleish, S., Labram, J.G., Li, Z., Wang, J., McNeill, C.R., Anthopoulos, T.D., Greenham, N.C., Robertson N. Indole-substituted nickel dithiolenes complexes in electronic and optoelectronic devices. *J. Mater. Chem.* **21** 5422-15430 (2011).

[11] Shahid, M., McCarthy-Ward, T., Labram, J.G., Rossbauer, S., Domingo, E.B., Watkins, S.E., Stingelin, N., Anthopoulos, T.D., Heeney M. Low band gap selenophenediketopyrrolopyrrole polymers exhibiting high and balanced ambipolar performance in bottom-gate transistors. *Chem. Sci.* **In Press** (2011).

[12] Labram, J.G., Kirkpatrick, J., Bradley, D.D.C., Anthopoulos, T.D. Impact of Fullerene Molecular Weight on P3HT:PCBM Microstructure Studied Using Organic Thin-Film Transistors *Adv. En. Mater.* **In Press** (2011).

[13] Credgington, C., Kim, Y., Labram, J.G., Anthopoulos T.D., Durrant, J.R. Analysis of recombination losses in an organic bilayer solar cell. *J. Phys. Chem.* **Accepted** (2011).

References

- [1] Lilienfield, E. Patent: Method and apparatus for controlling electric currents (1930).
- [2] Bardeen, J. & Brattain, W. Physical principles involved in transistor action. *Phys. Rev.* **75**, 1208 (1949).
- [3] Bardeen, J. & Brattain, W. Physical principles involved in transistor action. *Bell System Technical Journal* **28**, 239–277 (1949).
- [4] Shockley, W., Pearson, G. & Haynes, J. Hole injection in germanium - quantitative studies and filamentary transistors. *Bell System Technical Journal* **28**, 344–366 (1949).
- [5] Kumar, R. *Fabless Semiconductor Implementation* (McGraw-Hill, 2008).
- [6] Kittel, C. *Introduction to solid state physics* (Wiley, 2005).
- [7] Hook, J. & Hall, H. *Solid State Physics, Second Edition* (John Wiley and Sons, 1999).
- [8] Ashcroft, N. & Mermin, N. *Solid State Physics* (Holt, Rinehart and Winston, 1976).
- [9] Moore, G. Cramming more components onto integrated circuits. *Electronics* **38**, 114–117 (1965).
- [10] Chiang, C. *et al.* Electrical conductivity in doped polyacetylene. *Phys. Rev. Lett* **39**, 1098–1101 (1977).

- [11] McNeill, R., Siudak, R., Wardlaw, J. & Weiss, D. Electronic conduction in polymers; I. the chemical structure of polypyrrole. *Aust. J. Chem.* **16**, 1056–1075 (1963).
- [12] Bolto, B. & Weiss, D. Electronic conduction in polymers; II. the electrochemical reduction of polypyrrole at controlled potential. *Aust. J. Chem.* **16**, 1076–1089 (1963).
- [13] Bolto, B., McNeill, R. & Weiss, D. Electronic conduction in polymers; III. electronic properties of polypyrrole. *Aust. J. Chem.* **16**, 1076–1089 (1963).
- [14] Forrest, S. The path to ubiquitous and low-cost organic electronic appliances on plastic. *Nature* **428**, 911–918 (2004).
- [15] Ozaki, M. *et al.* Junction formation with pure and doped polyacetylene. *App. Phys. Lett.* **35**, 83–85 (1979).
- [16] Grant, P., Tani, T., Gill, W., Krounbi, M. & Clarke, T. Properties of metal/polyacetylene schottky barriers. *J. App. Phys.* **52**, 869–872 (1981).
- [17] Burroughes, J., Jones, C. & Friend, R. New semiconductor device physics in polymer diodes and transistors. *Nature* **335**, 137–141 (1988).
- [18] Chen, S. *et al.* Polyacetylene, $(\text{CH})_x$: Photoelectrochemical solar cell. *App. Phys. Lett.* **36**, 96–98 (1980).
- [19] Weinberger, B., Gau, S. & Kiss, Z. A polyacetylene:aluminum photodiode. *App. Phys. Lett.* **38**, 555–557 (1980).
- [20] Tang, C. & VanSlyke, S. Organic electroluminescent diodes. *App. Phys. Lett.* **51**, 913–915 (1987).
- [21] Burroughes, J. *et al.* Light-emitting diodes based on conjugated polymers. *Nature* **347**, 539–541 (1990).
- [22] Ebisawa, F., Kurokawa, T. & Nara, S. Electrical properties of polyacetylene/polysiloxane interface. *J. App. Phys.* **54**, 3255–3259 (1983).

-
- [23] Koezuka, H., Tsumura, A. & Ando, T. Field-effect transistor with polythiophene thin film. *Synth. Met.* **18**, 699–704 (1987).
- [24] Iijima, S. Helical microtubules of graphitic carbon. *Nature* **354**, 56–58 (1991).
- [25] Baughman, R., Zakhidov, A. & de Heer, W. Carbon nanotubes - the route toward applications. *Science* **297**, 787–792 (2002).
- [26] Novoselov, K. *et al.* Electric field effect in atomically thin carbon films. *Science* **306**, 666–669 (2004).
- [27] Geim, A. *et al.* Two-dimensional gas of massless dirac fermions in graphene. *Nature* **438**, 197–200 (2005).
- [28] Geim, A. & Novoselov, K. The rise of graphene. *Nature Materials* **6**, 183–191 (2007).
- [29] Sirringhaus, H., Kawase, T. & Friend, R. High-resolution ink-jet printing of all-polymer transistor circuits. *MRS Bull.* **26**, 539–543 (2001).
- [30] Hebner, T., Wu, C., Marcy, D., Lu, M. & Sturm, J. Ink-jet printing of doped polymers for organic light emitting devices. *Appl. Phys. Lett.* **72**, 519–521 (1998).
- [31] Voigt, M. *et al.* Polymer field-effect transistors fabricated by the sequential gravure printing of polythiophene, two insulator layers, and a metal ink gate. *Adv. Funct. Mater.* **20**, 239–246 (2010).
- [32] Dimitrakopoulos, C., Purushothaman, S., Kymissis, J., Callegari, A. & Shaw, J. Low-voltage organic transistors on plastic comprising high-dielectric constant gate insulators. *Science* **283**, 822–824 (1999).
- [33] Gelinck, G. *et al.* Flexible active-matrix displays and shift registers based on solution-processed organic transistors. *Nat. Mater.* **3**, 106–110 (2004).
- [34] Sekitani, T. *et al.* Stretchable active-matrix organic light-emitting diode display using printable elastic conductors. *Nat. Mater.* **8**, 494–499 (2009).
-

-
- [35] Mabeck, J. & Malliaras, G. Chemical and biological sensors based on organic thin-film transistors. *Anal. Bioanal. Chem.* **384**, 343–353 (2006).
- [36] Roberts, M. *et al.* Water-stable organic transistors and their application in chemical and biological sensors. *Proc. Nat. Acad. Sci.* **105**, 12134–12139 (2008).
- [37] Burch, R., Dong, Y., Fincher, C., Goldfinger, M. & Rouviere, P. Electrical properties of polyunsaturated natural products: field effect mobility of carotenoid polyenes. *Synth. Met.* **146**, 43–46 (2004).
- [38] Irimia-Vladu, M. *et al.* Biocompatible and biodegradable materials for organic field-effect transistors. *Adv. Funct. Mater.* **20**, 4069–4076 (2010).
- [39] Padinger, F., Rittberger, R. & Sariciftci, N. Effects of postproduction treatment on plastic solar cells. *Adv. Funct. Mater.* **13**, 85–88 (2003).
- [40] Gong, X. *et al.* High-detectivity polymer photodetectors with spectral response from 300 nm to 1450 nm. *Science* **325**, 1665–1667 (2009).
- [41] Rostalski, J. & Meissner, D. Monochromatic versus solar efficiencies of organic solar cells. *Sol. En. Mater. Sol. Cells* **61**, 87–95 (2000).
- [42] Smits, E. *et al.* Bottom-up organic integrated circuits. *Nature* **455**, 956–959 (2008).
- [43] Drury, C., Mutsaers, C., Hart, C., Matters, M. & de Leeuw, D. Low-cost all-polymer integrated circuits. *App. Phys. Lett.* **73**, 108–110 (1988).
- [44] Baude, P. *et al.* Pentacene-based radio-frequency identification circuitry. *App. Phys. Lett.* **82**, 3964–3966 (2003).
- [45] Rogers, J. *et al.* Paper-like electronic displays: Large-area rubberstamped plastic sheets of electronics and microencapsulated electrophoretic inks. *Proc. Natl. Acad. Sci. USA* **98**, 4835–4840 (2001).
- [46] Hepp, A. *et al.* Light-emitting field-effect transistor based on a tetracene thin film. *Phys. Rev. Lett.* **91**, 157406 (2003).
-

-
- [47] Zaumseil, J., Friend, R. & Sirringhaus, H. Spatial control of the recombination zone in an ambipolar light-emitting organic transistor. *Nat. Mater.* **5**, 69–74 (2006).
- [48] Smits, E. *et al.* Near-infrared light-emitting ambipolar organic field-effect transistors. *Adv. Mater.* **19**, 734–738 (2007).
- [49] Narayan, K. & Kumar, N. Light responsive polymer field-effect transistor. *App. Phys. Lett.* **79**, 1891–1893 (2001).
- [50] Hamilton, M., Martin, S. & Kanicki, J. Thin-film organic polymer phototransistors. *IEEE Trans. Electron Devices* **51**, 877–885 (2004).
- [51] Anthopoulos, T. Electro-optical circuits based on light-sensing ambipolar organic field-effect transistors. *App. Phys. Lett.* **91**, 113513 (2007).
- [52] Morana, M. *et al.* Organic field-effect devices as tool to characterize the bipolar transport in polymer-fullerene blends: The case of P3HT-PCBM. *Adv. Funct. Mater.* **17**, 3274–3283 (2007).
- [53] Lloyd-Hughes, J., Richards, T., Sirringhaus, H., Johnston, M. & Herz, L. Exciton dissociation in polymer field-effect transistors studied using terahertz spectroscopy. *Phys. Rev. B* **77**, 125203 (2008).
- [54] Ashraf, R. *et al.* Silaindacenodithiophene semiconducting polymers for efficient solar cells and high-mobility ambipolar transistors. *Chemistry of Materials* **23**, 768–770 (2010).
- [55] Kroto, H., Heath, J., O’Brien, S., Curl, R. & Smalley, R. C_{60} : Buckminsterfullerene. *Nature* **318**, 162–163 (1985).
- [56] Pauling, L. The nature of the chemical bond. Application of results obtained from the quantum mechanics and from a theory of paramagnetic susceptibility to the structure of molecules. *J. Am. Chem. Soc.* **53**, 13671400 (1931).
- [57] Fayer, M. *Elements of Quantum Mechanics* (Oxford University Press, New York, 2001).
-

-
- [58] Rae, A. *Quantum Mechanics* (Institute of Physics Publishing, 2002).
- [59] Clayden, J., Greeves, N., Warren, S. & Wothers, P. *Organic chemistry* (Oxford university press, 1999).
- [60] Brabec, C., Sariciftci, N. & Hummelen, J. Plastic solar cells. *Adv. Funct. Mater.* **11**, 15–26 (2001).
- [61] Gregg, B. Excitonic solar cells. *J. Phys. Chem. B* **107**, 4688–4698 (2003).
- [62] Hoppe, H. & Sariciftci, N. Organic solar cells: An overview. *J. Mater. Res.* **19**, 1924–1945 (2004).
- [63] Marajanović, N. *et al.* Photoresponse of organic field-effect transistors based on conjugated polymer/fullerene blends. *Org. Electron.* **7**, 188–194 (2006).
- [64] Wasapinyoukul, K., Milne, W. & Chu, D. Photoresponse and saturation behavior of organic thin film transistors. *J. Appl. Phys.* **105**, 024509 (2009).
- [65] Karl, N. *et al.* Fast electronic transport in organic molecular solids? *J. Vac. Sci.* **17**, 2318–2328 (1999).
- [66] Podzorov, V., Menard, E., Rogers, J. & Gershenson, M. Hall effect in the accumulation layers on the surface of organic semiconductors. *Phys. Rev. Lett.* **95** (2005).
- [67] Sakanoue, T. & Sirringhaus, H. Band-like temperature dependence of mobility in a solution-processed organic semiconductor. *Nat. Mater.* **9**, 736–740 (2010).
- [68] Horowitz, G., Hajlaoui, R., Fichou, D. & Kassmi, A. E. Gate voltage dependent mobility of oligothiophene field-effect transistors. *J. Appl. Phys.* **85**, 3202–3206 (1999).
- [69] Horowitz, G. & Hajlaoui, M. Mobility in polycrystalline oligothiophene field-effect transistors dependent on grain size. *Adv. Mater.* **12**, 1046–1050 (2000).

-
- [70] Vissenberg, M. & Matters, M. Theory of the field-effect mobility in amorphous organic transistors. *Phys. Rev. B* **57**, 12964–12967 (1998).
- [71] Anderson, P. Absence of diffusion in certain random lattices. *Phys. Rev.* **109**, 1492 (1958).
- [72] Mott, N. The random-phase model in non-crystalline systems. *Philos. Mag. B* **43**, 941–942 (1981).
- [73] Abrahams, E., Anderson, P., Licciardello, D. & Ramakrishnan, T. Scaling theory of localization: Absence of quantum diffusion in two dimensions. *Phys. Rev. Lett.* **42**, 673 (1979).
- [74] Chesterfield, R. *et al.* Variable temperature film and contact resistance measurements on operating n-channel organic thin film transistors. *J. Appl. Phys.* **95**, 6396–6405 (2004).
- [75] Miller, A. & Abrahams, E. Impurity conduction at low concentrations. *Phys. Rev.* **120**, 745 (1960).
- [76] Mott, N. & Davis, E. *Electronic processes in non-crystalline materials* (Clarendon Press, 1979).
- [77] Pike, G. & Seager, C. Percolation and conductivity: A computer study. I. *Phys. Rev. B* **10**, 1421 (1974).
- [78] Baranovskii, S., Zvyagin, I., Cordes, H., Yamasaki, S. & Thomas, P. Percolation approach to hopping transport in organic disordered solids. *Physica Stat. Solidi (b)* **230**, 281–288 (2002).
- [79] Kirkpatrick, S. Percolation and conduction. *Rev. Mod. Phys.* **45**, 574–588 (1973).
- [80] Broadbent, S. & Hammersley, J. Percolation processes. *Math. Proc. Cam. Phil. Soc.* **53**, 629–641 (1957).
- [81] Shante, V. & Kirkpatrick, S. An introduction to percolation theory. *Adv. Phys.* **20**, 325–357 (1971).
-

- [82] Kirkpatrick, S. The nature of percolation channels'. *Sol. State Comm.* **12**, 1279–1283 (1973).
- [83] Brown, A., Jarrett, C., de Leeuw, D. & Matters, M. Field-effect transistors made from solution-processed organic semiconductors. *Synth. Metals* **88**, 37–55 (1997).
- [84] Zaumseil, J. & Sirringhaus, H. Electron and ambipolar transport in organic field-effect transistors. *Chem. Rev.* **107**, 1296–1323 (2007).
- [85] Horowitz, G. Organic field-effect transistors. *Adv. Mater.* **10**, 365–377 (1998).
- [86] Dimitrakopoulos, C. & Malenfant, P. Organic thin film transistors for large area electronics. *Adv. Mater.* **14**, 99–117 (2002).
- [87] Sirringhaus, H. Device physics of solution-processed organic field-effect transistors. *Adv. Mater.* **17**, 2411–2425 (2005).
- [88] Klauk, H. Organic thin-film transistors. *Chem. Soc. Rev.* **39**, 2643–2666 (2010).
- [89] Street, R. & Salleo, A. Contact effects in polymer transistors. *Appl. Phys. Lett.* .
- [90] Newman, C., Chesterfield, R., Panzer, M. & Frisbie, D. High mobility top-gated pentacene thin-film transistors. *J. Appl. Phys.* **98** (2005).
- [91] McCulloch, I. *et al.* Liquid-crystalline semiconducting polymers with high charge-carrier mobility. *Nat. Mater.* **5**, 328–333 (2006).
- [92] Anthopoulos, T. *et al.* High performance n-channel organic field-effect transistors and ring oscillators based on C-60 fullerene films. *Appl. Phys. Lett.* **89**, 213504 (2006).
- [93] Hamilton, R. *et al.* High-performance polymer-small molecule blend organic transistors. *Adv. Mater.* **21**, 1166–1171 (2009).

- [94] Yan, H. *et al.* A high-mobility electron-transporting polymer for printed transistors. *Nature* **457**, 679–689 (2009).
- [95] Chen, Z. *et al.* High mobility ambipolar charge transport in polyselenophene conjugated polymers. *Adv. Mater.* **22**, 2371–2375 (2010).
- [96] Brown, A., Pomp, A., Hart, C. & de Leeuw, D. Logic gates made from polymer transistors and their use in ring oscillators. *Science* **270**, 972–974 (1995).
- [97] Lin, Y. *et al.* Organic complementary ring oscillators. *App. Phys. Lett* **74**, 2714–2716 (1999).
- [98] Crone, B. *et al.* Large-scale complementary integrated circuits based on organic transistors. *Nature* **404**, 521–523 (2000).
- [99] Halik, M. *et al.* Low-voltage organic transistors with an amorphous molecular gate dielectric. *Nature* **431**, 963–966 (2004).
- [100] H.Klauk, Zschieschang, U., Pflaum, J. & Halik, M. Ultralow-power organic complementary circuits. *Nature* **445**, 745–748 (2007).
- [101] Chua, L., Ho, P., Sirringhaus, H. & Friend, R. High-stability ultrathin spin-on benzocyclobutene gate dielectric for polymer field-effect transistors. *App. Phys. Lett.* **84**, 3400–3402 (2004).
- [102] Chua, L. *et al.* General observation of n-type field-effect behaviour in organic semiconductors. *Nature* **434**, 194–199 (2005).
- [103] Campoy-Quiles, M. *et al.* Morphology evolution via self-organization and lateral and vertical diffusion in polymer:fullerene solar cell blends. *Nature Mater.* **7**, 158–164 (2005).
- [104] Smith, J. *et al.* Solution-processed organic transistors based on semiconducting blends. *J. Mater. Chem.* **20**, 2562–2574 (2010).
- [105] Parker, I. Carrier tunneling and device characteristics in polymer light-emitting-diodes. *J. Appl. Phys.* **75**, 1656–1666 (1994).

- [106] Campbell, I. *et al.* Controlling schottky energy barriers in organic electronic devices using self-assembled monolayers. *Phys. Rev. B* **54**, 14321–14324 (1996).
- [107] Anthopoulos, T., Anyfantis, G., Papavassiliou, G. & de Leeuw, D. Air-stable ambipolar organic transistors. *App. Phys. Lett.* **90**, 122105 (2007).
- [108] Brabec, C. *et al.* Origin of the open circuit voltage of plastic solar cells. *Adv. Funct. Mater.* **11**, 374–380 (2001).
- [109] Meijer, E. *et al.* Solution-processed ambipolar organic field-effect transistors and inverters. *Nat. Mater.* **2**, 678–682 (2003).
- [110] Anthopoulos, T. *et al.* Ambipolar organic field-effect transistors based on a solution-processed methanofullerene. *Adv. Mater.* **16**, 2174–2179 (2004).
- [111] Wöbkenberg, P. *et al.* High mobility n-channel organic field-effect transistors based on soluble C-60 and C-70 fullerene derivatives. *Synth. Met.* **158**, 468–472 (2008).
- [112] van Duren, J. *et al.* Injection-limited electron current in a methanofullerene. *J. Appl. Phys.* **94**, 4477–4479 (2003).
- [113] Salleo, A. & Street, R. Light-induced bias stress reversal in polyfluorene thin-film transistors. *J. Appl. Phys.* **94**, 471–479 (2003).
- [114] Salleo, A., Endicott, F. & Street, R. Reversible and irreversible trapping at room temperature in poly(thiophene) thin-film transistors. *Appl. Phys. Lett.* **86**, 263505 (2005).
- [115] Gu, S., Kane, M., Doty, J. & Firester, A. Electron traps and hysteresis in pentacene-based organic thin-film transistors. *Appl. Phys. Lett.* **87**, 243512 (2005).
- [116] Mathijssen, S. *et al.* Dynamics of threshold voltage shifts in organic and amorphous silicon field-effect transistors. *Adv. Mater.* **19**, 2785–2789 (2007).

- [117] Sze, S. *Physics of semiconductor devices* (John Wiley and Sons, 1981).
- [118] Kim, C. & Matsumura, M. Short-channel amorphous-silicon thin-film transistors. *IEEE Trans. Electron Dev.* **43**, 2172–2176 (1996).
- [119] Burgi, L., Sirringhaus, H. & Friend, R. Noncontact potentiometry of polymer field-effect transistors. *Appl. Phys. Lett.* **80**, 2913–2915 (2002).
- [120] Sele, C., von Werne, T., Friend, R. & Sirringhaus, H. Lithography-free, self-aligned inkjet printing with sub-hundred-nanometer resolution. *Advanced Materials* **17**, 997–1001 (2005).
- [121] Noh, Y.-Y., Zhao, N., Caironi, M. & Sirringhaus, H. Downscaling of self-aligned, all-printed polymer thin-film transistors. *Nat. Nano.* **2**, 784–789 (2007). 10.1038/nnano.2007.365.
- [122] Horowitz, G., Hajlaoui, R. & Delannoy, P. Temperature-dependence of the field-effect mobility of sexithiophene - determination of the density of traps. *Journal De Physique III* **5**, 355–371 (1995).
- [123] Horowitz, G., Hajlaoui, M. & Hajlaoui, R. Temperature and gate voltage dependence of hole mobility in polycrystalline oligothiophene thin film transistors. *J. Appl. Phys.* **87**, 4456–4463 (2000).
- [124] Newman, C. *et al.* Introduction to organic thin film transistors and design of n-channel organic semiconductors. *Chem. Mater.* **16**, 4436–4451 (2004).
- [125] Veres, J., Ogier, S., Lloyd, G. & de Leeuw, D. Gate insulators in organic field-effect transistors. *Chem. Mater.* **16**, 4543–4555 (2004).
- [126] Facchetti, A., Yoon, M. & Marks, T. Gate dielectrics for organic field-effect transistors: New opportunities for organic electronics. *Adv. Mater.* **17**, 1705–1725 (2005).
- [127] Kobayashi, S. *et al.* Control of carrier density by self-assembled monolayers in organic field-effect transistors. *Nat. Mater.* **3**, 317–322 (2004).

-
- [128] Ball, J. *et al.* Solution processed low-voltage organic transistors and complementary inverters. *Appl. Phys. Lett.* **95** (2009).
- [129] Sirringhaus, H., Tessler, N. & Friend, R. Integrated optoelectronic devices based on conjugated polymers. *Science* **280**, 1741–1744 (1998).
- [130] Fontaine, P., Goguenheim, D., Deresmes, D., & Vuillaume, D. Octadecyltrichlorosilane monolayers as ultrathin gate insulating films in metal-insulator-semiconductor devices. *App. Phys. Lett.* **62**, 2256–2258 (1993).
- [131] Kalb, W., Mathis, T., Haas, S., Stassen, A. & Batlogg, B. Organic small molecule field-effect transistors with cytop (TM) gate dielectric: Eliminating gate bias stress effects. *Appl. Phys. Lett.* **90** (2007).
- [132] Noh, Y. & Sirringhaus, H. Ultra-thin polymer gate dielectrics for top-gate polymer field-effect transistors. *Org. Electron.* **10**, 174–180 (2009).
- [133] Collet, J., Tharaud, O., Chapoton, A. & Vuillaume, D. Low-voltage, 30 nm channel length, organic transistors with a self-assembled monolayer as gate insulating films. *App. Phys. Lett.* **76**, 1941–1943 (2000).
- [134] Boulas, C., Davidovits, J., Rondelez, F. & Vuillaume, D. Suppression of charge carrier tunneling through organic self-assembled monolayers. *Phys. Rev. Lett.* **76**, 4797–4800 (1996).
- [135] Park, Y. *et al.* Low-voltage polymer thin-film transistors with a self-assembled monolayer as the gate dielectric. *App. Phys. Lett.* **87**, 243509 (2005).
- [136] Wöbkenberg, P. *et al.* Low-voltage organic transistors based on solution processed semiconductors and self-assembled monolayer gate dielectrics. *App. Phys. Lett.* **93**, 013303 (2008).
- [137] Yoo, B. *et al.* High-mobility bottom-contact n-channel organic transistors and their use in complementary ring oscillators. *Appl. Phys. Lett.* **88**, 082104.

-
- [138] Sirringhaus, H. *et al.* Two-dimensional charge transport in self-organized, high-mobility conjugated polymers. *Nature* **401**, 685–688 (1999).
- [139] Scavia, G. *et al.* Effect of the silanization and annealing on the morphology of thin poly(3-hexylthiophene) (P3HT) layer on silicon oxide. *Surf. Sci.* **602**, 3106–3115 (2008).
- [140] Lim, S. *et al.* Surface-treatment effects on organic thin-film transistors. *Synth. Met.* **148**, 75–79 (2005).
- [141] Dodabalapur, A., Laquindanum, J., Katz, H. & Bao, Z. Complementary circuits with organic transistors. *App. Phys. Lett* **69**, 4227–4229 (1996).
- [142] Bode, D. *et al.* Noise-margin analysis for organic thin-film complementary technology. *IEEE. Trans. Electron Dev.* **57**, 201–208 (2010).
- [143] Gelinck, G., Heremans, P., Nomoto, K. & Anthopoulos, T. Organic transistors in optical displays and microelectronic applications. *Adv. Mater.* **22**, 3778–3798 (2010).
- [144] Smits, E. *et al.* Ambipolar charge transport in organic field-effect transistors. *Phys. Rev. B* **73**, 205316 (2006).
- [145] Wöbkenberg, P. *et al.* Ambipolar organic transistors and near-infrared phototransistors based on a solution-processable squarilium dye. *J. Mater. Chem.* **20**, 36733680 (2010).
- [146] Swensen, J., Soci, C. & Heeger, A. Light emission from an ambipolar semiconducting polymer field-effect transistor. *App. Phys. Lett.* **87**, 253511 (2005).
- [147] Zaumseil, J. *et al.* Quantum efficiency of ambipolar light-emitting polymer field-effect transistors. *J. Appl. Phys.* **103** (2008).
- [148] Capelli, R. *et al.* Organic light-emitting transistors with an efficiency that outperforms the equivalent light-emitting diodes. *Nature Materials* **9**, 496–503 (2010).

-
- [149] Dodabalapur, A., Katz, H., Torsi, L. & Haddon, R. Organic heterostructure field-effect transistors. *Science* **269**, 1560–1562 (1995).
- [150] Kuwahara, E. *et al.* Fabrication of ambipolar field-effect transistor device with heterostructure of C₆₀ and pentacene. *App. Phys. Lett.* **85**, 4765–4767 (2004).
- [151] Kang, S. *et al.* Ambipolar organic thin-film transistors using C-60/pentacene structure: Characterization of electronic structure and device property. *Appl. Phys. Lett.* **87**, 233502.
- [152] Tada, K., Harada, H. & Yoshino, K. Polymeric bipolar thin-film transistor utilizing conducting polymer containing electron transport dye. *Jap. J. Appl. Phys.* **35**, L944–L946 (1996).
- [153] Rost, C. *et al.* Ambipolar light-emitting organic field-effect transistor. *Appl. Phys. Lett.* **85**, 1613–1615 (2004).
- [154] Szendrei, K., Facchetti, A., Jarzab, D., Chen, Z. & Loi, M. Ambipolar all-polymer bulk heterojunction field-effect transistors. *J. Mater. Chem.* **20**, 1317–1321 (2010).
- [155] Mayer, A. *et al.* Bimolecular crystals of fullerenes in conjugated polymers and the implications of molecular mixing for solar cells. *Adv. Funct. Mater.* **19**, 1173–1179 (2009).
- [156] Cates, N., Gysel, R., Dahl, J., Sellinger, A. & McGehee, M. Effects of intercalation on the hole mobility of amorphous semiconducting polymer blends. *Chem. Mater.* **22**, 3543–3548 (2010).
- [157] Cho, S., Yuen, J., Kim, J., Lee, K. & Heeger, A. J. Photovoltaic effects on the organic ambipolar field-effect transistors. *App. Phys. Lett.* **90**, 063511 (2007).
- [158] Kim, J. & Frisbie, D. Correlation of phase behavior and charge transport in conjugated polymer/fullerene blends. *J. Phys. Chem. C* **112**, 17726–17736 (2008).
-

-
- [159] Germack, D. *et al.* Substrate-dependent interface composition and charge transport in films for organic photovoltaics. *Appl. Phys. Lett.* **94**, 233303 (2009).
- [160] Schmechel, R., Ahles, M. & von Seggern, H. A pentacene ambipolar transistor: Experiment and theory. *J. App. Phys.* **98**, 084511 (2005).
- [161] Anthopoulos, T. *et al.* Organic complementary-like inverters employing methanofullerene-based ambipolar field-effect transistors. *App. Phys. Lett.* **85**, 4205–4207 (2004).
- [162] Anthopoulos, T. *et al.* Air-stable complementary-like circuits based on organic ambipolar transistors. *Adv. Mater.* **18**, 1900–1904 (2006).
- [163] Chen, Z. *et al.* Enhanced charge transport by incorporating additional thiophene units in the poly(fluorene-thienyl-benzothiadiazole) polymer. *Org. Electron.* **12**, 461–471 (2011).
- [164] Chen, H. *et al.* Polymer solar cells with enhanced open-circuit voltage and efficiency. *Nature Photon.* **3**, 649–653 (2009).
- [165] Park, S. *et al.* Bulk heterojunction solar cells with internal quantum efficiency approaching 100%. *Nature Photon.* **3**, 297 (2009).
- [166] Liang, Y. *et al.* For the bright future bulk heterojunction polymer solar cells with power conversion efficiency of 7.4%. *Adv. Mater.* **22**, 135–138 (2010).
- [167] Yu, G. *et al.* Large area, full-color, digital image sensors made with semi-conducting polymers. *Synth. Met.* **111**, 133–137 (2000).
- [168] Ng, T., Wong, W., Chabinyk, M., Sambandan, S. & Street, R. Flexible image sensor array with bulk heterojunction organic photodiode. *App. Phys. Lett.* **92**, 213303 (2008).
- [169] Rauch, T. *et al.* Near-infrared imaging with quantum-dot-sensitized organic photodiodes. *Nature Photon.* **3**, 332–336 (2009).
-

-
- [170] Saragi, T., Pudzich, R., Fuhrmann, T. & Salbeck, J. Organic phototransistor based on intramolecular charge transfer in a bifunctional spiro compound. *App. Phys. Lett.* **84**, 2334–2336 (2004).
- [171] Noh, Y.-Y., Kim, D.-Y. & Yase, K. Highly sensitive thin-film organic phototransistors: Effect of wavelength of light source on device performance. *J. App. Phys.* **98**, 074505 (2005).
- [172] Lucas, B. *et al.* Ultraviolet light effect on electrical properties of a flexible organic thin film transistor. *Thin Sol. Films* **517**, 6280–6282 (2009).
- [173] Günes, S., Neugebauer, H. & Sariciftci, N. Conjugated polymer-based organic solar cells. *Chem. Rev.* **107**, 1324–1338 (2007).
- [174] Bässler, H. Charge transport in disordered organic photoconductors. *Phys. Stat. Sol. B* **175**, 15–56 (1993).
- [175] Choi, J.-M., Lee, J., Hwang, D., Kim, J. & Im, S. Comparative study of the photoresponse from tetracene-based and pentacene-based thin-film transistors. *App. Phys. Lett.* **88**, 043508 (2006).
- [176] Kim, C. *et al.* Bimolecular recombination in solution-processed 6, 13-bis(pentylphenylethynyl) pentacene thin-film transistor. *App. Phys. Lett.* **94**, 083308 (2009).
- [177] Singh, T., Koeppe, R., Sariciftci, N. S., Morana, M. & Brabec, C. Monitoring the channel formation in organic field-effect transistors via photoinduced charge transfer. *Adv. Funct. Mater.* **19**, 789–795 (2009).
- [178] Choi, C.-S. *et al.* High optical responsivity of InAlAs-InGaAs metamorphic high-electron mobility transistor on GaAs substrate with composite channels. *IEEE Photonics Technol. Lett.* **15**, 846–848 (2003).
- [179] Noh, Y.-Y. & Kim, D.-Y. Organic phototransistor based on pentacene as an efficient red light sensor. *Sol. State. Electron.* **51**, 1052–1055 (2007).

-
- [180] Rao, M. & Narayan, K. Evaluation of electrode-semiconductor barrier in transparent top-contact polymer field effect transistors. *App. Phys. Lett.* **92**, 223308 (2008).
- [181] Horowitz, G. Organic thin film transistors: From theory to real devices. *J. Mater. Res.* **19**, 1946–1962 (2004).
- [182] Noh, Y.-Y. *et al.* Effect of light irradiation on the characteristics of organic field-effect transistors. *J. App. Phys.* **100**, 094501 (2006).
- [183] J.M. Rabaey, A. C. & Nikolic, B. *Digital Integrated Circuits (2nd Edition)* (Prentice Hall, 2003).
- [184] Shirakawa, H., Louis, E., MacDiarmid, A., Chiang, C. & Heeger, A. Synthesis of electrically conducting organic polymers: Halogen derivatives of polyacetylene, $(\text{CH})_x$. *J.C.S. Chem. Comm.* 578–580 (1977).
- [185] Katz, H., Bao, Z. & Gilat, S. Synthetic chemistry for ultrapure, processable, and high-mobility organic transistor semiconductors. *Acc. Chem. Res.* **34**, 359–369 (2001).
- [186] Malliaras, G. & Friend, R. An organic electronics primer. *Phys. Today* **58**, 53–58 (2005).
- [187] Murphy, A. & Frechet, J. Organic semiconducting oligomers for use in thin film transistors. *Chem. Rev.* **107**, 1066–1096 (2007).
- [188] Anthony, J., Facchetti, A., Heeney, M., Marder, S. & Zhan, X. n-type organic semiconductors in organic electronics. *Adv. Mater.* **22**, 3876–3892 (2010).
- [189] Moon, J., Y.M., C. T., Sun & Heeger, A. Spontaneous formation of bulk heterojunction nanostructures: Multiple routes to equivalent morphologies. *Nano Lett.* **11**, 1036–1039 (2011).
- [190] de Leeuw, D., Simenon, M., Brown, A. & Einerhand, R. Stability of n-type doped conducting polymers and consequences for polymeric microelectronic devices. *Synth. Met.* **87**, 53–59 (1997).
-

-
- [191] Troshin, P. *et al.* Material solubility-photovoltaic performance relationship in the design of novel fullerene derivatives for bulk heterojunction solar cells. *Adv. Funct. Mater.* **19**, 779–788 (2009).
- [192] Sundar, V. *et al.* Elastomeric transistor stamps: Reversible probing of charge transport in organic crystals. *Science* **303**, 1644–1646 (2004).
- [193] Goldmann, C. *et al.* Hole mobility in organic single crystals measured by a “flip-crystal” field-effect technique. *J. Appl. Phys.* **96**, 2080–2086 (2004).
- [194] Stassen, A., de Boer, R., Iosad, N. & Morpurgo, A. Influence of the gate dielectric on the mobility of rubrene single-crystal field-effect transistors. *Appl. Phys. Lett.* **85**, 3899–3901 (2004).
- [195] Menard, E. *et al.* High-performance n- and p-type single-crystal organic transistors with free-space gate dielectrics. *Advanced Materials* **16**, 2097–2101 (2004).
- [196] Gundlach, D., Lin, Y., Jackson, T., Nelson, S. & Schlom, D. Pentacene organic thin-film transistors - molecular ordering and mobility. *IEEE Electron Dev. Lett.* **18**, 87–89 (1997).
- [197] Lin, Y., Gundlach, D., Nelson, S. & Jackson, T. Stacked pentacene layer organic thin-film transistors with improved characteristics. *IEEE Electron Dev. Lett.* **18**, 606–608 (1997).
- [198] Nelson, S., Lin, Y., Gundlach, D. & Jackson, T. Temperature-independent transport in high-mobility pentacene transistors. *Appl. Phys. Lett.* **72**, 1854–1856 (1998).
- [199] Klauk, H. *et al.* High-mobility polymer gate dielectric pentacene thin film transistors. *J. App. Phys.* **92**, 5259–5263 (2002).
- [200] Street, R., Knipp, D., Volkel, A. & Ho, J. Pentacene thin film transistors on inorganic dielectrics: Morphology, structural properties, and electronic transport. *J. Appl. Phys.* **93**, 347–355 (2003).
-

-
- [201] Anthony, J., Brooks, J., Eaton, D. & Parkin, S. Functionalized pentacene: Improved electronic properties from control of solid-state order. *J. American Chem. Soc.* **123**, 9482–9483 (2001).
- [202] Anthony, J., Eaton, D. & Parkin, S. A road map to stable, soluble, easily crystallized pentacene derivatives. *Org. Lett.* **4**, 15–18 (2002).
- [203] Payne, M., Parkin, S., Kuo, C., Jackson, T. & Anthony, J. Organic field-effect transistors from solution-deposited functionalized acenes with mobilities as high as $1 \text{ cm}^2/\text{Vs}$. *J. American Chem. Soc.* **127**, 4986–4987 (2005).
- [204] Subramanian, S. *et al.* Chromophore fluorination enhances crystallization and stability of soluble anthradithiophene semiconductors. *J. American Chem. Soc.* **130**, 2706–2707 (2008).
- [205] Bao, Z., Dodabalapur, A. & Lovinger, A. Soluble and processable regioregular poly(3-hexylthiophene) for thin film field-effect transistor applications with high mobility. *Appl. Phys. Lett.* **69**, 4108–4110 (1996).
- [206] Ma, W., Yang, C., Gong, X., Lee, K. & Heeger, A. Thermally stable, efficient polymer solar cells with nanoscale control of the interpenetrating network morphology. *Adv. Funct. Mater.* **15**, 1617–1622 (2005).
- [207] Smith, J. *et al.* High-performance organic integrated circuits based on solution processable polymer-small molecule blends. *Appl. Phys. Lett.* **93**, 253301 (2008).
- [208] Zhang, W. *et al.* Indacenodithiophene semiconducting polymers for high-performance, air-stable transistors. *J. American Chem. Soc.* **132**, 11437–11439 (2010).
- [209] Haddon, R. *et al.* C-60 thin-film transistors. *Appl. Phys. Lett.* **67**, 121–123 (1995).
- [210] Sariciftci, N., Smilowitz, L., Heeger, A. & Wudl, F. Photoinduced electron transfer from a conducting polymer to buckminsterfullerene. *Science* **258**, 1474–1476 (1992).
-

- [211] Haddon, R. C-70 thin film transistors. *J. American Chem. Soc.* **118**, 3041–3042 (1996).
- [212] Shibata, K. *et al.* Fabrication and characteristics of c-84 fullerene field-effect transistors. *Appl. Phys. Lett.* **84**, 2572–2574 (2004).
- [213] Hummelen, J. *et al.* Preparation and characterization of fulleroid and methanofullerene derivatives. *J Org. Chem.* **60**, 532–538 (1995).
- [214] Waldauf, C., Schilinsky, P., Perisutti, M., Hauch, J. & Brabec, C. Solution-processed organic n-type thin-film transistors. *Adv. Mater* **15**, 2084–2088 (2003).
- [215] Yu, G., Gao, J., Hummelen, J., Wudl, F. & Heeger, A. Polymer photovoltaic cells - enhanced efficiencies via a network of internal donor-acceptor heterojunctions. *Science* **270**, 1789–1791 (1995).
- [216] Shaheen, S. *et al.* 2.5% efficient organic plastic solar cells. *Appl. Phys. Lett.* **78**, 841–843 (2001).
- [217] Anthopoulos, T. *et al.* Solution processible organic transistors and circuits based on a C-70 methanofullerene. *J. Appl. Phys.* **98**, 054503 (2005).
- [218] Anthopoulos, T. *et al.* Air-stable n-channel organic transistors based on a soluble C₈₄ fullerene derivative. *Adv. Mater.* **18**, 1679–1684 (2006).
- [219] Faist, M. *et al.* Effect of multiple adduct fullerenes on charge generation and transport in photovoltaic blends with poly(3-hexylthiophene-2,5-diyl). *J. Poly. Sci.* **49**, 45–51 (2011).
- [220] Jones, B. *et al.* High-mobility air-stable n-type semiconductors with processing versatility: Dicyanoperylene-3,4 : 9,10-bis(dicarboximides). *Angewandte Chemie-International Edition* **43**, 6363–6366 (2004).
- [221] Yoo, B. *et al.* High-mobility bottom-contact n-channel organic transistors and their use in complementary ring oscillators. *Appl. Phys. Lett.* **88**, 082104 (2006).

-
- [222] Chen, Z., Zheng, Y., Yan, H. & Facchetti, A. Naphthalenedicarboximide- vs perylenedicarboximide-based copolymers. synthesis and semiconducting properties in bottom-gate n-channel organic transistors. *J. American Chem. Soc.* **131**, 8–9 (2009).
- [223] McNeill, C. & Greenham, N. Conjugated-polymer blends for optoelectronics. *Adv. Mater.* **21**, 3840–3850 (2009).
- [224] Zaumseil, J., Donley, C., Kim, J., Friend, R. & Sirringhaus, H. Efficient top-gate, ambipolar, light-emitting field-effect transistors based on a green-light-emitting polyfluorene. *Adv. Mater.* **18**, 2708–2712 (2006).
- [225] Bürgi, L. *et al.* High-mobility ambipolar near-infrared light-emitting polymer field-effect transistors. *Adv. Mater.* **20**, 2217–2224 (2008).
- [226] Bijleveld, J. *et al.* Poly(diketopyrrolopyrrole-terthiophene) for ambipolar logic and photovoltaics. *J. American Chem. Soc.* **131**, 16616–16617 (2009).
- [227] Zoombelt, A., Mathijssen, S., Turbiez, M., Wienk, M. & Janssen, R. Small band gap polymers based on diketopyrrolopyrrole. *J. Mater. Chem.* **20**, 2240–2246 (2010).
- [228] Bronstein, H. *et al.* Thieno[3,2-b]thiophene-diketopyrrolopyrrole-containing polymers for high-performance organic field-effect transistors and organic photovoltaic devices. *J. American Chem. Soc.* **133**, 3272–3275 (2011).
- [229] Shahid, M. *et al.* Low band gap selenophene-diketopyrrolopyrrole polymers exhibiting high and balanced ambipolar performance in bottom gate transistors. *Royal Soc. Chem.* **Accepted** (2011).
- [230] Peumans, P., Yakimov, A. & Forrest, S. Small molecular weight organic thin-film photodetectors and solar cells. *J. Appl. Phys.* **93**, 3693–3723 (2003).
- [231] Rowell, M. *et al.* Organic solar cells with carbon nanotube network electrodes. *Appl. Phys. Lett.* **88** (2006).
-

-
- [232] Zhi, L., Wang, X. & Mullen, K. Transparent, conductive graphene electrodes for dye-sensitized solar cells. *Nano Lett.* **8**, 323–327 (2008).
- [233] Frohne, H. *et al.* Influence of the anodic work function on the performance of organic solar cells. *ChemPhysChem* **3**, 795–799 (2002).
- [234] Chirvase, D., Parisi, J., Hummelen, J. & Dyakonov, V. Influence of nanomorphology on the photovoltaic action of polymer-fullerene composites. *Nanotech.* **15**, 1317–1323 (2004).
- [235] Kim, Y. *et al.* Device annealing effect in organic solar cells with blends of regioregular poly(3-hexylthiophene) and soluble fullerene. *Appl. Phys. Lett.* **86**, 063502 (2005).
- [236] Mihailetchi, V., Xie, H., de Boer, B., Koster, L. & Blom, P. Charge transport and photocurrent generation in poly (3-hexylthiophene): Methanofullerene bulk-heterojunction solar cells. *Adv. Funct. Mater.* **16**, 699–708 (2006).
- [237] Scharber, M. *et al.* Design rules for donors in bulk-heterojunction solar cells towards 10% energy-conversion efficiency. *Adv. Mater.* **18**, 789–794 (2006).
- [238] Riedel, I. & Dyakonov, V. Influence of electronic transport properties of polymer-fullerene blends on the performance of bulk heterojunction photovoltaic devices. *Phys. Status Solidi A* **201**, 1332–1341 (2004).
- [239] Brabec, C., Heeney, M., McCulloch, I. & Nelson, J. Influence of blend microstructure on bulk heterojunction organic photovoltaic performance. *Chem. Soc. Rev.* **40**, 1185–1199 (2011).
- [240] Hoppe, H. & Sariciftci, N. Morphology of polymer/fullerene bulk heterojunction solar cells. *J. of Mater. Chem.* **16**, 45–61 (2006).
- [241] Chen, L., Hong, Z., Li, G. & Yang, Y. Recent progress in polymer solar cells: Manipulation of polymer: Fullerene morphology and the formation of efficient inverted polymer solar cells. *Adv. Mater.* **21**, 1434–1449 (2009).
-

-
- [242] Giridharagopal, R. & Ginger, D. Characterizing morphology in bulk heterojunction organic photovoltaic systems. *J. Phys. Chem. Lett.* **1**, 1160–1169 (2010).
- [243] Sylvester-Hvid, K., Rettrup, S. & Ratner, M. Two-dimensional model for polymer-based photovoltaic cells: Numerical simulations of morphology effects. *J. Phys. Chem. B* **108**, 4296–4307 (2004).
- [244] He, X. *et al.* Formation of nanopatterned polymer blends in photovoltaic devices. *Nano Lett.* **10**, 1302–1307 (2010).
- [245] He, X. *et al.* Formation of well-ordered heterojunctions in polymer:PCBM photovoltaic devices. *Adv. Funct. Mater.* **21**, 139–146 (2011).
- [246] Ku, S.-Y. *et al.* Solution-processed nanostructured benzoporphyrin with polycarbonate binder for photovoltaics. *Adv. Mater.* **23**, 2289–2293 (2011).
- [247] Hoppe, H. *et al.* Nanoscale morphology of conjugated polymer/fullerene-based bulk-heterojunction solar cells. *Adv. Funct. Mater.* **14**, 1005–1011 (2004).
- [248] Kline, R., McGehee, M., Kadnikova, E., Liu, J. & Fréchet, J. Controlling the field-effect mobility of regioregular polythiophene by changing the molecular weight. *Adv. Mater.* **15**, 1519–1522 (2003).
- [249] Kim, Y. *et al.* A strong regioregularity effect in self-organizing conjugated polymer films and high-efficiency polythiophene: fullerene solar cells. *Nat. Mater.* **5**, 197–203 (2006).
- [250] Erb, T. *et al.* Correlation between structural and optical properties of composite polymer/fullerene films for organic solar cells. *Adv. Funct. Mater.* **15**, 1193–1196 (2005).
- [251] de Boer, B., Hadipour, A., Mandoc, M., van Woudenberg, T. & Blom, P. Tuning of metal work functions with self-assembled monolayers. *Adv. Mater.* **17**, 621–625 (2005).

-
- [252] Mathijssen, S. *et al.* Monolayer coverage and channel length set the mobility in self-assembled monolayer field-effect transistors. *Nature Nano.* **4**, 674–680 (2009).
- [253] Chung, K., Neudeck, G. & Bare, H. Analytical modeling of the CMOS-like a-Si:H TFT inverter circuit. *IEEE J. Sol. State Circ.* **23**, 566–572 (1988).
- [254] Yoo, S., , Domercq, B. & Kippelen, B. Efficient thin-film organic solar cells based on pentacene/C₆₀ heterojunctions. *Appl. Lett. Phys.* **85**, 5427–5429 (2004).
- [255] Ayzner, A., Tassone, C., Tolbert, S. & Schwartz, B. Reappraising the need for bulk heterojunctions in polymer-fullerene photovoltaics: The role of carrier transport in all-solution-processed P3HT/PCBM bilayer solar cells. *J. Phys. Chem. C* **113**, 20050–20060 (2009).
- [256] Lee, K. *et al.* Morphology of all-solution-processed “bilayer” organic solar cells. *Adv. Mater.* **23**, 766–770 (2011).
- [257] Ferenczi, T. *et al.* Planar heterojunction organic photovoltaic diodes via a novel stamp transfer process. *J. Phys. Cond. Matter* **20**, 1–8 (2008).
- [258] Wang, D. *et al.* Unexpected solid-solid intermixing in a bilayer of poly(3-hexylthiophene) and [6,6]-phenyl C₆₁-butyric acidmethyl ester via stamping transfer. *Org. Electron.* **11**, 1376–1380 (2010).
- [259] Treat, N. *et al.* Interdiffusion of PCBM and P3HT reveals miscibility in a photovoltaically active blend. *Adv. En. Mater.* **1**, 82–89 (2011).
- [260] Gather, M., Köhnen, A., H., A. F., Becker & Meerholz, K. Solution-processed full-color polymer organic light-emitting diode displays fabricated by direct photolithography. *Adv. Funct. Mater.* **17**, 191–200 (2007).
- [261] K., S. W., Kanai, Ouchi, Y. & Seki, K. Bottom contact ambipolar organic thin film transistor and organic inverter based on C₆₀/pentacene heterostructure. *Organic Electronics* **7**, 457–464 (2006).

- [262] Collins, B. *et al.* Molecular miscibility of polymer-fullerene blends. *J. Phys. Chem. Lett.* **1**, 3160–3166 (2010).
- [263] Kemerink, M. *et al.* Temperature- and density-dependent channel potentials in high-mobility organic field-effect transistors. *Phys. Rev. B* **80**, 115325 (2009).
- [264] Letizia, J., Rivnay, J., Facchetti, A., Ratner, M. & Marks, T. Variable temperature mobility analysis of n-channel, p-channel, and ambipolar organic field-effect transistors. *Adv. Funct. Mater.* **20**, 50–58 (2010).
- [265] Hallam, T. *et al.* Local charge trapping in conjugated polymers resolved by scanning kelvin probe microscopy. *Phys. Rev. Lett.* **103**, 256803 (2009).
- [266] von Hauff, E., Parisi, J. & Dyakonov, V. Field effect measurements on charge carrier mobilities in various polymer-fullerene blend compositions. *Thin Sol. Films* **511**, 506–511 (2006).
- [267] Vanlaeke, P. *et al.* P3HT/PCBM bulk heterojunction solar cells: Relation between morphology and electro-optical characteristics. *Sol. En. Mater. Sol. Cells* **90**, 2150–2158 (2006).
- [268] Müller, C. *et al.* Binary organic photovoltaic blends: A simple rationale for optimum compositions. *Adv. Mater.* **20**, 3510 (2008).
- [269] Camaioni, N., Ridolfi, G., Casalbore-Miceli, G., Possamai, G. & Maggini, M. The effect of a mild thermal treatment on the performance of poly(3-alkylthiophene)/fullerene solar cells. *Adv. Mater.* **14**, 1735 (2002).
- [270] Yang, X., van Duren, J., Janssen, R., Michels, M. & Loos, J. Morphology and thermal stability of the active layer in poly(p-phenylenevinylene)/methanofullerene plastic photovoltaic devices. *Macromolecules* **37**, 2151–2158 (2004).
- [271] Yang, X. *et al.* Nanoscale morphology of high-performance polymer solar cells. *Nano Lett.* **5**, 579–583 (2005).

- [272] Watts, B., Belcher, W., Thomsen, L., Ade, H. & Dastoor, P. A quantitative study of PCBM diffusion during annealing of p3ht: Pcbm blend films. *Macromolecules* **42**, 8392–8397 (2009).
- [273] Wienk, M. *et al.* Efficient methano[70]fullerene/MDMO-PPV bulk heterojunction photovoltaic cells. *Angew. Chemie.* **42**, 3371–3375 (2003).
- [274] Verploegen, E. *et al.* Effects of thermal annealing upon the morphology of polymerfullerene blends. *Adv. Funct. Mater.* **20**, 3519–3529 (2010).
- [275] Brabec, C., Padinger, F., Sariciftci, N. & Hummelen, J. Photovoltaic properties of conjugated polymer/methanofullerene composites embedded in a polystyrene matrix. *J. Appl. Phys.* **85**, 6866–6872 (1999).
- [276] Fisch, R. & Harris, A. Critical behavior of random resistor networks near the percolation threshold. *Phys. Rev. B* **18**, 416 (1978).
- [277] Kesten, H. The critical probability of bond percolation on the square lattice equals $1/2$. *Comm. Math. Phys.* **74**, 41–59 (1980).
- [278] Yang, J. & Nguyen, T.-Q. Effects of thin film processing on pentacene/C₆₀ bilayer solar cell performance. *Org. Electron.* **8**, 566–574 (2007).
- [279] Stephenson, G. *Mathematical Methods for Science Students* (Pearson, Harlow, 1973).